

TUMOR PROMOTING FUNCTIONS FOR THE METABOLIC REGULATOR SIRT5

A Dissertation

Presented to the Faculty of the Graduate School

of Cornell University

In Partial Fulfillment of the Requirements for the Degree of

Doctor of Philosophy

by

Yashira L. Negrón Abril

May 2018

© 2018 Yashira L. Negrón Abril

TUMOR PROMOTING FUNCTIONS FOR THE METABOLIC REGULATOR SIRT5

Yashira L. Negrón Abril, Ph. D.

Cornell University 2018

Cancer is among the leading causes of death worldwide, highlighting the urgent need for identification of new targets and the development of new strategies to intervene against this disease. Recently, it was reported that several members of the sirtuin family (Sirt1-7), the mammalian orthologs of the silent information regulator 2 (Sir2) in *Saccharomyces cerevisiae*, play important roles in carcinogenesis. In mammals there are three mitochondrial sirtuins, SIRT3, SIRT4, and SIRT5. Among these, SIRT5 is the only known enzyme that catalyzes nicotinamide adenine dinucleotide-dependent demalonylation, desuccinylation and deglutarylation. SIRT5 impacts diverse metabolic pathways. One substrate of SIRT5 is carbamoyl phosphate synthase 1 (CPS1), an enzyme involved in the rate-limiting step of the urea cycle. By deacylating CPS1, SIRT5 promotes urea cycle function and clearance of toxic ammonia. *Sirt5*-deficient mice fail to up-regulate CPS1 activity and show elevated blood ammonia during fasting. SIRT5 regulates mitochondrial respiration by targeting glyceraldehyde 3-phosphate dehydrogenase (GAPDH), pyruvate kinase M2 (PKM2), pyruvate dehydrogenase complex (PDH), isocitrate dehydrogenase 2 (IDH2) and succinate dehydrogenase (SDH). SIRT5 also controls glutamine metabolism by targeting glutaminase (GLS), and fatty acid metabolism by activating very long-chain acyl-CoA dehydrogenase (VLCAD), enoyl-CoA hydratase (ECHA) and 3-Hydroxy-3-Methylglutaryl-CoA Synthase 2

(HMGCS2). SIRT5 has also been implicated in regulating NADPH generation and redox potential by deglutarylating glucose 6-phosphate dehydrogenase (G6PD) and desuccinylating superoxide dismutase 1 (SOD1).

Recent studies revealed that *SIRT5* knock-down in human breast and lung cancer cells inhibited their transformed properties, whereas it had no significant effect on the growth of normal cells. Furthermore, it has been shown that the expression levels of *SIRT5* are increased in several human cancers, often due to gene amplification. We hypothesize that SIRT5 is required by cancer cells to regulate the post-translational modifications of key enzymes involved in cancer metabolism. This dissertation aims to (A) elucidate the role of SIRT5 in cancer by using both, *in vitro* and *in vivo* approaches, (B) identify targets for desuccinylation catalyzed by SIRT5 in cancer cells, (C) evaluate the impact of *Sirt5* loss on the expression of genes that might be critical for tumor progression, and (D) test the effect of SIRT5 inhibition in tumor progression.

To study the effect of *Sirt5* deficiency on mammary tumorigenesis, we used MMTV-PyMT transgenic mice, a genetically engineered model in which the animals develop metastatic mammary adenocarcinoma. We tested how mammary tumor latency, multiplicity, size and histological grade are affected by *Sirt5* loss, and found that *Sirt5* knockout (*Sirt5*^{-/-}) mice had delayed mammary tumor onset, significantly increased overall survival, and decreased incidence of lung metastasis as compared to controls. Thus, *SIRT5* loss significantly reduced cancer cell proliferation *in vitro* and mammary tumor growth *in vivo*.

To extend our knowledge of the pro-tumorigenic roles of SIRT5, we used another *in vivo* model that recapitulates glutamine-dependency of human cancers. We used a genetic mouse model in which *Sirt5* is knocked out and *c-Myc* is constitutively activated in B cells. Unexpectedly, *Sirt5* loss in E μ -*Myc* transgenic mice did not affect lymphoma incidence and mortality, even though it targets multiple key metabolic enzymes, suggesting that the pro-tumorigenic roles of SIRT5 are tissue or oncogene-specific.

Immunoblotting for succinyl-lysine levels in mammary tumor tissues from *Sirt5*^{-/-} PyMT and *Sirt5*^{+/+} PyMT mice revealed that there were several proteins with greatly increased succinylation in *Sirt5*^{-/-} PyMT mammary tumors. To identify targets for desuccinylation catalyzed by SIRT5, we performed liquid chromatography-mass spectrometry (LC-MS) analysis on tumor tissues from *Sirt5*^{-/-} PyMT and *Sirt5*^{+/+} PyMT mice. We identified many metabolic enzymes that were highly succinylated in *Sirt5*^{-/-} PyMT mammary tumors, many of which are known to play a critical role in the metabolic reprogramming of cancer cells.

To investigate how *Sirt5* loss affects gene expression, we performed a comparative analysis of expression profiles in mammary tumors from *Sirt5*^{+/+} PyMT and *Sirt5*^{-/-} PyMT mice. We identified significant dysregulation of 129 genes involved in multiple cellular processes such as cellular metabolism, circadian clock, and inflammation. Among these dysregulated genes, serum amyloid A (*Saa*), a gene that encodes for an acute phase protein linked to inflammation, was significantly downregulated in *Sirt5*^{-/-} PyMT mammary tumors. Increased levels of SAA have been linked to tumor pathogenesis and metastasis.

In light of the tumor promoting activity of SIRT5 and the grossly normal phenotype of *Sirt5*^{-/-} mice, we tested SIRT5-selective small molecule inhibitors as cancer therapeutics. Pharmacological inhibition of SIRT5 repressed the anchorage independent growth of cancer cells and suppressed tumor progression *in vivo*. Together, these data demonstrate the importance of SIRT5-regulated post-translational modification in cancer metabolism and highlight novel regulatory events that are important for cancer progression.

BIOGRAPHICAL SKETCH

Yashira L. Negrón Abril was born in Bayamón, Puerto Rico on January 7, 1989. She received her primary education in the same city and graduated from Papa Juan XXIII High School in 2007 with academy excellence and was awarded the Papa Juan XXIII Medal, price that is awarded to the student in highest academic standing within the graduating class.

She attended the University of Puerto Rico, Río Piedras (UPRRP) Campus majoring in Chemistry. As an undergraduate, she participated in the Minority Access to Research Careers (MARC) Program and worked in Dr. Ana Guadalupe's laboratory, where she synthesized styrene and acrylic acid N-hydroxysuccinimide (NAS) ester copolymers that were essential for the generation of an electrochemical biosensor that will enable the detection of Exotoxin A via the ADP-ribosylation of eukaryotic elongation factor 2 (eEF-2) in the presence of β -NAD⁺. In 2012, she graduated magna cum laude with a Bachelor in Chemistry.

During the same year, she joined the Ph.D program in the field of Chemistry and Chemical Biology. In May 2013, she joined the Weiss lab where she started working on a project that aimed to elucidate the roles of mitochondrial sirtuin, SIRT5 in cancer. In addition to her primary project on SIRT5, Yashira also has contributed in two independent projects. She contributed in studying the effects of SIRT2-selective inhibition *in vivo* as well as studying the effects of simultaneous disruption of Ribonucleotide Reductase in mice.

DEDICATION

I DEDICATE THIS WORK TO ALL CANCER PATIENTS

ACKNOWLEDGMENT

I would first like to express my sincere gratitude to my advisor Dr. Robert S. Weiss for his continuous advice and encouragement during the development of this work. His guidance helped me to become a better scientist.

Beside my advisor, I would like to thank the members of my committee: Dr. Hening Lin and Dr. Richard A. Cerione for their guidance and support throughout my Ph.D. study and for their insightful suggestions. Over the years, each has given me superb scientific guidance and demonstrated a sincere interest in my work.

I would also like to thank Dr. Sushabhan Sadhukhan for his expertise, advise and contributions on the SIRT5 project. Over the years, Sushabhan Sadhukhan has given his time to teach me several techniques and aid in experiments. His high standards when conducting research had really impacted me as a scientist. I would also like to acknowledge Dr. Teresa Southard and Andrew Miller for their help in performing the histopathological analysis of mouse tissues.

I would like to express the deepest gratitude to my family. Dad, Grandma, Jennifer and Jorge, you have all provided support, encouragement and interest in my thesis work. In particular, I will like to thank my dad, Jorge L. Negrón Reyes, for all the sacrifices he has made to give us a better education. Thanks for listening to my problems and providing perspective. I would not be who am I today without you all.

Finally, I would like to thank Jean C. Cruz Hernández, who has been a constant source of support and encouragement during the challenges of graduate school and life. You have been patient with me when I'm frustrated, you celebrate with me when even

the littlest things go right, and you are there whenever I need you to just listen. I am truly thankful for having you in my life, and I look forward to achieving and celebrating with you many individual successes.

PUBLICATIONS

- Page, J.L., **Negrón Abril, Y.L.**, *et al.* Simultaneous Disruption of Ribonucleotide Reductase Regulatory Mechanism Causes Synthetic Lethality in Mice. (In preparation).
- Bordeleau, F., Mason, B., Lollis, E., Mazzola, M., Somasegar, S., Califano, J., Montague, C., LaValley, D., Huynh, J., **Negrón Abril, Y.L.**, *et al.* Matrix stiffening promotes a tumor vasculature phenotype. *PNAS*, (2016), 114(3): 492-497.
- Jing, H., Hu, J., He, B., **Negrón Abril, Y.**, *et al.* A SIRT2-selective inhibitor promotes c-Myc oncoprotein degradation and exhibits broad anticancer activity. *Cancer Cell*, (2016), 29:1-14.
- Bordeleau, F., Califano, J., **Negrón Abril, Y.**, *et al.* Tissue stiffness regulates SR protein-mediated splicing of the EDB-fibronectin isoform in tumors. *PNAS*, (2015), 112(27): 8314-8319.
- Enríquez, Y., **Negrón, Y.**, *et al.* Development of an electrochemical biosensor for the detection of an ADP-ribosylating toxin, exo A from *Pseudomonas aeruginosa*. *Journal of Physics: Conference Series*, (2013), 421:012021.
- Petrovic, A., Vantomme, G., **Negrón-Abril, Y.L.**, *et al.* Bulky melamine-based Zn-porphyrin tweezer as a CD probe of molecular chirality. *Chirality*, (2011), 23(9): 808-819.

TABLE OF CONTENTS

Biographical Sketch.....	VI
Dedication.....	VII
Acknowledgments.....	VIII- IX
Publications.....	X
Table of Contents.....	XI-XIII
List of Figures.....	XIV-XVI
List of Tables.....	XVII-XVIII
CHAPTER 1. LITERATURE REVIEW	1-99
1.1 Breast cancer overview.....	1
1.2 Breast cancer type.....	1-7
1.3 Risk factors for breast cancer.....	8-14
1.4 Breast cancer treatments and new approaches.....	14-17
1.5 Cancer metabolism as a therapeutic target.....	17-25
1.6 The importance of specific post-translational modifications in cancer metabolism.....	25-28
1.7 Sirtuins Family.....	28-32
1.8 Nuclear Sirtuins.....	32-39
1.9 Cytoplasmic Sirtuin.....	39-41
1.10 Mitochondrial Sirtuins.....	41-58
1.11 Summary.....	58-61

1.12 References.....	62-99
CHAPTER 2. THE MITOCHONDRIAL SIRTUIN SIRT5 FACILITATES MAMMARY CANCER GROWTH <i>IN VIVO</i>	100-220
2.1 ABSTRACT.....	102-103
2.2 INTRODUCTION.....	104-105
2.3 MATERIALS AND METHODS.....	105-124
2.4 RESULTS.....	125-169
2.5 DISCUSSION.....	169-173
2.6 SUPPLEMENTAL MATERIALS.....	174-213
2.7 REFERENCES.....	214-220
CHAPTER 3. EVALUATING THE EFFECT OF <i>SIRT5</i> LOSS IN LYMPHOMAGENESIS	221-252
3.1 ABSTRACT.....	222-223
3.2 INTRODUCTION.....	224-225
3.3 MATERIALS AND METHODS.....	225-228
3.4 RESULTS.....	228-243
3.5 DISCUSSION.....	237, 244-246
3.6 SUPPLEMENTAL FIGURES AND TABLES.....	247-248
3.7 REFERENCES.....	249-252
CHAPTER 4. CONCLUSION AND FUTURE DIRECTIONS	253-265

4.1 CONCLUSION.....	253-255
4.2 FUTURE DIRECTIONS.....	255-260
4.3 REFERENCES.....	261-265
APPENDIX A. A SIRT2-Selective Inhibitor Promotes c-Myc Oncoprotein Degradation and Exhibits Broad Anticancer Activity.....	266-349
APPENDIX B. Simultaneous Disruption of Ribonucleotide Reductase Regulatory Mechanism Causes Synthetic Lethality in Mice.....	350-428

LIST OF FIGURES

Figure 1.1 Breast cancer incidences by age and race in the United States.

Figure 1.2 Lysine acetylation, malonylation, succinylation and glutarylation.

Figure 1.3 Sirtuins are a family of NAD⁺-dependent protein deacetylases/ADP ribosyltransferases that influences a wide range of biological processes.

Figure 1.4 Schematic illustration of the seven mammalian sirtuins

Figure 1.5 The overall structure of sirtuins.

Figure 1.6 SIRT5-catalyzed demalonylation, desuccinylation and deglutarylation reactions.

Figure 1.7 Crystal structure of SIRT5 bound to NAD⁺.

Figure 1.8 SIRT5 regulates cellular respiration, glutamine metabolism, urea cycle and the pentose phosphate pathway.

Figure 1.9 SIRT5 promotes fatty acid β -oxidation and ketone body synthesis.

Figure 1.10 Cross-cancer alteration summary for SIRT5 (166 studies).

Figure 2.1 Synthetic route for I5-2AM, a SIRT5 inhibitor (Compound I).

Figure 2.2 Synthetic route for MY01170, a SIRT5 inhibitor (Compound J).

Figure 2.3 *SIRT5* is often overexpressed in cancer and it is associated to poor survival.

Figure 2.4 *SIRT5* knock-down inhibits the anchorage independent growth of cancer cells.

Figure 2.5 *Sirt5* loss inhibits transformed MEFs proliferation and ability to growth in soft-agarose

Figure 2.6 *Sirt5* deletion delayed mammary tumor onset and significantly increased overall survival of mice.

Figure 2.7 Histological comparisons of mammary tumors from *Sirt5*^{+/+} PyMT and *Sirt5*^{-/-} PyMT mice.

Figure 2.8 Histopathology of *Sirt5*^{+/+} PyMT and *Sirt5*^{-/-} PyMT mammary tumors.

Figure 2.9 *Sirt5* deletion reduces metastasis burden in PyMT mice.

Figure 2.10 Succinylation levels in mammary tissues from *Sirt5*^{+/+} PyMT and *Sirt5*^{-/-} PyMT mice.

Figure 2.11 Succinylation and glutarylation levels in mammary tumors from *Sirt5*^{+/+} PyMT and *Sirt5*^{-/-} PyMT mice.

Figure 2.12 Metabolic pathways highly targeted by SIRT5.

Figure 2.13 TCA cycle enzymes are targeted by SIRT5.

Figure 2.14 *Sirt5* loss affect the expression of genes involved in different metabolic pathways.

Figure 2.15 Serum amyloid A expression is decreased in *Sirt5*^{-/-} PyMT mammary tumors.

Figure 2.16 SIRT5 inhibition reduces the proliferation of breast cancer cells.

Figure 2.17 Selective inhibition of SIRT5 reduces tumor load in PyMT mice.

Supplemental Figure 2.1 Hierarchical clustering analysis and Volcano plot for genes expressed in *Sirt5*^{+/+} PyMT and *Sirt5*^{-/-} PyMT mammary tumors.

Supplemental Figure 2.2 Potential anti-cancer effects of another SIRT5-inhibitor, MY01170.

Supplemental Figure 2.3 Clonogenic assay performed on AT3 cells upon treatment with different concentrations of I5-2AM.

Supplemental Figure 2.4 Clonogenic assay performed on HEK-293T cells upon treatment with different concentrations of I5-2AM.

Supplemental Figure 2.5 LC-MS data showing the presence of I5-2AM in the serum of I5-2AM-treated mouse after 30 minutes of I5-2AM-IP administration.

Supplemental Figure 2.6 LC-MS data showing the presence of I5-2AM in the abdominal fat of I5-2AM-treated mouse after 30 minutes of I5-2AM-IP administration.

Figure 3.1 Succinylation levels in normal and tumor tissues and *SIRT5* mRNA expression in lymphoma.

Figure 3.2 *Sirt5* deletion does not significantly affect lymphomagenesis *in vivo*.

Figure 3.3 Representative images of tumor tissues, spleen and liver tissues from *Sirt5*^{+/+} E μ -*Myc* and *Sirt5*^{-/-} E μ -*Myc* mice.

Figure 3.4 Succinylation levels in thymic tumors from *Sirt5*^{+/+} E μ -*Myc* and *Sirt5*^{-/-} E μ -*Myc* mice and metabolic pathways highly targeted by SIRT5.

Figure 4.1 Graphical summary model.

LIST OF TABLES

Table 1.1 Leading sites of estimated new cancer cases in the United States by 2017 in female.

Table 1.2 Leading sites of estimated deaths in the United States by 2017 in female.

Table 1.3 Metabolic inhibitors and targets to improve cancer therapeutics.

Table 2.1 Endpoint criteria established for the collection of experimental mice.

Table 2.2 Primers sequences used for RT-qPCR.

Table 2.3 List of hyper-succinylated proteins involved in the TCA cycle.

Table 2.4 List of hyper-succinylated proteins involved in the production and transport of ATP.

Table 2.5 List of hyper-succinylated proteins involved in lipid metabolism.

Table 2.6 List of differentially expressed genes involved in cellular metabolism.

Table 2.7 List of differentially expressed genes associated to the immune system.

Supplemental Table 2.1 Histological classification of mammary tumors into four distinctly identifiable stages of tumor progression.

Supplemental Table 2.2 List of all the succinylated proteins identified in the LC-MS analysis.

Supplemental Table 2.3 List of significantly differential genes between *Sirt5*^{+/+} PyMT and *Sirt5*^{-/-} PyMT mice.

Supplemental Table 2.4 List of GO Biological Pathways enriched with differential genes between *Sirt5*^{+/+} PyMT and *Sirt5*^{-/-} PyMT mice.

Table 3.1 Percent of mice with enlarged thymus, spleen and lymph nodes.

Table 3.2 List of hyper-succinylated proteins involved in the TCA cycle.

Table 3.3 List of hyper-succinylated proteins involved in the production and transport of
ATP.

Table 3.4 List of hyper-succinylated proteins involved in lipid metabolism.

Supplemental Table 3.1 List of mice that did not develop lymphomas nor showed signs
of illness at 17 weeks old or older.

CHAPTER 1. LITERATURE REVIEW

1.1 Breast cancer overview

Cancer is one of the leading causes of morbidity and mortality worldwide, with approximately 14 million new cases in 2012, and 8.8 million cancer deaths in 2015 (Ferlay *et al.* 2015). Among all cancer types, invasive breast cancer is one of the most common cancers diagnosed in women. In 2012, almost 1.7 million people were diagnosed with invasive breast cancer and about 500,000 died from this disease (Ferlay *et al.* 2015). According to the Breast Cancer Organization, 12% of all women in the U.S. will be diagnosed with invasive breast cancer over the course of their lifetime (Breast Cancer Organization, 2017). Statistical studies predict that by 2017, 252,719 women in the U.S will be diagnosed with invasive breast cancer (Table 1.1) (American Cancer Society, 2017).

A continuous decline in breast cancer death rates has been reported over the last two decades. This decline is mostly due to improvements in early detection and treatments. Despite this decline, it is estimated that 40,610 women will die from invasive breast cancer by the end of 2017 (Table 1.2). Furthermore, invasive breast cancer is still the second leading cause of cancer-related death in women in developed countries and the most common cause of death in women in less developed countries (Ferlay *et al.* 2015).

1.2 Breast cancer type

There are many types of breast cancer. Breast cancer is classified based on the type of cells in the breast that are affected. The most common type of breast cancer

Table 1.1 Leading sites of estimated new cancer cases in the United States by 2017 in female.*

Site	Number of cases	Percentage
Breast	252,710	30%
Lung & bronchus	105,510	12%
Colon & rectum	64,010	8%
Uterine corpus	61,380	7%
Thyroid	42,470	5%
Melanoma of the skin	34,940	4%
Non Hodgkin lymphoma	32,160	4%
Leukemia	25,840	3%
Pancreas	25,700	3%
Kidney & renal pelvis	25,700	3%
Others	182,210	21%
All sites	852,630	100%

* Estimated new cases are based on 1999-2013 incidence data reported by the North American Association of Central Cancer Registries (NAACCR). Estimates are rounded to the nearest 10. Data retrieved from the American Cancer Society, 2017.

Table 1.2 Leading sites of estimated deaths in the United States by 2017 in female.*

Site	Number of cases	Percentage
Lung & bronchus	71,280	25%
Breast	40,610	14%
Colon & rectum	23,110	8%
Pancreas	20,790	7%
Ovary	14,080	5%
Uterine corpus	10,920	4%
Leukemia	10,200	4%
Liver & intrahepatic bile duct	9,310	3%
Non-Hodgkin lymphoma	8,690	3%
Brain & other nervous system	7,080	3%
Others	66,430	24%
All sites	282,500	100%

* Estimated deaths are based on 2000-2014 US mortality data, National Center for Health Statistics, Centers for Disease Control and Prevention. Estimates are rounded to the nearest 10. Data retrieved from the American Cancer Society, 2017.

is carcinoma. Carcinomas are tumors that arise from the epithelial component of the breast and can originate in the ducts (ductal carcinoma) or the lobules (lobular carcinoma). Carcinomas are often divided into in situ and invasive. In situ breast cancers remain in a particular area of the breast without spreading. Invasive breast cancers, in the other hand, infiltrate outside of the normal breast tissues and spread to other parts of the body.

Among in situ carcinomas, ductal in situ carcinoma (DCIS) is the most common type. DCIS cells are usually confined in the lining of the milk ducts without spreading throughout the duct walls. This type of cancer, if not treated on time, can become invasive. According to the American Cancer Society, DCIS accounts for about 1 out of every 5 new breast cancer cases in the U.S. Women with DCIS have around 30% risk of recurrence after treatment (American Cancer Society 2017). Recurrence is often observed 5 to 10 years after the initial diagnosis.

The most common type of breast cancer overall is invasive ductal carcinoma (IDC). According to the American Cancer Society, 8 of 10 breast carcinomas are IDC. IDC originates in the cells that line a milk duct in the breast, breaks through the wall of the duct and invades nearby tissues (American Cancer Society 2017). Over time, IDC can spread to the lymph nodes and other parts of the body. The second most common type of breast cancer is invasive lobular carcinoma (ILC). Lobular carcinoma starts in the milk-producing gland and can also metastasize to other parts of the body. ILC accounts for 10% of all the breast cancers diagnosed each year (American Cancer Society 2017).

Other types of invasive breast carcinomas include: adenoid cystic carcinoma, low-grade adenosquamous carcinoma, medullary carcinoma, papillary carcinoma and tubular carcinoma. These types of invasive breast carcinomas are much less common and account for less than 5% of all breast cancers (American Cancer Society 2017).

Breast cancer is also categorized based on the molecular subtypes. There are five main molecular subtypes of breast cancer: Luminal A, Luminal B, human epidermal growth factor receptor-2 (HER2)-overexpressing, Triple-negative and Normal-like breast cancer.

Luminal A

Luminal A breast cancer is the most common subtype of breast cancer, accounting for approximately 50% of all subtypes (O'Brien *et al.* 2010; Voduc *et al.* 2010). Luminal A breast cancers are positive for estrogen and progesterone-receptors (ER+, PR+), and negative for HER2 (HER2-). This type of breast cancer is characterized by low levels of Ki-67, a protein that controls proliferation of cells. Luminal A cancers are usually low-grade cancers (grade 1 or 2). Patients with Luminal A breast cancer have the best prognosis, with high survival rates and low recurrence rates (Voduc *et al.* 2010; Carey *et al.* 2014; Foukakis *et al.* 2016). Given that Luminal A tumors are ER+, they respond well to hormone therapy (Brenton *et al.* 2005).

Luminal B

Luminal B breast cancer is the second most common breast cancer. It accounts for nearly 10-20% of all breast cancers (Voduc *et al.* 2010). Luminal B breast cancers are characterized by low expression of estrogen and progesterone-receptors and high expression of HER2. These tumors tend to grow slightly faster than Luminal A subtypes, and their prognosis is significantly worse (Sorlie *et al.* 2003). However, women with Luminal B tumors tend to have fairly high survival rates, although not as high as those with Luminal A tumors (Metzger-Filho *et al.* 2013; Foukakis *et al.* 2016). Combined therapeutic strategies of chemotherapy and hormonal treatment are often used to treat Luminal B cancers (Ades *et al.* 2014).

HER2-overexpressing

The HER2-overexpressing subtype accounts for about 5-15% of all breast cancers (Voduc *et al.* 2010). Tumors that overexpress HER2, are characterized by overexpression of other genes in the HER2 amplicon such as: GRB7, and PGAP3 (Dai *et al.* 2014). HER2 overexpressing tumors tend to grow faster than the luminal subtype and are more likely to be of grade 3. Compared to the luminal subtypes, patients with HER-overexpressing tumors, have a worse prognosis and high risk of early relapse (Brenton *et al.* 2005). Unlike other subtypes, HER2-overexpressing tumors can be treated with targeted therapies aimed at the HER2 protein. Among those targeted therapies include: Herceptin, Perjeta, Kadcylla, all of which are monoclonal antibodies, and Tykerb, a kinase inhibitor (Slamon *et al.* 2011).

Triple-Negative

Triple-Negative breast cancers (TNBC) are all tumors that lack the expression of estrogen and progesterone-receptors, as well as HER2. There are several subgroups of triple-negative breast cancer; including basal-like, mesenchymal stem-like, mesenchymal-related and immunomodulatory groups. Among these subgroups, basal-like breast cancers are the most frequent subtype of TNBC, accounting for 15-20% of all breast cancers (Prat *et al.* 2014). Unlike other subtypes, TNBC is associated with younger patient age and commonly develop in African-American and Hispanic women (Carey *et al.* 2006). In addition, most *BRCA1*-related breast cancers are both triple negative and basal-like (Hartman *et al.* 2012; Carey *et al.* 2014). Patients with TNBC typically have a relatively poor prognosis when compared to other breast cancer subtypes due to an inherently rapid growth and invasiveness, and the lack of molecular targets for therapy (Perou *et al.* 2000; Rakha *et al.* 2008). The most common treatment for TNBC patients is chemotherapy.

Normal-like

Normal-like breast cancer accounts for about 5-10% of all breast carcinomas. This subtype of breast cancer features expression of the hormone-receptors (ER+ and PR+) but is HER2 negative. In addition, like Luminal A cancers, normal-like breast cancers have low levels of the protein Ki-67. Although the Normal-like breast subtype shares the same hormone receptor status as Luminal A, it has different gene expression patterns and a slightly worse outcome than the Luminal A subtype (Breast Cancer Organization, 2017).

1.3 Risk factors for breast cancer

Doctors and researchers cannot explain why some individuals develop cancers while others don't. However, research has demonstrated that there are certain risk factors that increase the chances of developing cancer. Among the risk factors that increase the risk of developing invasive breast cancer include: gender, aging, genetic alterations, race, hormone changes, obesity, lack of exercise and alcohol consumption (American Cancer Society, 2017).

Gender and Aging

The main risk factors for developing invasive breast cancer are gender and aging. The risk of developing invasive breast cancer in women is much more higher than men. There are estimated to be about 250,000 new cases of breast cancer this year in American women, while approximately 2,000 cases of breast cancer are expected to be diagnosed in American men (American Cancer Society, 2017). The main reason for the difference in breast cancer rates between women and men is because women breast cells are highly proliferative and responsive to hormone changes while men breast cells are mostly inactive and the levels of estrogen are very low. The responsiveness of female breast cells to hormonal changes increases significantly the risk of women to develop breast cancer when compared to men.

The risk of developing invasive breast cancer rises sharply as women age. According to the American Cancer Society, women under 20 years old have 0.1% probability of developing invasive breast cancer, while women in their 30s, 40s and 50s have 0.5%, 1.5% and 2.3% probability respectively. However, a woman's risk of

invasive breast cancer increases to 3.5% or higher if she is 60 or older (American Cancer Society 2017) (Figure 1.1A).

There is no single explanation for why an aging body is more susceptible to cancer development. However, accumulating evidences suggests that breast cancer develop in older women because cells accumulate more mutations the longer we live (DePinho 2000). In addition, studies have shown that aging is associated with gradual breast tissue changes that alter gene expression and induces a more favorable microenvironment for cancer cells to growth (LaBarge *et al.* 2016).

Genetic alterations

The second risk of breast cancer is genetic alterations. About 5-10% of breast cancer can be linked to inherited genetic mutations, such as, mutations of the *BRCA* genes (Easton 1999). *BRCA* are genes produce tumor suppressor proteins that are involved in the repair of damaged DNA. Mutations of any these genes, may affect the proper repair of damaged DNA and therefore, induce genetic alterations that can lead to cancer. Epidemiologic studies have shown that women who have an abnormal *BRAC1* and/or *BRAC2* can have up to 80% risk of being diagnosed with invasive breast cancer (Francken et.al, 2013). In addition to *BRAC1* and *BRAC2* genes, alteration of other genes, such as *ATM*, *BRIP1*, *CDH1*, *PALB2*, *PTEN*, *TP53* and *CHEK2* are associated with invasive breast cancer (Mavaddat *et al.* 2010). However, mutations in these genes are much less common and do not seem to increase the risk of developing invasive breast cancer to the same extent as abnormal *BRAC1* and *BRAC2* genes.

Nevertheless, 85% of invasive breast cancers occur in women with no family history of breast cancer (American Cancer Society, 2017).

Race

Race is another important factor that correlates with the risk of occurrence of invasive breast cancer. Breast cancer incidence and mortality rates vary substantially by race in the U.S. According to the American Cancer Society, White women are slightly more likely to develop invasive breast cancer (128.7 per 100,000) when compared to African American (125.5 per 100,000), Asian (98.5 per 100,000), Hispanic (93.1 per 100,000) and American Indian (82.2 per 100,000) women (Copeland *et al.* 2017) (Figure 1.1B). However, the incidence of breast cancer-associated death is higher in African American women. This is due to the fact that African American women tend to develop more aggressive breast cancer. Hispanics, on the other hand, tend to develop breast cancer at younger age and often develop invasive breast cancers that lack the expression of estrogen (ER-) and progesterone (PR-) receptors (Ban and Godellas 2014).

Hormone changes

Estrogens are natural hormones that are essential for the development of the female reproductive system. Before menopause, estrogens are mainly produced in the ovaries. After menopause, they are produced in fat tissues. Studies have shown that high estrogen levels increase the chances of developing breast cancer, mainly in

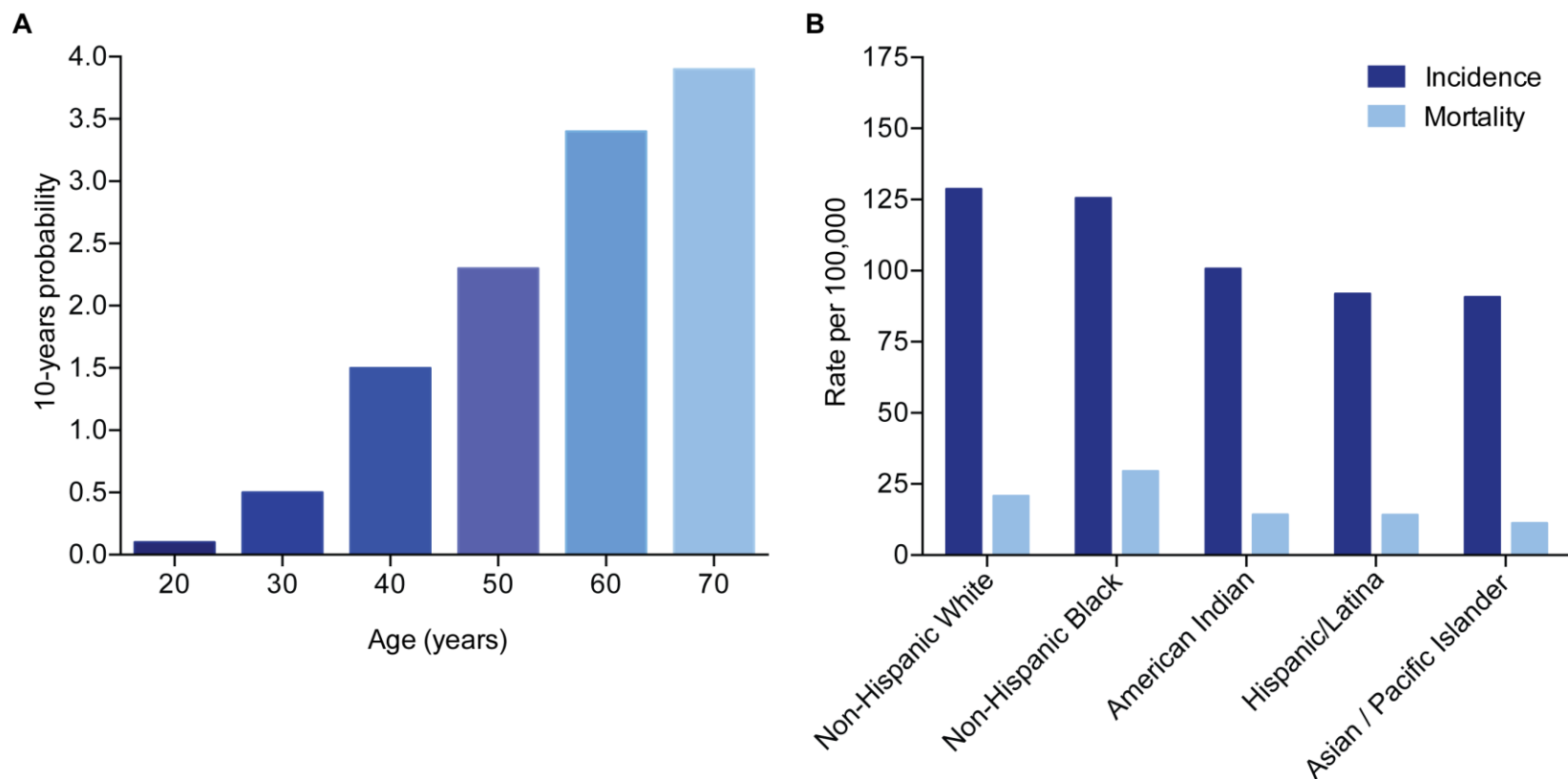


Figure 1.1 Breast cancer incidences by age and race in the United States. (A) Age-specific probability of developing invasive breast cancer among women. The probability is among those females free of cancer at beginning of age interval. Based on cases diagnosed 2012-2014. (B) Female breast cancer incidence (2010-2014) and mortality (2011-2015) rates by race. Statistics are based on data from Contract Health Service Delivery Area (CHSDA) counties. Date retrieved on February 12, 2018 (American Cancer Society 2017; Copeland *et al.* 2017).

postmenopausal women (Key *et al.* 2011; Zhang *et al.* 2013). Similarly, increased breast cancer risk is observed in women who use menopausal hormone treatments with estrogen and progestin. Women who used the hormone treatment for 5 years have a 15% risk of developing breast cancer, while those who have used it for 10 years has a 34% risk (Ban and Godellas 2014).

The relation between the use of oral contraceptives and breast cancer risk is still controversial. Some studies of oral contraceptives suggest that the risk of developing breast cancer increases 24% in women who use oral contraceptives when compared to those who have never used them (Ban and Godellas 2014). On the other hand, other studies have shown no association between the use of oral contraception and the risk of breast cancer (Westhoff 1999; Marchbanks *et al.* 2002).

Pregnancy and breastfeeding, on the other hand, decrease breast cancer risk by reducing the number of menstrual cycles in a woman and consequently, the cumulative exposure to endogenous hormones (Ruso *et al.* 2005; Britt *et al.* 2007). A meta-analysis of eight studies revealed that women who give birth to their first child at age 35 or younger tend to get a protective benefit from pregnancy (Ewertz *et al.* 1990). Global gene expression and epigenetic profiles of multiple cell types from normal breast tissue of nulliparous and parous women revealed that pregnancy at young ages (20-30) lower the number of mammary gland progenitors and therefore, reduces the probability for these cells to become malignant (Choudhury *et al.* 2013).

Obesity

Obesity is a growing health problem in the U.S. and growing evidences suggest a direct correlation between obesity and increased risk of breast cancer development. Multiple studies have demonstrated that, in postmenopausal women, a higher body mass index increases the risk of breast cancer. A 5-unit increase in body mass index is associated to with a 12% increase risk in developing breast cancer (Renehan *et al.* 2008). Furthermore, women who are overweight or obese at the time of breast cancer diagnosis are at increased risk of recurrence (30%) and death (50%) when compared with leaner women (Sparano *et al.* 2012).

The link between obesity and breast cancer is still under investigation. However, some evidence suggests that excess fat tissue in obese women results in elevated serum estrogen levels that ultimately cause breast cancer development (Margot and Grossmann 2009).

Alcohol consumption

Alcohol consumption is consistently associated with risk of breast cancer. Compared to other tissues, women's breast tissue seems to be very sensitive to the carcinogenic effects of alcohol. Several epidemiologic studies have shown that the risk of breast cancer is significantly increased by 4–15% for light alcohol consumption (Chen *et al.* 2011; Seitz *et al.* 2012). Furthermore, it has been shown that 4-10% of breast cancers in the U.S. are attributed to alcohol consumption.

The mechanisms by which alcohol consumption increases breast cancer risk remain unclear. Some evidence suggests that alcohol increases breast cancer risk by damaging the DNA of breast cells and by altering epigenetic regulation of gene

expression (Varela-Rey *et al.* 2013). Other studies suggest that alcohol can increase estrogen levels and other hormone associated with hormone-receptor-positive breast cancer (Meng *et al.* 2000; Seitz and Maurer 2007).

1.4 Breast cancer treatments

Breast cancer treatments are chosen based on the type and the stage of the cancer. Breast cancer treatments can be classified into two types: local treatment and systemic treatment. While local treatment (e.g. surgery and radiation therapy) is used to remove the cancer from a limited area, systemic treatment (e.g. chemotherapy, hormone therapy and targeted therapy) is often used to get rid of all cancer cells that may spread from the breast to other parts of the body.

Local treatment

Surgery

The aim of surgery is to remove the entire tumor from the breast. In some cases, the lymph nodes in the axillary nodes may also be removed. Surgery of the breast can be divided into two types: lumpectomy or mastectomy (Robinson 2007). When lumpectomy of the breast is performed, only the tumor and a small portion of normal tissue that surrounds the tumors is removed. Mastectomy, in the other hand, removes the whole breast, including the nipple and parts of the skin. This type of surgery is often performed when the tumor is large, diffused or located in the center of the breast. Mastectomy is also performed when there are multiple tumors in the breast.

Radiation therapy

Radiotherapy is another type of local treatment that is often used to treat women who have early stage breast cancer. It is also used in most patients who have lumpectomy and sometimes, it is recommended after mastectomy. The main purpose of treating patients with radiotherapy is to kill cancer cells that might be left in the breast after surgical removal of the tumors. Studies have shown that radiation therapy after mastectomy can reduce the risk of recurrence by up to 70% (Orecchia 2014).

Systemic treatment

Chemotherapy

Chemotherapy is one of the main systemic treatments used to destroy cancer cells. Chemotherapy may be given to breast cancer patients before surgery to shrink the size of the tumor. It is also used after surgery to reduce the risk of recurrence. There is a wide range of chemotherapy medicines that are used to treat breast cancer, including, Capecitabine, Carboplatin, Doxorubicin, 5-fluorouracil, Gemcitabine and Paclitaxel. The mechanism of action of these chemotherapies varies, however most of them cause DNA damage or inhibit DNA synthesis (Plunkett *et al.* 1995; Longley *et al.* 2003; Walko *et al.* 2005; Tacar *et al.* 2013; Dasari and Tchounwou 2015). Paclitaxel on the other hand, blocks cell division by inhibiting the disassembly of microtubules during mitosis (Jordan and Wilson 2004).

These chemotherapy medicines can be given as an individual dose or in combination. Studies have shown that combination of chemotherapy medicines lowers the risk of cancer recurrence in patients with early-stage breast cancer, and significantly

reduces the tumor (30-60%) in patients with advanced breast cancer (Bonadonna *et al.* 1976; American Cancer Society 2017). Although chemotherapy can be beneficial in treating breast cancers, these treatments often have significant side effects, including, mouth sores, hair loss, nausea, vomiting, and diarrhea.

Hormone therapy

Hormone therapy is a form of systemic treatment used to block the growth of tumors that express estrogen (ER+) or progesterone (PR+) receptors (American Cancer Society 2017). These types of breast cancers depend on the female's hormones (estrogen and progesterone) ability to promote growth, and blockage of these hormones by hormone therapy significantly reduces tumor growth. There are several strategies to treat hormone sensitive tumors. Among those include: blocking ovary function, blocking estrogen production or blocking estrogen effects.

Hormone therapy is often used after surgery to reduce the risk of relapse, and sometimes is used before surgery. Studies have shown that five years of hormone therapy treatment after surgery can reduce the risk of breast cancer recurrence and improve overall survival (Early Breast Cancer Trialists' Collaborative Group *et al.* 2011; Dowsett *et al.* 2015). Furthermore, clinical trials have shown that hormone therapy can also be used to prevent breast cancer in women who are at increased risk of developing the disease (Vogel *et al.* 2006; Cuzick *et al.* 2015).

Targeted therapy

Targeted therapy is a treatment that targets breast cancer's specific genes or proteins that contribute to breast cancer growth and survival. Most targeted therapies use small molecule drugs or monoclonal antibodies that specifically target cancer cells. Among the targeted therapies that are currently used to treat breast cancer include: mTOR inhibitors, HER2 receptor inhibitors, PARP inhibitors and cyclin-dependent kinase 4/6 inhibitors (Mitri *et al.* 2012; Vicier *et al.* 2014; Ponec *et al.* 2017; Griggs and Wolff 2017). Clinical studies have shown that combination of Herceptin, an mTOR inhibitor, with chemotherapy increases the overall survival of women with early stage HER2-positive breast cancers (Perez *et al.* 2014). Although this type of treatment mostly targets cancer cells and not healthy cells, there are several drawbacks: (1) cancer cells often become resistant to the therapy, (2) biopsy of the tumor might be needed to determine whether a patient can be treated with a specific targeted therapy (3) drugs for some targets are hard to develop.

1.5 Cancer metabolism as a therapeutic target

Significant progress has been made in breast cancer treatment over the past decades, yet breast cancer is still one of the leading causes of cancer-related death in women, underlining the need for new therapeutic treatments. Recently, altered metabolism has become one of the hallmarks of cancer and drug resistance (Pavlova and Thompson 2016). Therefore, much more interest has been focused on targeting cellular metabolism as a promising strategy to target cancer and to overcome drug resistance.

The metabolism of breast tumors, like most cancers, heavily relies on the use of both aerobic glycolysis and glutamine catabolism to support cancer cell growth (Long *et al.* 2016). For more than a century, it has been known that most cancer cells increase glucose consumption to produce the necessary nutrients for proliferation. This metabolic shift, known as Warburg effect, can be observed regardless of oxygen availability (Warburg, 1925). Although aerobic oxidation is an inefficient pathway for energy production, cancer cells rely on aerobic glycolysis for several reasons: i) Glycolysis provides most of the building blocks required for cell proliferation. Since cancer cells grow faster than normal cells, they not only need energy, but also need metabolic intermediates to synthesize macromolecules, such as nucleic acids, lipids and proteins, which are required for cancer growth and proliferation (Kroemer *et al.* 2008; Lunt and Vander 2011). ii) Aerobic glycolysis maintains high glycolytic flux through lactate production. Much of the glucose is converted to lactate. The conversion of pyruvate to lactate regenerates NAD⁺; which is essential for high glycolytic flux maintenance (Long *et al.* 2016). iii) Glycolysis helps cancer cells to grow under hypoxic environment. Cancer cells excrete high levels of lactate into the extracellular space, which acidifies the tumor environment. The acidic environment provides an advantage to cancer cells to grow, invade, metastasize and suppress anticancer T cell immune responses (Fischer *et al.* 2007; Gillies and Gatenby 2007; Doherty and Cleveland 2013).

The expression of many glycolytic enzymes has been shown to be dysregulated in breast cancer. GLUT1, GLUT2 and GLUT3 are often amplified in several subtypes of breast cancer. Studies have also shown a correlation between glycolysis levels and expression of GLUT (Choi *et al.* 2013; Gao *et al.* 2013). The molecular subtypes of

invasive breast cancer, TNBC and HER-2 positive, exhibit the highest expression of GLUT-1 when compared to other molecular subtypes and show the higher levels of glycolysis (Choi *et al.* 2013). Increased expression of lactate dehydrogenase isoforms (LDHA, LDHB), have also been observed in breast cancer (Zhao YH *et al.* 2009). Abrogation of LDHA and LDHB impair breast cancer cell proliferation and caused tumour regression *in-vivo* (Fantin *et al.* 2006; McClelland *et al.* 2012).

In addition to altered glucose metabolism, cancer cells exhibit a notorious dependency on glutamine metabolism for their survival and enhanced proliferation. Glutamine breakdown by-products serve as a carbon source to maintain the citric acid cycle and to continue fatty acid synthesis (Wise *et al.* 2011). After entering cells, glutamine is hydrolyzed by glutaminase (GLS) to glutamate and ammonia. Glutamate can be converted to α -ketoglutarate and enter the TCA cycle to supply energy and intermediates (e.g. nonessential amino acids such as aspartate, asparagine, glutamate and proline) for cell growth. This process also produces NADH and FADH₂; which are essential for the maintenance of mitochondrial integrity and function. Glutamate can also serve as a nitrogen donor to amino acids. Immunohistochemical staining of breast cancer tissues indicated that among the different molecular subtypes of breast cancer, HER-2 positive and TNBC exhibited the most frequent expression of glutamine metabolism related proteins, including glutaminase 1 (GLS1), glutamate dehydrogenase (GDH) and amino acid transporter-2 (ASCT2) (Kim *et al.* 2013).

Beside these two pathways, breast cancer deregulates fatty acid metabolism to support its malignant transformation. Cancer cells often increase fatty acid synthesis to provide lipids for membrane biogenesis and signaling molecules (Currie *et al.* 2014). In

response to nutrient deprivation conditions, fatty acid can also be consumed through β -oxidation to provide ATP and total NADPH for cancer cell survival (Qu *et al.* 2016). Recent studies have shown that the expression and activity of many enzymes involved in fatty acid synthesis are upregulated in many types of cancers (Menendez and Lupu 2007; Vander Heiden *et al.* 2009; Cairns *et al.* 2011). Among those, fatty acid synthase (FASN), has been reported to be upregulated in breast cancer and associated with tumor recurrence and poor prognosis (Alo' *et al.* 1996; Menendez and Lupu 2007; Vazquez-Martin *et al.* 2008).

These metabolic changes, together with the alteration of several signaling pathways (e.g. PI3K/Akt pathway), allow cancer cells to convert available resources into biomass in efficient way, and to support their proliferative phenotype. Here, I discuss the main metabolic reprogramming of breast cancer and the recent advances in targeting cancer metabolism and the development of new therapeutic strategies.

Targeting glycolytic enzymes

Given that the glycolytic pathway requires multiple enzymes to transport and breakdown glucose, researchers have developed anticancer drugs that target selected enzymes in the glycolytic pathway. Among these enzymes include, glucose transporters (GLUT), Hexokinase (HK) and lactate dehydrogenase A (LDHA) (Table 1.3).

To acquire additional glucose, cancer cells up-regulate the expression of multiple glucose transporters. Among the 14 glucose transporters, GLUT1 seems to be the main glucose transporter in breast cancer. Research has shown that inhibition of GLUT1 halts cell proliferation of MCF-7 breast cancer cells (Liu *et al.* 2012). In addition, a

synergistic effect has been observed when WZB117 (GULT1 inhibitor) is combined with other anticancer drugs such as cisplatin (Liu *et al.* 2012).

HK plays an important role in glycolysis, and inhibition of HK with deoxyglucose (2-DG) or 3-bromopyruvate (3-BrPA) increases cell death and combats drug resistance when combined with chemotherapy (Table 1.3). Clinical studies have shown that combination of 2- DG with trastuzumab, an HER2 targeted cancer therapy, potentiates the tumor-destroying effects and overcome trastuzumab resistance (Zhao *et al.* 2011). On the other hand, inhibition of HK-2 with 3BrPA has been shown to improve tamoxifen cytotoxicity of breast cancer cell lines by increasing oxidative stress (Attia *et al.* 2015). Studies in mice have shown 3Br-PA treatment significantly abolishes breast cancer growth, without damaging normal tissues (Gao *et al.* 2016). Although the potent anticancer effects of this drug, 3-BP has not yet been approved for use in humans.

LDHA catalyzes the final step in the glycolytic pathway, the conversion of pyruvate to lactate. Increased evidence has shown that LDHA plays a critical role in tumor maintenance. Inhibition of LDHA selectively inhibits the growth of HER2+ overexpressing breast cancer cells and overcome trastuzumab-resistance (Zhao *et al.* 2011). Furthermore, downregulation of LDHA re-sensitizes taxol-resistant cells to taxol treatment (Zhou *et al.* 2010).

Targeting glutamine metabolism

In addition to altered glucose metabolism, cancer cells exhibit a notorious dependency on glutamine metabolism for their survival and enhanced proliferation (Long *et al.* 2016). Targeting glutamine transport and glutamine addiction has become a

potential anticancer therapeutic strategy. Blockage of GLS with CB-839 has shown to halt the growth of TNBC cells lines, but not in ER+ cell lines (Gross *et al.* 2014). Clinical data have shown that combination of CB-839 with paclitaxel in patients with TNBC increases therapy response and overcomes resistance to paclitaxel (Calithera Biosciences 2016). Inhibition of glutaminase C (GAC) with benzophenanthridinone, known as 968, induces cytotoxic effects in breast cancer cell lines and stimulates the down-regulation of anti-apoptotic and metastatic genes (Table 1.3). Furthermore, 968 enhances the sensitivity of MDA-MB 231 cancer cells to doxorubicin chemotherapy (Katt *et al.* 2012; Simpson *et al.* 2012).

Targeting fatty acid metabolism

Breast cancer, like most cancers, also shows alteration of multiple lipogenic pathways (Menendez and Lupu 2007; Hilvo *et al.* 2011). The most common altered enzyme involved in lipid metabolism is FASN. Studies have shown that inhibition of FASN causes depletion of the end product long chain fatty acids and the accumulation of the substrate malonyl-CoA (Pizer *et al.* 2000). Furthermore, FASN blockage with cerulenin overcomes HER2-induced breast cancer resistance to docetaxel and induces synergistic chemosensitization to other chemotherapy agents, such as, paclitaxel and vinorelbine (Menendez *et al.* 2004; Menendez *et al.* 2005). However, inhibition of FASN has shown dramatic effects on whole body metabolism causing substantial weight loss in mice (Loftus *et al.* 2000). Another key enzyme involved in altered lipid metabolism is monoacylglycerol lipase (MAGL). MAGL is elevated in aggressive cancer cells and accumulating evidence suggests that it promotes cancer cell survival and migration by

controlling free fatty acid (FFA) levels (Nomura *et al.* 2010). Inhibition of MAGL decreases lipid messenger production and the metastatic potential of breast cancer cells (Nomura *et al.* 2010).

Targeting the TCA cycle

The tricarboxylic acid (TCA) cycle is a central hub for the production of ATP, macromolecules and redox balance. Aberrant function of the TCA cycle has been implicated in cancer progression, and increased efforts have been made to target TCA cycle enzymes as a therapeutic strategy. Some cancers harbor mutations in metabolic enzymes, such as IDH1, IDH2, FH and SDH, leading to metabolic alterations that promote and support cancer cell growth (Dang *et al.* 2009; Sudarshan *et al.* 2009; Bardella *et al.* 2011; Kim *et al.* 2013; Sajnani *et al.* 2017). Among all the TCA cycle enzymes, sporadic cases of fumarate hydratase (FH) and isocitrate dehydrogenase 1/2 (IDH1/2) mutations have been reported in breast cancer (Lehtonen *et al.* 2006; Cerami *et al.* 2012). In addition, studies have shown down-regulation of oxoglutarate dehydrogenase (OGDH) in breast cancer (Fedorova *et al.* 2015). Recently, the U.S. Food and Drug Administration (FDA) approved Idhifa (enasidenib) for the treatment of adult patients with relapsed or refractory acute myeloid leukemia (AML) who have IDH2 mutation (U.S. Food and Drug Administration 2017). Clinical data revealed that 19% of 199 people with AML treated with Idhifa showed complete remission after being treated with Idhifa for approximately 8 months (U.S. Food and Drug Administration 2017). Interestingly, among the reported drugs that target TCA cycle enzymes, none have been reported in breast cancer.

Table 1.3 Metabolic inhibitors and targets to improve cancer therapeutics.

Targeted pathway	Targeted enzyme	Metabolic Inhibitors	Cancer therapeutics*	References
Glycolysis	GLUT1	WZB117	Cisplatin/paclitaxel	Liu Y <i>et al.</i> 2012
	HK	2-DG	Trastuzumab	Zhao Y <i>et al.</i> 2011
		3-BrPA	Tamoxifen	Attia Y <i>et al.</i> 2015
	LDHA	Oxamate	Trastuzumab	Zhao Y <i>et al.</i> 2011
Glutamine metabolism	GAC	968	Paclitaxel	Katt W <i>et al.</i> 2012
	GAC	968	Doxorubicin	Simpson NE <i>et al.</i> 2012
Fatty acid metabolism	FASN	Cerulenin	Docetaxel	Menendez JA <i>et al.</i> 2004
			Vinorelbine	Menendez JA <i>et al.</i> 2004
			Paclitaxel	Menendez JA <i>et al.</i> 2005

*Most metabolic therapeutics are combined with conventional cancer treatments to improve the efficacy of cancer therapy and to overcome therapeutic resistance.

Summary

In summary, advances in understanding breast cancer metabolism have led to the discovery of metabolic dependencies that can serve as potential therapeutic strategies. Inhibition of metabolic enzymes has shown the ability to enhance the efficacy of existing therapies and in many cases has also overcome drug resistance. Although most metabolic therapies have only been evaluated in preclinical models, in recent years, an increased number of metabolic therapies have been pre-clinically tested. Although more efforts are needed to fully understand breast cancer metabolic dependencies, recent advances suggest that metabolic profiling can provide new opportunities to improve breast cancer treatment.

1.6 The importance of specific post-translational modifications in cancer metabolism

Post-translational modifications (PTM) can influence a broad range of biological processes such as gene regulation, cell proliferation and apoptosis by affecting enzymes activity, protein turnover and localization, protein-protein interactions and protein stability (Hitosugi and Chen 2014). Given the pivotal role of PTMs in the regulation of cellular processes, there is a constant effort in understanding the roles of PTMs in influencing cell signaling and metabolic pathways that contribute to the diverse metabolic phenotypes found in cancer.

To date, more than a hundred types of PTMs have been identified. Among those, lysine malonylation, succinylation and glutarylation are new post-translational modifications that have been implicated in regulating metabolic enzymes (Zhang *et al.*

2011; Peng *et al.* 2011; Xie *et al.* 2012; Tan *et al.* 2014). These three lysine modifications are structurally similar, but have the potential to regulate different proteins in multiple metabolic pathways (Figure 1.2) (Park *et al.* 2013; Weinert *et al.* 2013; Radin *et al.* 2013; Tan *et al.* 2014). Most of the proteins known to be malonylated are found in the cytoplasm, whereas the vast majority of succinylated and glutarylated proteins are found in the mitochondria. However, there is a subset of non-mitochondrial proteins that are succinylated and glutarylated (e.g. ribosomes) (Xie *et al.* 2012). Pathways analysis has shown that malonylation is mostly enriched in the glycolytic pathway, whereas the top metabolic pathways identified as having succinylated and glutarylated lysines include fatty acid metabolism and amino acid metabolism (Park *et al.* 2013; Radin *et al.* 2013; Tan *et al.* 2014; Nishida *et al.* 2015). No clear picture has emerged on the regulatory role of malonylation, succinylation, and glutarylation. Some proteins show increased activity in the acylated states, while other proteins show reduced activity.

Despite the advances on discovering proteins that are acylated, less is known about the enzymes that catalyze acylation of targeted proteins (Wagner and Payne 2013). Lysine malonyltransferase, succinyltransferase, or glutaryltransferase enzymes have not been identified in any subcellular compartment (Park *et al.* 2013; Weinert *et al.* 2013). Recent evidences support the idea that protein acylation is predominantly mediated in a non-enzymatic manner and it is favored by the high concentrations of acyl-CoA (Newman *et al.* 2012; Wagner and Payne 2013).

In the context of cancer, it has been shown that oncogenic activation can alter PTM signaling cascades that contribute to a complete reprogramming of metabolism. To date, limited information is available on the contributions of lysine malonylation,

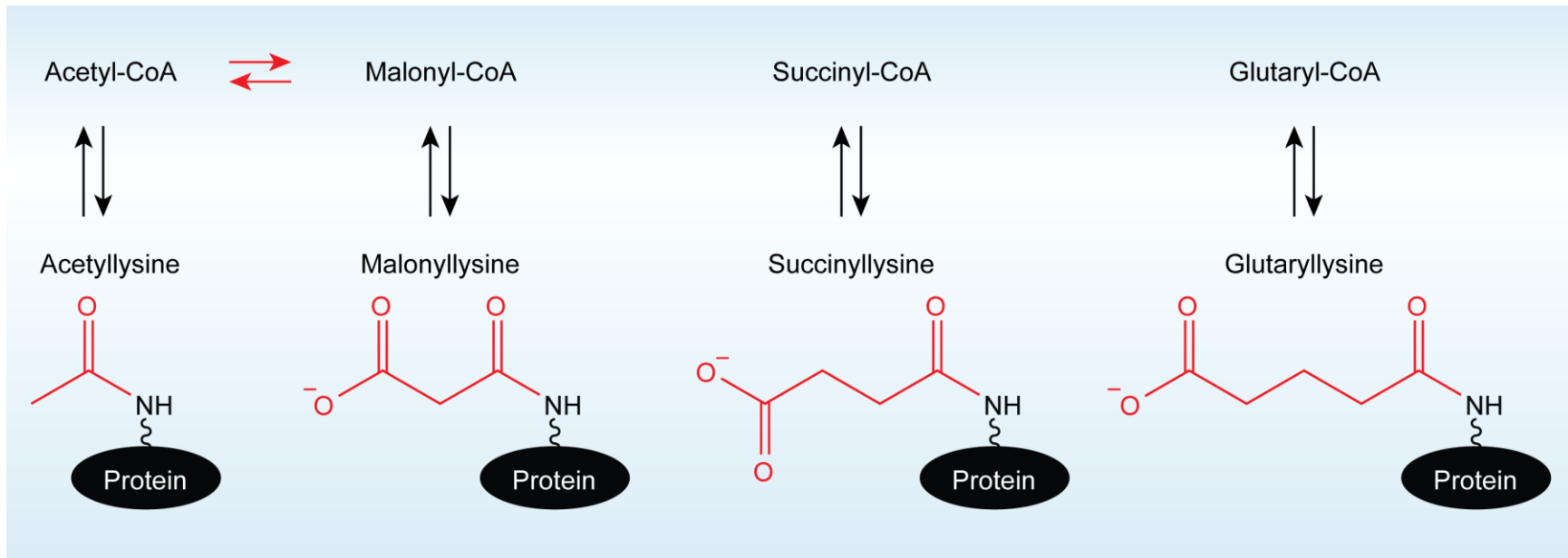


Figure 1.2 Lysine acetylation, malonylation, succinylation and glutarylation. The addition of acyl groups from acyl-CoA to lysine residues may be non-catalytic or proceed by as yet unknown acyltransferases. Lysine malonylation, succinylation, and glutarylation are targeted for removal by the NAD⁺-dependent deacylase SIRT5.

succinylation and glutarylation to cancer cells metabolic reprogramming. Understanding the roles of these new PTMs in cancer metabolism will help to identify and generate novel therapies to target cancer.

1.7 Sirtuins Family

1.7.1 Sirtuins are NAD⁺-dependent deacylases

Sirtuins are a family of ubiquitously expressed and evolutionarily conserved nicotinamide adenine dinucleotide (NAD⁺)-dependent deacylases/mono-ADP-ribosyltransferases that influence a wide range of cellular processes, including longevity, cell cycle, transcription, metabolism, inflammation and genome stability (North and Verdin 2004; Chalkiadaki *et al.* 2015) (Figure 1.3). In mammals, there are seven sirtuins (SIRT1-SIRT7), each with diverse sub-cellular localization. SIRT1, SIRT6 and SIRT7 are mainly localized in the nucleus, whereas SIRT3, SIRT4 and SIRT5 are found in the mitochondria. SIRT2 is localized in the cytoplasm, but translocates to the nucleus during G2/M phase (Ford *et al.* 2006; Tanno *et al.* 2007; Michan and Sinclair 2007; Haigis and Sinclair 2010) (Figure 1.4). Besides the distinct cellular localizations, the seven mammalian sirtuins exert different enzymatic activities. SIRT1, SIRT2 and SIRT3 display robust deacetylation activity (North *et al.* 2003). SIRT5 functions as a protein demalonylase, desuccinylase and deglutarylase, while SIRT6 removes long-chain acyl modifications and also has been reported to have mono-ADP-ribosyl transferase activity. (Du *et al.* 2011; Tan *et al.* 2014). The activities of SIRT4 and SIRT7 are still unclear. Studies have reported that SIRT4 catalyze ADP-ribosyltransfer of glutamate

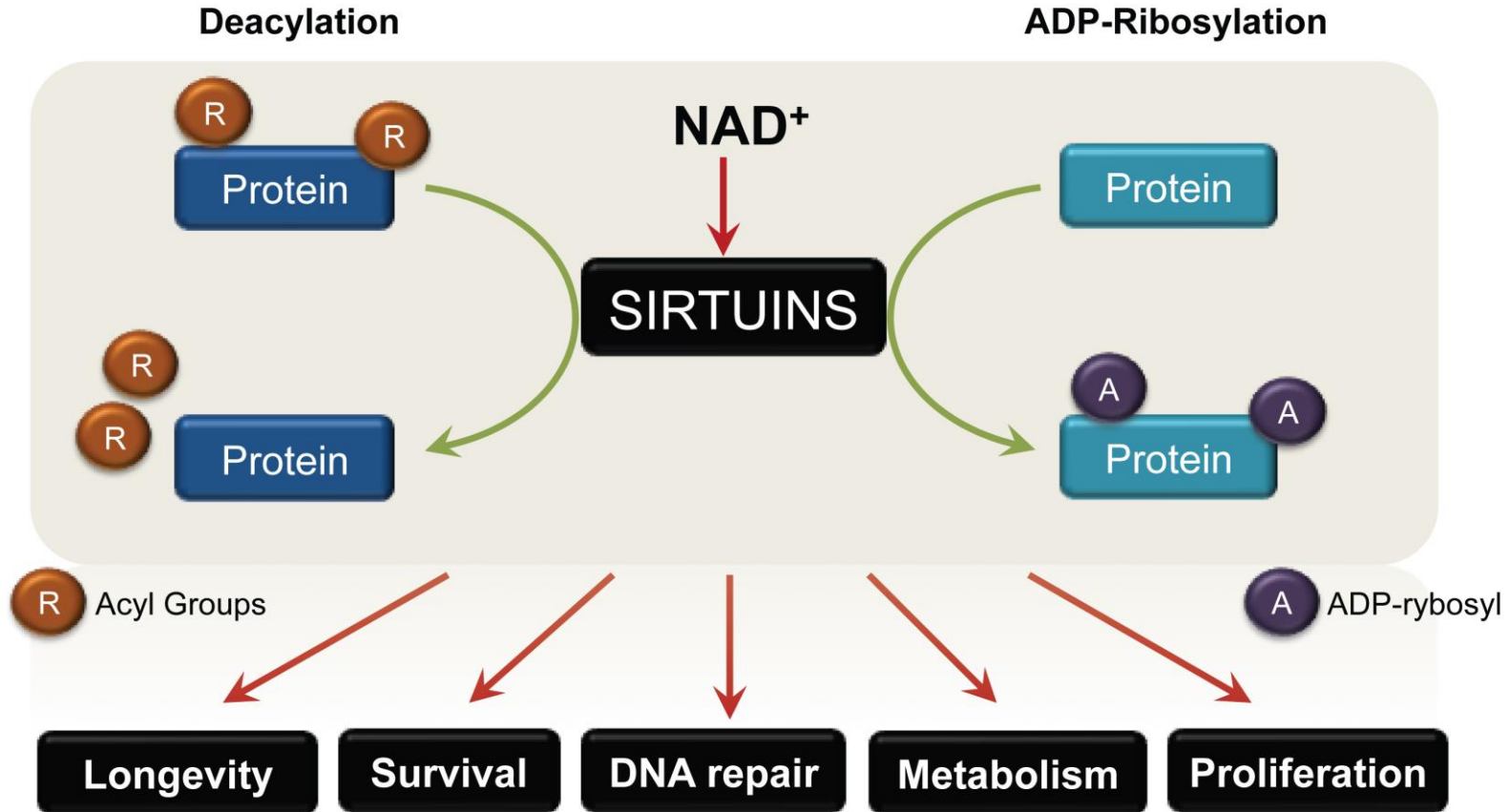


Figure 1.3 Sirtuins are a family of NAD⁺-dependent protein deacetylases/ADP ribosyltransferases that influences a wide range of biological processes. Some sirtuins are known to remove deacyl group from targeted enzymes, while others are known to transfer ADP-ribose group. Adapted from Oellerich *et al.* 2012.

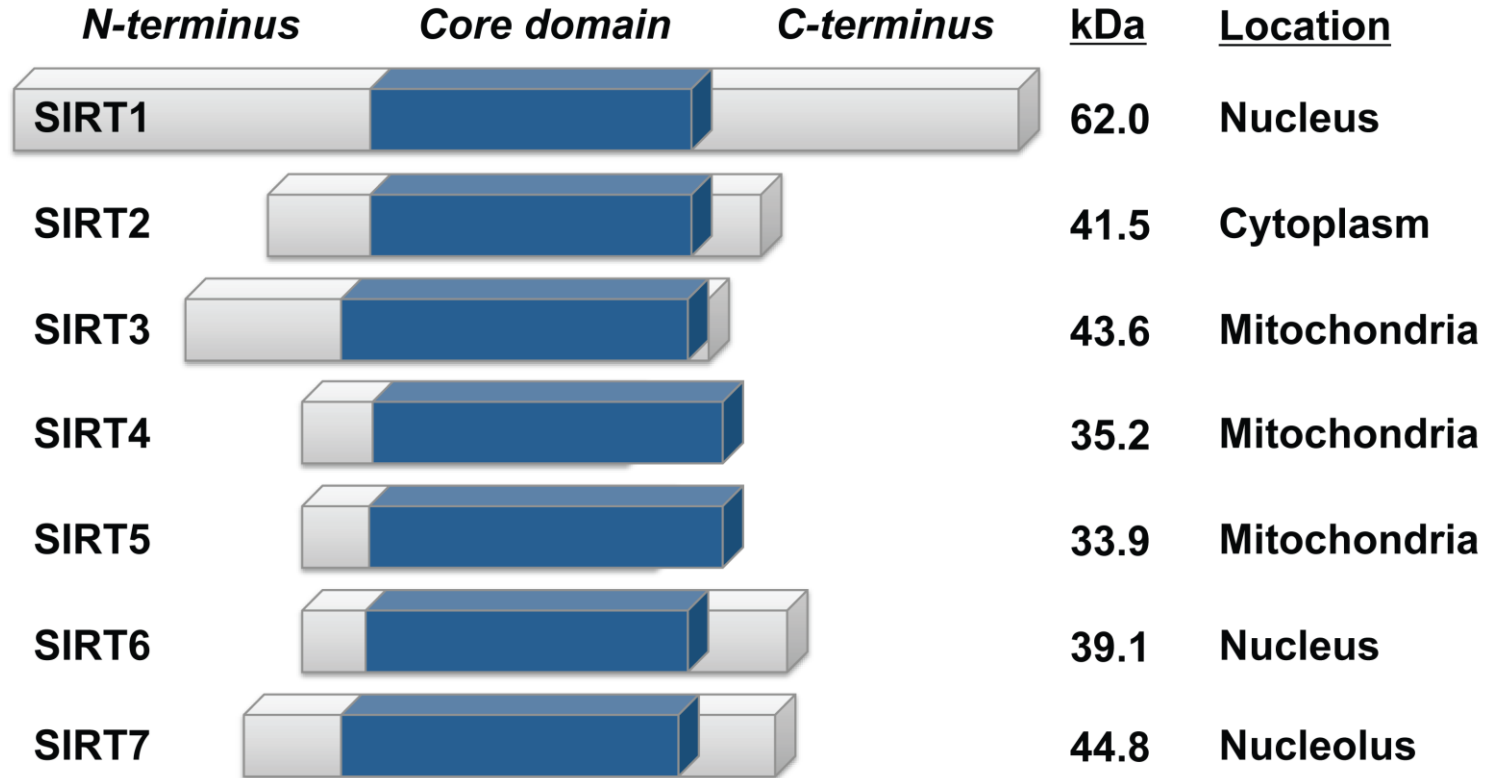


Figure 1.4 Schematic illustration of the seven mammalian sirtuins. All of the sirtuins contains a conserved core domain that comprises the NAD⁺-binding domain and the catalytic site (blue), and a N- and C- terminals that vary in lengths (gray). The seven sirtuins also show different cellular localization. This figure was adapted from Michan and Sinclair 2007.

dehydrogenase, while SIRT7 is known to have weak deacetylase activity (Haigis *et al.* 2006; Pan *et al.* 2011).

1.7.2 Phylogenetic classification of mammalian sirtuins

The divergences of enzymatic activity among the seven mammalian sirtuins might be explained by their phylogeny. Phylogenetic analysis of the core domain of sirtuins from a diverse array of organism places the seven mammalian sirtuins into four different classes designated as classes I-IV (Frye, 2000). Mammalian SIRT1, SIRT2 and SIRT3; all of which exhibit strong deacetylase activity are known as Class I sirtuins. SIRT1 belongs to Class Ia, while SIRT2 and SIRT3 are part of sub-class Ib with fungi and protozoan sirtuins. SIRT4 and SIRT5, which are known to have weak deacetylase activity, belong to Class II and Class III, respectively. Class II and Class III sirtuins include sirtuins from bacteria, archae, protozoan and nematodes. SIRT6 and SIRT7 belongs to Class IV; a class that only includes sirtuins from eukaryotes. According to the phylogenetic classification, sirtuins from Class II, III and U appeared earliest in evolution.

1.7.3 Sirtuin structure and chemistry

Every member of the sirtuin family contains a highly conserved core NAD⁺-binding domain and catalytic site, despite the existence of minor differences in the active site, which could account for the ADP-ribosyltransferase activity of certain sirtuins (Finnin *et al.* 2001). Structural analysis reveals that sirtuins' core domain is composed of two subdomains, a large Rossmann fold domain, which consists of six parallel β strands

forming a β sheet, and a small domain that contains the α -helical and the Zn^{2+} binding subdomains (Min J *et al.* 2001; Chen *et al.* 2015). The NAD^+ and the substrate bind at the interface of the large and small subdomains (Figure 1.5). In contrast to the well-conserved core domain, the amino and carboxyl termini of sirtuins vary in length and chemical composition. These differences can account for the divergence of function and targets.

1.7.4 Sirtuin enzymatic activity and cellular regulation

Initially, it was reported that the activity of sirtuins was NAD^+ -dependent ADP-ribosylation, however in the past decades, NAD^+ -dependent protein deacylation has been the most prevalent reaction that sirtuin enzymes catalyze (Hirschey 2011). Sirtuin-mediated deacylation occurs in two continuous steps. The first step is initiated by the cleavage and release of nicotinamide (NAM) derived from NAD^+ , and the formation of an O-alkylamidate intermediate (Sauve *et al.* 2010). In the second step, the acyl group from the substrate is transferred to the ADP-ribose, generating O-acyl-ADP-ribose (OAADPr) and the newly deacylated substrate (Sauve *et al.* 2010). NAM, the product of sirtuins' first step reaction, is recycled back to NAD^+ via a salvage pathway. The enzyme that catalyzes this reaction is nicotinamide phosphoribosyltransferase (NAMPT) (Revollo *et al.* 2004). In addition, NAM serves as an endogenous inhibitor of sirtuins (Bitterman *et al.* 2002; Sauve *et al.* 2006).

1.8 Nuclear Sirtuins

1.8.1 SIRT1

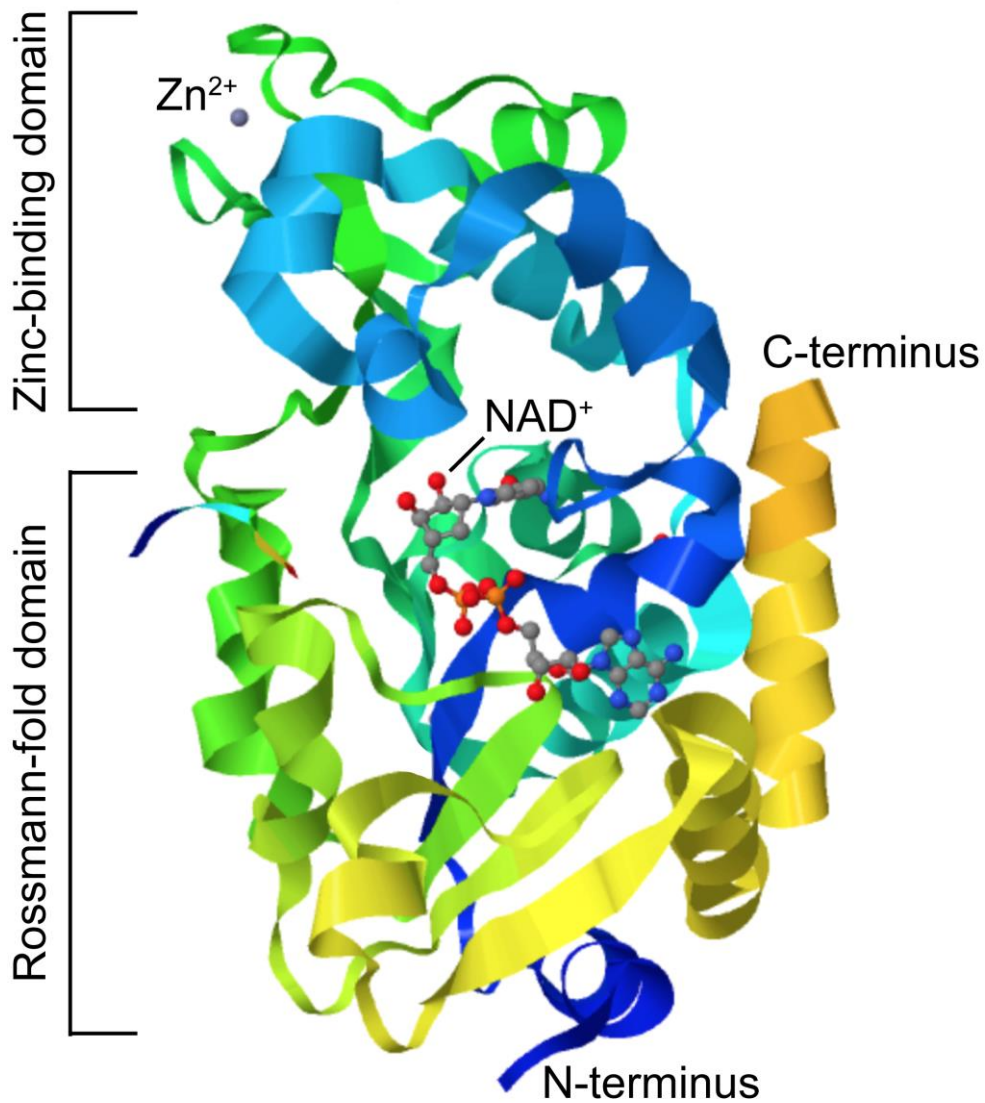


Figure 1.5 The overall structure of sirtuins. The catalytic core of human SIRT3 (rainbow ribbon) in complex with carba-NAD⁺ (ball and sticks) (PSB ID 4FVT). The catalytic core domain is composed of the large Rossmann-fold domain and the small zinc-binding domain containing the Zn²⁺ ion (gray). The modified structure was obtained from Szczepankiewicz *et al.* 2012.

SIRT1, the best-studied Sirtuin, is a NAD⁺-dependent deacetylase enzyme that performs a wide variety of function in biological systems (Rahman and Islam 2011). SIRT1 is known to mediate chromatin silencing and heterochromatin formation through the deacetylation of specific histones including histones H1, H3, and H4 (Imai *et al.* 2000; Vaquero *et al.* 2004; Zhang and Kraus 2010). In addition to histones, SIRT1 deacetylates non-histone proteins including several transcription factors and coregulators, tumor suppressors and signaling proteins (Rahman and Islam 2011). SIRT1 is known to inhibit cell death by deacetylating and inactivating the transcriptional activity of tumor suppressor p53 (Vaziri *et al.* 2001). SIRT1 also control cell cycle arrest and apoptosis by regulating the activity of several members of the forkhead box factors regulated by insulin/Akt (FOXO) family; FOXO1, FOXO3, FOXO4 and FOXO6 (Brunet *et al.* 2004; Van der Horst *et al.* 2004).

In addition to controlling cell death, SIRT1 have been implicated in regulating inflammation by deacetylating nuclear factor kappa B (NF- κ B), a transcription factor that signals pathways involved in the innate immune response (Yeung *et al.* 2004; Lin and Fang 2013). SIRT1 also blocks pro-inflammatory pathways by inhibiting the transcriptional activity of AP-1 through the deacetylation of c-JUN (Gao and Ye 2008). Recent studies have shown that SIRT1 negatively regulates inflammation by promoting autophagy through the deacetylation of ATG5, ATG7 and ATG8 (Lee *et al.* 2008).

Another cellular process regulated by SIRT1 is metabolism. SIRT1 is an important regulator of energy homeostasis in response to nutrient availability (Xiaoling 2013). Multiple reports have shown that SIRT1 is an important regulator of hepatic glucose and fatty acid metabolism. During short-term fasting, SIRT1 reduces

gluconeogenesis by inhibiting the activity of rapamycin complex 2 (TORC2), a CREB-regulated transcription coactivator that is important for cAMP/CREB-mediated activation of gluconeogenesis genes (Liu *et al.* 2008). SIRT1 also induces fatty acid β -oxidation through the PPAR α /PGC-1 α pathway (Purushotham *et al.* 2009). Hepatic deletion of *Sirt1* increases the susceptibility of mice to high-fat diet-induced dyslipidemia, hepatic steatosis and inflammation (Purushotham *et al.* 2009). In addition to glucose and fatty acid metabolism, it has been reported that SIRT1 controls cholesterol metabolism by activating LXRs, a nuclear receptor that enhance cholesterol transport from peripheral tissues to the liver (Li *et al.* 2007). SIRT1 also activates sterol-regulatory-element-binding protein-1 (SREBP-1) and promotes the expression of lipogenic and cholesterologenic genes for fat storage (Walker *et al.* 2010).

Numerous studies suggest that SIRT1 could act as either a tumor promoter or tumor suppressor depending on its targets in specific signaling pathways or in specific cancers (Luo *et al.* 2001; Vaziri *et al.* 2001; Howitz *et al.* 2003; Motta *et al.* 2004; Pruitt *et al.* 2006; Dai *et al.* 2007; Wong and Weber 2007; Firestein *et al.* 2008; Wang *et al.* 2008). The first evidence of SIRT1 as a tumor promoter came from experiments showing that SIRT1 deacetylates and inactivates p53 (Vaziri *et al.* 2001; Luo *et al.* 2001). Other studies show that overexpression of SIRT1 represses expression and/or activity of many tumor suppressor genes and proteins including, members of FOXO family, p73, RB, GATA4 and CDH1 (Motta *et al.* 2004; Pruitt *et al.* 2006; Dai *et al.* 2007; Wong and Weber 2007). On the other hand, recent studies have shown that SIRT1 serves as a tumor suppressor. Overexpression of *Sirt1* in *APC^{min/+}* mice reduces colon cancer formation through SIRT1-mediated deacetylation of

β -catenin (Firestein *et al.* 2008). Studies in breast cancer show that SIRT1 acts as a tumor suppressor in BRCA1-associated breast cancers. The expression of *SIRT1* is often reduced in this type of cancer and restoration of SIRT1 levels in BRCA1 mutant cancer cells inhibited cell proliferation and tumor growth (Howitz *et al.* 2003; Wang *et al.* 2008). Recent studies reported that SIRT1 plays an important role in DNA damage repair and Sirt5-deficient cells displayed genomic instability that lead to tumorigenesis (Wang *et al.* 2008; Oberdoerffer *et al.* 2008).

1.8.2 SIRT6

SIRT6 is a nuclear protein that is associated with chromatin. SIRT6 functions mainly as a NAD⁺-dependent deacetylase enzyme (Yang *et al.* 2009; Michishita *et al.* 2008; Michishita *et al.* 2009). However, studies have reported other functions including, NAD⁺-dependent ADP-ribosylation and hydrolysis of long-chain fatty acyl groups (Liszt *et al.* 2005; Mao *et al.* 2012; Feldman *et al.* 2013; Jiang *et al.* 2013; Van Meter *et al.* 2014). SIRT6 impacts multiple cellular processes including, DNA repair and maintenance, metabolism and inflammation. SIRT6 is best characterized as a H3K9 and H3K56 histone deacetylase (Michishita *et al.* 2008; Michishita *et al.* 2009). Deacetylation of histones H3K9 and H3K56 reduces chromatin accessibility impacting the expression of genes that are modulated by nuclear factor kB (NF-kB), c-JUN, FOXO3, MYC, HIF1 α (Kugel and Mostoslavsky 2014). In addition, SIRT6 maintains genome integrity by decreasing H3K56Ac levels following double strand breaks (DSB) and by regulating H3K9Ac and H3K56Ac levels within telomeric regions (Michishita *et al.* 2008). SIRT6 has also been found to ADP-ribosylate PARP1 in and stimulate its

poly-ADP ribosylation activity upon DNA damage caused by oxidative stress (Mao *et al.* 2011). SIRT6 interact with SNF2H to enhance its recruitment to sites of damage thereby enhancing DSB repair (Toiber *et al.* 2013).

SIRT6 impacts cell homeostasis by regulating glucose and lipid metabolism. SIRT6 was found to suppress the expression of multiple glucose-metabolic genes including, glucose transporter-1 (GLUT1), pyruvate dehydrogenase kinase-1 (PDK1), phosphofruktokinase-1 (PFK1) and lactate dehydrogenase (LDH), by suppressing the activity of HIF1 α (Sebastian *et al.* 2012; Toiber *et al.* 2013). In addition to impacting glycolysis, SIRT6 directly regulates gluconeogenesis by modulating the activity of peroxisome proliferator-activated receptor- α coactivator 1a (PGC-1a), the main regulator of gluconeogenesis (Puigserver *et al.* 2003). SIRT6 also regulates cholesterol biosynthesis by repressing the sterol-regulatory element binding protein (SREBP) (Tao *et al.* 2013).

Recent studies have shown that SIRT6 preferentially hydrolyzes long-chain fatty acyl groups, including myristoyl and palmitoyl groups, from lysine residues (Jiang *et al.* 2013). SIRT6 regulates TNF- α secretion through hydrolysis of long-chain fatty acyl lysine (Jiang *et al.* 2013).

Recent studies suggest that SIRT6 function as a tumor suppressor (Mahlknecht *et al.* 2006; Das *et al.* 2009; Marquardt *et al.* 2013). Sirt6 is often mutated in a variety of cancer types including, breast cancer, liver cancer and lung cancer (Mahlknecht *et al.* 2006; Kanfi *et al.* 2012; Marquardt *et al.* 2013; Van Meter *et al.* 2014). In addition, deletion of *SIRT6* in cells increases hyperacetylation of H3K56, a chromatin modification that is associated to tumorigenesis (Das *et al.* 2009). *In vivo*

studies show that overexpression of *Sirt6* delays lung tumor onset in mice (Kanfi *et al.* 2012). Mechanisms by which SIRT6 protects against tumor formation include, SIRT6-mediated promotion of genome stability, SIRT6-mediated suppression of inflammation and SIRT6-mediated regulation of cellular metabolism (Van Meter *et al.* 2014).

1.8.2 SIRT7

SIRT7, as other sirtuins, has NAD⁺-dependent deacetylase activity and is a key mediator of many cellular activities. SIRT7 is enriched in the nucleolus, where it activates the transcription of ribosomal DNA (rDNA) by facilitating association of RNA pol I (Chen *et al.* 2013). SIRT7 has also been found to deacetylate U3-55k, a core component of the U3 snoRNP complex, and thus promoting pre-rRNA processing (Chen *et al.* 2016). SIRT7 has also been reported to deacetylates p53, however, the role of SIRT7-mediated deacetylation of p53, remains controversial (Vakhrusheva *et al.* 2008; Barber *et al.* 2012).

SIRT7 has been implicated in regulating metabolic homeostasis by repressing the Myc activity. SIRT7-mediated repression of Myc blocks ribosomal protein expression and alleviates the endoplasmic reticulum stress (Shin *et al.* 2013). In addition to Myc, SIRT7 is known to negatively regulate the levels and activity of HIF1 α and HIF2 α , which are central players in energy metabolism (Hubbi *et al.* 2013). Furthermore, a recent report shows that SIRT7 controls mitochondrial function by deacetylating and increasing the activity of GABP β 1; a central mediator of mitochondrial function (Ryu *et al.* 2014). *Sirt7*-deficient mice displayed pathologies that resemble phenotypes of mitochondrial diseases (Nunnari and Suomalainen 2012).

Several studies have attributed SIRT7 an oncogenic potential (Ford *et al.* 2006; Barber *et al.* 2012; Zhang *et al.* 2015; Aljada *et al.* 2015; Wang *et al.* 2015). SIRT7 expression correlates with cancer aggressive phenotypes and poor prognosis (Zhang *et al.* 2015; Aljada *et al.* 2015; Wang *et al.* 2015). However, increased expression of SIRT7 is not sufficient to induce the transformation of primary fibroblasts (Barber *et al.* 2012). Multiple mechanisms by which SIRT7 exert oncogenic properties have been proposed. Among those includes, attenuation of the transcription of genes associated to tumor suppression, by deacetylating H3K18, upregulation of rRNA synthesis, which is essential for cancer cell growth, and repression of microRNA miR-34a expression (Ford *et al.* 2006; Barber *et al.* 2012; Zhang *et al.* 2015).

1.9 Cytoplasmic Sirtuins

1.9.1 SIRT2

SIRT2, like SIRT1 removes lysine acetyl groups in a NAD⁺-dependent manner. SIRT2 is the only Sirtuin family member that is preferentially localized in the cytoplasm. However, multiple studies have shown that it can translocate into the nucleus (Dryden *et al.* 2003; North *et al.* 2003; North and Verdin 2007). SIRT2 have a number of biological functions, including cell cycle control, microtubule dynamics and metabolic network. SIRT2 controls the anaphase promoting complex/cyclosome (APC/C) ubiquitin ligase complex activity by deacetylating cell division cycle protein 20 (CDC20) and fizzy and cell division cycle 20 related 1 (FZR1) protein (Kim *et al.* 2011). In addition, SIRT2 regulates the cell cycle through deacetylation of histones H3 and H4 mitosis (Imai *et al.* 2000; Vaquero *et al.* 2006).

SIRT2 regulates microtubule dynamics deacetylating α -tubulin and destabilizing microtubules. In addition to α -tubulin, SIRT2 deacetylates multiple proteins involved in cellular metabolism. SIRT2 regulates glucose homeostasis by deacetylating and stabilizing phosphoenolpyruvate carboxykinase (PEPCK) (North *et al.* 2003; Jiang *et al.* 2011). Recent studies also show that SIRT2 controls fatty acid synthesis by deacetylating ATP-citrate lyase (ACLY), a lipogenic enzyme that catalyzes the conversion of cytosolic citrate to acetyl coenzyme A (acetyl-CoA). SIRT2-mediated deacetylation induces ACLY degradations (Lin *et al.* 2013).

SIRT2 also deacetylates multiple transcription factors including several members of the FOXO family. SIRT2-dependent deacetylation of FOXO1 results in the repression of peroxisome proliferator-activated receptor gamma (PPAR γ) transcription and the inhibition of adipocyte differentiation (Jing *et al.* 2007). Deacetylation of FOXO3 results in upregulation of antioxidant enzymes expression and the reduction of ROS levels (Wang *et al.* 2012). In addition to transcription factors, SIRT2 also regulates tumor suppressors and oncogenes. SIRT2 inhibits transcription activation of TP53 by deacetylating p300, a histone acetyltransferase (Han *et al.* 2008). SIRT2-mediated deacetylation stabilizes c-Myc oncoprotein and promotes cancer (Liu *et al.* 2013; Jing *et al.* 2016).

As SIRT1, evidences suggest dual roles of SIRT2 in cancer. Some studies indicate that SIRT2 acts as a tumor suppressor, while others suggest that SIRT2 has oncogenic functions (Hiratsuka *et al.* 2003; Inoue *et al.* 2007). Several evidences show that *SIRT2* is often downregulated in gliomas, gastric carcinoma and melanomas (Hiratsuka *et al.* 2003; Inoue *et al.* 2007; Jing *et al.* 2016; Shah *et al.* 2016; Zhou *et al.*

2016). Studies indicate that loss of SIRT2 compromises the mitotic checkpoint, contributing to genomic instability and tumorigenesis (Hiratsuka *et al.* 2003; Inoue *et al.* 2007). On the other hand, recent studies have shown that SIRT2 serves as a tumor promoter by promoting the stabilization of oncogenic proteins such as Slug and c-Myc (Jing *et al.* 2016; Shah *et al.* 2016; Zhou *et al.* 2016). Evidences suggest that SIRT2 inactivation antagonizes aggressive traits and tumorigenesis in basal-like breast cancer (Zhou *et al.* 2016). Others have shown that selective inhibition of SIRT2 induces c-myc degradation, and reduces cancer cell growth *in vitro* and tumorigenesis *in vivo*. (Liu *et al.* 2013; Jing *et al.* 2016; Shah *et al.* 2016).

1.10 Mitochondrial Sirtuins

1.10.1 SIRT3

As described above, mammals have three mitochondrial sirtuins, SIRT3, SIRT4 and SIRT5. These mitochondrial sirtuins are considered metabolic sensors of cellular energetic status due to their dependence on NAD⁺. Among the mitochondrial sirtuins, SIRT3 is the main deacetylase responsible for regulating global mitochondrial lysine acetylation. Basal SIRT3 expression varies widely, however it is highly expressed in metabolically active tissues including liver, heart and kidney (Ahn *et al.* 2008). SIRT3 is known to control acetyl CoA levels by deacetylating and activating acetylcoenzyme A synthase 2 (AceCS2) (Hallows *et al.* 2006). SIRT3 regulates fatty acid oxidation and ketone body synthesis by activating Acyl-CoA Dehydrogenase, Long Chain (LCAD) and 3-hydroxy-3-methylglutaryl-CoA synthase 2 (HMGCS2) (Hirschey *et al.* 2010; Shimazu *et al.* 2010). Mice lacking *Sirt3* accumulate β -oxidation precursors and intermediates and show reduced fasting serum levels of ketone bodies (Hirschey *et al.* 2010; Shimazu

et al. 2010). SIRT3 is also involved in regulating mitochondrial oxidative phosphorylation (OXPHOS) by deacetylating and activating several components of the respiratory transport chain, including succinate dehydrogenase complex, subunit A (SDHA) (Ahn *et al.* 2008; Finley *et al.* 2011).

Studies have shown that SIRT3 can regulate glycolysis by inactivating peptidyl-prolyl isomerase cyclophilin D and consequently, inducing the dissociation of hexokinase II (HK2) from the mitochondria (Shulga *et al.* 2010). Dissociation from the mitochondria inactivates HK2 and reduces the production of glucose 6-phosphate. In addition, SIRT3 controls the Warburg effect in cancer cells by controlling ROS levels (Someya *et al.* 2010). Studies have shown that SIRT3 deacetylates and activates isocitrate dehydrogenase 2 (IDH2), the major source of NADPH. Maintenance of NADPH levels is essential for the regeneration of reduced glutathione (GSH), the major antioxidant responsible for preventing ROS damage. SIRT3 also deacetylates and activates mitochondrial superoxide dismutase 2 (MnSOD); a major mitochondrial antioxidant enzyme (Qiu *et al.* 2010).

Growing evidences have shown that SIRT3 acts as a tumor suppressor in multiple cancers (Kim *et al.* 2010; Finley *et al.* 2011; Haigis *et al.* 2012). *Sirt3* is deleted in human breast cancer, lung cancer and ovarian cancer (Kim *et al.* 2010; Finley *et al.* 2011). Furthermore, mice lacking *Sirt3* develop hormone receptor-positive mammary tumors (Kim *et al.* 2010).

1.10.2 SIRT4

Unlike SIRT3, SIRT4 has no detectable NAD⁺-dependent deacetylase activity. Mice lacking *Sirt4* show no significant change in protein acetylation levels (Haigis *et al.* 2006). Interestingly, it has been reported that SIRT4 has ADP-ribosyltransferase activity. SIRT4 blocks glutaminolysis by ADP-ribosylating glutamate dehydrogenase (GDH) to block glutaminolysis (Haigis *et al.* 2006; Jeong *et al.* 2013). By inhibiting GDH, SIRT4 also inhibits amino acid-stimulated insulin secretion (Ahuja *et al.* 2007). SIRT4 also has been reported to promote lipid anabolism by regulating malonyl CoA decarboxylase (MCD) (Laurent *et al.* 2013).

Recently, it has been reported that SIRT4 has tumor-suppressor effects (Jeong *et al.* 2013). Loss of *Sirt4* in a mouse model of *Myc*-induced Burkitt lymphoma accelerates the growth of lymphomas (Jeong *et al.* 2014). Furthermore, the loss of SIRT4 appears to be a result of mammalian target of rapamycin complex 1 (mTORC1). mTOR downregulates the expression of *Sirt4* by destabilizes cAMP-responsive element binding 2 (CREB2). Further studies need to be done to fully understand the roles of SIRT4 in cellular metabolism and cancer (Csibi *et al.* 2013).

1.10.3. SIRT5

SIRT5 was an enzymatic enigma until recent years. It was initially characterized as a weak deacetylase enzyme. However, recent findings showed that SIRT5 has potent desuccinylase, demalonylase and deglutarylase activities (Figure 1.6). (Du *et al.* 2011; Zhou *et al.* 2012) After the discovery of these novel enzymatic activities, SIRT5 has become an active topic of research towards its biological and physiological functions.

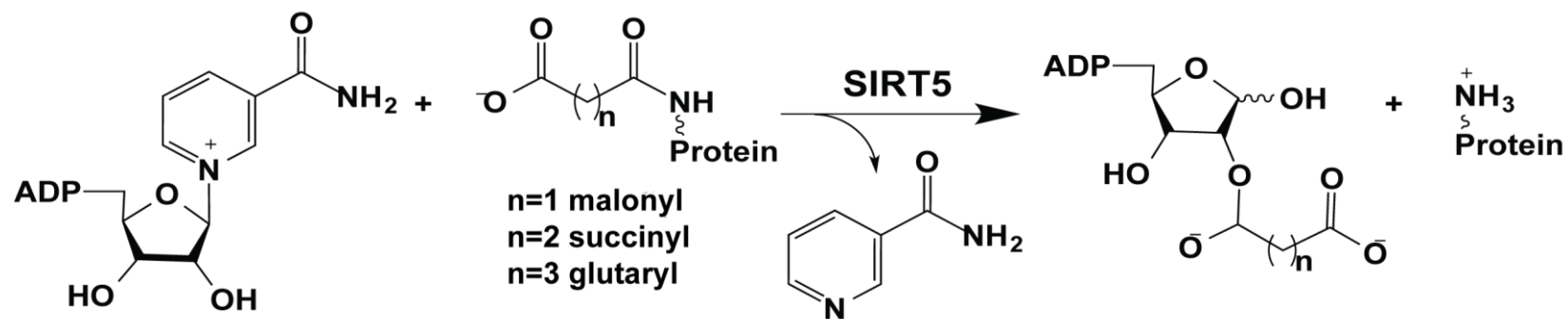


Figure 1.6 SIRT5-catalyzed demalonylation, desuccinylation and deglutarylation reactions. In the reaction, NAD^+ is consumed to release nicotinamide, while the ADP-Ribose moiety serve as the final acceptor of the acyl group (malonyl, succinyl, glutaryl). The modified figure was obtained from the Lin lab.

1.10.3.1 SIRT5 enzymatic activity

The weak deacetylase and strong demalonylase, desuccinylase and deglutarylase activity of SIRT5 is mainly due to slight variations in the catalytic pocket when compared to SIRT1, SIRT2 and SIRT3. SIRT5 consists of 14 α helices and 9 β strands, which are organized into two main domains: the Rossmann fold domain and the Zn²⁺-binding domain (Figure 1.7) (Schuetz *et al.* 2007; Du *et al.* 2011; Zhou *et al.* 2012; Szczepankiewicz *et al.* 2012; Roessler *et al.* 2014). Crystal structure comparisons show that SIRT5 has similar overall domain organization to the structures of SIRT1, SIRT2, and SIRT3 (Yang *et al.* 2017). Interestingly, SIRT5 has specific residues in the catalytic pocket – tyrosine (Y102) and arginine (R105) that are required for its demalonylase, desuccinylase and deglutarylase activities. These unique residues in the catalytic site can form hydrogen-bonding and ionic-bonding interactions with the negatively charged acyl groups such as malonyl, succinyl or glutaryl-lysine (Du *et al.* 2011). In addition, SIRT5 harbors a larger acyl-lysine binding pocket when compared to other sirtuins. SIRT5 contains a smaller residue (Ala86), while SIRT1, SIRT2 and SIRT3 contain a phenylalanine residue (Zhou *et al.* 2012). These subtle variations in the catalytic pocket explain SIRT5 preference for malonyl, succinyl and glutaryl groups.

1.10.3.2 SIRT5 substrates

At present, an extensive number of potential SIRT5 targets have been identified by proteomic studies. SIRT5 has been implicated in regulating multiple metabolic pathways by targeting enzymes involved in amino acid degradation, glycolysis, TCA cycle, oxidative phosphorylation and fatty acid metabolism (Xie *et al.*

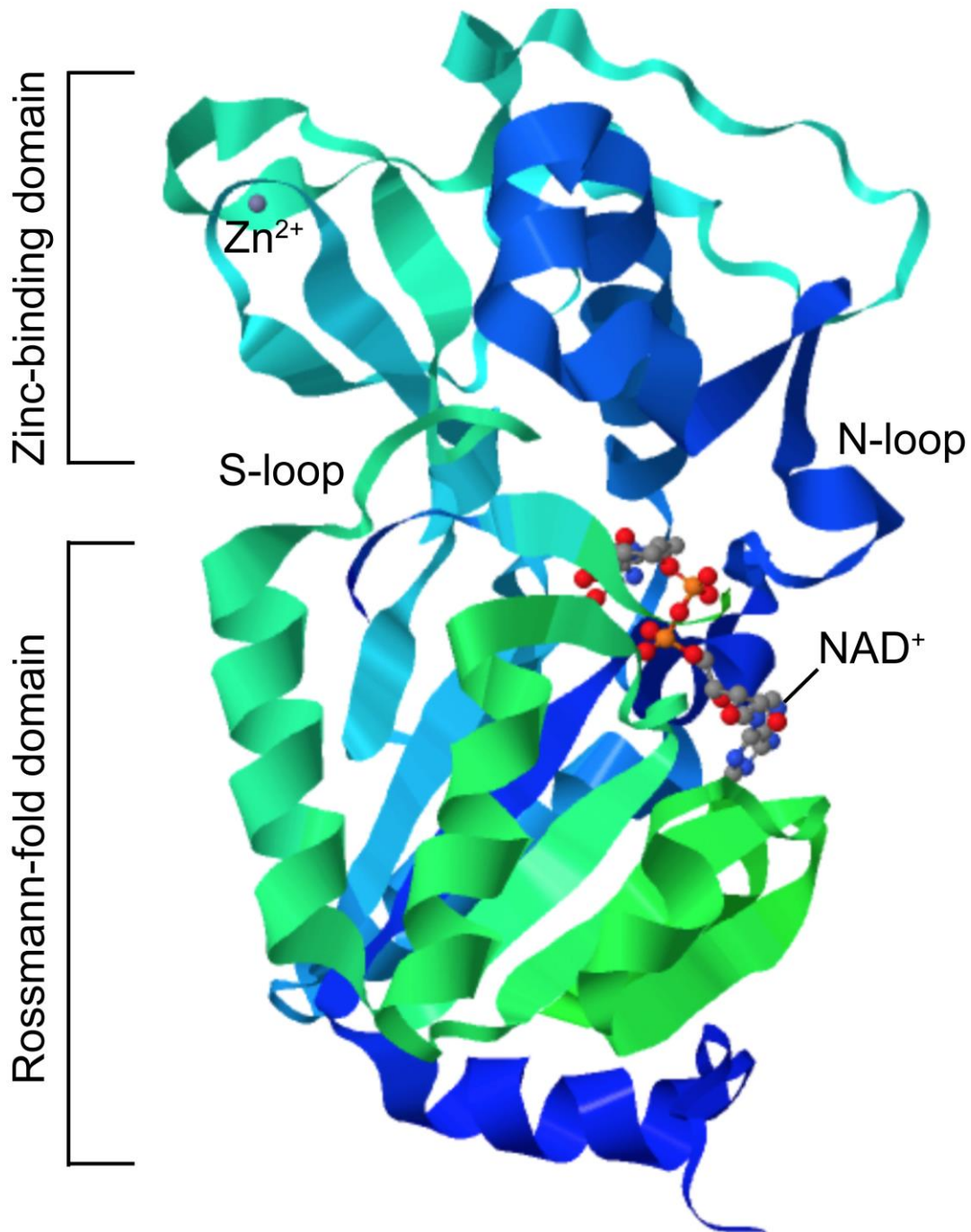


Figure 1.7 Crystal structure of SIRT5 bound to NAD⁺. The crystal structure (PDB: 3RIY) was obtained from Du *et al.* 2011.

2012; Tan *et al.* 2014; Hirschey and Zhao 2015). However, Sirt5KO mice do not show remarkable phenotypes or metabolic disorders (Yu *et al.* 2013).

Roles of SIRT5 in the urea cycle

The first identified substrate of SIRT5 was carbamoyl phosphate synthetase 1 (CPS1), an enzyme that catalyzes the rate-limiting step of the urea cycle for ammonia detoxification (Figure 1.8) (Nakagawa *et al.* 2009). SIRT5 deacetylates and activates CPS1. Mice lacking *Sirt5* showed increased levels of blood ammonia due to the lack of SIRT5-mediated activation of CPS1 (Nakagawa *et al.* 2009). Later, studies reported that SIRT5 desuccinylates and deglutarylates CPS1. Desuccinylation and deglutarylation of CPS1 also induces its activity (Yu *et al.* 2013; Tan M *et al.* 2014).

Increased levels of ammonia have been implicated in inducing autophagy in tumor cells. Recently it was reported that SIRT5 modulates ammonia-induced autophagy and survival in cancer cells by controlling glutamine metabolism (Polleta *et al.* 2015). Polleta *et al.* reported that SIRT5 desuccinylates and inactivates glutaminase (GLS2), thereby reducing the levels of glutamate and ammonia production (Figure 1.8). Overexpression of SIRT5 in breast cancer (MDA-MB 231) and mouse myoblast (C2C12) cell lines causes decreased levels of ammonia production and a reduced expression of autophagy and mitophagy proteins (Polleta *et al.* 2015). Knockdown and pharmacological inhibition of SIRT5 showed the opposite phenotype. These findings demonstrate the important role of SIRT5 in ammonia detoxification.

Roles of SIRT5 in cellular respiration

SIRT5 also has been implicated in regulating cellular respiration (Figure 1.8). Global lysine malonylation proteome studies in mouse liver tissues revealed that the pathways most enriched with SIRT5-regulated malonylated proteins were gluconeogenesis and glycolysis, while the pathways most enriched with SIRT5-regulated succinylated and glutarylated proteins were involved in mitochondria metabolism (Park *et al.* 2013; Radin *et al.* 2013; Nashida *et al.* 2015).

Among all the glycolytic enzymes, Aldolase B and Glyceraldehyde 3-phosphate dehydrogenase (GAPDH), exhibited the highest increase in lysine malonylation in the absence of SIRT5. Nashida and coworkers showed that SIRT5 demalonylates and activates GAPDH, the enzyme that catalyzes the conversion of glyceraldehyde 3-phosphate to glycerate 1,3-bisphosphate (Nashida *et al.* 2015). SIRT5-mediated activation of GAPDH increased glycolytic flux and lactate production in primary mouse hepatocytes *in vitro*. In accordance with these data, an independent study reported a correlation between *Sirt5* and *Ldha* mRNA expression. Knockdown of *Sirt5* in a lung cancer cell line decreased *Ldha* expression (Lv *et al.* 2015).

Augmented lactate production is a key feature of many cancer cells. It has been reported that suppression of pyruvate dehydrogenase diminishes the amount of acetyl-CoA entering into the TCA cycle and promotes its transformation to lactate in the cytoplasm (Zhang *et al.* 2015). Studies have reported that SIRT5 desuccinylates and inactivates pyruvate dehydrogenase complex (PDC) E1 α subunit (Park *et al.* 2013). These data together suggest that SIRT5 promotes the Warburg effect and supports the malignant phenotype of cancer cells.

Recently, it was reported that SIRT5 desuccinylates and inactivates pyruvate kinase M2 (PKM2) (Xiangyun *et al.* 2017). Blockage of PKM2 has been reported to be a common metabolic way of cancer cells to divert glucose flux to the pentose phosphate pathway and increase antioxidant response (Christofk *et al.* 2008). Inhibition of PKM2 by SIRT5 promoted cell proliferation of non-small cell lung cancer cells (A549) *in vitro* and tumor growth *in vivo* (Xiangyun *et al.* 2017). These data support the tumor promoting roles of SIRT5 by protecting cancer cells from oxidative stress. Interestingly, an independent study in LPS-activated macrophages reported that SIRT5 desuccinylates and activates PKM2 to block macrophage IL-1 β production and inflammation (Wang *et al.* 2017). These data suggest that the impact of SIRT5 on PKM2 may be context-dependent.

As discussed above, most of the SIRT5 identified targets via desuccinylation are involved in the TCA cycle and the oxidative phosphorylation pathway. Recent data suggest that SIRT5 not only blocks the TCA cycle by limiting the formation of Acetyl CoA via PDC, but also, by desuccinylating and inactivating succinate dehydrogenase (SDH), subunit A (SDHA) (Park *et al.* 2013). The SDH complex is composed of four subunits, SDHA-SDHD, that catalyze the oxidation of succinate to fumarate with the concomitant reduction of ubiquinone to ubiquinol. Park *et al.* reported that knockdown of *Sirt5* in 293T cells substantially increased SDH activity and cellular respiration (Park *et al.* 2013). It has been reported that inhibition or dysregulation of SDH activity results in the accumulation of succinate and reduced levels of fumarate and malate, which lead to disruption of multiple metabolic pathways including central carbon metabolism (Pollard *et al.* 2005; Aspuria *et al.* 2014). Furthermore, elevated levels of succinate induce

epigenetic alterations, activation of HIF α , cancer progression and angiogenesis. The work of Park *et al.* implicates SIRT5 in promoting the Warburg effect by inhibiting SDH activity (Park *et al.* 2013).

Interestingly, two independent studies have shown opposite effects of SIRT5-mediated desuccinylation on SDH activity. Both works suggest that SIRT5 induces SDH activity. Li *et al.* reported that expression of a succinylation mimetic SDHB mutant in cultured cells decreased SDH activity, while overexpression of *Sirt5* increased SDH activity (Li *et al.* 2015). In support of these findings, a recent work showed that deletion of *Sirt5 in vivo* compromised SDH (complex II) and ATP synthase function (Zhang *et al.* 2017). These findings support the view of SIRT5 as a promoter of mitochondrial respiration through the TCA cycle and oxidative phosphorylation.

SIRT5 has also been implicated in promoting the TCA cycle by desuccinylation and activating IDH2 (Zhou *et al.* 2016). Zhou *et al.* showed that knockdown of *Sirt5* in 293T cells decreased IDH2 activity by 41%, while overexpression of *Sirt5* significantly increased its activity (Zhou *et al.* 2016). Furthermore, the study reported that SIRT5-mediated activation of IDH2 preserved cellular antioxidant capacity by the production of NADPH, an essential metabolite for the regeneration of GSH. These findings provide evidences of SIRT5-mediated oxidative protection.

Roles of SIRT5 in the pentose phosphate pathway

The pentose phosphate pathway represents one of the major pathways for cellular NADPH generation in most tissues, together with the IDH1/2 pathway. Zhou *et al.* also reported that SIRT5 maintains cellular NADPH homeostasis and redox balance

by deglutarylating and activating glucose 6-phosphate dehydrogenase (G6PD), the enzyme that converts D-glucose 6-phosphate and NADP⁺ into 6-phospho-D-glucono-1,5-lactone + NADPH (Figure 1.8) (Zhou *et al.* 2016).

Production of NADPH is essential for maintaining the levels of glutathione, which in turn protect the cells against oxidative damage. Beside its function in promoting NADPH production, SIRT5 has been implicated in reducing reactive oxygen species (ROS) by desuccinylating and activating superoxide dismutase 1 (SOD1) (Figure 1.8) (Lin *et al.* 2013). SOD1 is a member of a class of enzymes that catalyzes the detoxification of superoxide into oxygen and hydrogen peroxide (McCord and Fridovich 1969). In the study, Lin *et al.* reported that overexpression of SIRT5 increased SOD1 activity by 50% and that SIRT5-mediated desuccinylation of SOD1 was essential for tumor cell growth (Lin *et al.* 2013). Together, these data support the roles of SIRT5 in promoting cell survival by promoting NADPH homeostasis, redox potential and reducing ROS levels.

Roles of SIRT5 in the fatty acid metabolism

SIRT5 has been implicated in fatty acid β -oxidation and ketone body synthesis (Radin *et al.* 2013; Zhang *et al.* 2015; Sadhukhan *et al.* 2016). Lysine succinylome analysis in liver mitochondria showed that 14 out of 15 proteins involved in fatty acid β -oxidation, and 4 of 4 proteins in the ketone body synthesis were targeted by SIRT5. Radin *et al.* reported reduced fatty acid β -oxidation and accumulation of medium- and long-chain acylcarnitines in *Sirt5*KO mouse liver and skeletal muscle (Radin *et al.* 2013). In concordance with these data, it was recently reported that SIRT5

regulates very long-chain acyl-CoA dehydrogenase (VLCAD) (Figure 1.9) (Zhang *et al.* 2015). SIRT5-mediated desuccinylation and SIRT3-mediated deacetylation promotes VLCAD activity and binding to cardiolipin (Zhang *et al.* 2015). Along with the activation of VLCAD, SIRT5 has been implicated in regulating the activity of mitochondrial enoyl-CoA hydratase/3-hydroxyacyl-CoA dehydrogenase/3-ketoacyl-CoA thiolase trifunctional enzyme. SIRT5 specifically desuccinylates and activates enoyl-CoA hydratase (ECHA), thereby promoting lipid metabolism (Figure 1.9) (Sadhukhan *et al.* 2016). Sadhukhan *et al.* reported that SIRT5 deficiency in mice, leads to cardiomyopathy due to decreased ECHA activity and reduced cardiac energy metabolism (Sadhukhan *et al.* 2016). Consistently, Boylston *et al.* showed that *Sirt5KO* mice are more susceptible to ischemia-reperfusion injury compared with *Sirt5WT* due to increased succinylation (Boylston *et al.* 2015).

SIRT5 has been also implicated in regulating ketogenesis. Succinylome studies reported that all four key enzymes in the ketone body synthesis are highly succinylated and targeted by SIRT5. Furthermore, *Sirt5*-deficient mice showed decreased ketone body production and hypersuccinylation of 3-Hydroxy-3-Methylglutaryl-CoA Synthase 2 (HMGCS2), the rate-limiting step of ketone body synthesis (Figure 1.9) (Radin *et al.* 2013). Together, these data demonstrate that SIRT5 promotes ATP generation through fatty acid β -oxidation and ketone body production.

1.10.3.3 *Sirt5* gene and tissue distribution

Human *SIRT5* gene is located at chromosome locus 6p23 and consists of eight exons (Exon 1-8) (Mahlknecht *et al.* 2006). Exon 1 codes for the N-terminal

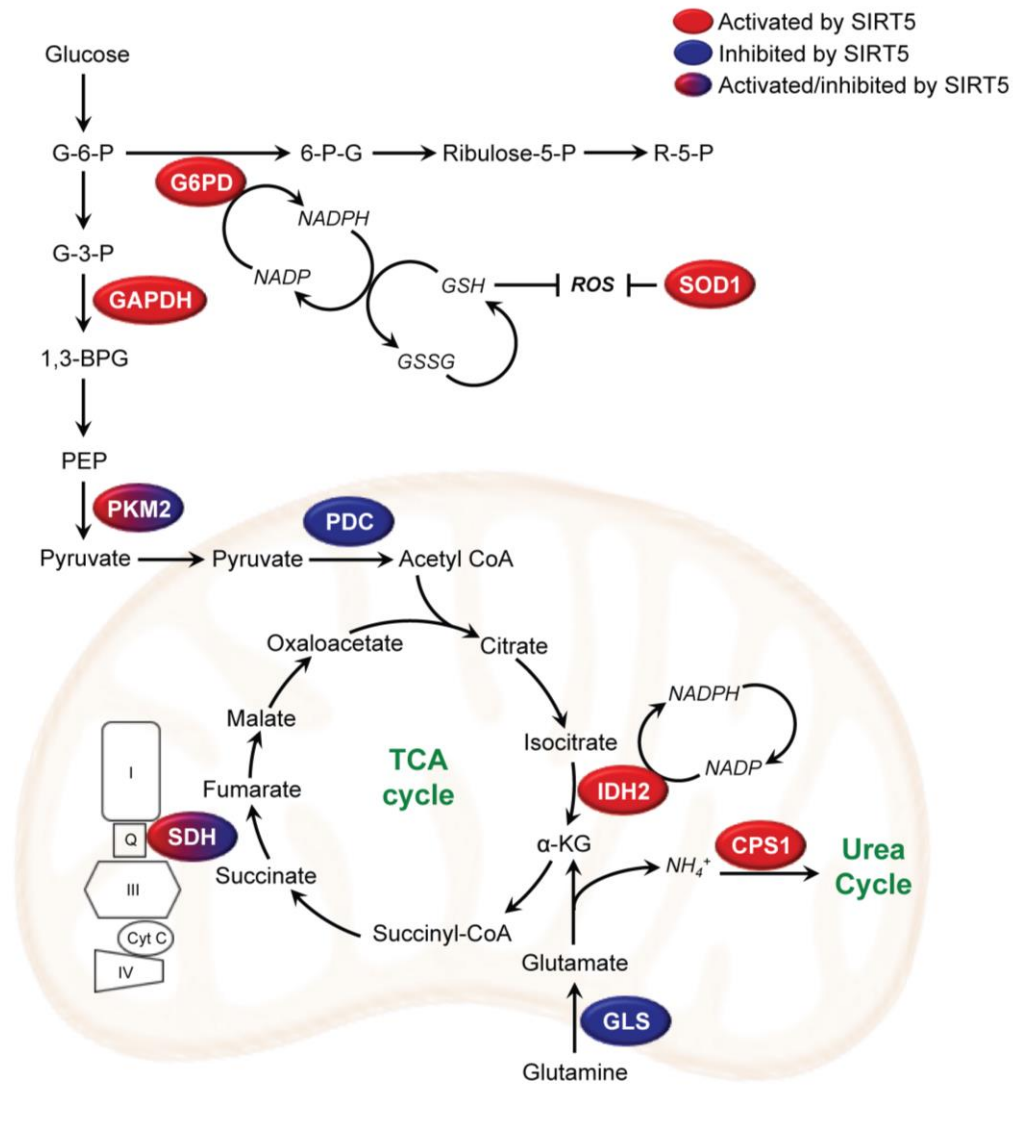


Figure 1.8 SIRT5 regulates cellular respiration, glutamine metabolism, urea cycle and the pentose phosphate pathway. Multiple studies have reported that SIRT5-mediated deacetylation increases the activity of G6PD, GAPDH, IDH2, CPS1 and SOD1 (red ovals) and reduces the activity of PDC and GLS (blue ovals). The impact of SIRT5-mediated deacetylation on PKM2 and SDH activity varies, depending on cell context (red-blue ovals). Note that the schematic representation of key metabolic pathways is simplified. Multiple steps and connections between pathways were not shown to emphasize the steps discussed in the text. G-6-P, Glucose 6 phosphate; G-3-P,

Glucose 3 phosphate; GAPDH, Glyceraldehyde phosphate dehydrogenase; 1,3-BPG, 1,3-Bisphosphoglycerate; PEP, Phosphoenolpyruvate; PKM2, Pyruvate kinase muscle isoform 2; PDC, Pyruvate dehydrogenase complex; Acetyl-CoA, Acetyl-Coenzyme A; IDH2, Isocitrate dehydrogenase 2; α KG, Alpha ketoglutarate; Succiny-CoA, Succinyl-Coenzyme A; SDH, Succinate dehydrogenase; Cyt C, Cytochrome C; GLS, Glutaminase; CPS1, Carbamoyl phosphate synthetase 1; 6-G-P; 6-Phosphogluconate; Ribulose-5-P, Ribulose 5 phosphate isomerase; R-5-P, Ribose 5 phosphate; ROS, Reactive oxygen species; SOD1, Superoxide dismutase 1; GSH, Glutathione; GSSG, Oxidized glutathione; NADP/NADPH, Nicotinamide adenine dinucleotide phosphate.

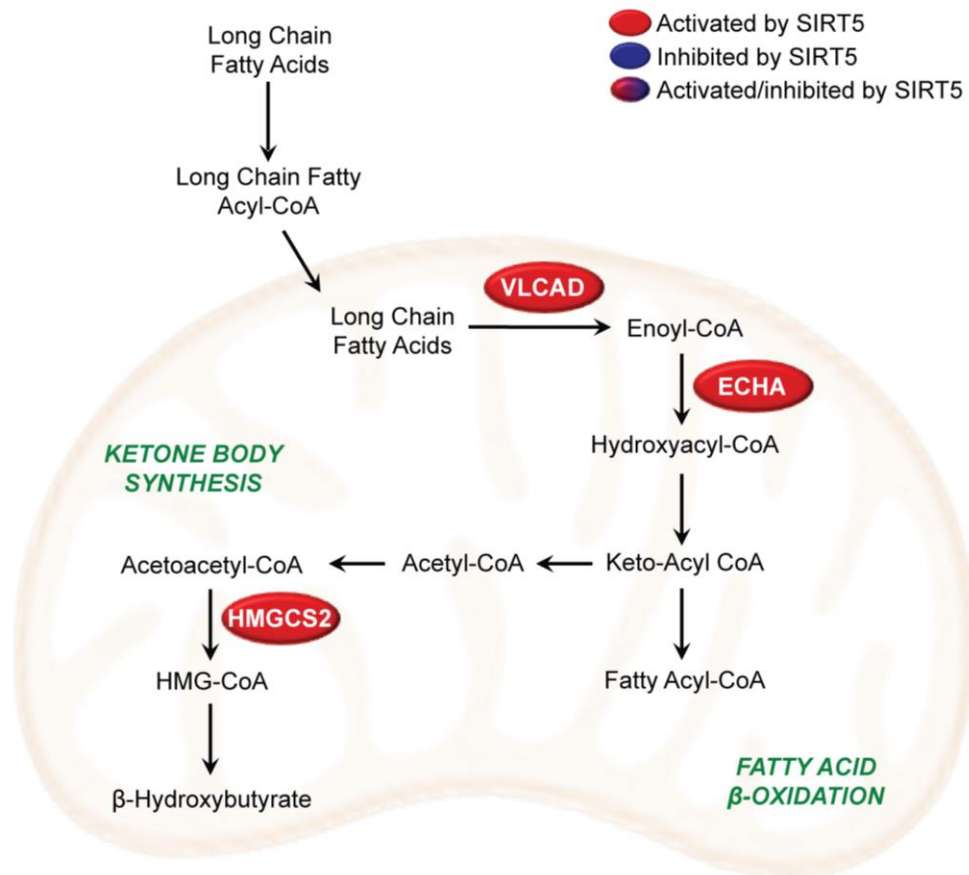


Figure 1.9 SIRT5 promotes fatty acid β -oxidation and ketone body synthesis. SIRT5-mediated deacylation increases the activity of VLCAD, ECHA and HMGCS2 (red ovals). Note that the schematic representation of key metabolic pathways is simplified. To emphasize the steps discussed in the text, multiple steps and connections between pathways were not shown. VLCAD, Very long-chain acyl-coenzyme A dehydrogenase; ECHA, Enoyl-coenzyme A hydratase; HMGCS2, 3-hydroxy-3-methylglutaryl-CoA synthase 2; HMG-CoA, hydroxymethylglutaryl-CoA.

sequence, while Exons 2-8, code for the catalytic core. In humans, *SIRT5* is found in two isoforms, which encode a 310 aa and a 299 aa protein, respectively (Mahlknecht *et al.* 2006). These two isoforms have been reported to localize in different compartments in the cell. *SIRT5*^{iso1} was found in the nucleus and the cytoplasm, while *SIRT5*^{iso2} localized in the mitochondria (Matsushita *et al.* 2011). Studies have reported that human *SIRT5* is predominantly expressed in heart muscle cells and in lymphoblasts (Mahlknecht *et al.* 2006). However, other studies testing for tissue distribution reported high *SIRT5* expression levels in brain, heart, liver, kidney, skeletal muscle, and testis (Michishita *et al.* 2005; Nakagawa *et al.* 2009).

The murine *Sirt5* gene is located at chromosome 13A4 and consists of 8 exons. It encodes a 310 aa protein with a molecular weight of 34.1 kDa. Mouse *Sirt5* is ubiquitously expressed in various tissues, with relatively high *Sirt5* expression level in the heart, skeletal muscle, brain, liver, testis and kidney (Su *et al.* 2002; Su *et al.* 2004; Michishita *et al.* 2005; Mahlknecht *et al.* 2006; Nakamura *et al.* 2008).

1.10.3.4 SIRT5 and diseases

Despite the large number of metabolic targets, there is no overt metabolic dysfunction seen in *SIRT5*-deficient mice (Yu *et al.* 2013). After prolonged fasting, *SIRT5*-deficient mice display elevated ammonia levels due to inactivation of CPS1 (Nakagawa *et al.* 2009; Yu *et al.* 2013). Metabolic characterization of these mice fed with chow and high fat diet, showed minor metabolic consequences (Yu *et al.* 2013).

SIRT5 is highly expressed in the heart compared to other tissues (Nishida *et al.* 2015; Sadhukhan *et al.* 2016). Several studies have shown that deletion of *Sirt5*

in mice has unfavorable effects on the heart. SIRT5-deficient mice show reduction in cardiac function in early adulthood, and acute stress of cardiac ischemia-reperfusion results in an increased infarct area in mice lacking SIRT5 (Boylston *et al.* 2015; Sadhukhan *et al.* 2016). Mechanistic studies have identified decreased activity of hydroxyacyl-CoA dehydrogenase alpha subunit (HADHA) and increased SDH activity as the main factors contributing to these cardiac phenotypes in SIRT5-deficient mice (Boylston *et al.* 2015; Sadhukhan *et al.* 2016). Together, these studies demonstrate that SIRT5 regulates heart metabolism and function via its desuccinylase activity.

SIRT5 is also highly expressed in the brain (Su *et al.* 2002; Su *et al.* 2004; Michishita *et al.* 2005; Mahlknecht *et al.* 2006; Nakamura *et al.* 2008). Multiple studies suggest that SIRT5 has neuroprotective roles (Parihar, *et al.* 2014; Liu *et al.* 2015). SIRT5-deficient mice show accelerated neurodegeneration in a neurotoxin-induced model of Parkinson's disease by altering mitochondrial antioxidant capacity (Liu *et al.* 2015). SIRT5-deficient mice also show increased mortality to epileptic seizures and neuronal loss when exposed to Kainate, a potent neuroexcitatory amino acid agonist that acts by activating receptors for glutamate (Li and Liu 2016). Together, these studies show the potential of SIRT5 to serve as protector of neurodegenerative diseases.

1.10.3.5. SIRT5 and cancer

The role of SIRT5 in the pathogenesis of human diseases is currently being investigated. The *SIRT5* gene is situated on chromosome locus 6p23, a region that has been reported to be involved in a variety of chromosomal abnormalities associated with malignant diseases (Mitelman *et al.* 1997). *SIRT5* mRNA expression is often increased

in several human cancers when compared to normal tissue. The increased levels of *SIRT5* mRNA in cancer are often due to gene amplification (Figure 1.10) (Finley, *et al.* 2011; Cerami *et al.* 2012; Gao *et al.* 2013; Lu *et al.* 2014).

SIRT5 was reported to be overexpressed in bone marrow lymphoplasmacytic cells from Waldenstrom's macroglobulinemia patients and in multiple types of pancreatic cancers (Ouaissi *et al.* 2008; Sun *et al.* 2011). An independent study reported that *Sirt5* is highly expressed in non-small cell lung cancer (NSCLC) and associated with poor survival rates (Lu *et al.* 2014). In concordance with these data, a recent study in human breast cancer showed that the expression levels of *Sirt5* were significantly overexpressed in breast cancer tissues and elevated in two breast cancer cell lines, MCF-7 and SKBR3 (Igci *et al.* 2016). Alongside, multiple studies using mouse models, also have reported the oncogenic potential of *SIRT5* (Lu *et al.* 2014; Xiangyun *et al.* 2017). Together, these data suggest that *SIRT5* may have crucial roles in the development of cancer.

Interestingly, some studies have reported a reduction of *Sirt5* expression in some cancers when compared to healthy tissue. *SIRT5* was found to be downregulated in head and neck squamous cell carcinoma when compared to healthy tissues (Lai *et al.* 2013). Interestingly, downregulation of *Sirt5* was more pronounced in advanced stages when compared to earlier stages, indicating that downregulation of *Sirt5* expression might contribute to the development of cancer in some context (Lai *et al.* 2013).

1.11 Summary

Breast cancer is the most commonly diagnosed cancer in women and the

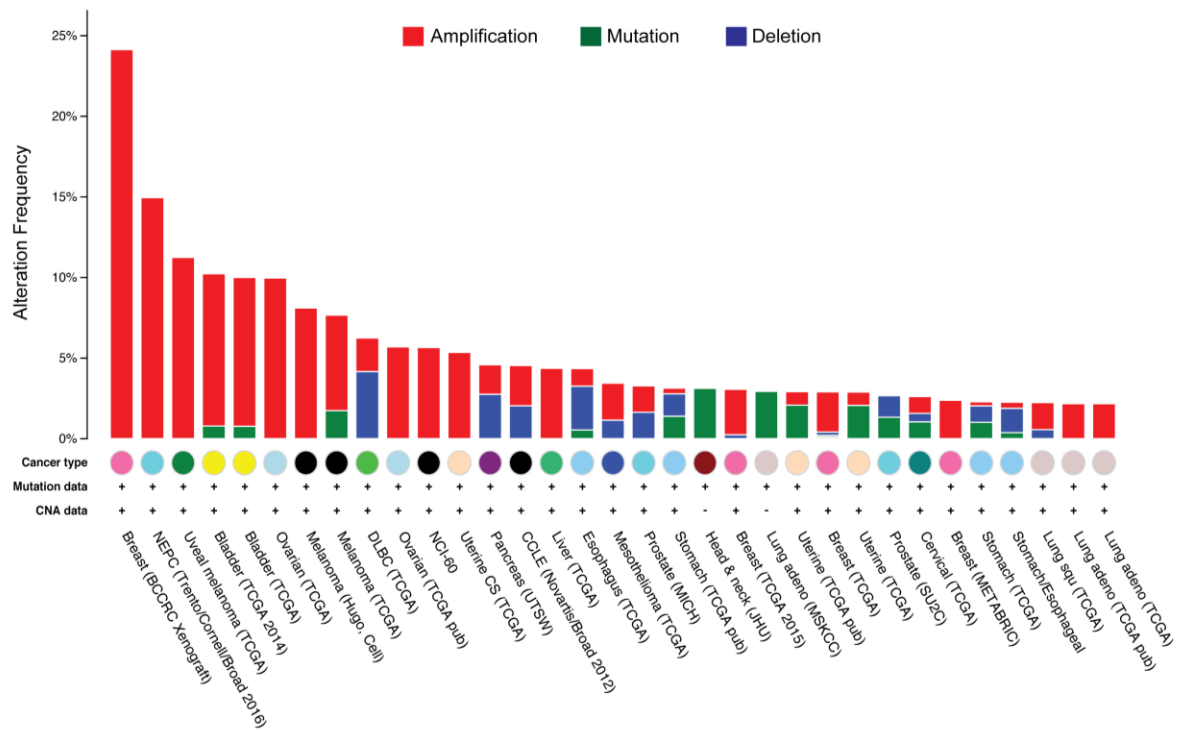


Figure 1.10 Cross-cancer alteration summary for SIRT5 (166 studies). According to cBioPortal web-based tool, SIRT5 gene copy number is often amplified (red bars) in many cancer types. Some cancers show other types of SIRT5 alterations such as mutation (green bars) or deletion (blue bars). Data was retrieved from BioPortal (Gao *et al.* 2013) on December 3, 2013.

second leading cause of cancer death. Besides new advances, the identification of new targets and the development of new strategies are necessary to intervene against this disease. Cancer cells possess an altered metabolism to obtain the energy and the essential building blocks to sustain their relentless proliferation. Most cancer cells increase glucose uptake to produce lactate even when oxygen is plentiful, a phenomenon known as the “Warburg effect”. In addition, cancer cells exhibit an increased rate of glutamine metabolism to replenish the Krebs cycle. For the past 50 years, numerous therapeutic approaches to target cancer metabolism have been developed. Unfortunately, many of these treatments fail to effect cures because small populations of cancer cells become resistant to treatment. This highlights the urgent need to identify new targets and develop new strategies to intervene against cancer.

Studies over the last decade strongly indicate that several members of the sirtuin family play important roles in carcinogenesis. Furthermore, recent findings have highlighted the importance of mitochondrial sirtuins (SIRT3, SIRT4, and SIRT5) in regulating multiple metabolic pathways. Among these, SIRT5 is the only known nicotinamide adenine dinucleotide-dependent deacetylase, desuccinylase and deglutarylase enzyme. SIRT5 is known to regulate multiple metabolic pathways including urea cycle, mitochondria respiration, pentose phosphate pathway, and glutamine metabolism.

Growing evidences implicate SIRT5 in contributing cancer growth and metabolic reprogramming. Sirt5 is often amplified in cancer and robust evidences have shown that SIRT5-mediated desumalonylation, desuccinylation and deglutarytion

support cancer proliferation by promoting the Warburg effect, antioxidant defense and resistance to chemotherapy.

This dissertation investigates the importance of SIRT5-regulated post-translational modification in cancer progression, identifies SIRT5 targets that are essential for cancer cell metabolic reprogramming, and evaluates the impact of *Sirt5* loss on the expression of genes that might be critical for tumor progression. In addition, this dissertation highlights the potential of SIRT5 as pharmacological target for treatment of specific cancer types.

1.12 REFERENCES

- Ades F, Zardavas D, Bozovic-Spasojevic I, Pugliano L, Fumagalli D, de Azambuja E, Viale G, Sotiriou C, Piccart M. Luminal B Breast Cancer: Molecular Characterization, Clinical Management, and Future Perspectives. *J. Clin. Oncol.* 2014; 32:2794-280.
- Ahn BH, Kim HS, Song S, Lee IH, Liu J, Vassilopoulos A, Deng CX, Finkel T. A role for the mitochondrial deacetylase Sirt3 in regulating energy homeostasis *Proc. Natl. Acad. Sci. USA.* 2008; 105:14447-14452.
- Ahuja N, Schwer B, Carobbio S, Waltregny D, North BJ, Castronovo V, Maechler P, Verdin E: Regulation of insulin secretion by SIRT4, a mitochondrial ADP-ribosyltransferase. *J. Biol. Chem.* 2007, 282(46):33583-33592.
- Aljada A, Saleh AM, Alkathiri M, Shamsa HB, Al-Bawab A, Nasr A. Altered Sirtuin 7 expression is associated with early stage breast cancer. *Breast Cancer (Auckl)* 2015; 9:3-8.
- Alo' PL, Visca P, Marci A, Mangoni A, Botti C, Di Tondo U. Expression of fatty acid synthase (FAS) as a predictor of recurrence in stage I breast carcinoma patients. *Cancer.* 1996; 77:474-482.
- American Cancer Society. *Cancer Facts & Figures 2017.* Atlanta: American Cancer Society; 2017.
- Aspuria PJ, Lunt SY, Varemo L, Vergnes L, Gozo M, Beach JA, Salumbides B, Reue K, Wiedemeyer WR, Nielsen J, Karlan BY, Orsulic S. Succinate dehydrogenase inhibition leads to epithelial-mesenchymal transition and reprogrammed carbon metabolism. *Cancer Metab.* 2014; 2:21.

- Attia YM, El-Abhar HS, Al Marzabani MM, Shouman SA. Targeting glycolysis by 3-bromopyruvate improves tamoxifen cytotoxicity of breast cancer cell lines. *BMC Cancer*. 2015.
- Ban KA, Godellas CV. Epidemiology of breast cancer. *Surg. Oncol. Clin. N. Am.* 2014; 23(3):409-422.
- Barber MF, Michishita-Kioi E, Xi Y, Tasselli L, Kioi M, Moqtaderi Z, Tennen RI, Paredes S, Young NL, Chen K, Struhl K, Garcia BA, Gozani O, Li W, Chua KF. SIRT7 links H3K18 deacetylation to maintenance of oncogenic transformation. *Nature*. 2012; 487:114-118.
- Bardella C, Pollard PJ, Tomlinson I. SDH mutations in cancer. *Biochim. Biophys. Acta*. 2011; 1807:1432-1443.
- Bitterman KJ, Anderson RM, Cohen HY, Latorre- Esteves M, Sinclair DA. Inhibition of silencing and accelerated aging by nicotinamide, a putative negative regulator of yeast sir2 and human SIRT1. *J. Biol. Chem.* 2002; 277:45099-45107.
- Bonadonna G, Brusamolino E, Valagussa P, Rossi A, Brugnatelli L, Brambilla C, De Lena M, Tancini G, Bajetta E, Musumeci R, Veronesi U. Combination Chemotherapy as an Adjuvant Treatment in Operable Breast Cancer. *N. Engl. J. Med.* 1976; 294:405-410.
- Boylston JA, Sun J, Chen Y, Gucek M, Sack MN, Murphy E. Characterization of the cardiac succinylome and its role in ischemia-reperfusion injury. *J. Mol. Cell Cardiol.* 2015; 88:73-81.
- Brenton JD, Carey LA, Ahmed AA, Caldas C. Molecular classification and molecular forecasting of breast cancer: ready for clinical application? *J. Clin. Oncol.* 2005;

23(29):7350-7360.

Britt K, Ashworth A, Smalley M. Pregnancy and the risk of breast cancer. *Endocrine-Related Cancer*. 2007; 14(4):907-933.

Brunet A, Sweeney LB, Sturgill JF, Chua KF, Greer PL, Lin Y, Tran H, Ross SE, Mostoslavsky R, Cohen HY, Hu LS, Cheng HL, Jedrychowski MP, Gygi SP, Sinclair DA, Alt FW, Greenberg ME. Stress-dependent regulation of FOXO transcription factors by the SIRT1 deacetylase. *Science*. 2004; 303:2011-2015.

Cairns RA, Harris IS, Mak TW. Regulation of cancer cell metabolism. *Nat. Rev. Cancer*. 2011; 11:85-95.

Calithera Bioscience. (2016). Calithera Biosciences Reports CB-839 Phase I Triple Negative Breast Cancer Combination Data at the 2016 San Antonio Breast Cancer Symposium. [Press release]. Retrieved from <http://ir.calithera.com/node/6731/pdf>.

Carey LA, Perou CM, Livasy CA, Dressler LG, Cowan D, Conway K, Karaca G, Troester MA, Tse CK, Edmiston S, Deming SL, Geradts J, Cheang MC, Nielsen TO, Moorman PG, Earp HS, Millikan RC. Race, breast cancer subtypes, and survival in the Carolina Breast Cancer Study. *JAMA*. 2006; 295(21):2492-2502.

Carey LA, Cheang MCU, Perou CM. Chapter 29: Genomics, Prognosis, and Therapeutic Interventions, in Harris JR, Lippman ME, Morrow M, Osborne CK. *Diseases of the Breast*, 5th edition, Lippincott Williams & Wilkins, 2014.

Cerami E, Gao J, Dogrusoz U, Gross BE, Sumer SO, Aksoy BA, Jacobsen A, Byrne CJ, Heuer ML, Larsson E, Antipin Y, Reva B, Goldberg AP, Sander C, Schultz N. The cBio cancer genomics portal: an open platform for exploring

- multidimensional cancer genomics data. *Cancer Discov.* 2012; 2(5):401-404.
- Chalkiadaki A, Guarente L. The multifaceted functions of sirtuins in cancer. *Nat. Rev. Cancer.* 2015; 15:608- 624.
- Chen B, Zang W, Wang J, Huang Y, He Y, Yan L, Liu J, Zheng W. The chemical biology of sirtuins. *Chem. Soc. Rev.* 2015; 44(15):5246-5264.
- Chen S, Seiler J, Santiago-Reichert M, Felbel K, Grummt I, Voit R. Repression of RNA polymerase I upon stress is caused by inhibition of RNA-dependent deacetylation of PAF53 by SIRT7. *Mol. Cell.* 2013; 52:303-313.
- Chen S, Blank MF, Iyer A, Huang B, Wang L, Grummt I, Voit R. SIRT7-dependent deacetylation of the U3-55k protein controls pre-rRNA processing. *Nat. Commun.* 2016; 7:10734.
- Chen WY, Rosner B, Hankinson SE, Colditz GA, Willett WC. Moderate alcohol consumption during adult life, drinking patterns, and breast cancer risk. *JAMA.* 2011; 306(17):1884-90.
- Choi J, Jung WH, Koo JS. Metabolism-related proteins are differentially expressed according to the molecular subtype of invasive breast cancer defined by surrogate immunohistochemistry. *Pathobiology.* 2013; 80:41-52.
- Choudhury S, Almendro V, Merino VS, Wu Z, Maruyama R, Su Y, Martins FC, Fackler MJ, Bessarabova M, Kowalczyk A, Conway T, Beresford-Smith B, Macintyre G, Cheng YK, Lopez-Bujanda Z, Kaspi A, Hu R, Robens J, Nikolskaya T, Haakensen VD, Schnitt SJ, Argani P, Ethington G, Panos L, Grant M, Clark J, Herlihy W, Lin SJ, Chew G, Thompson EW, Greene-Colozzi A, Richardson AL, Rosson GD, Pike M, Garber JE, Nikolsky Y, Blum JL, Au A, Hwang S, Tamimi

- RM, Michor F, Haviv I, Liu XS, Sukumar S. Molecular Profiling of Human Mammary Gland Links Breast Cancer Risk to a p27+ Cell Population with Progenitor Characteristics. *Cell Stem Cell*. 2013; 13(1):117-130.
- Christofk HR, Vander Heiden MG, Harris MH, Ramanathan A, Gerszten RE, Wei R, Fleming MD, Schreiber SL, Cantley LC. The M2 splice isoform of pyruvate kinase is important for cancer metabolism and tumour growth. *Nature*. 2008; 452:230-233.
- Cleary MP, Grossmann ME. Obesity and Breast Cancer: The Estrogen Connection. *Endocrinology*. 2009; 150(6):2537-2542.
- Copeland G, Lake A, Firth R, Wohler B, Wu XC, Schymur MJ, De P, Hofferkamp J, Sherman R, Kohler B. *Cancer in North America: 2010-2014. Volume One: Combined Cancer Incidence for the United States, Canada and North America*. Springfield, IL: North American Association of Central Cancer Registries, Inc, June 2017.
- Copeland G, Lake A, Firth R, Wohler B, Wu XC, Schymur MJ, De P, Hofferkamp J, Sherman R, Kohler B. *Cancer in North America: 2010-2014. Volume Two: Registry-specific Cancer Incidence for the United States, Canada and North America*. Springfield, IL: North American Association of Central Cancer Registries, Inc, June 2017.
- Csibi A, Fendt SM, Li C, Poulogiannis G, Choo AY, Chapski DJ, Jeong SM, Dempsey JM, Parkhitko A, Morrison T. The mTORC1 Pathway Stimulates Glutamine Metabolism and Cell Proliferation by Repressing SIRT4. *Cell*. 2013; 153:840-854.
- Currie E, Schulze A, Zechner R, Walther TC, Farese RV. Cellular Fatty Acid Metabolism

- and Cancer. *Cell Metab.* 2013; 18(2):153-161.
- Cuzick J, Sestak I, Cawthorn S, Hamed H, Holli K, Howell A, Forbes JF; IBIS-I Investigators. Tamoxifen for prevention of breast cancer: extended long-term follow-up of the IBIS-I breast cancer prevention trial. *Lancet Oncology.* 2015; 16(1):67-75.
- Dai JM, Wang ZY, Sun DC, Lin RX, Wang SQ. SIRT1 interacts with p73 and suppresses p73-dependent transcriptional activity. *J. Cell Physiol.* 2007; 210:161-166.
- Dai X, Chen A, Bai Z. Integrative investigation on breast cancer in ER, PR and HER2-defined subgroups using mRNA and miRNA expression profiling. *Sci. Rep.* 2014; 4:6566.
- Dang L, White DW, Gross S, Bennett BD, Bittinger MA, Driggers EM, Fantin VR, Jang HG, Jin S, Keenan MC, Marks KM, Prins RM, Ward PS, Yen KE, Liao LM, Rabinowitz JD, Cantley LC, Thompson CB, Vander Heiden MG, Su SM. Cancer-associated IDH1 mutations produce 2-hydroxyglutarate. *Nature.* 2009; 462:739-744.
- Das C, Lucia MS, Hansen KC, Tyler JK. CBP/p300-mediated acetylation of histone H3 on lysine 56. *Nature.* 2009; 459:113-117.
- Dasari S, Tchounwou PB, Cisplatin in cancer therapy: molecular mechanism of action. *Eur. J. Pharmacol.* 2015; 0: 364-378.
- DePinho RA. The age of cancer. *Nature.* 2000; 408:248-254.
- Doherty, J.; Cleveland, J. Targeting lactate metabolism for cancer therapeutics. *J. Clin Invest.* 2013; 123(9):3685-3692.

- Dryden SC, Nahhas FA, Nowak JE, Goustin AS, Tainsky MA. Role for human SIRT2 NAD-dependent deacetylase activity in control of mitotic exit in the cell cycle. *Mol. Cell. Biol.* 2003; 23:3173-3185.
- Du J, Zhou Y, Su X, Yu JJ, Khan S, Jiang H, Kim J, Woo J, Kim JH, Choi BH, He B, Chen W, Zhang S, Cerione RA, Auwerx J, Hao Q, Lin H. *Science.* 2011; 334, 806-809.
- Early Breast Cancer Trialists' Collaborative Group (EBCTCG), Dowsett M, Forbes JF. Aromatase inhibitors versus tamoxifen in early breast cancer: patient-level meta-analysis of the randomised trials. *Lancet.* 2015; 386(10001):1341-1352.
- Easton DF. How many more breast cancer predisposition genes are there? *Breast Cancer Research.* 1999; 1(1):14-17.
- Endogenous Hormones and Breast Cancer Collaborative Group, Key TJ, Appleby PN, Reeves GK, Roddam AW, Helzlsouer KJ, Alberg AJ, Rollison DE, Dorgan JF, Brinton LA, Overvad K, Kaaks R, Trichopoulos A, Clavel-Chapelon F, Panico S, Duell EJ, Peeters PH, Rinaldi S, Fentiman IS, Dowsett M, Manjer J, Lenner P, Hallmans G, Baglietto L, English DR, Giles GG, Hopper JL, Severi G, Morris HA, Hankinson SE, Tworoger SS, Koenig K, Zeleniuch-Jacquotte A, Arslan AA, Toniolo P, Shore RE, Krogh V, Micheli A, Berrino F, Barrett-Connor E, Laughlin GA, Kabuto M, Akiba S, Stevens RG, Neriishi K, Land CE, Cauley JA, Lui LY, Cummings SR, Gunter MJ, Rohan TE, Strickler HD. Circulating sex hormones and breast cancer risk factors in postmenopausal women: reanalysis of 13 studies. *Br. J. Cancer.* 2011; 105(5):709-722.
- Ewertz M, Duffy SW, Adami HO, Kvåle G, Lund E, Meirik O, Mellempgaard A, Soini I,

- Tulinius H. Age at first birth, parity and risk of breast cancer: a meta-analysis of 8 studies from the Nordic countries. *Int. J. Cancer*. 1990; 46(4):597-603.
- Fan S, Meng Q, Gao B, Grossman J, Yadegari M, Goldberg ID, Rosen EM. Alcohol stimulates estrogen receptor signaling in human breast cancer cell lines. *Cancer Res*. 2000; 60(20):5635-5639.
- Fantin VR, St-Pierre J, Leder P. Attenuation of LDH-A expression uncovers a link between glycolysis, mitochondrial physiology, and tumor maintenance. *Cancer Cell*. 2006; 9:425-434.
- Fedorova MS, Kudryavtseva AV, Lakunina VA, Snezhkina AV, Volchenko NN, Slavnova EN, Danilova TV, Sadritdinova AF, Melnikova NV, Belova AA Klimina KM, Sidorov DV, Alekseev BY, Kaprin AD, Dmitriev AA, Krasnov GS. Downregulation of OGDHL expression is associated with promoter hypermethylation in colorectal cancer. *Mol. Biol. (Mosk)*. 2015; 49:678-688.
- Feldman JL, Baeza J, Denu, JM. Activation of the protein deacetylase SIRT6 by long-chain fatty acids and widespread deacylation by mammalian sirtuins. *J. Biol. Chem*. 2013; 288:31350-31356.
- Ferlay J, Soerjomataram I, Dikshit R, Eser S, Mathers C, Rebelo M, Maxwell Parkin D, Forman D, Bray F. Cancer incidence and mortality worldwide: Sources, methods and major patterns in GLOBOCAN 2012. *Int. J. Cancer*. 2015; 136:E359-E386.
- Finley LW, Carracedo A, Lee J, Souza A, Egia A, Zhang J, Teruya-Feldstein J, Moreira PI, Cardoso SM, Clish CB, Pandolfi PP, Haigis MC. SIRT3 opposes reprogramming of cancer cell metabolism through HIF1 α destabilization. *Cancer Cell*, 2011; 19:416-428.

- Finley LW, Haas W, Desquiret-Dumas V, Wallace DC, Procaccio V, Gygi SP, Haigis MC. Succinate dehydrogenase is a direct target of sirtuin 3 deacetylase activity. *PLoS ONE*. 2011; 6:e23295.
- Finnin MS, Donigian JR, Pavletich NP: Structure of the histone deacetylase SIRT2. *Nat Struct Biol*. 2001; 8:621-625.
- Firestein R, Blander G, Michan S, Oberdoerffer P, Ogino S, Campbell J, Bhimavarapu A, Luikenhuis S, de Cabo R, Fuchs C, Hahn WC, Guarente LP, Sinclair DA. The SIRT1 deacetylase suppresses intestinal tumorigenesis and colon cancer growth. *PLoS ONE*. 2008; 3:e2020.
- Fischer, K.; Hoffmann, P.; Voelkl, S.; Meidenbauer, N. Inhibitory effect of tumor cell-derived lactic acid on human T cells. *Blood*. 2007;109:3812-3819.
- Ford E, Voit R, Liszt G, Magin C, Grummt I, Guarente L. Mammalian Sir2 homolog SIRT7 is an activator of RNA polymerase I transcription. *Genes & Development*. 2006; 20:1075-1080.
- Foukakis T, Bergh J. Prognostic and predictive factors in early, non-metastatic breast cancer. In: *UpToDate*. Hayes DF, Vora SR (eds.). Waltham, MA: UpToDate, 2016.
- Francken AB, Schouten PC, Bleiker EM, Linn SC, Rutgers EJ. Breast cancer in women at high risk: the role of rapid genetic testing for BRCA1 and -2 mutations and the consequences for treatment strategies. *Breast*. 2013; 22(5):561-568.
- Frye RA. Phylogenetic classification of prokaryotic and eukaryotic Sir2-like proteins. *Biochem. Biophys. Res. Commun*. 2000; 273(2):793-798.
- Gao J, Aksoy BA, Dogrusoz U, Dresdner G, Gross B, Sumer SO, Sun Y, Jacobsen

- A, Sinha R, Larsson E, Cerami E, Sander C, Schultz N. Integrative analysis of complex cancer genomics and clinical profiles using the cBioPortal. *Sci. Signal.* 2013; 6(269).
- Gao S, Chen X, Jin H, Ren S, Liu Z, Fang X, Xhang G. Overexpression of ErbB2 renders breast cancer cells susceptible to 3-BrPA through the increased dissociation of hexokinase II from mitochondrial outer membrane. *Oncol. Lett.* 2016; 11(2): 156-1573.
- Gao Z, Ye J. Inhibition of transcriptional activity of c-JUN by SIRT1. *Biochem. Biophys. Res. Commun.* 2008; 376(4):793-796.
- Gillies RJ, Gatenby RA, Hypoxia and adaptive landscapes in the evolution of carcinogenesis. *Cancer Metastasis Rev.* 2007; 26:311-317.
- Godwin J, Gray R, Clarke M, Cutter D, Darby S, McGale P, Pan HC, Taylor C, Wang YC, Dowsett M, Ingle J, Peto R, Early Breast Cancer Trialists' Collaborative Group (EBCTCG), Davies C. Relevance of breast cancer hormone receptors and other factors to the efficacy of adjuvant tamoxifen: patient-level meta-analysis of randomised trials. *Lancet.* 2011; 378(9793):771-784.
- Griggs JJ, Wolff A. Cyclin-Dependent Kinase 4/6 Inhibitors in the Treatment of Breast Cancer: More Breakthroughs and an Embarrassment of Riches. *J. Clin. Oncol.* 2017; 35(25): 2857-2859.
- Gross MI, Demo SD, Dennison JB, Chen L, Chernov-Rogan T, Goyal B, Janes JR, Laidig GJ, Lewis ER, Li J, Mackinnon AL, Parlati F, Rodriguez ML, Shwonek PJ, Sjogren EB, Stanton TF, Wang T, Yang J, Zhao F, Bennett MK. Antitumor activity of the glutaminase inhibitor CB-839 in triple-negative breast cancer. *Mol. Cancer*

- Ther. 2014; 13(4):890-901.
- Haigis MC, Mostoslavsky R, Haigis KM, Fahie K, Christodoulou DC, Murphy AJ, Valenzuela DM, Yancopoulos GD, Karow M, Blander GWolberger C, Prolla TA, Weindruch R, Alt FW, Guarente L. GuarenteSIRT4 inhibits glutamate dehydrogenase and opposes the effects of calorie restriction in pancreatic beta cells. *Cell*. 2006; 126:941-954.
- Haigis MC, Sinclair DA. Mammalian Sirtuins: Biological Insights and Disease Relevance. *Annual Review of Pathology-Mechanisms of Disease*. 2010; 5:253-295.
- Haigis MC, Deng CX, Finley LWS, Kim HS, Gius D. SIRT3 is a Mitochondrial Tumor Suppressor: A Scientific Tale that Connects Aberrant Cellular ROS, the Warburg Effect, and Carcinogenesis. *Cancer Res*. 2012; 72(10):2468-2472.
- Hallows WS, Lee S, Denu JM. Sirtuins deacetylate and activate mammalian acetyl-CoA synthetases. *Proc. Natl. Acad. Sci. USA*. 2006; 103:10230-10235.
- Han Y, Jin YH, Kim YJ, Kang BY, Choi HJ, Kim DW, Yeo CY, Lee KY. Acetylation of Sirt2 by p300 attenuates its deacetylase activity. *Biochem. Biophys. Res. Commun*. 2008; 375:576-580.
- Hartman AR, Kaldate RR, Sailer LM, Painter L, Grier CE, Endsley RR, Griffin M, Hamilton SA, Frye CA, Silberman MA, Wenstrup RJ, Sandbach JF. Prevalence of BRCA mutations in an unselected population of triple-negative breast cancer. *Cancer*. 2012; 118(11):2787-2795.
- Hilvo M, Denkert C, Lehtinen L, Muller B, Brockmoller S, Seppanen-Laakso T, Budczies J, Bucher E, Yetukuri L, Castillo S, Berg E, Nygren H, Sysi-Aho M, Griffin JL,

- Fiehn O, Loibl S, Richter-Ehrenstein C, Radke C, Hyötyläinen T, Kallioniemi O, Iljin K, Oresic M. Novel theranostic opportunities offered by characterization of altered membrane lipid metabolism in breast cancer progression. *Cancer Res* 2011; 71:3236-45.
- Hiratsuka M, Inoue T, Toda T, Kimura N, Shirayoshi Y, Kamitani H, Watanabe T, Ohama E, Tahimic CG, Kurimasa A, Oshimura M. Proteomics-based identification of differentially expressed genes in human gliomas: down-regulation of SIRT2 gene. *Biochem. Biophys. Res. Commun.* 2003; 309:558-566.
- Hirschey MD, Shimazu T, Goetzman E, Jing E, Schwer B, Lombard DB, Grueter CA, Harris C, Biddinger S, Ilkayeva OR, Stevens RD, Li Y, Saha AK, Ruderman NB, Bain JR, Newgard CB, Farese RV Jr, Alt FW, Kahn CR, Verdin E. SIRT3 regulates mitochondrial fatty-acid oxidation by reversible enzyme deacetylation *Nature*. 2010; 464:121-125.
- Hirschey MD. Old enzymes, new tricks: sirtuins are NAD(+)-dependent de-acylases. *Cell Metab.* 2011; 14(6):718-719.
- Hirschey MD, Zhao Y. Metabolic regulation by lysine malonylation, succinylation, and glutarylation. *Mol. Cell. Proteomics.* 2015; 14:2308-2315.
- Hitosugi T, Chen J: Post-translational modifications and the Warburg effect. *Oncogene.* 2014, 33:4279-4285.
- Howitz KT, Bitterman KJ, Cohen HY, Lamming DW, Lavu S, Wood JG, Zipkin RE, Chung P, Kisielewski A, Zhang LL, Scherer B, Sinclair DA. Small molecule activators of sirtuins extend *Saccharomyces cerevisiae* lifespan. *Nature.* 2003; 425:191-196.

- Hubbi ME, Hu H, Kshitiz Gilkes DM, Semenza GL. Sirtuin-7 inhibits the activity of hypoxia-inducible factors. *J. Biol. Chem.* 2013; 288:20768-20775.
- Igci M, Kalender ME, Borazan E, Bozgeyik I, Bayraktar R, Bozgeyik E, Camci C, Arslan A. High-throughput screening of Sirtuin family of genes in breast cancer. *Gene.* 2016; 586(1):123-128.
- Imai S, Armstrong CM, Kaeberlein M, Guarente L. Transcriptional silencing and longevity protein Sir2 is an NAD-dependent histone deacetylase. *Nature.* 2000; 403:795-800.
- Inoue T, Hiratsuka M, Osaki M, Oshimura M. The molecular biology of mammalian SIRT proteins: SIRT2 in cell cycle regulation. *Cell Cycle.* 2007; 6:1011-1018.
- Jeong SM, Xiao C, Finley LWS, Lahusen T, Souza AL, Pierce K, Li YH, Wang X, Laurent G, German NJ, Xu X, Li C, Wang RH, Lee J, Csibi A, Cerione RA, Blenis J, Clish CB, Kimmelman A, Deng CX, Haigis M. SIRT4 has tumor-suppressive activity and regulates the cellular metabolic response to DNA damage by inhibiting mitochondrial glutamine metabolism. *Cancer Cell.* 2013; 23:450-463.
- Jeong SM, Lee A, Lee J, Haigis, MC. SIRT4 protein suppresses tumor formation in genetic models of Myc-induced B cell lymphoma. *J. Biol. Chem.* 2014; 289:4135-4144.
- Jiang H, Khan S, Wang Y, Charron G, He B, Sebastian C, Du J, Kim R, Ge E, Mostoslavsky R, Hang HC, Hao Q, Lin H. SIRT6 regulates TNF-alpha secretion through hydrolysis of long-chain fatty acyl lysine. *Nature.* 2013; 496:110-113.
- Jiang W, Wang S, Xiao M, Lin Y, Zhou L, Lei Q, Xiong Y, Guan KL, Zhao S. Acetylation

- regulates gluconeogenesis by promoting PEPCK1 degradation via recruiting the UBR5 ubiquitin ligase. *Mol. Cell.* 2011; 43:33-44.
- Jing E, Gesta S, Kahn CR. SIRT2 regulates adipocyte differentiation through FoxO1 acetylation/deacetylation. *Cell Metab.* 2007; 6:105-114.
- Jing H, Hu J, He B, Negrón Abril YL, Stupinski J, Weiser K, Carbonaro M, Chiang YL, Southard T, Giannakakou P, Weiss RS, Lin H. A SIRT2-selective inhibitor promotes c-Myc oncoprotein degradation and exhibits broad anticancer activity. *Cancer Cell.* 2016; 29:1-14.
- Jonas, E.A.; Hickman, J.; Chachar, M.; Polster, B.; Brandt, T.; Fannjiang, Y.; Ivanovska, I.; Basanez, G.; Kinnally, K.; Zimmerberg, J. Proapoptotic N-truncated BCL-xL protein activates endogenous mitochondrial channels in living synaptic terminals. *Proc. Natl. Acad. Sci. USA.* 2004; 101:13590-13595.
- Jordan MA, Wilson L. Microtubules as a target for anticancer drugs. *Nat. Rev. Cancer.* 2004; 4(4):253-265.
- Kanfi Y, Naiman S, Amir G, Peshti V, Zinman G, Nahum L, Bar-Joseph Z, Cohen HY. The sirtuin SIRT6 regulates lifespan in male mice. *Nature.* 2012; 483:218-221.
- Katt WP, Ramachandran S, Erickson JW, Cerione RA. Dibenzophenanthridines as inhibitors of glutaminase C and cancer cell proliferation. *Mol. Cancer Ther.* 2012; 11(7):1269-1278.
- Kim HS, Patel K, Muldoon-Jacobs K, Bisht KS, Aykin-Burns N, Pennington JD, van der Meer R, Nguyen P, Savage J, Owens KM, Vassilopoulos A, Ozden O, Park SH, Singh KK, Abdulkadir SA, Spitz DR, Deng CX, Gius D. SIRT3 is a mitochondria-localized tumor suppressor required for maintenance of

- mitochondrial integrity and metabolism during stress. *Cancer Cell*. 2010; 17:41-52.
- Kim HS, Vassilopoulos A, Wang RH, Lahusen T, Xiao Z, Xu X, Li C, Veenstra TD, Li B, Yu H, Ji J, Wang XW, Park SH, Cha YI, Gius D, Deng CX. SIRT2 maintains genome integrity and suppresses tumorigenesis through regulating APC/C activity. *Cancer Cell*. 2011; 20(4):487-499.
- Kim S, Kim DH, Jung WH, Koo JS. Expression of glutamine metabolism-related proteins according to molecular subtype of breast cancer. *Endocr. Relat. Cancer*. 2013; 20:339-348.
- Kim S, Kim DH, Jung WH, Koo JS. Succinate dehydrogenase expression in breast cancer. *Springerplus*. 2013; 2:299.
- Kroemer G, Pouyssegur J. Tumor cell metabolism: cancer's Achilles' heel. *Cancer Cell*. 2008; 13:472-482.
- Kugel S, Mostoslavsky R. Chromatin and beyond: the multitasking roles for SIRT6. *Trends in Biochemical Sciences*. 2014; 39(2):72-81.
- LaBarge MA, Mora-Blanco EL, Samson S, Miyano M. Breast Cancer beyond the Age of Mutation. *Gerontology*. 2016; 62:434-442.
- Lai CC, Lin PM, Lin SF, Hsu CH, Lin HC, Hu ML, Hsu CM, Yang MY. Altered expression of SIRT gene family in head and neck squamous cell carcinoma. *Tumour Biol*. 2013; 34:1847-1854.
- Laurent G, German NJ, Saha AK, de Boer VC, Davies M, Koves TR, Dephoure N, Fischer F, Boanca G, Vaitheesvaran B, Lovitch SB, Sharpe AH, Kurland IJ, Steegborn C, Gygi SP, Muoio DM, Ruderman NB, Haigis MC: SIRT4 coordinates

- the balance between lipid synthesis and catabolism by repressing malonyl CoA decarboxylase. *Mol. Cell.* 2013, 50(5):686-698.
- Lee IH, Cao L, Mostoslavsky R, Lombard DB, Liu J, Bruns NE, Tsokos M, Alt FW, Finkel T. A role for the NAD-dependent deacetylase Sirt1 in the regulation of autophagy. *PNAS.* 2008; 105(9):3374-3379.
- Lehtonen JH, Kiuru M, Ylisaukko SK, Roja R, Salovaara R, Herva R, Koivisto PA, Vierimaa O, Aittomäki K, Pukkala E, Launonen V, Aaltonen LA. Increased risk of cancer in patients with fumarate hydratase germline mutation. *J. Med. Gent.* 2006; 43(6):523-526.
- Li F, He X, Ye D, Lin Y, Yu H, Yao C, Huang L, Zhang J, Wang F, Xu S, Wu X, Liu L, Yang C, Shi J, He X, Liu J, Qu Y, Guo F, Zhao J, Xu W, Zhao S. NADP(+)-IDH Mutations Promote Hypersuccinylation that Impairs Mitochondria Respiration and Induces Apoptosis Resistance. *Mol. Cell.* 2015; 60:661-675.
- Li F, Liu L. SIRT5 Deficiency Enhances Susceptibility to Kainate-Induced Seizures and Exacerbates Hippocampal Neurodegeneration not through Mitochondrial Antioxidant Enzyme SOD2. *Front Cell Neurosci.* 2016; 10:171.
- Li X, Zhang S, Blander G, Tse JG, Krieger M, Guarente L. SIRT1 deacetylates and positively regulates the nuclear receptor LXR. *Mol. Cell.* 2007; 28:91-106.
- Lin R, Tao R, Gao X, Li T, Zhou X, Guan KL, Xiong Y, Lei QY. Acetylation stabilizes ATP-citrate lyase to promote lipid biosynthesis and tumor growth. *Mol. Cell.* 2013; 51(4):506-518.
- Lin Z, Fang D. The roles of SIRT1 in cancer. *Genes Cancer.* 2013; 421(2):384-388.
- Lin ZF, Xu HB, Wang JY, Lin Q, Ruan Z, Liu FB, Jin W, Huang HH, Chen X. SIRT5

- desuccinylates and activates SOD1 to eliminate ROS. *Biochem. Biophys. Res. Commun.* 2013; 441:191-195.
- Liszt, G, Ford E, Kurtev M, Guarente L. Mouse Sir2 homolog SIRT6 is a nuclear ADP-ribosyltransferase. *J Biol. Chem.* 2005; 280:21313-21320.
- Liu L, Peritore C, Ginsberg J, Shih J, Arun S, Donmez G. Protective role of SIRT5 against motor deficit and dopaminergic degeneration in MPTP-induced mice model of Parkinson's disease. *Behav. Brain Res.* 2015; 281:215-221.
- Liu PY, Xu N, Malyukova A, Scarlett CJ, Sun YT, Zhang XD, Ling D, Su SP, Nelson C, Chang DK, Koach J, Tee AE, Haber M, Norris MD, Toon C, Rooman I, Xue C, Cheung BB, Kumar S, Marshall GM, Biankin AV, Liu T. The histone deacetylase SIRT2 stabilizes Myc oncoproteins. *Cell Death Differ.* 2013; 20(3):503-514.
- Liu Y, Dentin R, Chen D, Hedrick S, Ravnskjaer K, Schenk S, Milne J, Meyers DJ, Cole P, Yates J, Olefsky J, Guarente L, Montminy M. A fasting inducible switch modulates gluconeogenesis via activator/coactivator exchange. *Nature.* 2008; 456:269-273.
- Liu Y, Cao Y, Zhang W, Bergmeier S, Qian Y, Akbar H, Colvin R, Ding J, Tong L, Wu S, Hines J, Chen X. A small-molecule inhibitor of glucose transporter 1 downregulates glycolysis, induces cellcycle arrest, and inhibits cancer cell growth in vitro and in vivo. *Mol. Cancer Ther.* 2012; 11:1672-1682.
- Loftus TM, Jaworsky DE, Frehywot GL, Townsend CA, Ronnett GV, Lane MD, Kuhajda FP. Reduced food intake and body weight in mice treated with fatty acid synthase inhibitors. *Science.* 2000; 288:2379-2381.
- Long JP, Li XN, Zhang F. Targeting metabolism in breast cancer: How far we can go?

- World J. Clin. Oncol. 2016; 7(1):122-130.
- Longley DB, Harkin DP, Johnston PG. 5-fluorouracil: mechanisms of action and clinical strategies. *Nat. Rev. Cancer.* 2003; 3(5):330-338.
- Lu W, Zuo Y, Feng Y, Zhang M. SIRT5 facilitates cancer cell growth and drug resistance in non-small cell lung cancer. *Tumor Biol.* 2014; 35(11):10699-10705.
- Lunt SY, Vander V. Aerobic glycolysis: meeting the metabolic requirements of cell proliferation. *Annu. Rev. Cell Dev. Biol.* 2011; 27:441-464.
- Luo J, Nikolaev AY, Imai S, Chen E, Su F, Shiloh A, Guarente L, Gu W. Negative control of p53 by Sir2alpha promotes cell survival under stress. *Cell.* 2001; 107:137-148.
- Lv XB, Liu L, Cheng C, Yu B, Xiong L, Hu K, Tang J, Zeng L, Sang Y. SUN2 exerts tumor suppressor functions by suppressing the Warburg effect in lung cancer. *Sci Rep* 2015; 5:17940.
- Mahlknecht U, Ho AD, Letzel S, Voelter-Mahlknecht S. Assignment of the NAD-dependent deacetylase sirtuin 5 gene (SIRT5) to human chromosome band 6p23 by in situ hybridization. *Cytogenet. Genome Res.* 2006; 112:208-212.
- Mahlknecht U, Ho AD, Voelter-Mahlknecht S. Chromosomal organization and fluorescence in situ hybridization of the human Sirtuin 6 gene. *Int. J. Oncol.* 2006; 28:447-456.
- Mao Z, Hine C, Tian X, Van Meter M, Au M, Vaidya A, Seluanov A, Gorbunova V. SIRT6 promotes DNA repair under stress by activating PARP1. *Science.* 2011; 332:1443-1446.
- Mao Z, Tian X, Van Meter M, Ke Z, Gorbunova V, Seluanov A. Sirtuin 6 (SIRT6)

- rescues the decline of homologous recombination repair during replicative senescence. *Proc. Natl. Acad. Sci. USA.* 2012; 109:11800-11805.
- Marchbanks PA, McDonald JA, Wilson HG, Folger SG, Mandel MG, Daling JR, Bernstein L, Malone KE, Ursin G, Strom BL, Norman SA, Wingo PA, Burkman RT, Berlin JA, Simon MS, Spirtas R, Weiss LK. Oral contraceptives and the risk of breast cancer. *N. Engl. J. Med.* 2002; 346:2025-2032.
- Marquardt JU, Fischer K, Baus K, Kashyap A, Ma S, Krupp M, Linke M, Teufel A, Zechner U, Strand D, Strand D, Thorgeirsson SS, Galle PR, Strand S. Sirtuin-6-dependent genetic and epigenetic alterations are associated with poor clinical outcome in hepatocellular carcinoma patients. *Hepatology.* 2013; 58(3):1054-1064.
- Matsushita N, Yonashiro R, Ogata Y, Sugiura A, Nagashima S, Fukuda T, Inatome R, Yanagi S. Distinct regulation of mitochondrial localization and stability of two human Sirt5 isoforms. *Genes Cells.* 2011; 16(2):190-202.
- Mavaddat N, Antoniou AC, Easton DF, Garcia-Closas M. Genetic susceptibility to breast cancer. *Mol. Oncol.* 2010; 4(3):174-191.
- McClelland ML, Adler AS, Shang Y, Hunsaker T, Truong T, Peterson D, Torres E, Li L, Haley B, Stephan JP, Belvin M, Hatzivassiliou G, Blackwood EM, Corson L, Evangelista M, Zha J, Firestein R. An Integrated Genomic Screen Identifies LDHB as an Essential Gene for Triple-Negative Breast Cancer. *Cancer Res.* 2012, 72:5812-5823.
- McCord JM, Fridovich I. Superoxide dismutase. An enzymic function for erythrocyte hemocuprein (hemocuprein). *J. Biol. Chem.* 1969; 244:6049-6055.

- Menendez JA, Colomer R, Lupu R. Inhibition of tumor-associated fatty acid synthase activity enhances vinorelbine (Navelbine)-induced cytotoxicity and apoptotic cell death in human breast cancer cells. *Oncol. Rep.* 2004; 12:411-422.
- Menendez JA, Lupu R, Colomer R. Inhibition of tumor associated fatty acid synthase hyperactivity induces synergistic chemosensitization of HER-2/neu-overexpressing human breast cancer cells to docetaxel (taxotere). *Breast Cancer Res. Treat.* 2004; 84:183-195.
- Menendez JA, Vellon L, Colomer R, Lupu R. Pharmacological and small interference RNA-mediated inhibition of breast cancer-associated fatty acid synthase (oncogenic antigen-519) synergistically enhances Taxol (paclitaxel)-induced cytotoxicity. *Int. J. Cancer.* 2005; 115:19-35.
- Menendez JA, Lupu R. Fatty acid synthase and the lipogenic phenotype in cancer pathogenesis. *Nat Rev Cancer* 2007; 7:763-777.
- Metzger-Filho O, Sun Z, Viale G, Price KN, Crivellari D, Snyder RD, Gelber RD, Castiglione-Gertsch M, Coates AS, Goldhirsch A, Cardoso F. Patterns of recurrence and outcome according to breast cancer subtypes in lymph node-negative disease: results from international breast cancer study group trials VIII and IX. *J. Clin. Oncol.* 2013; 31(25):3083-3090.
- Michan S, Sinclair D. Sirtuins in mammals: insights into their biological function. *Biochem. J.* 2007; 404:1-13.
- Michishita E, Park JY, Burneskis JM, Barrett JC, Horikawa I. Evolutionarily conserved and nonconserved cellular localizations and functions of human SIRT proteins. *Mol. Biol. Cell.* 2005; 16:4623-4635.

- Michishita E, McCord RA, Berber E, Kioi M, Padilla-Nash H, Damian M, Cheung P, Kusumoto R, Kawahara TL, Barrett JC, Chang HY, Bohr VA, Ried T, Gozani O, Chua KF. SIRT6 is a histone H3 lysine 9 deacetylase that modulates telomeric chromatin. *Nature*. 2008; 452:492-496.
- Michishita E, McCord RA, Boxer LD, Barber MF, Hong T, Gozani O, Chua KF. Cell cycle-dependent deacetylation of telomeric histone H3 lysine K56 by human SIRT6. *Cell Cycle*. 2009; 8:2664-2666.
- Min J, Landry J, Sternglanz R, Xu RM: Crystal structure of a SIR2 homolog-NAD complex. *Cell*. 2001; 105:269-279.
- Mitelman F, Mertens F, Johansson B. A breakpoint map of recurrent chromosomal rearrangements in human neoplasia. *Nat. Genet. Spec*. 1997; 417-474.
- Mitri Z, Constantine T, O'Regan R. The HER2 Receptor in Breast Cancer: Pathophysiology, Clinical Use, and New Advances in Therapy. *Chemother. Res. Pract.* 2012; 743193.
- Motta MC, Divecha N, Lemieux M, Kamel C, Chen D, Gu W, Bultsma Y, McBurney M, Guarente L. Mammalian SIRT1 represses forkhead transcription factors. *Cell*. 2004; 116:551-563.
- Nakagawa T, Lombard DJ, Haigis MC, Guarente L. SIRT5 deacetylates carbamoyl phosphate synthetase 1 and regulates the urea cycle. *Cell*. 2009; 137:560-570.
- Nakamura Y, Ogura M, Tanaka D and Inagaki N. Localization of mouse mitochondrial SIRT proteins: shift of SIRT3 to nucleus by co-expression with SIRT5. *Biochem. Biophys. Res. Commun.* 2008; 366:174-179.
- Newman JC, He W, Verdin E. Mitochondrial Protein Acylation and Intermediary

- Metabolism: Regulation by Sirtuins and Implications for Metabolic Disease. *J Biol. Chem.* 2012; 287(51):42436-42443.
- Nishida Y, Rardin MJ, Carrico C, He W, Sahu AK, Gut P, Najjar R, Fitch M, Hellerstein M, Gibson BW, Verdin E. SIRT5 Regulates both Cytosolic and Mitochondrial Protein Malonylation with Glycolysis as a Major Target. *Mol Cell.* 2015; 59(2): 321-332.
- Nomura DK, Long JZ, Niessen S, Hoover HS, Ng SW, Cravatt BF. Monoacylglycerol lipase regulates a fatty acid network that promotes cancer pathogenesis. *Cell.* 2010; 140:49-61.
- North BJ, Marshall BL, Borra MT, Denu JM, Verdin E. The human Sir2 ortholog, SIRT2, is a NAD⁺-dependent tubulin deacetylase. *Mol Cell.* 2003; 11(2):437-444.
- North BJ, Verdin E. Sirtuins: Sir2-related NAD-dependent protein deacetylases. *Genome Biol.* 2004; 5(5):224.
- North BJ, Verdin E. Interphase nucleo-cytoplasmic shuttling and localization of SIRT2 during mitosis. *PLoS ONE.* 2007; 2:e784.
- Nunnari J, Suomalainen A. Mitochondria: in sickness and in health. *Cell* 2012; 148:1145-1159.
- Oberdoerffer P, Michan S, McVay M, Mostoslavsky R, Vann J, Park SK, Hartlerode A, Stegmuller J, Hafner A, Loerch P, Wright SM, Mills KD, Bonni A, Yankner BA, Scully R, Prolla TA, Alt FW, Sinclair DA. SIRT1 redistribution on chromatin promotes genomic stability but alters gene expression during aging. *Cell.* 2008; 135:907-918.
- O'Brien KM, Cole SR, Tse CK, Perou CM, Carey LA, Foulkes WD, Dressler LG,

- Geradts J, Millikan RC. Intrinsic breast tumor subtypes, race, and long-term survival in the Carolina Breast Cancer Study. *Clin. Cancer Res.* 2010; 16(24):6100-6110.
- Oellerich MF, Potente M, Sinclair D, North B. FOXOs and Sirtuins in Vascular Growth, Maintenance, and Aging. *Circulation Research.* 2012; 110(9).
- Orecchia, R. Breast cancer: Post-mastectomy radiotherapy reduces recurrence and mortality. *Nat. Rev. Clinical Oncology.* 2014; 11:382-384.
- Ouaissi M, Sielezneff I, Silvestre R, Sastre B, Bernard JP, Lafontaine JS, Payan MJ, Dahan L, Pirrò N, Seitz JF, Mas E, Lombardo D, Ouaissi A. High histone deacetylase 7 (HDAC7) expression is significantly associated with adenocarcinomas of the pancreas. *Ann. Surg. Oncol.* 2008; 15(8):2318-2238.
- Pan PW, Feldman JL, Devries MK, Dong A, Edwards AM, Denu JM. Structure and biochemical functions of SIRT6. *J. Biol. Chem.* 2011; 286:14575-14587.
- Parihar P, Solanki I, Mansuri ML, Parihar MS. Mitochondrial sirtuins: emerging roles in metabolic regulations, energy homeostasis and diseases. *Exp. Gerontol.* 2015; 61:130-140.
- Park J, Chen Y, Tishkoff DX, Peng C, Tan M, Dai L, Xie Z, Zhang Y, Zwaans BM, Skinner ME., Lombard DB, Zhao Y. SIRT5-mediated lysine desuccinylation impacts diverse metabolic pathways. *Mol. Cell.* 2013; 50:919-930.
- Pavlova NN, Thompson CB. The Emerging Hallmarks of Cancer Metabolism. *Cell Metabolism.* 2016; 23-47.
- Peng C, Lu Z, Xie Z, Cheng Z, Chen Y, Tan M, Luo H, Zhang Y, He W, Yang K, Zwaans BM, Tishkoff D, Ho L, Lombard D, He TC, Dai J, Verdin E, Ye Y, Zhao Y. The

- first identification of lysine malonylation substrates and its regulatory enzyme. *Mol. Cell. Proteomics*. 2011; 10:M111012658.
- Perez EA, Romond EH, Suman VJ, Jeong JH, Sledge G, Geyer CE Jr, Martino S, Rastogi P, Gralow J, Swain SM, Winer EP, Colon-Otero G, Davidson NE, Mamounas E, Zujewski JA, Wolmark N. Trastuzumab Plus Adjuvant Chemotherapy for Human Epidermal Growth Factor Receptor 2–Positive Breast Cancer: Planned Joint Analysis of Overall Survival From NSABP B-31 and NCCTG N9831. *J. Clin. Oncol*. 2014.
- Perou CM, Sørlie T, Eisen MB, van de Rijn M, Jeffrey SS, Rees CA, Pollack JR, Ross DT, Johnsen H, Akslen LA, Fluge Ø. Molecular portraits of human breast tumours. *Nature*. 2000; 406(6797): 747-752.
- Pizer ES, Thupari J, Han WF, Pinn ML, Chrest FJ, Frehywot GL, Townsend CA, Kuhajda FP. Malonyl-coenzyme-A is a potential mediator of cytotoxicity induced by fatty-acid synthase inhibition in human breast cancer cells and xenografts. *Cancer Res*. 2000; 60:213-218.
- Plunkett W, Huang P, Xu YZ, Heinemann V, Grunewald R, Gandhi V. Gemcitabine: metabolism, mechanisms of action, and self-potential. *Semin. Oncol*. 1995; 22(4):3-10.
- Pollard PJ, Briere JJ, Alam NA, Barwell J, Barclay E, Wortham NC, Hunt T, Mitchell M, Olpin S, Moat SJ, Hargreaves IP, Heales SJ, Chung YL, Griffiths JR, Dalglish A, McGrath JA, Gleeson MJ, Hodgson SV, Poulson R, Rustin P, Tomlinson IP. Accumulation of Krebs cycle intermediates and over-expression of HIF1alpha in tumours which result from germline FH and SDH mutations. *Hum. Mol. Genet*.

2005; 14:2231-2239.

Polletta L, Vernucci E, Carnevale I, Arcangeli T, Rotili D, Palmerio S, Steegborn C, Nowak T, Schutkowski M, Pellegrini L, Sansone L, Villanova L, Runci A, Pucci B, Morgante E, Fini M, Mai A, Russo MA, Tafani M. SIRT5 regulation of ammonia-induced autophagy and mitophagy. *Autophagy*. 2015; 11:253-270.

Ponec RM, Peddi P, Callahan RD. PARP Inhibitors in Breast Cancer: Latest Evidence. *Curr. Breast Cancer Reports*. 2017; 9(3): 18-194.

Prat, A, Lluch A, Albanell J, Barry WT, Fan C, Chacón JI, Parker JS, Calvo L, Plazaola A, Arcusa A, Seguí-Palmer MA, Burgues O, Ribelles N, Rodriguez-Lescure A, Guerrero A, Ruiz-Borrego M, Munarriz B, López JA, Adamo B, Cheang MC, Li Y, Hu Z, Gulley ML, Vidal MJ, Pitcher BN, Liu MC, Citron ML, Ellis MJ, Mardis E, Vickery T, Hudis CA, Winer EP, Carey LA, Caballero R, Carrasco E, Martín M, Perou CM, Alba E. Predicting response and survival in chemotherapy-treated triple-negative breast cancer. *Br. J. Cancer*. 2014; 111:1532-1541.

Pruitt K, Zinn RL, Ohm JE, McGarvey KM, Kang SH, Watkins DN, Herman JG, Baylin SB. Inhibition of SIRT1 reactivates silenced cancer genes without loss of promoter DNA hypermethylation. *PLoS Genet*. 2006;2:e40.

Puigserver P, Rhee J, Donovan J, Walkey CJ, Yoon JC, Oriente F, Kitamura Y, Altomonte J, Dong H, Accili D, Spiegelman BM. Insulin-regulated hepatic gluconeogenesis through FOXO1-PGC-1 α interaction. *Nature*. 2003; 423, 550-555.

Purushotham A, Schug TT, Xu Q, Surapureddi S, Guo X, Li X. Hepatocyte-specific deletion of SIRT1 alters fatty acid metabolism and results in hepatic steatosis

- and inflammation. *Cell Metab.* 2009; 9:327-338.
- Qiu X, Brown K, Hirschey MD, Verdin E, Chen D. Calorie restriction reduces oxidative stress by SIRT3-mediated SOD2 activation. *Cell Metab.* 2010; 12:662-667.
- Qu Q, Zeng F, Liu Z, Wang QJ, Deng F. Fatty acid oxidation and carnitine palmitoyltransferase I: emerging therapeutic targets in cancer. *Cell Death & Disease.* 2016; 7:e2226.
- Raghow R, Yellaturu C, Deng X, Park EA, Elam MB. SREBPs: the crossroads of physiological and pathological lipid homeostasis. *Trends Endocrinol. Metab.* 2008; 19:65-73.
- Rahman S, Islam R. Mammalian Sirt1: insights on its biological functions. *Cell Commun. Signal.* 2011; 9:11.
- Rakha EA, Reis-Filho JS, Ellis IO. Basal-like breast cancer: a critical review. *J. Clin. Oncol.* 2008; 26(15):2568-2581.
- Rardin MJ, He W, Nishida Y, Newman JC, Carrico C, Danielson SR, Guo A, Gut P, Sahu AK, Li B, Uppala R, Fitch M, Riiff T, Zhu L, Zhou J, Mulhern D, Stevens RD, Ilkayeva OR, Newgard CB, Jacobson MP, Hellerstein M, Goetzman ES, Gibson BW, Verdin E. SIRT5 regulates the mitochondrial lysine succinylome and metabolic networks. *Cell Metab.* 2013; 18:920-933.
- Rehman AG, Tyson M, Egger M, Heller RF, Zwahlen M. Body-mass index and incidence of cancer: a systematic review and meta-analysis of prospective observational studies. *Lancet.* 2008; 371(9612):569-578.
- Revollo JR, Grimm AA, Imai S. The NAD biosynthesis pathway mediated by nicotinamide phosphoribosyltransferase regulates Sir2 activity in mammalian

- cells. *J. Biol. Chem.* 2004; 279:50754-50763.
- Robinson B. *Biomedicine: A Textbook for Practitioners of Acupuncture & Oriental Medicine.* 2007.
- Roessler C, Nowak T, Pannek M, Gertz M, Nguyen GTT, Scharfe M, Born I, Sippl W, Steegborn C, Schutkowski M. Chemical probing of the human sirtuin 5 active site reveals its substrate acyl specificity and peptide-based inhibitors. *Angew. Chem. Int. Engl.* 2014; 53:10728-10732.
- Russo J, Moral R, Balogh GA, Mailo D, Russo IH. The protective role of pregnancy in breast cancer. *Breast Cancer Research.* 2005; 7(3):131-142.
- Ryu D, Jo YS, Lo Sasso G, Stein S, Zhang H, Perino A, Lee JU, Zeviani M, Romand R, Hottiger MO, Schoonjans K, Auwerx J. A SIRT7-dependent acetylation switch of GABP β 1 controls mitochondrial function. *Cell Metab.* 2014; 20:856-869.
- Sadhukhan S, Liu X, Ryu D, Nelson OD, Stupinski JA, Li Z, Chen W, Zhang S, Weiss RS, Locasale JW, Auwerx J, Lin H. Metabolomics- assisted proteomics identifies succinylation and SIRT5 as important regulators of cardiac function. *Proc. Natl. Acad. Sci. USA.* 2016; 113:4320-4325.
- Sajjani K, Islam F, Smith RA, Gopalan V, Lam AK. Genetic alterations in Krebs cycle and its impact on cancer pathogenesis. *Biochimie.* 2017; 135:164-172.
- Sauve AA, Wolberger C, Schramm VL, Boeke JD. The biochemistry of sirtuins. *Annu. Rev. Biochem.* 2006; 75:435-465.
- Sauve AA, Sirtuin chemical mechanisms. *Biochim. Biophys. Acta.* 2010; 1804(8):1591-603.
- Schuetz A, Min J, Antoshenko T, Wang CL, Allali-Hassani A, Dong A, Loppnau P,

- Vedadi M, Bochkarev A, Sternglanz R, Plotnikov AN. Structural basis of inhibition of the human NAD⁺-dependent deacetylase SIRT5 by suramin. *Structure*. 2007; 5: 377-389.
- Sebastian C, Zwaans BM, Silberman DM, Gymrek M, Goren A, Zhong L, Ram O, Truelove J, Guimaraes AR, Toiber D, Cosentino C, Greenson JK, MacDonald AI, McGlynn L, Maxwell F, Edwards J, Giacosa S, Guccione E, Weissleder R, Bernstein BE, Regev A, Shiels PG, Lombard DB, Mostoslavsky R. The histone deacetylase SIRT6 is a tumor suppressor that controls cancer metabolism. *Cell*. 2012; 151:1185-1199.
- Seitz HK, Maurer B. The relationship between alcohol metabolism, estrogen levels, and breast cancer risk. *Alcohol Res. Health*. 2007; 30(1):42-43.
- Seitz HK, Pelucchi C, Bagnardi V, La Vecchia C. Epidemiology and pathophysiology of alcohol and breast cancer: Update 2012. *Alcohol. Alcohol*. 2014; 47(3):204-212.
- Shah AA, Ito A, Nakata A, Yoshida M. Identification of a selective SIRT2 inhibitor and its anti-breast cancer activity. *Biol. Pharm. Bull*. 2016; 39:1739-1742.
- Shimazu T, Hirschey MD, Hua L, Dittenhafer-Reed KE, Schwer B, Lombard DB, Li Y, Bunkenborg J, Alt FW, Denu JM, Jacobson MP, Verdin E. SIRT3 deacetylates mitochondrial 3-hydroxy-3-methylglutaryl CoA synthase 2 and regulates ketone body production. *Cell Metab*. 2010; 12:654-661.
- Shin J, He M, Liu Y, Paredes S, Villanova L, Brown K, Qiu X, Nabavi N, Mohrin M, Wojnoonski K, Li P, Cheng HL, Murphy AJ, Valenzuela DM, Luo H, Kapahi P, Krauss R, Mostoslavsky R, Yancopoulos GD, Alt FW, Chua KF, Chen D. SIRT7 represses Myc activity to suppress ER stress and prevent fatty liver disease. *Cell*

Rep. 2013; 5:654-665.

Shulga N, Wilson-Smith R, Pastorino JG. Sirtuin-3 deacetylation of cyclophilin D induces dissociation of hexokinase II from the mitochondria. *J. Cell Sci.* 2010; 123:894-902.

Simpson, N.E.; Tryndyak, V.P.; Pogribna, M.; Beland, F.A.; Pogribny, I.P. Modifying metabolically sensitive histone marks by inhibiting glutamine metabolism affects gene expression and alters cancer cell phenotype. *Epigenetics* 2012; 7:1413-1420.

Slamon D, Eiermann W, Robert N, Pienkowski T, Martin M, Press M, Mackey J, Glaspy J, Chan A, Pawlicki M, Pinter T, Valero V, Liu MC, Sauter G, von Minckwitz G, Visco F, Bee V, Buyse M, Bendahmane B, Tabah-Fisch I, Lindsay MA, Riva A, Crown J. Breast Cancer International Research Group. Adjuvant trastuzumab in HER2-positive breast cancer. *N. Engl. J. Med.* 2011; 365(14):1273-1283.

Someya S, Yu W, Hallows WC, Xu J, Vann JM, Leeuwenburgh C, Tanokura M, Denu JM, Prolla TA. Sirt3 mediates reduction of oxidative damage and prevention of age-related hearing loss under caloric restriction. *Cell.* 2010; 143:802-812.

Sorlie T, Tibshirani R, Parker J, Hastie T, Marron JS, Nobel A, Deng S, Johnsen H, Pesich R, Geisler S, Demeter J, Perou CM, Lønning PE, Brown PO, Børresen-Dale AL, Botstein D. Repeated observation of breast tumor subtypes in independent gene expression data sets. *Proc. Natl. Acad. Sci. USA.* 2003; 100(14):8418-8423.

Sparano JA, Wang, M, Zhao F, Stearns V, Martino S, Ligibel JA, Perez EA, Saphner T, Wolff AC, Sledge GW, Wood WC, Fetting J, Davidson NE. Obese and

Overweight Women May Have Higher Risk of Recurrence. *J. Cancer*. 2012; 118:5937-5946.

Su A, Cooke MP, Ching KA, Hakak Y, Walker JR, Wiltshire T, Orth AP, Vega RG, Sapinoso LM, Moqrich A, Patapoutian A, Hampton GM, Schultz PG, Hogenesch JB. Large-scale analysis of the human and mouse transcriptomes. *Proc. Natl. Acad. Sci. USA*. 2002; 99(7):4465-4470.

Su A, Wiltshire T, Batalov S, Lapp H, Ching KA, Block D, Zhang J, Soden R, Hayakawa M, Cooke MP, Walker JR, Hogenesch JB. A gene atlas of the mouse and human protein-encoding transcriptomes. *Proc. Natl. Acad. Sci. USA*. 2004; 101:6062-6067.

Sudarshan S, Sourbier C, Kong HS, Block K, Valera Romero VA, Yang Y, Galindo C, Mollapour M, Scroggins B, Goode N, Lee MJ, Gourlay CW, Trepel J, Linehan WM, Neckers L. Fumarate hydratase deficiency in renal cancer induces glycolytic addiction and hypoxia-inducible transcription factor 1 alpha stabilization by glucose-dependent generation of reactive oxygen species. *Mol. Cell Biol*. 2009; 29:4080-4090.

Sun JY, Xu L, Tseng H, Ciccarelli B, Fulciniti M, Hunter ZR, Maghsoudi K, Hatjiharissi E, Zhou Y, Yang G, Zhu B, Liu X, Gong P, Ioakimidis L, Sheehy P, Patterson CJ, Munshi NC, O'Connor OA, Treon SP. Histone deacetylase inhibitors demonstrate significant preclinical activity as single agents, and in combination with bortezomib in Waldenstrom's macroglobulinemia. *Clin. Lymphoma Myeloma Leuk*. 2011; 11:152-156.

Symptoms of Breast Cancer. BreastCancer.org.

http://www.breastcancer.org/symptoms/understand_bc/statistics. Accessed on September 29, 2017.

Szczepankiewicz BG, Dai H, Koppetsch KJ, Qian D, Jiang F, Mao C, Perni RB. Synthesis of Carba-NAD and the Structures of Its Ternary Complexes with SIRT3 and SIRT5. *J. Org. Chem.* 2012; 77:7319-7329.

Tacar O, Sriamornsak P, Dass CR. Doxorubicin: an update on anticancer molecular action, toxicity and novel drug delivery systems. *J. Pharm. Pharmacol.* 2013; 65 (2):157-170.

Tan M, Peng C, Anderson KA, Chhoy P, Xie Z, Dai L, Park J, Chen Y, Huang H, Zhang Y, Ro J, Wagner GR, Green MF, Madsen AS, Schmiesing J, Peterson BS, Xu G, Ilkayeva OR, Muehlbauer MJ, Braulke T, Mühlhausen C, Backos DS, Olsen, CA, McGuire PJ, Pletcher SD, Lombard DB, Hirschey MD, Zhao Y. Lysine glutarylation is a protein post-translational modification regulated by SIRT5. *Cell Metab.* 2014; 19:605-617.

Tanno M, Sakamoto J, Miura T, Shimamoto K, Horio Y. Nucleocytoplasmic shuttling of the NAD(+)-dependent histone deacetylase SIRT1. *Journal of Biological Chemistry.* 2007; 282:6823-6832.

Tao R, Xiong X, DePinho RA, Deng CX, Dong XC. Hepatic SREBP-2 and cholesterol biosynthesis are regulated by FoxO3 and Sirt6. *J. Lipid Res.* 2013; 54(10):2745-53.

Toiber D, Erdel F, Bouazoune K, Silberman DM, Zhong L, Mulligan P, Sebastian C, Cosentino C, Martinez-Pastor B, Giacosa S, D'Urso A, Näär AM, Kingston R, Rippe K, Mostoslavsky R. SIRT6 recruits SNF2H to DNA break sites, preventing

- genomic instability through chromatin remodeling. *Mol. Cell.* 2013; 51:454-468.
- U.S. Food and Drug Administration. (2017). FDA approves new targeted treatment for relapsed or refractory acute myeloid leukemia. [Press release]. Retrieve from <https://www.fda.gov/NewsEvents/Newsroom/PressAnnouncements/ucm569421.htm>.
- Vakhrusheva O, Smolka C, Gajawada P, Kostin S, Boettger T, Kubin T, Braun T, Bober E. Sirt7 increases stress resistance of cardiomyocytes and prevents apoptosis and inflammatory cardiomyopathy in mice. *Circ. Res.* 2008; 102:703-710.
- Van der Horst A, Tertoolen LG, de Vries-Smits LM, Frye RA, Medema RH, Burgering BM. FOXO4 is acetylated upon peroxide stress and deacetylated by the longevity protein hSir2 (SIRT1). *J. Biol. Chem.* 2004; 279:28873-28879.
- Van der Knaap JA, Verrijzer CP. Undercover: gene control by metabolites and metabolic enzymes. *Genes & Dev.* 2016; 30:2345-2369.
- Van Meter M, Gorbunova V, Seluanov A. SIRT6: A Promising Target for Cancer Prevention and Therapy. In: Grimm S. (eds) *Anticancer Genes. Advances in Experimental Medicine and Biology.* 2014; 818. Springer, London.
- Van Meter M, Kashyap M, Rezazadeh S, Geneva AJ, Morello TD, Seluanov A, Gorbunova V. SIRT6 represses LINE1 retrotransposons by ribosylating KAP1 but this repression fails with stress and age. *Nature communications.* 2014; 5:5011.
- Vander Heiden MG, Cantley LC, Thompson CB. Understanding the Warburg effect: the metabolic requirements of cell proliferation. *Science.* 2009; 324:1029-1033.
- Vaquero A, Scher M, Lee D, Erdjument-Bromage H, Tempst P, Reinberg D. Human SirT1 interacts with histone H1 and promotes formation of facultative

- heterochromatin. *Mol. Cell.* 2004; 16(1):93-105.
- Vaquero A, Scher MB, Lee DH, Sutton A, Cheng HL, Alt FW, Serrano L, Sternglanz R, Reinberg D. SirT2 is a histone deacetylase with preference for histone H4 Lys 16 during mitosis. *Genes Dev.* 2006; 20:1256-1261.
- Varela-Rey M, Woodhoo A, Martinez-Chantar ML, Mato JM, Lu SC. Alcohol, DNA methylation, and cancer. *Alcohol Res.* 2013; 35(1):25-35.
- Vaziri H, Dessain SK, Ng Eaton E, Imai SI, Frye RA, Pandita TK, Guarente L, Weinberg RA. hSIR2(SIRT1) functions as an NAD-dependent p53 deacetylase. *Cell.* 2001; 107:149-159.
- Vazquez-Martin A, Colomer R, Brunet J, Lupu R, Menendez JA. Overexpression of fatty acid synthase gene activates HER1/HER2 tyrosine kinase receptors in human breast epithelial cells. *Cell Prolif.* 2008; 41:59-85.
- Vicier C, Dieci MV, Arnedos M, Delalogue S, Viens P, Andre F. Clinical development of mTOR inhibitors in breast cancer. *Breast Cancer Research.* 2014; 16:203.
- Voduc KD, Cheang MC, Tyldesley S, Gelmon K, Nielsen TO, Kennecke H. Breast cancer subtypes and the risk of local and regional relapse. *J. Clin. Oncol.* 2010; 28(10):1684-1691.
- Vogel VG, Costantino JP, Wickerham DL, Cronin WM, Cecchini RS, Atkins JN, Bevers TB, Fehrenbacher L, Pajon ER Jr, Wade JL 3rd, Robidoux A, Margolese RG, James J, Lippman SM, Runowicz CD, Ganz PA, Reis SE, McCaskill-Stevens W, Ford LG, Jordan VC, Wolmark N; National Surgical Adjuvant Breast and Bowel Project (NSABP). Effects of tamoxifen vs raloxifene on the risk of developing invasive breast cancer and other disease outcomes: the NSABP Study of

- Tamoxifen and Raloxifene (STAR) P-2 trial. *JAMA*. 2006; 295(23):2727-2741.
- Wagner GR, Payne RM. Widespread and enzyme-independent N{epsilon}-acetylation and N{epsilon}-succinylation in the chemical conditions of the mitochondrial matrix. *J. Biol. Chem.* 2013; 288(40):29036–29045.
- Walker AK, Yang F, Jiang K, Ji JY, Watts JL, Purushotham A, Boss O, Hirsch ML, Ribich S, Smith JJ, Israelian K, Westphal CH, Rodgers JT, Shioda T, Elson SL, Mulligan P, Najafi-Shoushtari H, Black JC, Thakur JK, Kadyk LC, Whetstine JR, Mostoslavsky R, Puigserver P, Li X, Dyson NJ, Hart AC, Näär AM. Conserved role of SIRT1 orthologs in fasting-dependent inhibition of the lipid/cholesterol regulator SREBP. *Genes Dev.* 2010; 24:1403-1417.
- Walko CM, Lindley C: Capecitabine: a review. *Clin. Ther.* 2005; 27(1):23-44.
- Wang F, Chan CH, Chen K, Guan X, Lin HK, Tong Q. Deacetylation of FOXO3 by SIRT1 or SIRT2 leads to Skp2-mediated FOXO3 ubiquitination and degradation. *Oncogene.* 2012; 31:1546-1557.
- Wang F, Wang K, Xu W, Zhao S, Ye D, Wang Y, Xu Y, Zhou L, Chu Y, Zhang C, Qin X, Yang P, Yu H. SIRT5 Desuccinylates and Activates Pyruvate Kinase M2 to Block Macrophage IL-1 β Production and to Prevent DSS-Induced Colitis in Mice. *Cell Rep.* 2017; 19(11):2331-2344.
- Wang HL, Lu RQ, Xie SH, Zheng H, Wen XM, Gao X, Guo L. SIRT7 exhibits oncogenic potential in human ovarian cancer cells. *Asian Pac. J. Cancer Prev.* 2015; 16:3573-3577.
- Wang RH, Sengupta K, Li C, Kim HS, Cao L, Xiao C, Kim S, Xu X, Zheng Y, Chilton B, Jia R, Zheng ZM, Appella E, Wang XW, Ried T, Deng CX. Impaired DNA

- damage response, genome instability, and tumorigenesis in SIRT1 mutant mice. *Cancer Cell*. 2008; 14:312-323.
- Wang RH, Zheng Y, Kim HS, Xu X, Cao L, Luhasen T, Lee MH, Xiao C, Vassilopoulos A, Chen W, Gardner K, Man YG, Hung MC, Finkel T, Deng CX. Interplay among BRCA1, SIRT1, and Survivin during BRCA1-associated tumorigenesis. *Mol Cell*. 2008; 32:11-20.
- Warburg, O. On the origin of cancer cell. *Science*. 1925; 123:309-314.
- Weinert BT, Iesmantavicius V, Moustafa T, Scholz C, Wagner SA, Magnes C, Zechner R, Choudhary C. Acetylation dynamics and stoichiometry in *Saccharomyces cerevisiae*. *Mol. Syst. Biol*. 2013; 10:716.
- Weinert BT, Schölz C, Wagner SA, Iesmantavicius V, Su D, Daniel JA, Choudhary C. Lysine succinylation is a frequently occurring modification in prokaryotes and eukaryotes and extensively overlaps with acetylation. *Cell Rep*. 2013; 4, 842-851.
- Westhoff CL. Breast cancer risk: perception versus reality. *Contraception*. 1999; 59:25-28.
- Wise, D.R.; Ward, P.S.; Shay, J.E.; Cross, J.R.; Gruber, J.J.; Sachdeva, U.M.; Platt, J.M.; De Matteo, R.G.; Simon, M.C.; Thompson, C.B. Hypoxia promotes isocitrate dehydrogenase-dependent carboxylation of alpha-ketoglutarate to citrate to support cell growth and viability. *Proc. Natl. Acad Sci. USA*. 2011; 108: 19611-19616.
- Wong S, Weber JD. Deacetylation of the retinoblastoma tumour suppressor protein by SIRT1. *Biochem. J*. 2007; 407:451-460.

- Xiangyun Y, Xiaomin N, Linping G, Yunhua X, Ziming L, Yongfeng Y, Zhiwei C, Shun L. Desuccinylation of pyruvate kinase M2 by SIRT5 contributes to antioxidant response and tumor growth. *Oncotarget*. 2017; 8:6984-6993.
- Xiaoling L. SIRT1 and energy metabolism. *Acta Biochim. Biophys. Sin. (Shanghai)*. 2013; 45(1):51-60.
- Xie Z, Dai J, Dai L, Tan M, Cheng Z, Wu Y, Boeke JD, Zhao Y. Lysine succinylation and lysine malonylation in histones. *Mol. Cell. Proteomics*. 2012; 11:100-107.
- Yang B, Zwaans BM, Eckersdorff M, Lombard DB. The sirtuin SIRT6 deacetylates H3 K56Ac in vivo to promote genomic stability. *Cell Cycle*. 2009; 8:2662-2663.
- Yang L, Ma X, He Y, Yuan C, Chen Q, Li G, Chen X. Sirtuin 5: a review of structure, known inhibitors and clues for developing new inhibitors. *Sci. China Life Sci*. 2017; 60(3):249-256.
- Yeung F, Hoberg JE, Ramsey CS, Keller MD, Jones DR, Frye RA, Mayo MW. Modulation of NF- κ B-dependent transcription and cell survival by the SIRT1 deacetylase. *EMBO J*. 2004; 23:2369-2380.
- Yu J, Sadhukhan S, Noriega LG, Moullan N, He B, Weiss RS, Lin H, Schoonjans K, Auwerx J. Metabolic characterization of a Sirt5 deficient mouse model. *Sci. Rep*. 2013; 3:2806.
- Zhang S, Chen P, Huang Z, Hu X, Chen M, Hu S, Hu Y, Cai T. SIRT7 promotes gastric cancer growth and inhibits apoptosis by epigenetically inhibiting miR-34a. *Sci. Rep*. 2015; 5:9787.
- Zhang T, Kraus WL. SIRT1-dependent regulation of chromatin and transcription: linking NAD⁺ metabolism and signaling to the control of cellular functions.

- Biochim. Biophys. Acta. 2010; 1804(8):1666-1675.
- Zhang W, Zhang SL, Hu X, Tam KY. Targeting Tumor Metabolism for Cancer Treatment: Is Pyruvate Dehydrogenase Kinases (PDKs) a Viable Anticancer Target? *Int. J. Biol. Sci.* 2015; 11(12):1390-1400.
- Zhang X, Tworoger SS, Eliassen AH, Hankinson SE. Postmenopausal plasma sex hormone levels and breast cancer risk over 20 years of follow-up. *Breast Cancer Res. Treat.* 2013; 137(3):883-892.
- Zhang Y, Bharathi SS, Rardin MJ, Uppala R, Verdin E, Gibson BW, Goetzman ES. SIRT3 and SIRT5 regulate the enzyme activity and cardiolipin binding of very long- chain acyl- CoA dehydrogenase. *PLoS One.* 2015; 10:e0122297.
- Zhang Y, Bharathi SS, Rardin MJ, Lu J, Maringer KV, Sims-Lucas S, Prochownik EV, Gibson BW, Goetzman ES. Lysine desuccinylase SIRT5 binds to cardiolipin and regulates the electron transport chain. *J. Biol. Chem.* 2017; 292:10239.
- Zhang Z, Tan M, Xie Z, Dai L, Chen Y, Zhao Y. Identification of lysine succinylation as a new post-translational modification. *Nat. Chem. Biol.* 2011; 7:58-63.
- Zhao Y, Liu H, Liu Z, Ding Y, Ledoux SP, Wilson GL, Voellmy R, Lin Y, Lin W, Nahta R, Liu B, Fodstad O, Chen J, Wu Y, Price JE, Tan M. Overcoming trastuzumab resistance in breast cancer by targeting dysregulated glucose metabolism. *Cancer Res* 2011; 71: 4585-4597.
- Zhao YH, Zhou M, Liu H, Ding Y, Khong HT, Yu D, Fodstad O, Tan M. Upregulation of lactate dehydrogenase A by ErbB2 through heat shock factor 1 promotes breast cancer cell glycolysis and growth. *Oncogene.* 2009; 28:3689-3701.
- Zhou L, Wang F, Sun R, Chen X, Zhang M, Xu Q, Wang Y, Wang S, Xiong Y, Guan

- KL, Yang P, Yu H, Ye D. SIRT5 promotes IDH2 desuccinylation and G6PD deglutarylation to enhance cellular antioxidant defense. *EMBO* 2016; 17:811-822.
- Zhou M, Zhao Y, Ding Y, Liu H, Liu Z, Fodstad O, Riker AI, Kamarajugadda S, Lu J, Owen LB, Ledoux SP, Tan M. Warburg effect in chemosensitivity: targeting lactate dehydrogenase-A re-sensitizes taxol-resistant cancer cells to taxol. *Mol Cancer*. 2010; 9:33.
- Zhou W, Ni TK, Wronski A, Glass B, Skibinski A, Beck A, Kuperwasser C. The SIRT2 deacetylase stabilizes Slug to control malignancy of Basal-like breast cancer. *Cell Rep*. 2016; 17(5):1302-1317.
- Zhou Y, Zhang H, He B, Du J, Lin H, Cerione RA, Hao Q. The bicyclic intermediate structure provides insights into the desuccinylation mechanism of human sirtuin 5 (SIRT5). *J. Biol. Chem*. 2012; 287:28307-28314.

CHAPTER 2. THE MITOCHONDRIAL SIRTUIN SIRT5 FACILITATES MAMMARY CANCER GROWTH *IN VIVO*

Author Contributions

Yashira L. Negrón Abril generated all or partial data for the following figures of

Chapter 2:

Figure 2.1

Figure 2.3

Figure 2.4

Figure 2.5

Figure 2.6

Figure 2.7

Figure 2.8

Figure 2.9

Figure 2.10

Figure 2.11

Figure 2.12

Figure 2.13

Figure 2.14

Figure 2.15

Supplemental Figure 2.1

Supplemental Figure 2.3

Supplemental Figure 2.4

Authors Contribution

Figure 2.2 Cerione's Lab

Supplemental Figure 2.2 Sushabhan Sadhukhan

Supplemental Figure 2.5-2.6 Jun Young Hong and Irma Fernández

2.1 ABSTRACT

The sirtuins are a family of NAD⁺-dependent enzymes that regulate a wide range of biological pathways involved in longevity, survival, DNA repair, metabolism, and proliferation. Among the 3 mitochondrial sirtuins, SIRT5 is the only known enzyme that catalyzes NAD⁺-dependent demalonylation, desuccinylation and deglutarylation of protein substrates. SIRT5 expression is increased in several human cancers and knockdown of *Sirt5* represses breast cancer cell growth and transformation *in vitro*. Here, we used MMTV-PyMT transgenic mice, a genetically engineered mouse model featuring metastatic mammary adenocarcinoma to study the roles of SIRT5 in mammary tumorigenesis. MMTV-PyMT mice with targeted *Sirt5* deletion (*Sirt5*^{-/-}) showed delayed mammary tumor onset, significantly increased overall survival, and decreased incidence of lung metastasis, as compared to controls. Immunoblotting for succinyl-lysine levels in mammary tumor tissues from *Sirt5*^{+/+} PyMT and *Sirt5*^{-/-} PyMT mice revealed that there were several proteins with greatly increased succinylation in *Sirt5*^{-/-} PyMT mammary tumors. Liquid chromatography-mass spectrometry (LC-MS) analysis identified 413 lysine succinylation sites across 147 proteins in mammary tumors from *Sirt5*^{-/-} PyMT and *Sirt5*^{+/+} PyMT mice, with many metabolic enzymes highly succinylated in *Sirt5*^{-/-} samples. To evaluate the impact of *Sirt5* loss on the expression of genes that might be critical for tumor progression, we performed a comparative analysis of expression profiles between *Sirt5*^{+/+} PyMT and *Sirt5*^{-/-} PyMT mice. We identified significant deregulation of 129 genes involved in multiple cellular processes such as cellular metabolism, circadian clock, and inflammation. Pharmacological inhibition of SIRT5 reduced tumor progression in MMTV-PyMT mice. These data highlight the

importance of SIRT5-regulated post-translational modification in cancer metabolism and emphasize novel regulatory events that are important for cancer progression.

2.2 INTRODUCTION

Breast cancer is among the most common cancer types diagnosed in women. Despite advances in early detection and treatments, acquired resistance to chemotherapy and disease recurrence remain a challenge, making breast cancer one of the leading causes of cancer-deaths worldwide (Ferlay *et al.* 2015). Breast cancer cells, as other cancer types, rewire their metabolism to sustain their biosynthetic and bioenergetics needs. Even in the presence of oxygen, cancer cells utilize most of the glucose to produce lactate rather than fueling it in the oxidative phosphorylation pathway (the “Warburg effect”) (Warburg 1925; Kroemer and Pouyssegur 2008; Lunt and Vander 2011). In addition to altered glucose metabolism, cancer cells increase fatty acid synthesis and glutamine metabolism as an alternative source of energy for their survival and enhanced proliferation (Wise *et al.* 2011). These metabolic changes, together with alterations of several signaling pathways, have been recognized as hallmarks of cancer progression and associated to cancer therapeutic resistance. On the basis of these observations, much attention has been given on the development of therapies that target cancer metabolism.

Emerging evidences show that post-translational modifications (PTMs); such as acetylation, succinylation, malonylation and glutarylation, play crucial role in cancer progression and drug resistance by regulating cell metabolism and signaling pathways (Karve and Cheema 2011; Hirschev and Zhao 2015). Therefore, targeting enzymes that regulate these specific PTMs hold a lot of potential for cancer treatment. Protein acetylation, succinylation, malonylation and glutarylation are regulated in part by sirtuins, a family of nicotinamide adenine dinucleotide (NAD⁺)-dependent protein

deacetylases (He *et al.* 2012; Houtkooper *et al.* 2012). Sirtuins have been implicated to play crucial roles in cancer by regulating cellular metabolism (Lee *et al.* 2016). Among the seven mammalian sirtuins, SIRT5 is the only known enzyme that catalyzes nicotinamide adenine dinucleotide-dependent demalonylation, desuccinylation and deglutarylation of metabolic enzymes involved in glycolysis, glutamine metabolism, fatty acid oxidation and the pentose phosphate pathway (Du *et al.* 2011; Bringman-Rodenbarger *et al.* 2017). To date, the role of SIRT5 in cancer is still under investigation. Recent findings indicate that *Sirt5* is overexpressed in multiple cancer types (Ouaissi *et al.* 2008; Sun *et al.* 2011; Lu *et al.* 2014). High expression of *Sirt5* is associated poor survival in patients with NSCLC (Lu *et al.* 2014). Furthermore, recent studies have shown that SIRT5 promotes proliferation of cancer cells by targeting multiple metabolic enzymes, including IDH2, G6PD and PKM2 (Zhou *et al.* 2016; Xiangyun *et al.* 2017).

Here, we put forward the idea that SIRT5 is essential for breast cancer cells to regulate post-translational modifications of proteins involved in cancer metabolism. To elucidate the function of SIRT5 in breast cancer, we used MMTV-PYMT transgenic mice, a genetically engineered model in which the animals develop mammary adenocarcinoma with metastasis to lung (Guy *et al.* 1992). In the study, we show that *Sirt5* deficiency reduces tumor proliferation and the incidence of lung metastasis.

2.3 MATERIALS AND METHODS

Antibodies

Rabbit pan-specific antisuccinyllysine (PTM-401) and antiglutaryllysine (PTM-1151) antibodies were purchased from PTM Biolab, Inc. The SIRT5 rabbit monoclonal antibody (8782) and CD31 (PECAM1-D8V9E) antibody were purchased from Cell Signaling. Ki67 antibody (06-570) was purchased from Millipore. Apoptag kit for Tunnel staining was purchased from Millipore. F4/80 (sc-377009) and CD68 (sc-20060) antibodies were purchased from Santa Cruz Biotechnology.

Cell Culture and Mouse Embryonic Fibroblasts (MEFs) preparation

All cultured cells were grown in Dulbecco's modified Eagle's medium (DMEM) (Corning Inc.) supplemented with 10% bovine calf serum (Thermo Scientific Hyclone, SH30072), 1% nonessential amino acids (Corning Cellgro, 25-025-CI), 1% L-glutamate (25-005-CI), and 1% penicillin and streptomycin (30-002-CI). MEFs were prepared from 13.5 dpc embryos from timed matings between heterozygous *Sirt5* mice (*Sirt5*^{+/-}) and *Sirt5*^{+/-} carrying the conditional oncogenic Kras allele, LSL-Kras^{G12D} (*Sirt5*^{+/-} Kras^{+/LSL}) (Jackson *et al.* 2001; Yu *et al.* 2013). Embryos were dissected from the deciduum and cultured in DMEM supplemented with 10% fetal bovine serum, 1% nonessential amino acids, 1% L-glutamate and 1% penicillin and streptomycin.

Immortalization of Mouse Embryonic Fibroblasts

After five days, 500,000 primary MEFs cells were seeded into 60 mm dishes. The day after, a mixture of 2.5 mL of media, 2.5 uL polybrene and 250 uL of T-large antigen virus were added onto the cells. Transfected MEFs cells were selected in culture medium containing 1.83 µg/mL puromycin, replaced every other day for two weeks.

Stable drug-resistant cells were cultured according to the 3T3 passaging protocol for maintenance and experimental use.

Viral infection

Virus was prepared as described by Zhu (Zhu and Weiss 2007). For infections, 1,000,000 MEFs cells were plated into a 10 cm culture dish. The next day, the cells were infected with 1.95×10^{11} Ad-cre particles in 2.5 mL of culture medium at 37 °C for 6 hours. Media was removed and replaced by fresh medium. Cells were cultured according the 3T3 passaging protocol for maintenance and experimental use.

Short and long term survival assays

For short-term survival assays, 50,000 cells were seeded in triplicate in 6-well plates. Cells were allowed to grow for 3 days. On the third day, cells were properly counted using a hemocytometer. For long-term survival assays, 5,000 cells were seeded in triplicate in 6-well plates. At day 4 post-culture, media was replaced with fresh medium. Cells were allowed to grow for a week, fixed with methanol and stained with 0.5% crystal violet solution. For treatments, 5,000 cells were seeded in 6-well plates. After 24hrs, cells were treated with different concentrations of SIRT5 inhibitor (0, 5, 10, 25, 50 and 100 μ M). The medium and inhibitor were replaced with new ones at day 4 post-culture. After 7 days treatment, cells were fixed with methanol and stained with 0.5% crystal violet solution.

Soft agar colony formation assay

For colony formation 100 μ L of Kras expressing MEFs (1.0×10^6 cells/mL) were mixed with 0.3 mL of 0.4% low melting point agarose and 2.6 mL of DMEM-supplemented media (10% BCS, 1% nonessential amino acids, 1% L-glutamate and 1% penicillin and streptomycin) and seeded onto 60 mm plates coated with 0.6% agarose in DMEM-supplemented media. Cells were allowed to growth for 2 weeks. For treatments, 67 μ L of human breast cancer cells (200,000 cells/mL) were mixed with 0.2 mL of 0.4% low melting point agarose, 1.7 mL of DMEM-supplemented media and 67 μ L of I5-2AM (final concentration 10 μ M or 50 μ M) or vehicle. Cells were allowed to growth for 2 weeks. The medium and inhibitor were replaced with new ones every 3 days. Colonies were photographed and counted 2 weeks after incubation.

Animals

Sirt5 transgenic mice were obtained from Johan Auwerx (Yu *et al.* 2013). These mice were backcrossed with C57BL/6 mice. MMTV-PyMT transgenic mice on a pure FVB/N background were obtained from the Jackson Laboratory (Guy *et al.* 1992). Male PyMT mice were mated with female *Sirt5*^{+/-} mice to obtain heterozygous *Sirt5* PyMT (*Sirt5*^{+/-} PyMT) males. *Sirt5*^{+/-} PyMT males were bred with heterozygous (*Sirt5*) *Sirt5*^{+/-} females to generate female littermates that were *Sirt5*^{+/+} PyMT and *Sirt5*^{-/-} PyMT.

Genotyping

Genotyping was performed by polymerase chain reaction (PCR) amplification using allele-specific primers and genomic DNA extracted from mouse-tails. Identification of the PYMT transgene was determined using the following PYMT primers:

(F) 5'-GGAAGCAAGTACTTCACAAGGG-3'

(R) 5'-GGAAAGTCACTAGGAGAGGG-3'

PCR reaction conditions were 94 °C (3 minutes), followed by 30 cycles of 94 °C (30 seconds), 64 °C (1 minute), 72 °C (1 minute), and 72 °C (2 minutes). Identification of the Sirt5 genotyping was performed using the following Sirt5 primers:

5'-CTTGAGCAGAAAACCCACAGAGGAGAGAAC-3',

5'-GTGTATAGTTGTGTGCTGTGTGCTTGTAC-3'

5'-GGGAAAGATCTGGGGTTGGAATTTACC-3'

PCR reaction conditions were 95 °C (5 minutes), followed by 30 cycles of 95 °C (30 seconds), 64.6 °C (30 seconds), 72 °C (1 minute), and 72 °C (7 minutes).

Monitoring mammary tumor development and tissue collection

Sirt5^{+/+} PyMT and *Sirt5*^{-/-} PyMT female mice were palpated for tumors every other day beginning at 4 weeks of ages. After the detection of palpable tumors, mice were monitored for tumor growth with caliper twice a week. Tumor onset was measured upon detection of any palpable tumor mass. For the Kaplan-Meier survival, tumor endpoint was defined as a mouse having any one tumor of 1.5 cm with multiple tumors bigger than 0.5 cm or when any one tumor reached 2.0 cm (*Cohort 1*) (Table 2.1). For the quantification of tumor load and lung metastasis, a second cohort of experimental mice was collected 50 days after the onset of the first tumor (*Cohort 2*). A third cohort of experimental females was sacrificed at 42 days old of age to perform whole mount (*Cohort 3*). When experimental mice met the endpoint criteria, mice were euthanized by CO₂ asphyxiation. All mammary glands were dissected and weighed. Mammary tumors

and other tissues were collected, fixed with 4% paraformaldehyde (PFA), embedded in paraffin, sectioned, and stained with hematoxylin and eosin (H&E). H&E-stained sections were scanned using an Aperio ScanScope and analyzed by a veterinarian certified in anatomic pathology by the American College of Veterinary Pathologists blinded to treatment group. Serum, tumor tissues and organs were snap frozen in liquid N₂ and stored at -80 °C for subsequent analyses.

Immunohistochemistry on tissue sections

Tissue sections (5µm thickness) were deparaffinized, rehydrated in graded alcohols. Antigen retrieval was performed by microwaving slides in citrate buffer, pH 6.0. Slides were immersed in 30% hydrogen peroxide in methanol for 10 minutes to inhibit endogenous peroxidase activity. Slides were blocked in BSA to prevent non-specific antibody binding, and then incubated with Ki67 antibody overnight at 4 °C. Slides were incubated in biotinylated secondary antibody, followed by streptavidin HRP conjugate (Invitrogen Histostain SP) at room temperature. Immunoreactivity was visualized using DAB (Invitrogen), counterstained with hematoxylin (Fisher CS401-1D), dehydrated and mounted. Slides were scanned using an Aperio ScanScope and analyzed using Image J.

For terminal dUTP nick-end labelling (TUNEL) staining, tissue sections (5µm thickness) were deparaffinized, rehydrated in graded alcohols and digested with Protein Kinase. Slides were immersed in 30% hydrogen peroxide in methanol for 10 minutes and incubated in TdT Enzyme for an hour at 37 °C. Slides were washed and incubated

Table 2.1 Endpoint criteria established for the collection of experimental mice.

Cohort	Endpoint criteria
Cohort 1	A mouse was euthanized if (a) it had multiple tumors smaller than 0.5 cm and one tumor reached 2.0 cm, or if (b) it had multiple tumors bigger or equal to 0.5 cm and one tumor reached 1.5 cm.
Cohort 2	A mouse was euthanized 50 days after palpating the first tumor
Cohort 3	A mouse was euthanized at 42 days old (6 weeks) of age.

in Anti-Digoxigenin Conjugate solution for 30 minutes at room temperature. DAB peroxidase kit (Invitrogen), was use to visualize TUNEL-positive cells. Sections were counterstained with hematoxylin, dehydrated and mounted. Slides were analyzed as described above.

Whole mount staining

Whole abdominal mammary gland was dissected as described by Plante *et al.* and mounted on slides (Plante *et al.* 2011). The mammary gland was fixed in 4% PFA overnight, washed in a gradient of ethanol solutions and stained for two days in Carmine Alum (Fisher). Mammary gland was then dehydrated.

Immunoblot analysis

Tissue extracts were prepared using lysis buffer (50 mM Tris-HCl, pH 8.0, 150 mM NaCl, 1 mM EDTA, 1% Nonidet P-40, 5 mM nicotinamide) supplemented with protease and phosphatase inhibitors. Tissues were homogenized in a tissue homogenizer. The lysates were centrifuged at 20,000 × *g* for 30 min at 4 °C to remove the cell debris. Protein concentration of the supernatant was measured using the Bradford method. Fifty micrograms of protein were loaded and separated on 10% polyacrylamide gel and transferred to PVDF membrane (Perkin Elmer). The membrane was blocked using 5% BSA or milk in TBST (25 mM Tris-HCl, pH 7.4, 150 mM NaCl, and 0.1% Tween-20), incubated with antibodies in 5% BSA or milk in TBST. Chemiluminescent signal was detected on a VersaDoc Imaging system and quantified using Quantity One software (Bio-Rad Laboratories).

Nano LC/MS-MS

Frozen powdered mammary tumor tissues from *Sirt5*^{+/+} PyMT and *Sirt5*^{-/-} PyMT mice were homogenized and lysed as previously described. One milligram of total protein from *Sirt5*^{+/+} PyMT and *Sirt5*^{-/-} PyMT *tumor* samples was digested with trypsin and labeled with light and heavy dimethyl groups, respectively. The isotopically labeled peptides were mixed and enriched using antisuccinyllysine antibody as described by Sadhukhan *et al.* (Sadhukhan *et al.* 2016). Nano LC-MS/MS was used for the identification and quantification of succinyl-lysine peptides (Sadhukhan *et al.* 2016).

Extraction of RNA

Total RNA was extracted from mammary tumor tissues or lung tissue using RNA STAT-60. The concentration and quality (A260/230 and A260/280 ratios) of total RNA were determined by using the Nanodrop (Thermo Fisher Scientific Inc, Wilmington, DE). RNA integrity was confirmed by Fragment Analyzer (Advanced Analytical).

RNA-Sequencing and analysis

Ribosomal RNA was subtracted by hybridization from total RNA samples using the RiboZero Magnetic Gold Mouse Kit (Illumina) and quantified with a Qubit 2.0 (RNA HS kit; Thermo Fisher). TruSeq-barcoded RNAseq libraries were generated with the NEBNext Ultra II Directional RNA Library Prep Kit (New England Biolabs) and quantified with a Qubit 2.0 (dsDNA HS kit; Thermo Fisher). The size distribution of the libraries was determined with a Fragment Analyzer (Advanced Analytical) prior to pooling and sequenced on a NextSeq500 instrument (Illumina). Reads were trimmed for low quality

and adaptor sequences with cutadapt v1.8 as described by Martin (Martin, 2011). Reads were mapped to the mouse genome using tophat v2.1 (Kim *et al.* 2013). Cufflinks v2.2 was used to generate FPKM values and statistical analysis of differential gene expression (Trapnell *et al.* 2013).

Reverse transcription (RT)-PCR analysis

cDNA was synthesized using High Capacity cDNA Reverse Transcription Kit (Applied Biosystem). Amplification of genes of interest was performed using 20 μ L total volume, containing 5 μ L of 5 ng/ μ L cDNA, 1 μ L of each primer and 13 μ L of master mix buffer. Samples were run on a C1000 Touch Thermal Cycler, CFX96 Real-Time System, Bio Rad machine. Two different housekeeping genes were used to normalize the expression of the gene of interest. A list of primers is provided in Table 2.2.

Detection of SIRT5 inhibitors in blood serum and tissue samples

Treated MMTV-PyMT mice were euthanized at different timepoints (24 hrs, 3 hrs or 30 minutes) after performing the last injection of I5-2AM, MY01170 or vehicle solution. Blood serum, tumor tissues and fat were collected and snap frozen in liquid N₂ and stored at -80 °C. Serum samples (100 μ L) and small pieces of tissue or fat were homogenized with 100 μ L of pure methanol for 30 seconds using tissue homogenizer. Samples were centrifuged at maximum speed for 10 minutes at 4°C. The supernatant was collected, sonicated for 5 minutes and centrifuged at maximum speed for 10 minutes at 4°C. Supernatant was analyzed by High Performance Liquid Chromatography (HPLC) with Kinetex 5u EVO C18 100A 30 x 2.1 mm Column and Mass Spectrometry

using Thermo LCQ Fleet MS. HPLC grade water with 0.1 % acetic acid was used as Buffer A and HPLC grade acetonitrile with 0.1% acetic acid was used as Buffer B. 100 μ L of the supernatant was loaded and eluted at gradient of 0% Buffer B in the first 2 minutes, 20% in the next 2 minutes, 40% in 13 minutes, 40% in 2 minutes and 100% in 6 minutes, and lastly 100% in 4 minutes (total 29 minutes). The elutions are monitored by two wavelengths 215 nm and 254 nm. After the run, Thermo Xcalibur Qual program was used for further analysis. As the positive control samples, purified I5-2AM and MY01170 were dissolved in methanol, and diluted in 1:1 mixture of water and acetonitrile to inject into the LC-MS.

Blood ammonia measurements

The day before reaching the established endpoint, mice were fasted. Twentyfour hours after, mice were euthanized and blood was collected by cardiac puncture. Serum was immediately frozen in liquid nitrogen and used for measurement of ammonia levels. Serum ammonia measurements were performed as described by Yu *et al.* (Yu *et al.* 2013).

Table 2.2 Primers sequences used for RT-qPCR.

Gene	Forward	Reverse
<i>PyMT</i>	5'-CGGCGGAGCGAGGAACTGAGGAGAG-3'	5'-TCAGAAGACTCGGCAGTCTTAGGCG-3'
<i>Sirt5</i>	5'-GGGTTCCCACTTTCAGAG-3'	5'-ACACCTGTGATGGGTTTC-3'
<i>Saa</i>	5'-AGGATGAAGCTACTCACCAG -3'	5'-GCTTCCTTCATGTCAGTGTAG-3'
<i>Fgg</i>	5'-CTGTTGCATCCTAGATGAGAG-3'	5'-GCGTTCGGAGATCATTGT-3'
<i>IL-6</i>	5'-CAGGCTTTCCTCCAGATAAAC-3'	5'-TCAAGGTAAGTCTCCCTTCC-3'
<i>Vegfa</i>	5'-GTCTACCAGCGAAGCTACT-3'	5'-ACAGGACGGCTTGAAGAT-3'
<i>Tnfβ</i>	5'-GAACCAAGGAGACGGAATAC-3'	5'-GGCTGATCCCGTTGATTT-3'
<i>Hprt</i>	5'-CCTAAGATGAGCGCAAGTTGAA-3'	5'-CCACAGGACTAGAACACCTGCTAA-3'
<i>Rpl13a</i>	5'-CCTAAGATGAGCGCAAGTTGAA-3'	5'-CCACAGGACTAGAACACCTGCTAA-3'
<i>Mfge8</i>	5'-CGCCTCGTCTGTGTATATG-3'	5'-ATCATAGTTGCTGGCTGTC-3'
<i>IL-6</i>	5'-CAGGCTTTCCTCCAGATAAAC-3'	5'-TCAAGGTAAGTCTCCCTTCC-3'
<i>Cd68</i>	5'-ACTACATGGCGGTGGAATA-3'	5'-GGAGCTCTCGAAGAGATGAA-3'
<i>Fgg</i>	5'-CTGTTGCATCCTAGATGAGAG-3'	5'-GCGTTCGGAGATCATTGT-3'

Synthesis of SIRT5-specific inhibitor

Synthetic Route for I5-2AM (Compound I)

To a solution of 3-Boc-amino propionic acid (**A**, 1.0 g, 5.3 mmol) in acetonitrile (30mL) at room temperature was added triethylamine (0.886 mL, 6.36 mmol) and bromomethyl acetate (**B**, 0.624 mL, 6.36 mmol). The resulting reaction solution was stirred at room temperature for overnight (16 hrs). Acetonitrile was removed and residue was dissolved in ethyl acetate (30 mL) and washed by water and brine and dried. After removed solvent, crude compound **C** was obtained. The crude compound **C** (~5.3 mmol) was dissolved in DCM (30 mL), to this solution was added TFA (3 mL). The solution was stirred at room temperature for 1 hr. TLC showed no compound **C** left. The solution was concentrated and residue was azeotropic evaporated two times with toluene (10 mL X2) to obtain crude compound **D**. To a solution of crude compound **D** (~5.3 mmol) in dry THF (20 mL) was added triethylamine (0.813 mL, 5.83 mmol) following thiocarbonyldiimidazole (0.945 g, 5.3 mmol). The reaction mixture was stirred at room temperature for overnight (18 hrs). THF was removed under vacuum, the residue was dissolved in DCM (30 mL) and washed by water and brine and dried on sodium sulfate. After removed solvent, the residue was passed through a little long pad of silica gel, eluted by Hexane /ethyl acetate (4:1) to collected product. Totally, 0.569 g (51.7% for three steps) of compound **E** was obtained, which was used to next step reaction and no more purification.

To a solution of N^α-Z-N^ε-Boc-L-Lysine (**Compound F**, 1.5 g, 3.9 mmol) in DCM (25 mL) at room temperature was added NMM (0.686 mL, 6.24 mmol), following t-butyl chloroformate (0.712 mL, 5.45 mmol) was added drop wise. The solution was stirred at

room temperature for 1 hr. 3-aminophenol (511 mg, 4.68 mmol) was added one portion. The resulting reaction mixture was stirred at room temperature for overnight (18hrs.). 0.5 N HCl (8 mL) was added. Organic solution was isolated and washed by water and brine and dried on sodium sulfate and concentrated. The residue was purified by column (hexane:ethyl acetate= 2:1) to afford **Compound G** (1.65 g, 88%) as white solid. LC-MS: Calcd: 471.55; Found: 471.92 (M); 372.21 (M-Boc+1). To a solution of **Compound G** (0.84 g, 1.8 mmol) in DCM (20 mL) was added TFA (5 mL). The solution was stirred at room temperature for 1 hrs. The solvent was removed under vacuum. The residue was azeotropic evaporated two times with toluene (10 mL X2) to obtain crude **Compound H**, which was used to next step reaction without more purification. The crude **Compound H** (~1.8 mmol) was dissolved in dry THF (30 mL), to this solution was added triethylamine (0.753 mL, 5.4 mmol), following, **Compound E** (0.549 g, 2.7 mmol) was added. The resulting reaction mixture was stirred at room temperature for overnight (18 hrs). THF was removed under vacuum, the residue was dissolved in DCM (50 mL) and washed by water and brine and dried on sodium sulfate. After concentrated, the residue was purified by column (hexane:ethyl acetate=1:1) to afford **I5-2AM (Compound I**, 650 mg, 66%) as white solid. ¹H NMR (CDCl₃, 400Hz): δ (ppm) 8.96 (s, 1H), 7.81 (s, 1H), 7.42 (s, 1H), 7.28 (s, 5H), 7.12-7.10 (t, 2H), 6.86 (s, 1H), 6.72 (s, 1H), 6.65 (t, 2H), 6.02-6.00 (t, 2H), 5.31 (s, 1H), 5.12-5.02 (q, 2H), 4.39 (m, 1H), 4.12-4.09 (q, 2H), 3.79 (m, 2H), 3.28 (b, 1H), 2.33 (s, 3H), 1.96 (m, 2H), 1.65 (m, 2H), 1.25 (m, 2H). LC-MS: Calcd: 574.65; Found: 575.03(M+1).

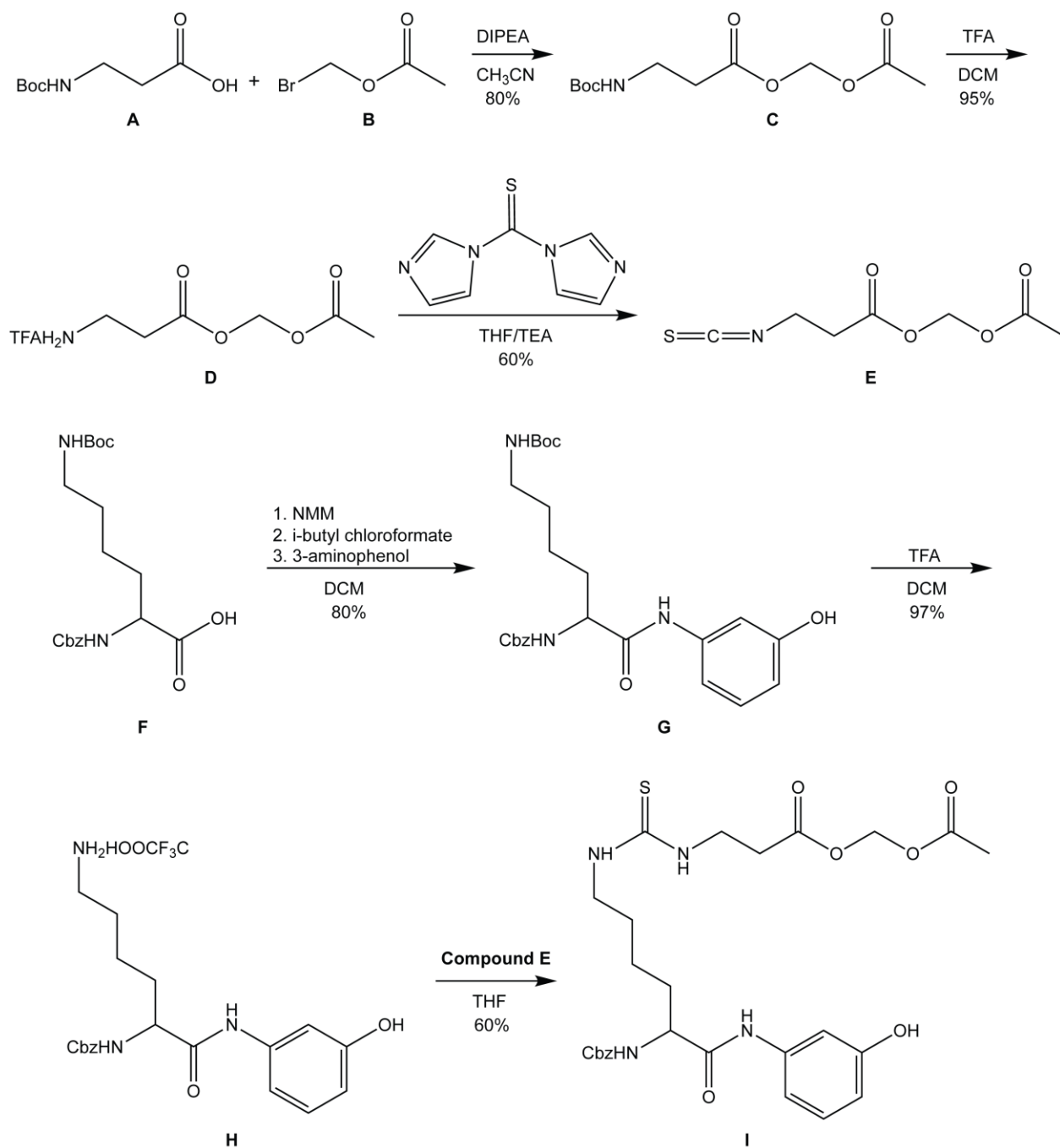


Figure 2.1 Synthetic route for I5-2AM, a SIRT5 inhibitor (Compound I).

Synthetic Route for MY01170 (Compound J)

To a solution of compound **A** (1 g, 3.77 mmol) in DCM (20 mL) at room temperature NHS was added (520mg, 4.52 mmol), followed by EDC:HCl (1.08 g, 5.66 mmol). The resulting solution was stirred at room temperature overnight (~16 hrs). The reaction mixture was washed with water and brine, and dried on sodium sulfate. The residue was dissolved in DCM and fast pass through a pad of silica gel to afford compound **B** (1.2g, 88%) as colorless oil. Compound **B** was used for the next step reaction without further purification.

To a solution of compound **C** (100 mg, 0.624 mmol) in DCM (10 mL) at room temperature NHS was added (86.15 mg, 0.749 mmol), followed by EDC:HCl (179.4 mg, 0.936 mmol). The solution was stirred at room temperature overnight (~16 hrs.). The reaction mixture was washed with water and brine, and dried on sodium sulfate. The residue was purified by column to afford compound **D** (115 mg, 70%) as colorless oil. ¹H NMR (CDCl₃, 400Hz): δ4.19 (q, 2H); 2.88 (s, 4H); 2.75 (t, 2H); 2.49 (t, 2H); 2.11 (dt, 2); 1.30 (t, 3H).

L-Lys (Boc)-OH (compound **E**, 0.93 g, 3.77 mmol) was dissolved in THF (18 mL). Then, NaHCO₃ (0.633 g, 7.54 mmol) and water (20 mL) were added. The suspension was stirred until converted into a clear solution. Compound **B** (1.36 g, 3.77 mmol, dissolved in minimum THF) was added to this solution and the reaction mixture was stirred at room temperature overnight (~18 hrs.). The reaction mixture was diluted with water (50 mL), acidified with 15% citric acid (10 mL, pH~3-4), and extracted with ethyl acetate (3X50 mL). Combined organic layer was washed with water (1X) and brine and dried with. The residue was purified with column to afford compound **F** (1.83 g, 98%) as

colorless oil. LC-MS Calcd: 493.59; Found: 394.21 (M-Boc+1). To a solution of compound **F** (1.83 g, 3.77 mmol) in DCM (20 ml) at room temperature TFA (5 mL) was added. The mixture was stirred for 2 hrs. The solvent and TFA were removed by evaporation. The residue was co-evaporated with toluene (2X). The crude compound **G** (light yellow oil) was used for the next step reaction without further purification. The crude compound **G** (~3.77mmol) was dissolved in DMF (30 mL) and cooled down. Triethylamine (1.5 mL, 11.1 mmol) was added, followed by compound **D** (0.951 g, 3.77 mmol, in minimum DMF). The reaction mixture was stirred at room temperature overnight (~16hrs), diluted with DCM (100 mL), washed with water (2X80 mL) and brine, and dried with sodium sulfate. The residue was purified with column (DCM:MeOH:Acetic acid = 300:10:3 to 250:10:3) to afford compound **H** (1.18 g, 60%) as colorless oil. LC-MS Calcd: 535.63; Found: 536.13 (M+1). Compound **H** (0.658 g, 1.2 mmol) was dissolved in dry THF (10 mL). Lawesson's reagent (0.485 g, 1.2 mmol) was added. The reaction mixture was stirred for 15 hrs. Concentrated and residue was purified with column (DCM:MeOH:Acetic acid = 300:10:3) to afford compound **I** (0.617g, 93%) as colorless oil. LC-MS Calcd: 551.70; Found: 552.12 (M+1). To a solution of compound **I** (617 mg, 1.18 mmol) in DCM (25 mL) NMM (0.19 mL, 1.725 mmol) was added and the mixture was stirred for 5 minutes at room temperature, Isobutyl chloroformate (0.169 mL, 1.294 mmol) was added and the mixture was stirred for 1 hr. 3-aminophenol (141.2 mg, 1.294 mmol) was added and the reaction was stirred for 18 hrs at room temperature. The mixture was diluted with DCM (50 mL), washed with 1N HCl (20 mL), water and brine, and dried with sodium sulfate. Concentrated and residue were purified with column to afford **MY01170 (Compound J)**, 450 mg, 60%) as colorless

oil. ^1H NMR (CDCl_3 , 400Hz): δ (ppm) 9.39 (s, 1H), 8.62 (s, 1H), 7.42 (s, 1H), 7.38 (s, 5H), 7.16-6.53 (m, 4H), 5.00 (s, 2H), 4.57 (t, 1H), 4.17 (t, 1H), 4.01 (q, 2H), 3.35 (t, 2H), 2.60 (t, 2H), 2.25 (t, 2H), 1.84 (t, 2H), 1.75-1.28 (m, 11H), 1.13 (t, 3H), 0.80 (d, 6H). LC-
Ms, Calcd: 642.81; Found: 643.07 (M+1).

Inhibition assays on SIRT5 with HPLC

To a solution of SIRT5 (final concentration = 1 μ M) and 1 mM NAD in assay buffer (20 mM of Tris-HCl, pH 7.4) was added the inhibitor at various concentrations (0.68, 2.06, 6.17, 18.52, 55.56, 166.67 μ M). The resulting mixture was incubated for 10 min at 37 °C. Then, 50 μ M succinyl peptide (H3K9WWSu) was added to the mixture. After incubation at 37 °C for 15 min, the reactions were stopped by adding 60 μ L of an aqueous solution containing 200 mM of HCl and 320 mM of acetic acid. The reaction mixtures were centrifuged at 17000g for 10 min and the supernatant was analyzed on an analytical HPLC with Kinetex 5u EVO C18 100A column (100 mm \times 4.60 mm, 5.0 μ m, Phenomenex). The gradient was: 0% B for 2 min, 0 to 30% B in 13 min, and then 30% to 100% in 10 min at a flow rate of 0.5 mL/min. All reactions were done in duplicate. The product and the substrate peaks were quantified based on the area of absorbance monitored at 280 nm. IC₅₀ values were determined with SigmaPlot software. IC₅₀ for I5-2 on SIRT5 is 2.05 μ M.

Treatment of MMTV-PyMT mice with SIRT5-specific inhibitor

MMTV-PyMT transgenic female mice were treated with IP injections (5 days/week) of vehicle (60% DMSO in water) or 50 mg/kg I5-2AM in dissolved in 60% DMSO over six weeks. Mice were monitored daily for health status and tumors size was measured twice per week. After six weeks of treatment or if mice met humane endpoint criteria, mice were euthanized by CO₂ asphyxiation and necropsied. Tissues were collected and analyzed as described above.

2.4 RESULTS

2.4.1 *SIRT5* is overexpressed in human breast cancer and is associated with poor survival

Previous works have reported that *SIRT5* is overexpressed in multiple cancer types (Ouaissi *et al.* 2008; Sun *et al.* 2011; Lu *et al.* 2014). To profile the importance of *SIRT5* in human breast cancer, we first used cBioPortal web-based tool incorporated in TCGA website to display gene copy number alterations (Gao *et al.* 2013). Our analysis revealed that 2.9% of breast invasive carcinomas have alterations in *SIRT5* gene. Among those, 2.5% accounts for amplifications of *SIRT5* (Figure 2.3A). We further analyzed the mRNA expression of *SIRT5* in breast cancer cell lines using the dataset from Cancer Cell Line Encyclopedia and found that *SIRT5* is overexpressed in many breast cancer cell lines (Figure 2.3B) (Broad Institute of MIT and Harvard). Next, we analyzed the correlation of *SIRT5* mRNA expression with the clinical outcome of untreated and treated breast cancer patients using the Kaplan Meier Plotter web-based tool (Gyorffy, *et al.* 2010). The analysis revealed that high *SIRT5* mRNA levels are associated with poor overall and post progression survival, indicating that overexpression of *SIRT5* supports cancer progression (Figure 2.3C and D).

2.4.2 *SIRT5* deficiency affects the malignant transformation *in vitro*

To examine the importance of *SIRT5* for the development of transformed phenotypes in human cancer cells, we first knocked-down *SIRT5* in two independent cancer cell lines; SKBR3 (human breast cancer) and CRL-5800 (human lung cancer) and assessed their ability to grow in soft-agarose. We found that knock-down of *SIRT5*

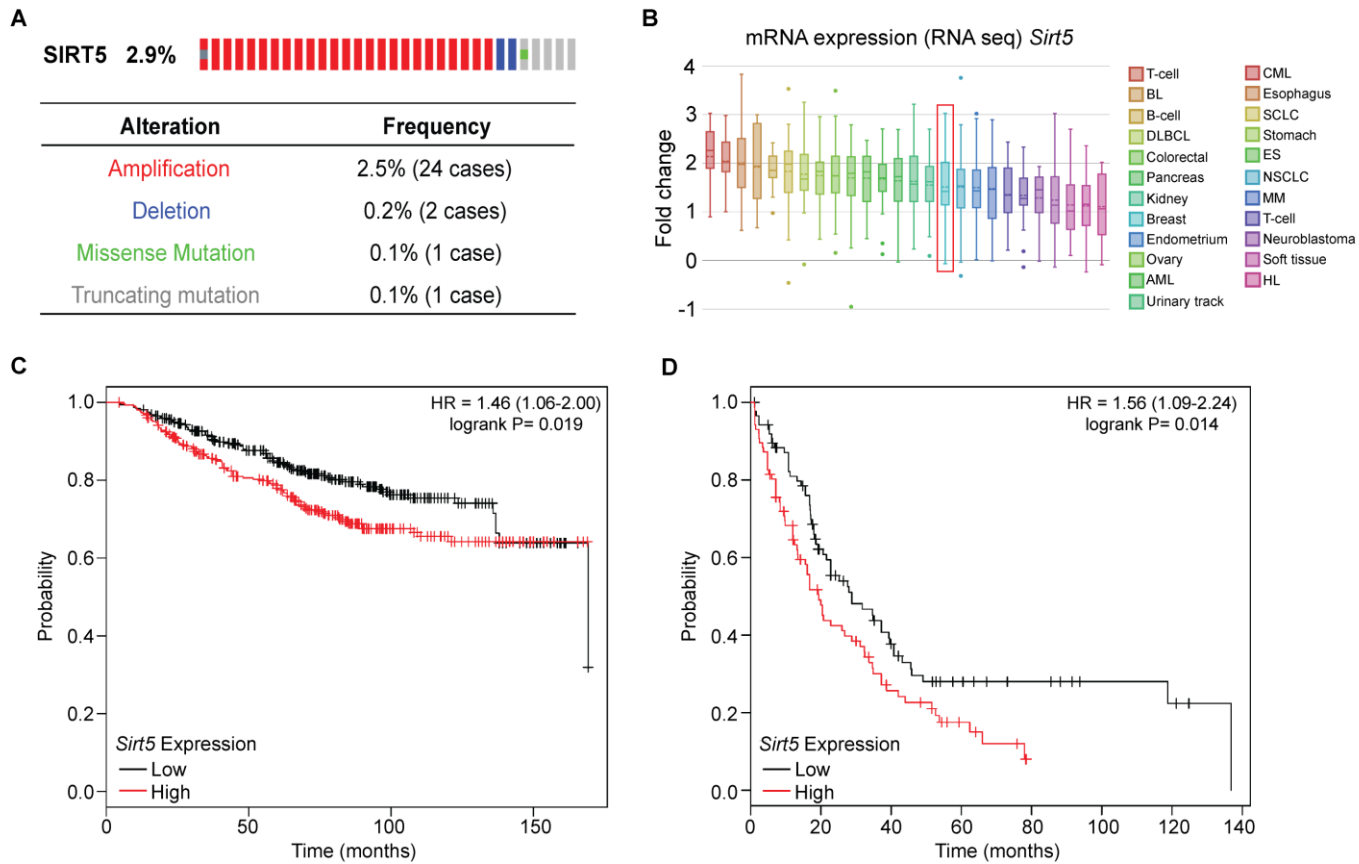


Figure 2.3 *SIRT5* is often overexpressed in cancer and it is associated to poor survival. **(A)** Alterations of *SIRT5* gene in Breast invasive carcinoma (TCGA, 963 cases) Retrieved from cBioPortal. **(B)** *SIRT5* mRNA expression in multiple cancer cell lines. Red box highlights breast cancer cell lines. Data retrieved from Cancer Cell Line Encyclopedia. **(C-D)** Kaplan-Meier curves comparing the overall survival and post-progression survival of breast cancer

patients with low and high *SIRT5* expression. Data retrieved from Kaplan Meier Plotter web-based tool. BL, Burkitt Lymphoma; DLBCL, Diffuse Large B Cell Lymphoma; AML, Acute Myeloid Leukemia; CML, Chronic Myeloid Leukemia; SCLC, Small Cell Lung Cancer; ES, Ewing Sarcoma; NSCLC, Non Small Cell Lung Cancer; MM, Multiple Myeloma; HL, Hodgkin Lymphoma.

markedly reduced their ability to exhibit anchorage-independent growth. Furthermore, we did not observe any significant effect on the growth of normal (non-transformed) cells (Figure 2.4 A-C).

To extend our analysis, we prepared mouse embryonic fibroblasts from heterozygous *Sirt5* mice carrying the conditional oncogenic Kras allele, LSL-Kras^{G12D}. This Kras allele features the G12D activating mutation at the endogenous Kras locus as well as a lox-stop-lox cassette to control expression (Jackson *et al.* 2001). To explore whether SIRT5 is essential for the ability of MEFs to undergo transformation following expression of activated oncogene, we first immortalized primary mouse embryonic fibroblasts (*Sirt5*^{+/+}, *Sirt5*^{+/+} Kras^{+/LSL} and *Sirt5*^{-/-} Kras^{+/LSL}) and infected them with Cre recombinase as described in the Materials and Methods Section. Addition of Cre recombinase deletes the stop cassette, allowing for activated Kras expression in *Sirt5*^{+/+} Kras^{+/LSL} and *Sirt5*^{-/-} Kras^{+/LSL}, but not in *Sirt5*^{+/+} control cells. Proliferation assays revealed increased proliferation rate of *Sirt5*^{+/+} Kras^{+/LSL} when compared to *Sirt5*^{+/+} control cells. Interestingly, deletion of *Sirt5* significantly reduced the proliferation rate of Kras-transformed MEFs (Figure 2.5A and B). We also tested whether deletion of *Sirt5* affects the transformative properties of Kras expressing cells. Excitingly, we observed reduced number of colonies in *Sirt5*^{-/-} Kras^{+/LSL} when compared to *Sirt5*^{+/+} Kras^{+/LSL}. (Figure 2.5C and D). Together, these data show that SIRT5 is essential for the transformed phenotype of cancer cells.

2.4.2 Mammary tumor progression is impaired upon genetic deletion of *Sirt5*.

Recent studies have implicated SIRT5 in stimulating human lung cancer

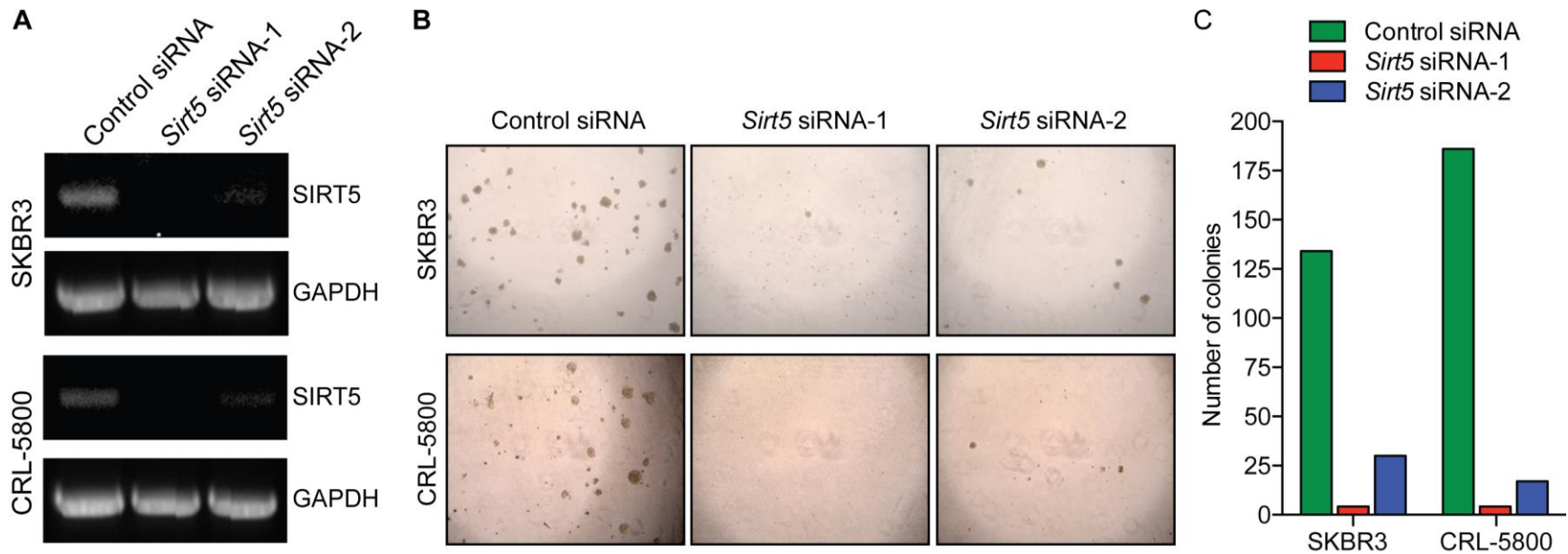


Figure 2.4 *SIRT5* knock-down inhibits the anchorage independent growth of cancer cells. **(A)** RT-PCR results showing that *SIRT5* is knocked-down by both siRNA in SKBR3 (breast cancer) and CRL-5800 (lung cancer) cells. **(B)** Soft-agarose assay demonstrating that *SIRT5* knockdown inhibits the colony formation in SKBR3 and CRL-5800 cancer cells. **(C)** Bar graph showing the number of colonies formed in the soft-agarose assay. Data generated in the Cerione lab.

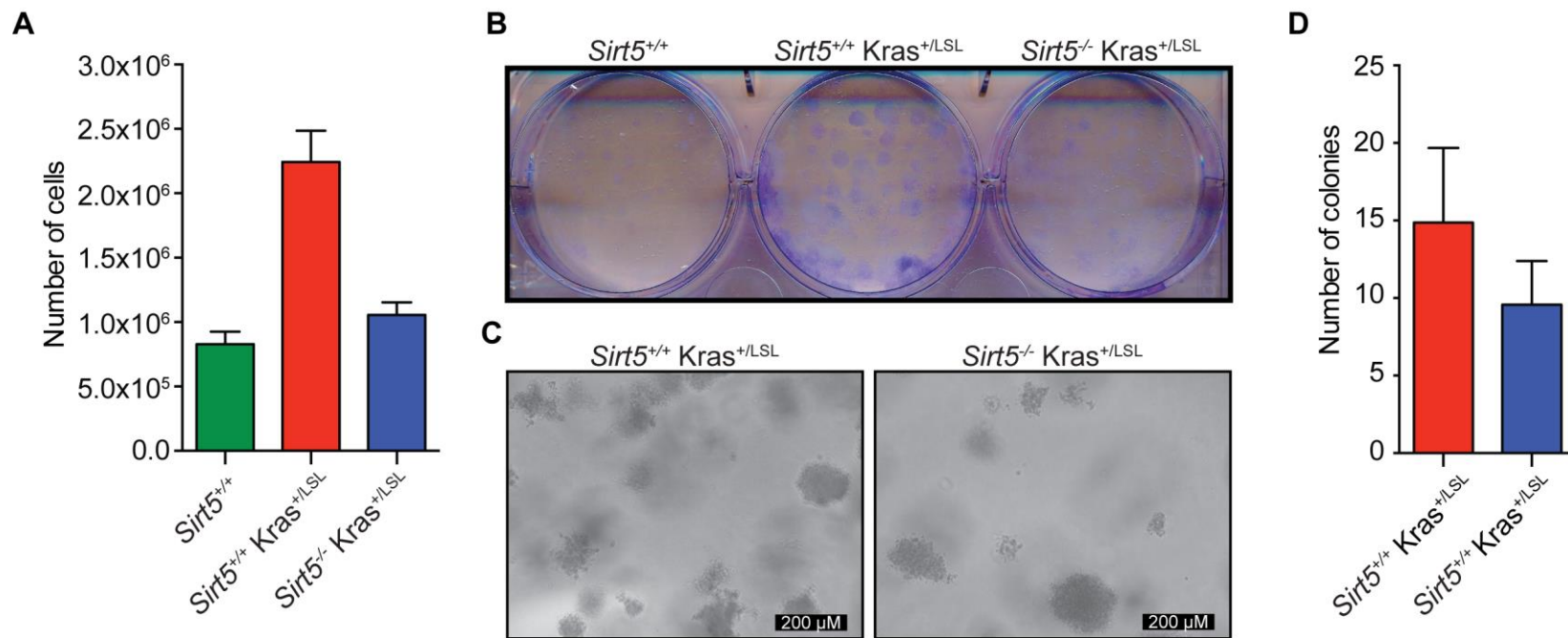


Figure 2.5 *Sirt5* loss inhibits transformed MEFs proliferation and ability to grow in soft-agarose. (A-B) Deletion of *Sirt5* inhibits the proliferation of transformed *Kras*-expressing MEFs. **(A)** Graph showing the number of cells after growing for 3 days (p -value = 0.0001, One-way ANOVA) **(B)** Clonogenic assay showing reduced colonies in *Sirt5*^{-/-} *Kras*^{+/-LSL} cells when compared to *Sirt5*^{+/+} *Kras*^{+/-LSL} cells. **(C-D)** Soft-agar colony formation of *Sirt5*^{+/+} *Kras*^{+/-LSL} and *Sirt5*^{-/-} *Kras*^{+/-LSL} cells. Representative images of colonies are shown on panel **(C)**. Quantification of the colony numbers is shown on panel **(D)** (p -value = 0.039, Mann-Whitney test).

growth and drug resistance (Lu, *et al.* 2014; Xiangyun *et al.* 2017). However, the oncogenic effects of SIRT5 have not been reported in other cancer types and it is not clear whether SIRT5 oncogenic potential is tissue specific. Here we examined roles of SIRT5 in mammary tumor progression using mouse mammary tumor virus (MMTV)-polyoma middle T (PyMT) transgenic mice. In this model, the expression of PyMT antigen is under the control of mouse mammary tumor virus promoter, resulting in highly penetrant mammary tumors and extensive lung metastasis (Guy *et al.* 1992; Lin *et al.* 2003; Herschkowitz *et al.* 2007).

To determine the effects of *Sirt5* deletion on mammary gland tumor formation and metastasis, *Sirt5* heterozygous females (*Sirt5*^{+/-}) were crossed to MMTV-PyMT males to obtain *Sirt5*^{+/-} PyMT mice. *Sirt5*^{+/-} PyMT males were then crossed to *Sirt5*^{+/-} females to generate experimental cohorts (*Sirt5*^{+/+} PyMT and *Sirt5*^{-/-} PyMT). To detect mammary tumor formation, virgin mammary glands from *Sirt5*^{+/+} PyMT and *Sirt5*^{-/-} PyMT females were monitored every other day beginning at 4 weeks of ages. Our examinations revealed that the tumor onset in *Sirt5*^{-/-} PyMT was slightly delayed when compared to *Sirt5*^{+/+} PyMT mice (Figure 2.6A). *Sirt5*^{+/+} PyMT females developed palpable mammary tumors at around 51 days after birth and by day 55, 60% of these mice had palpable tumors. Interestingly, the tumor onset median value was 59 days for *Sirt5*^{-/-} PyMT females and only 36% developed palpable tumors by day 55 after birth. Although *Sirt5* deletion slightly delayed mammary tumor development, this difference was not found to be significant. To further analyze tumor initiation, we collected abdominal mammary glands from *Sirt5*^{+/+} PyMT and *Sirt5*^{-/-} PyMT females at 6 weeks of age (*Cohort 3*) and performed whole

mount examination of mammary glands using Carmine Alum-staining (mammary gland 4) and H&E staining (mammary glands 2-3). Analysis of the whole mammary gland showed multiple small lesions near to the main duct, however these lesions were not significantly different between *Sirt5*^{+/+} PyMT and *Sirt5*^{-/-} PyMT mice (Figure 2.6B). Closer examination revealed no differences between *Sirt5*^{+/+} PyMT and *Sirt5*^{-/-} PyMT mice. Mammary glands showed proliferative acini with mild atypia.

Next, we addressed whether *Sirt5* deficiency affected tumor growth. Mammary tumors from *Sirt5*^{+/+} PyMT and *Sirt5*^{-/-} PyMT females were allowed to grow and reach a diameter of 1.5 cm or 2.0 cm (*Cohort 1*) (as described in the Materials and Methods section). Interestingly, *Sirt5* loss slowed down tumor growth and significantly prolonged the survival of PyMT mice (p-value=0.0256) (Figure 2.6C). The median survival for *Sirt5*^{+/+} PyMT was 121 days old while the median survival for *Sirt5*^{-/-} PyMT was 142 days old. These results indicate that SIRT5 is required for PyMT-induced mammary tumor growth.

Given that *Sirt5* deletion slightly delayed tumor initiation and increased the overall survival of PyMT mice, we next examined tumor multiplicity and total tumor burden in *Sirt5*^{+/+} PyMT and *Sirt5*^{-/-} PyMT females. Mammary glands from virgin females were monitored as previously indicated and tumors were allowed to grow for 50 days after the detection of the first tumor (*Cohort 2*). Upon reaching the endpoint, mice were euthanized, the numbers of tumor-affected mammary glands were counted and the total mammary tumors were weighted. We found no significant difference in the number of mammary glands affected, however tumors size and total wet weight of all mammary tumors per animal were significantly lower in *Sirt5*^{-/-} PyMT mice (0.5822

± 0.1681 g) when compared to *Sirt5*^{+/+} PyMT controls (1.405 ± 0.3562 g) (p-value =0.0395) (Figure 2.6D-E). Taken together, these results strongly show the oncogenic roles of SIRT5 in mammary tumor formation and progression.

2.4.3 Histological analysis of mammary tumors upon deletion of *Sirt5*.

To investigate the basis for extended survival in *Sirt5*^{-/-} PyMT mice, the histology of the primary tumors were evaluated in a blinded fashion. Analysis of mammary tumors collected upon reaching 1.5 cm or 2.0 cm of diameter did not show significant histological differences. Most tumors showed tumor acini with solid sheets of epithelial cells, characteristic of a late carcinoma stage. In addition, mammary tumors showed some areas of extensive necrosis (27.3% for *Sirt5*^{+/+} PyMT and 11.1% for *Sirt5*^{-/-} PyMT).

Histological analysis of mammary tumors from mice that were euthanized 50 days after detecting the first tumor (*Cohort 2*) revealed small histopathological differences between the two groups. Most tumors from these mice showed the presence of cytological atypia, acini filled by solid sheets of cells, and stromal invasion, which are features of advance malignant lesions (Figure 2.7A) (Lin *et al.* 2003). To characterize mammary tumors, we used the four-distingly identifiable stages of tumor progression previously established in PyMT mice (Lin *et al.* 2003). Stage classification includes, hyperplasia, adenoma/mammary intraepithelial neoplasia (MIN), early carcinoma, and late carcinoma (Cardiff *et al.* 2000; Lin *et al.* 2003). Mammary tumors from PyMT mice are often heterogeneous. As expected, *Sirt5*^{+/+} PyMT and *Sirt5*^{-/-} PyMT

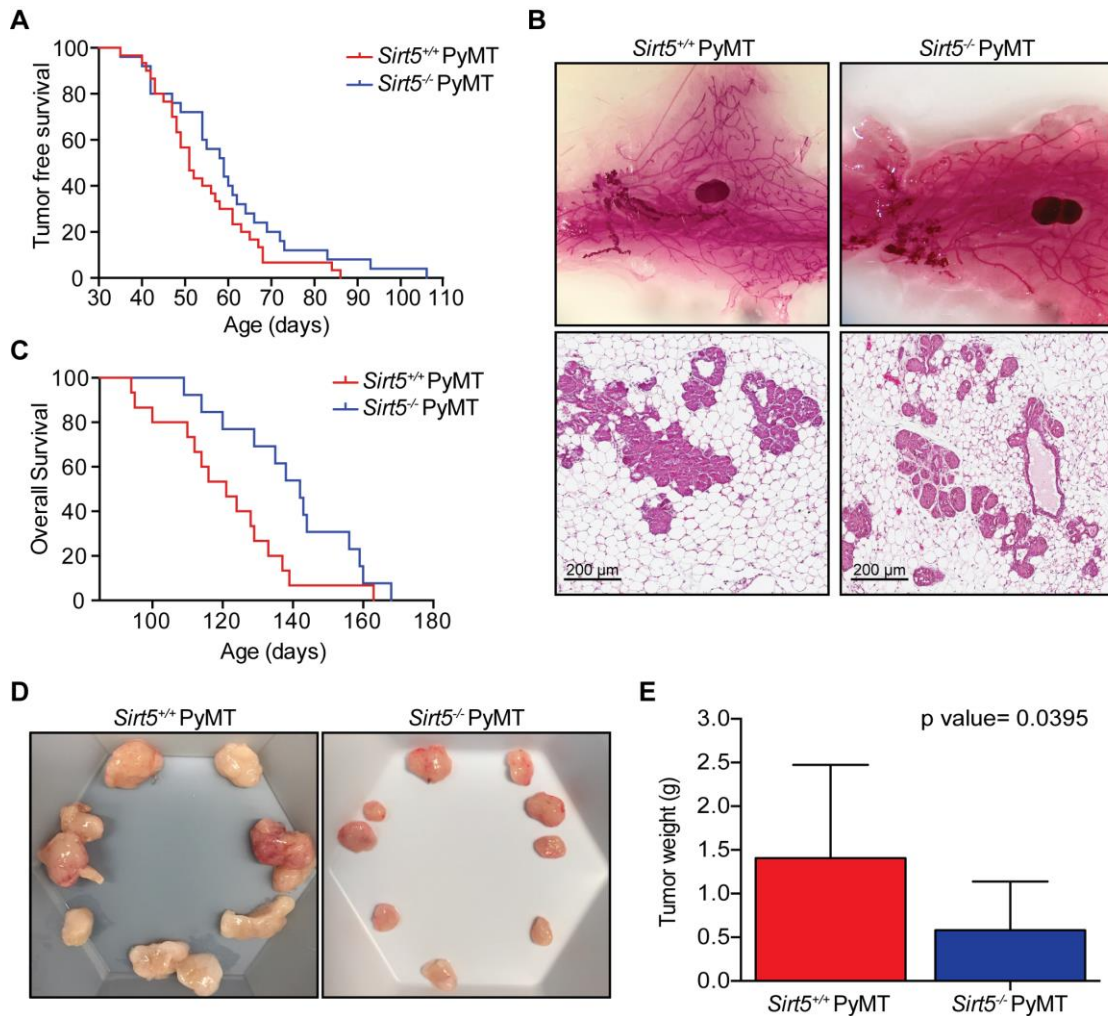


Figure 2.6 *Sirt5* deletion delayed mammary tumor onset and significantly increased overall survival of mice. **(A)** Kaplan Meier tumor free survival curve for *Sirt5*^{+/+} PyMT and *Sirt5*^{-/-} PyMT mice. A slight delay in mammary tumor development was observed in *Sirt5*^{-/-} PyMT mice ($p = 0.1352$, Logrank (Mantel-Cox test)). **(B)** Carmine alum and H&E stained whole mammary glands from 42 days old *Sirt5*^{+/+} PyMT and *Sirt5*^{-/-} PyMT mice. **(C)** Kaplan Meier overall survival curve for *Sirt5*^{+/+} PyMT and *Sirt5*^{-/-} PyMT mice. Increased survival was observed in *Sirt5*^{-/-} PyMT mice ($p = 0.0256$, Logrank (Mantel-Cox test)). **(D)** Representative images of mammary tumors. **(E)** Total tumor weight fifty days after palpation of the first tumor ($p = 0.0395$, Unpaired t-test).

mice showed multiple histological stages within the same tumor. To perform an accurate analysis, we classified and quantified the areas (in percentage) within each tumor in these four stages. Only 7% of *Sirt5*^{+/+} PyMT mammary tumors were hyperplastic, while greater areas were classified as adenoma/MIN (41%), early carcinoma (17%) and late carcinoma (17%) (Figure 2.7B). Similar to *Sirt5*^{+/+} PyMT mammary tumors, only 9% of *Sirt5*^{-/-} PyMT mammary tumors were hyperplastic, while larger areas of the tumors were classified as adenoma/MIN (49%), early carcinoma (26%) and late carcinoma (16%) (Figure 2.7B). Although there were no significant differences, smaller areas of tumors from *Sirt5*^{-/-} PyMT mice were categorized in the advanced stages (e.g. early and late carcinoma) when compared to the control group, indicating a slight delay in tumor progression.

We also categorized each tumor within these four stages based on the highest percentage affected. We found that the largest area for most mammary tumors from *Sirt5*^{+/+} PyMT mice were classified as early carcinoma (48%, 11 out of 22), while the largest area for most tumors from *Sirt5*^{-/-} PyMT mice were categorized as adenoma/MIN (52%, 15 out of 27) (Figure 2.7C, Supplemental Table 1). Together, these data supports the idea that *Sirt5* deletion affects tumor progression in PyMT mice.

To investigate whether the lack of *Sirt5* in PyMT mice inhibited proliferation, the proliferative rate of the primary tumors was measured by immunohistochemical detection of the proliferation marker Ki67. We found a significant decrease in proliferation of tumor cells in *Sirt5*^{-/-} PyMT mice relative to *Sirt5*^{+/+} PyMT as measured by Ki67 staining (Figure 2.8A-B). We further investigated if *Sirt5* loss affects apoptosis

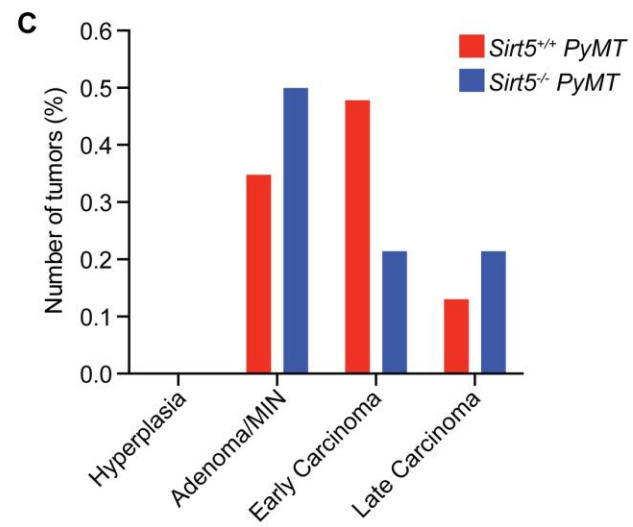
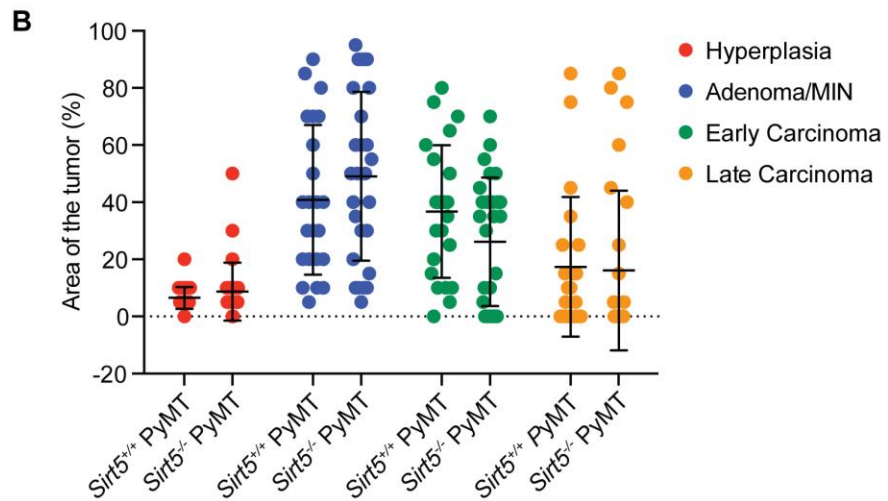
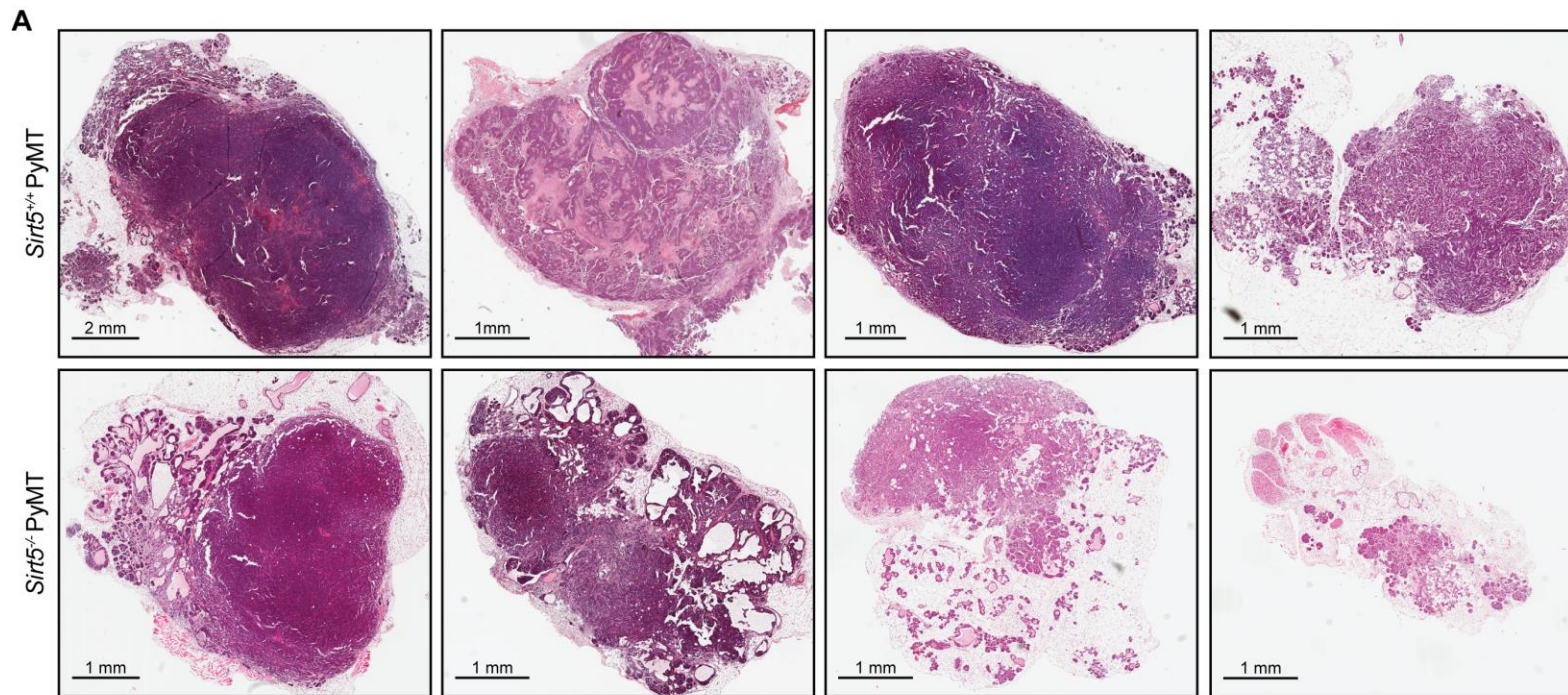


Figure 2.7 Histological comparisons of mammary tumors from *Sirt5*^{+/+} PyMT and *Sirt5*^{-/-} PyMT mice. (A) H&E staining of mammary tumor sections from *Sirt5*^{+/+} PyMT and *Sirt5*^{-/-} PyMT mice. Tumors were harvested 50 days after the detection of the first tumors. **(B)** Graph showing the area of individual tumors (in percentage) featuring one of the four histological stages; hyperplasia, adenoma/MIN, and early and late carcinoma. Unpaired T-test with Welch's correction was performed for each histological stage (Hyperplasia p-value=0.3084; Adenoma/MIN p-value=0.3036; Early Carcinoma p-value= 0.1084; Late Carcinoma p-value=0.9738). **(C)** Graph showing the number of tumors (in percentage) with the largest area featuring, hyperplasia, adenoma/MIN, early carcinoma or late carcinoma. Tumors were classified based on the stage of the largest area. The percentage of tumors per stage was determined dividing the number of tumors per stage by the total number of tumors.

in mammary tumor tissues. Quantification of TUNEL-positive cells revealed no genotype-dependent difference in cell death (Figure 2.8C-D). Immunoblot analysis of mammary tumor extract using cleaved caspase-3 antibody also revealed no differences in apoptotic index (Figure 2.8E). Together, these data demonstrates that *Sirt5* loss affects tumor growth by diminishing the proliferation rate.

2.4.4 *Sirt5* deficiency delays progression of mammary tumor metastases in MMTV-PyMT mice.

We next investigated whether pulmonary metastasis of mammary tumors is affected upon *Sirt5* deletion by examining the frequency of lung metastasis in *Sirt5*^{+/+} PyMT and *Sirt5*^{-/-} PyMT females. Mice were sacrificed 50 days after palpating the first mammary tumor, thus tumors from *Sirt5*^{+/+} PyMT and *Sirt5*^{-/-} PyMT mice had the equivalent growth period at the experimental endpoint (*Cohort 2*). At this stage, metastatic tumors were not visible to the naked eye. We next examined H&E-stained lung sections of five independent sectional planes to quantify metastatic burden (Figure 2.9A). Interestingly, ~40.0% of *Sirt5*^{+/+} PyMT mice but no *Sirt5*^{-/-} PyMT mice exhibited lung micro-metastasis (Figure 2.9A-B). The number of lung micro-metastases in *Sirt5*^{+/+} PyMT mice fluctuated between 1 and 6 per mouse (Figure 2.9C). We next analyzed the incidence of metastasis when tumors reached 1.5 cm in size (*Cohort 1*). Surprisingly, we found no differences in the number of metastasis in *Sirt5*^{+/+} PyMT and *Sirt5*^{-/-} PyMT lung tissues. Together, these data indicate that *Sirt5* loss delays pulmonary metastasis of mammary tumors, but does not abolish it completely.

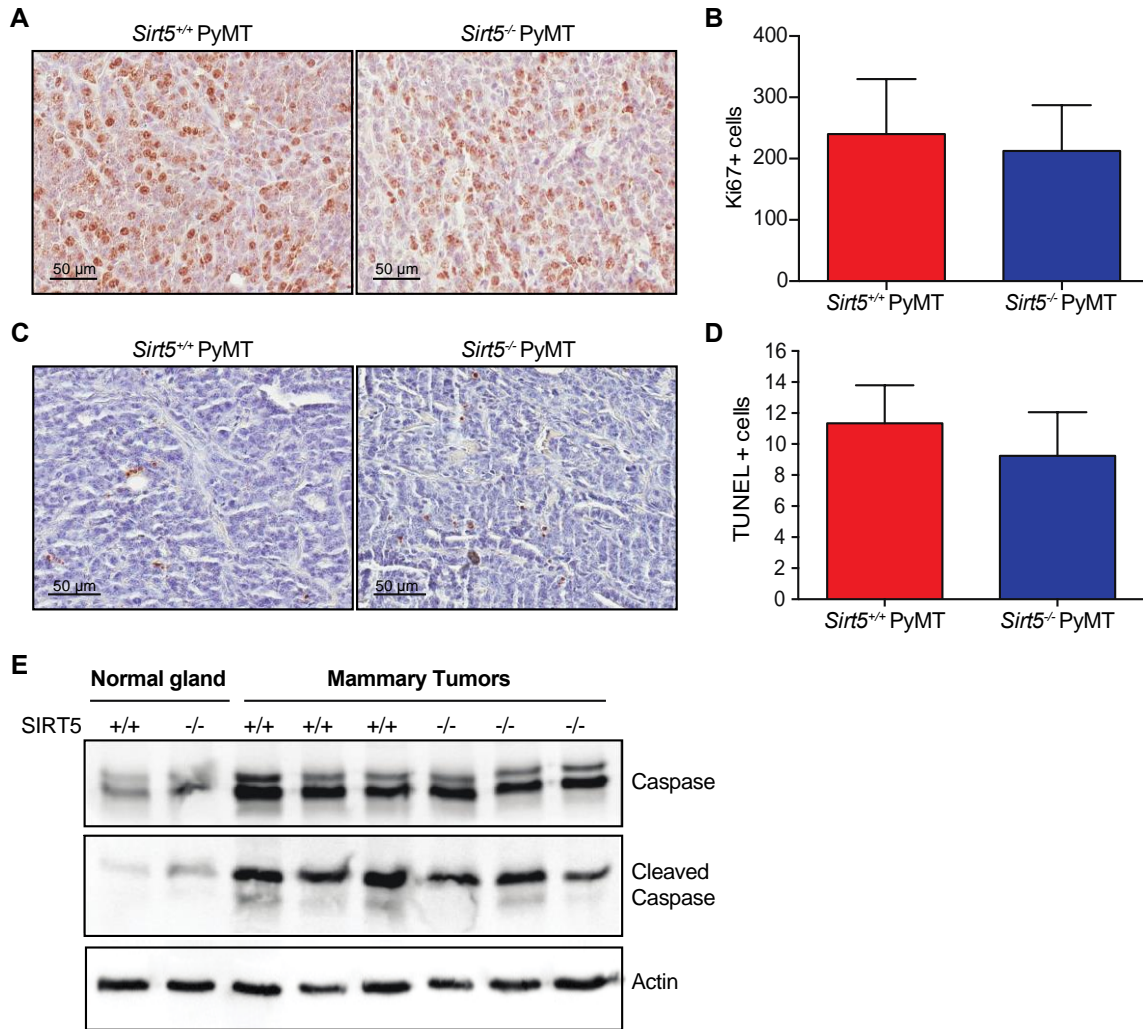


Figure 2.8 Histopathology of *Sirt5*^{+/+} PyMT and *Sirt5*^{-/-} PyMT mammary tumors.

(A) Representative images of Ki67 immunohistochemical staining of tumor tissues. **(B)** Quantification of Ki-67 positive cells. The proportion of Ki-67 proliferating cells was significantly lower in *Sirt5*^{-/-} PyMT mammary tumors when compared to *Sirt5*^{+/+} PyMT (p-value = 0.0372, Mann-Whitney U-test). **(C)** Representative examples of immunolabeling for TUNNEL in *Sirt5*^{+/+} PyMT and *Sirt5*^{-/-} PyMT mice. **(D)** Quantification of TUNNEL positive cells. The proportion of apoptotic cells was not significantly different

between genotypes (p-value = 0.3290, Mann-Whitney U-test). **(E)** Immunoblot for caspase and cleaved caspase. Actin was used as a loading control.

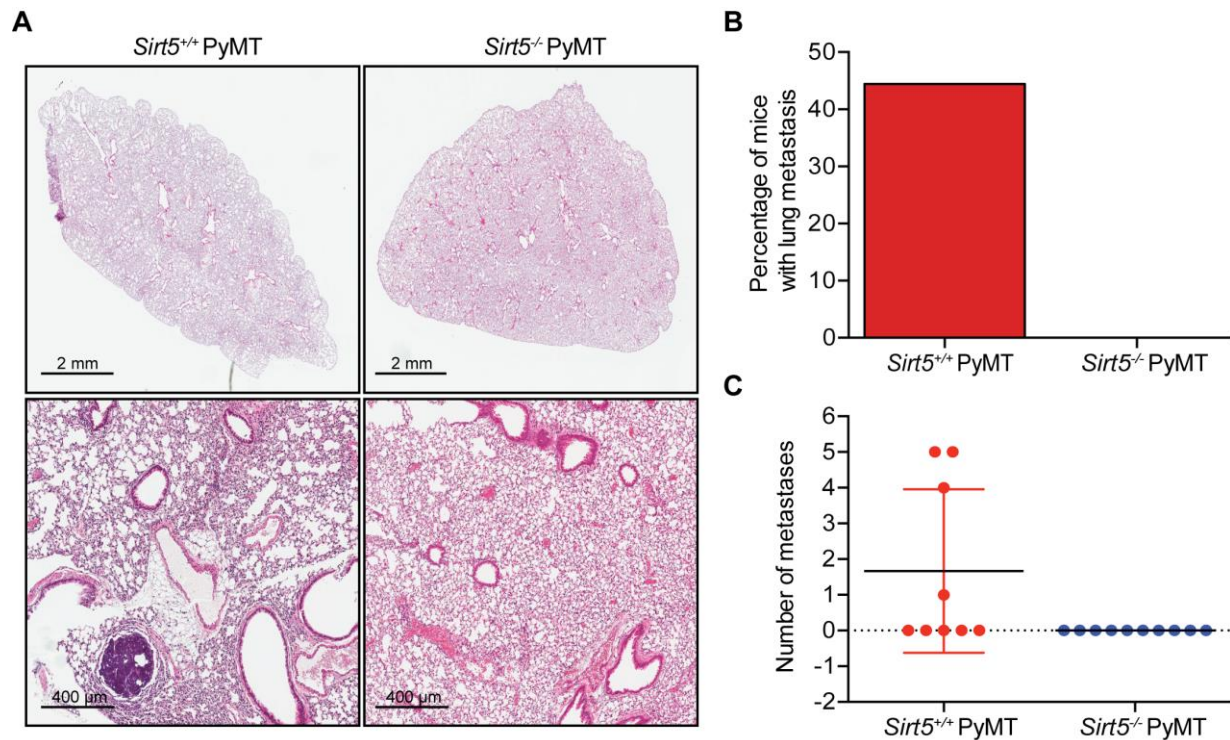


Figure 2.9 *Sirt5* deletion reduces metastasis burden in PyMT mice. **(A)** Representative images of lung tissues from *Sirt5*^{+/+} PyMT and *Sirt5*^{-/-} PyMT mice. Top image, low magnification of one lobe. Bottom image, high magnification showing lung metastasis in the *Sirt5*^{+/+} PyMT lungs, but not in *Sirt5*^{-/-} PyMT mice. **(B)** Quantification of percentage of mice with lung metastasis (*Sirt5*^{+/+} PyMT, n = 9 and *Sirt5*^{-/-} PyMT, n = 10). **(C)** Quantification of number of foci observed in lung tissues from *Sirt5*^{+/+} PyMT and *Sirt5*^{-/-} PyMT mice.

2.4.5 Prominent increase of succinylated proteins in *Sirt5*^{-/-} PyMT mammary tumors.

We screened global protein succinylation in normal mammary glands and mammary tumors from *Sirt5*^{+/+} PyMT and *Sirt5*^{-/-} PyMT mice. In agreement with published data, we found a prominent increase in succinylated proteins in *Sirt5*^{-/-} PyMT mice when compared to control mice in normal mammary gland and mammary tumor tissues (Figure 2.10A). To validate these results, we treated *Sirt5*^{-/-} PyMT mammary tumor lysates with recombinant SIRT5 and found that numerous proteins were regulated by SIRT5 (Figure 2.10B). Given that SIRT5 also deglutarylates a set of enzymes, we investigated protein lysine glutarylation status in *Sirt5*^{+/+} PyMT and *Sirt5*^{-/-} PyMT mammary tumors. Glutarylation levels were not significantly different in mammary tumors from *Sirt5*^{+/+} PyMT and *Sirt5*^{-/-} PyMT mice (Figure 2.11).

To identify proteins that were regulated by SIRT5 in mammary tumor tissues, we performed a comparative proteomic analysis using a stable-isotope reductive dimethylation approach, followed by enrichment of succinylated peptides and LC-MS/MS analysis as described by Sadhukhan *et al.* (Sadhukhan *et al.* 2016). LC-MS/MS analysis identified 413 lysine succinylation sites across 147 proteins in mammary tumors from *Sirt5*^{+/+} PyMT and *Sirt5*^{-/-} PyMT mice. Among these 413 peptides, 286 peptides were only succinylated in *Sirt5*^{-/-} PyMT mammary tumors and 86 were highly abundant in *Sirt5*^{-/-} PyMT when compared to *Sirt5*^{+/+} PyMT (Figure 2.12A). This accounts for a total of 132 hypersuccinylated proteins upon *Sirt5* loss. Interestingly, most of the identified proteins showed only one unique succinylated site, however, other proteins had between two to seventeen unique succinylated sites (Figure 2.12B).

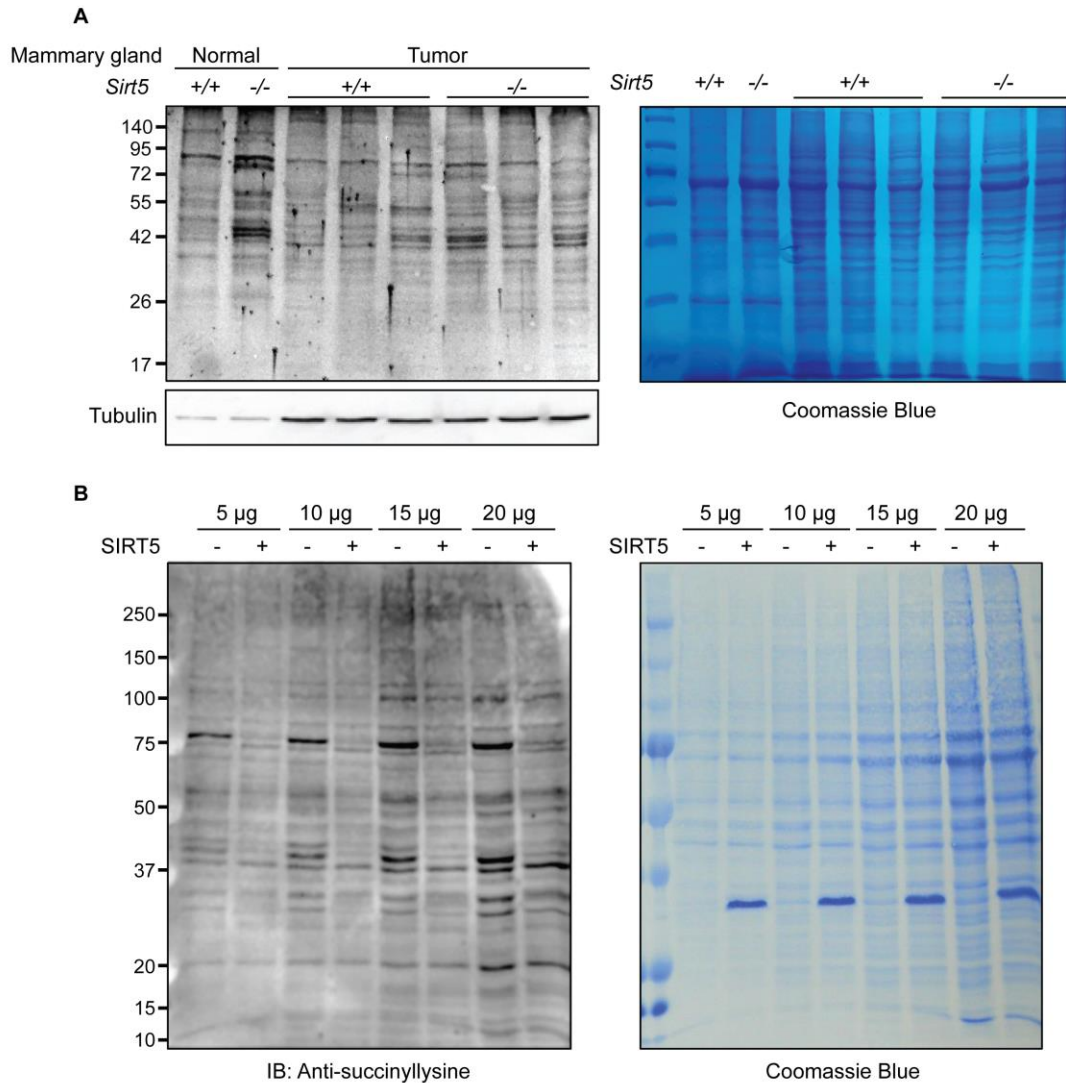


Figure 2.10 Succinylation levels in mammary tissues from *Sirt5*^{+/+} PyMT and *Sirt5*^{-/-} PyMT mice. (A) Western blot of normal mammary tissues and mammary tumors lysates (50 µg) against Anti-succinyllysine antibody. Tissues from *Sirt5*^{-/-} PyMT mice showed increased succinylation levels when compared to *Sirt5*^{+/+} PyMT. Tubulin levels and coomassie blue staining were used as loading controls. Tissue lysates were prepared using tumor tissues from mice that were euthanized 50 days after detecting the first tumor (Cohort 2). **(B)** *In-vitro* reaction of SIRT5 with mammary tumors from *Sirt5*^{-/-} PyMT mice. Five microliters of recombinant SIRT5 were added into a mixture

containing 5, 10, 15 and 20 μ L of tumor tissue lysate from a *Sirt5*^{-/-} PyMT mouse and incubated at 45 °C for an hour. Lysates were used to run a western blot. Anti-succinyllysine antibody was used to examine the succinylation levels. A reduction of succinylation levels was observed in upon the addition of recombinant SIRT5. Coomassie blue staining was used as loading control. Data shown in Figure 2.10B correspond to Sushabhan Sadhukhan.

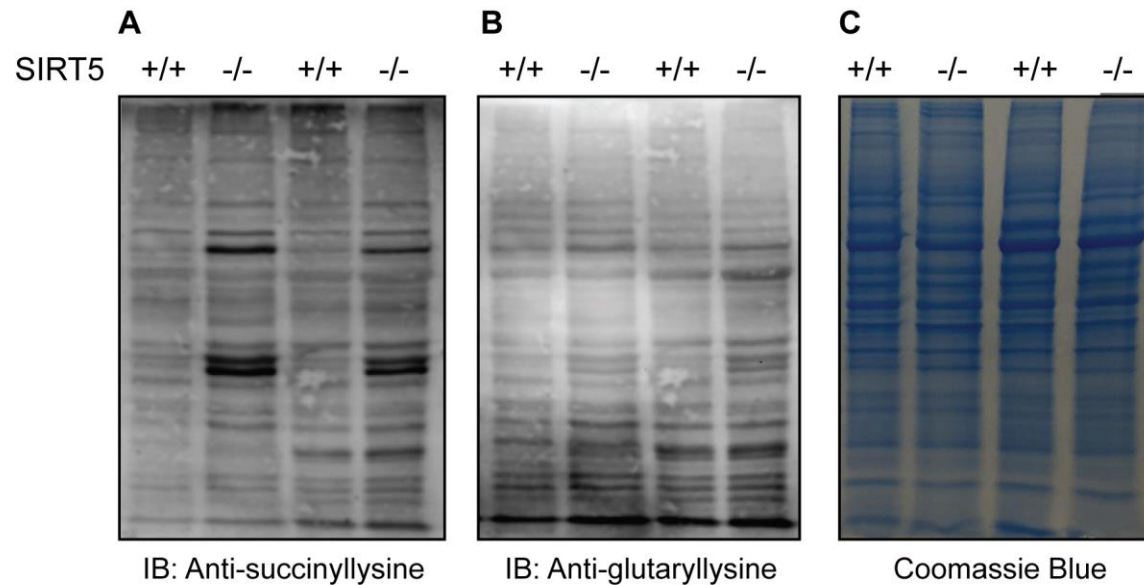


Figure 2.11 Succinylation and glutarylation levels in mammary tumors from *Sirt5*^{+/+} PyMT and *Sirt5*^{-/-} PyMT mice.

Western blot of mammary tumors lysates (50 μ g) against **(A)** Anti-succinyllysine antibody and **(B)** Anti-glutaryllysine antibody. Mammary tumors from *Sirt5*^{-/-} PyMT mice showed higher succinylation levels when compared to *Sirt5*^{+/+} PyMT mice. Glutarylation levels were not distinct between the two groups. Succinylation and glutarylation levels were measured in the same membrane. Western blot membrane was blotted with Anti-glutaryllysine ab. After stripping 30 minutes, the membrane was blocked with 5% milk in TBST solution and blotted with Anti-succinyllysine ab. An independent experiment was performed using different membranes and same results were obtained. **(C)** Coomassie blue stained-gel was used as loading control.

Analysis of the cellular localization of the identified proteins revealed that 61% of the succinylated proteins localize in the mitochondria, consistent with earlier reports, while the rest of the identified proteins are cytoplasmic or secreted (Radin, *et al.* 2013; Sadhukhan *et al.* 2016). To gain an insight into how succinylation and SIRT5 regulate metabolic networks, we performed pathway enrichment analysis using Reactome (www.reactome.org). Interestingly, most of the succinylated proteins identified (66%) in our LC-MS analysis were enzymes involved in cellular metabolism. Other cellular pathways, such as, organelle biogenesis, cellular transport, immune system and homeostasis, were enriched to a lesser extent with succinylation targeted enzymes (Figure 2.12C). Further analysis of metabolic pathways revealed that the top pathways enriched with succinylation-targeted proteins were the TCA cycle and respiratory electron transport, as well as metabolism of lipids (Figure 2.12D). Interestingly, 7 out of 8 enzymes involved in the TCA cycle were highly succinylated in *Sirt5*^{-/-} PyMT mammary tumors (Figure 2.13, Table 2.3, Supplemental Table 2.2). Besides the TCA cycle, multiple subunits of ATP synthase as well as enzymes involved in ATP transport were also hypersuccinylated in *Sirt5*^{-/-} PyMT mammary tumors (Table 2.4, Supplemental Table 2.2).

Another pathway that is highly enriched with SIRT5 targets is lipid metabolism, specifically fatty acid β oxidation pathway. Among the identified hyper-succinylated proteins in *Sirt5*^{-/-} PyMT mammary tumors, the trifunctional enzyme subunit α had the highest amount of succinylated sites (9 unique succinylation sites) as described by Sadhukhan *et al.* (Sadhukhan *et al.* 2016) (Table 2.5, Supplemental Table 2.2). Other

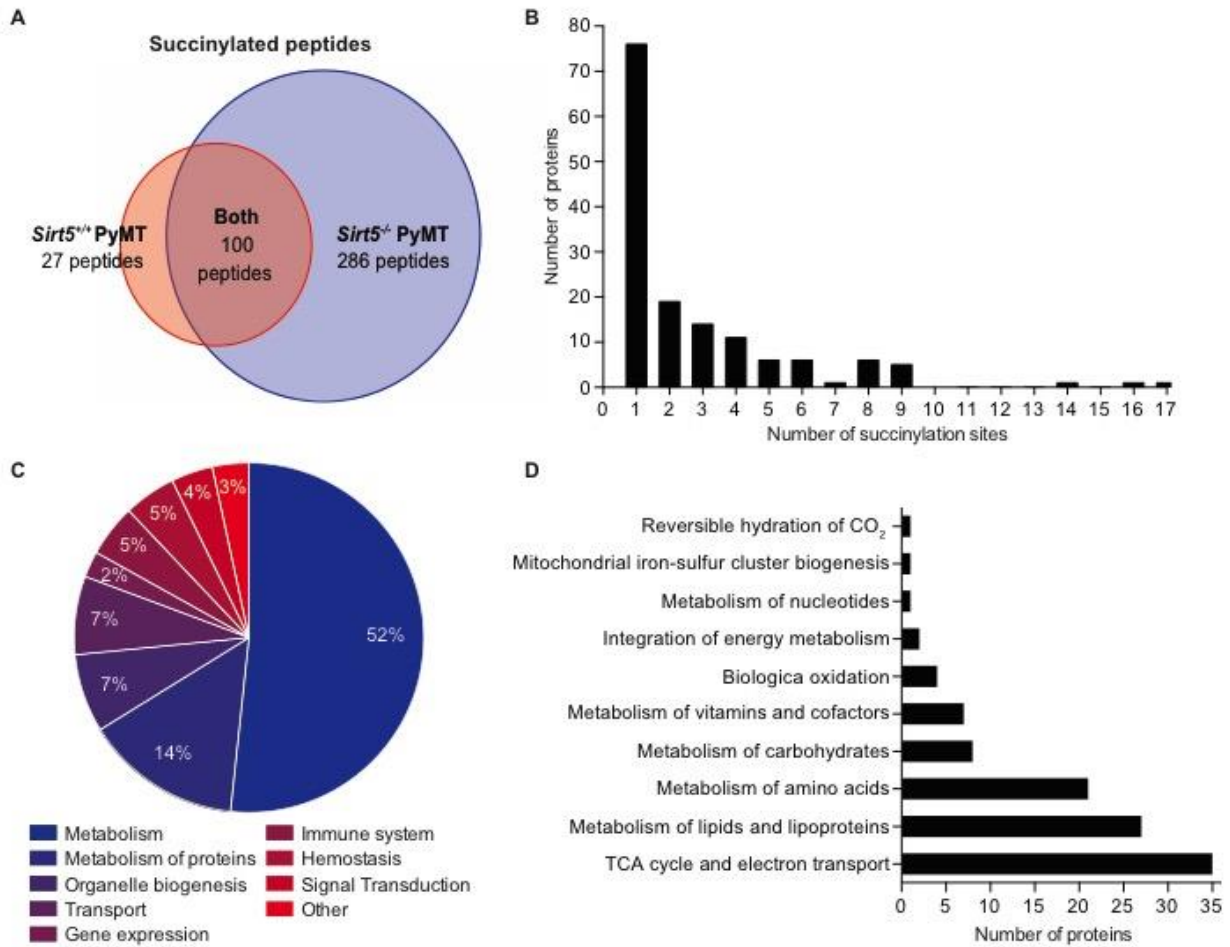


Figure 2.12 Metabolic pathways highly targeted by SIRT5. (A) Venn diagram showing the number of unique succinylated peptides identified in *Sirt5*^{+/+} PyMT and *Sirt5*^{-/-} PyMT mammary tumors. (B) Distribution of number of lysine succinylation sites per proteins. (C) Cellular processes enriched by succinylation-targeted proteins. (D) Metabolic pathways enriched with lysine succinylated proteins.

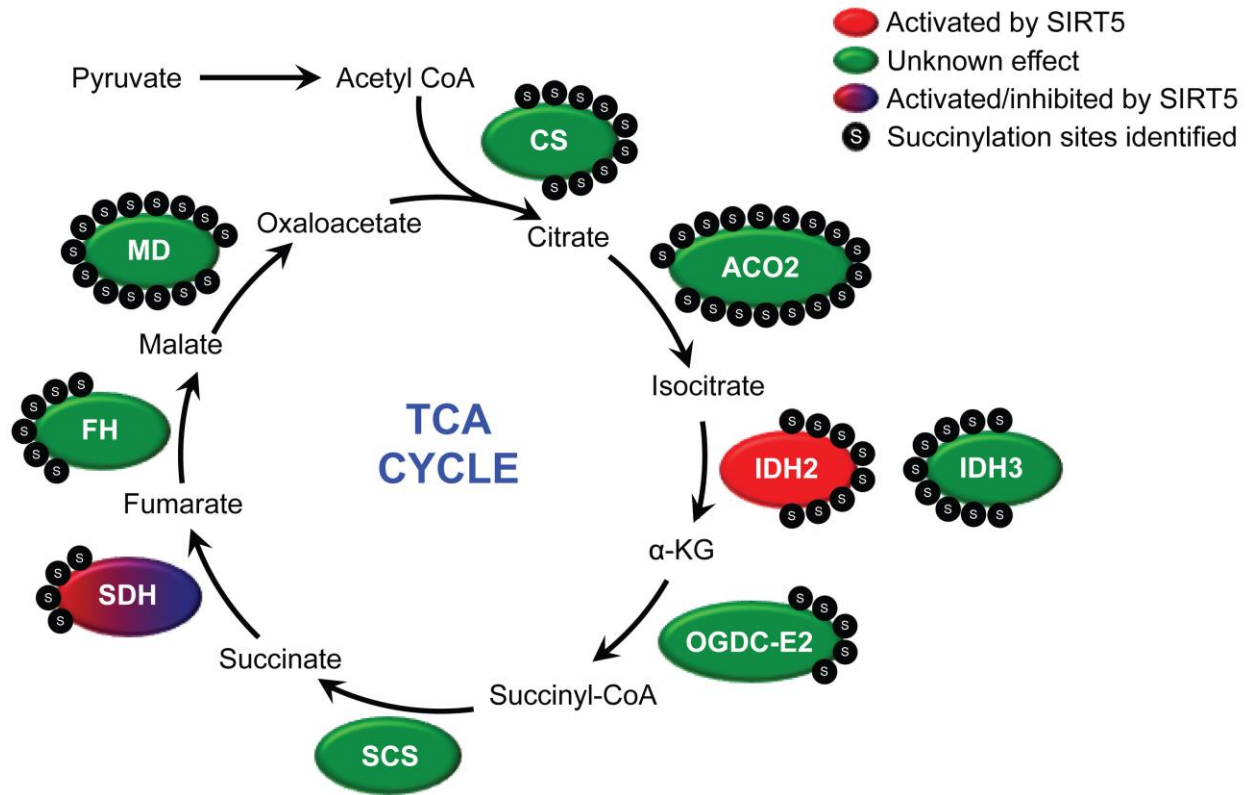


Figure 2.13 TCA cycle enzymes are targeted by SIRT5. Acetyl-CoA, Acetyl-Coenzyme A; CS, Citrate synthase; ACO2, Aconitase 2; IDH2/3, Isocitrate dehydrogenase 2/3; α KG, Alpha ketoglutarate; OGDC-E2, 2-oxoglutarate dehydrogenase complex 2; Succinyl-CoA, Succinyl-Coenzyme A; SDH, Succinate dehydrogenase; FH, Fumarate hydratase; MD, malate dehydrogenase.

Table 2.3 List of hyper-succinylated proteins involved in the TCA cycle.*

Protein	Unique succinylation sites	Sites in <i>Sirt5</i>^{+/+} PyMT	Sites in <i>Sirt5</i>^{-/-} PyMT	Sites in <i>Sirt5</i>^{+/+} and <i>Sirt5</i>^{-/-} PyMT
Citrate synthase	9	2	7	0
Aconitate hydratase	17	0	11	6
Isocitrate dehydrogenase 2	8	0	6	2
Isocitrate dehydrogenase 3	9	0	8	1
2-oxoglutarate dehydrogenase complex, E2 subunit	5	1	4	0
Succinate dehydrogenase	4	0	4	0
Fumarate hydratase	6	0	4	2
Malate dehydrogenase	14	1	6	7

*Data shown in this table was obtained from a comparative proteomic analysis using stable-isotope reductive dimethylation approach, followed by enrichment of succinylated peptides and LC-MS/MS analysis. Unique succinylated sites in *Sirt5*^{+/+} PyMT and *Sirt5*^{-/-} PyMT mammary tumors were quantified manually.

Table 2.4 List of hyper-succinylated proteins involved in the production and transport of ATP.

Protein	Unique succinylation sites	Sites in <i>Sirt5</i>^{+/+} PyMT	Sites in <i>Sirt5</i>^{-/-} PyMT	Sites in <i>Sirt5</i>^{+/+} and <i>Sirt5</i>^{-/-} PyMT
ATP synthase				
Subunit α	8	1	6	1
Subunit β	4	0	1	3
Subunit γ	1	1	0	0
Subunit d	3	1	1	1
Subunit O	6	0	4	2
Subunit ϵ	1	0	1	0
ADP/ATP translocase 1	3	1	2	0
ADP/ATP translocase 2	4	0	2	2
ATPase inhibitor	2	0	2	0

*Data shown in this table was obtained from a comparative proteomic analysis using stable-isotope reductive dimethylation approach, followed by enrichment of succinylated peptides and LC-MS/MS analysis. Unique succinylated sites in *Sirt5*^{+/+} PyMT and *Sirt5*^{-/-} PyMT mammary tumors were quantified manually.

Table 2.5 List of hyper-succinylated proteins involved in lipid metabolism.

Protein	Unique succinylation sites	Sites in <i>Sirt5</i>^{+/+} PyMT	Sites in <i>Sirt5</i>^{-/-} PyMT	Sites in <i>Sirt5</i>^{+/+} and <i>Sirt5</i>^{-/-} PyMT
serum albumin precursor	16	1	6	9
trifunctional enzyme subunit alpha	9	0	9	0
acetyl-CoA acetyltransferase	8	0	7	1
3-ketoacyl-CoA thiolase	6	0	3	3
enoyl-CoA delta isomerase 1	5	0	3	3
hydroxyacyl-coenzyme A dehydrogenase	4	0	4	0

enoyl-CoA delta isomerase 2b	4	0	4	0
very long-chain specific acyl-CoA dehydrogenase	3	0	3	0
long-chain specific acyl-CoA dehydrogenase	3	0	2	1
enoyl-CoA hydratase	3	0	2	1
acyl-coenzyme A thioesterase 13	3	0	2	1
trifunctional enzyme subunit beta	2	0	2	0
methylmalonyl-CoA epimerase	2	0	2	0
medium-chain specific acyl-CoA dehydrogenase	1	0	0	1

carbonyl reductase family member 4	1	0	1	0
estradiol 17-beta-dehydrogenase 8	1	0	1	0
acyl-CoA synthetase family member 3	1	0	1	0
2,4-dienoyl-CoA reductase	1	0	1	0
succinyl-CoA:3-ketoacid coenzyme A transferase 1	3	1	1	1
trans-2-enoyl-CoA reductase	1	0	1	0
carnitine O-palmitoyltransferase 2	1	0	1	0

*Data shown in this table was obtained from a comparative proteomic analysis using stable-isotope reductive dimethylation approach, followed by enrichment of succinylated peptides and LC-MS/MS analysis. Unique succinylated sites in *Sirt5*^{+/+} PyMT and *Sirt5*^{-/-} PyMT mammary tumors were quantified manually.

proteins that were found to be hyper-succinylated are acetyl-CoA acetyltransferase and 3-ketoacyl-CoA thiolase. Together, these data highlight the importance of SIRT5-mediated desuccinylation in the regulation of mammary tumor metabolism.

2.4.6 *Sirt5* deficiency alters gene expression

There is increasing evidence for a direct involvement of metabolic enzymes and metabolites in regulating gene expression (Raghow *et al.* 2008; van der Knaap and Verrijzer 2016). Given that SIRT5 regulates multiple metabolic enzymes and its activity is associated to metabolic states, we wanted to evaluate the impact of *Sirt5* loss on the expression of genes that might be critical for tumor progression. We performed a comparative analysis of expression profiles between mammary tumors from *Sirt5*^{+/+} PyMT and *Sirt5*^{-/-} PyMT mice and identified significant dysregulation of 129 genes in *Sirt5*^{-/-} PyMT mice when compared to the control group (Figure 2.14A, Supplemental Table 2.3). Of these, 68 genes were down-regulated and 61 were up-regulated in *Sirt5*^{-/-} PyMT mice when compared to *Sirt5*^{+/+} PyMT (Figure 2.14B).

Principal component analysis and unsupervised hierarchical clustering of 1,620 genes identified did not show similar expression profile between samples within the same group (Figure 2.14C, Supplemental Figure 2.1A). Interestingly, heatmap analysis of the 129 differentially expressed genes showed distinct segregation between *Sirt5*^{-/-} PyMT and control group (Figure 2.14D). Among the differentially expressed gene, *Sirt5* was one of the genes with the lowest p-values and highest fold-change (Supplemental Figure 2.1B). To validate this data, we analysed *Sirt5* expression for each sample using

RT-qPCR and observed no detectable expression of *Sirt5* in *Sirt5*^{-/-} PyMT mammary tumors, confirming the genotyping results (Figure 2.14E).

To determine the biological functions of these differentially expressed genes, we performed GO enrichment analysis. Among the biological processes enriched with the identified differential genes included: positive/negative regulation of metabolic processes, response to stimuli, signal transduction, cell communication, cell differentiation and regulation of cell proliferation (Figure 2.14F, Supplemental Table 2.4). We also assigned these genes to Reactome database and found enrichment of genes involved in cellular metabolism, signal transduction and regulation of inflammation (Figure 2.14G).

Given that SIRT5 regulates many metabolic enzymes, we expected to observe dysregulation in the expression of genes that regulate metabolism and mitochondrial function. Although some metabolic genes were altered by *Sirt5* deletion (Table 2.6), we did not observe enrichment of a specific metabolic pathway (FDR < 0.05), suggesting that deletion of *Sirt5* does not impact the expression of genes involved in major metabolic pathways.

Surprisingly, we did observe enrichment of pathways associated with the immune system, including cytokine-signaling pathways (Figure 2.15A, Table 2.7). Among the differentially expressed genes involved in the immune system, two that caught our attention were the serum amyloid A genes (*Saa1* and *Saa2*). *Saa1* and *Saa2* genes are highly related genes that encode a family of apolipoproteins, known as the serum amyloid A (SAA) proteins. SAA proteins are secreted during the acute phase of inflammation and have been associated to perform multiple functions;

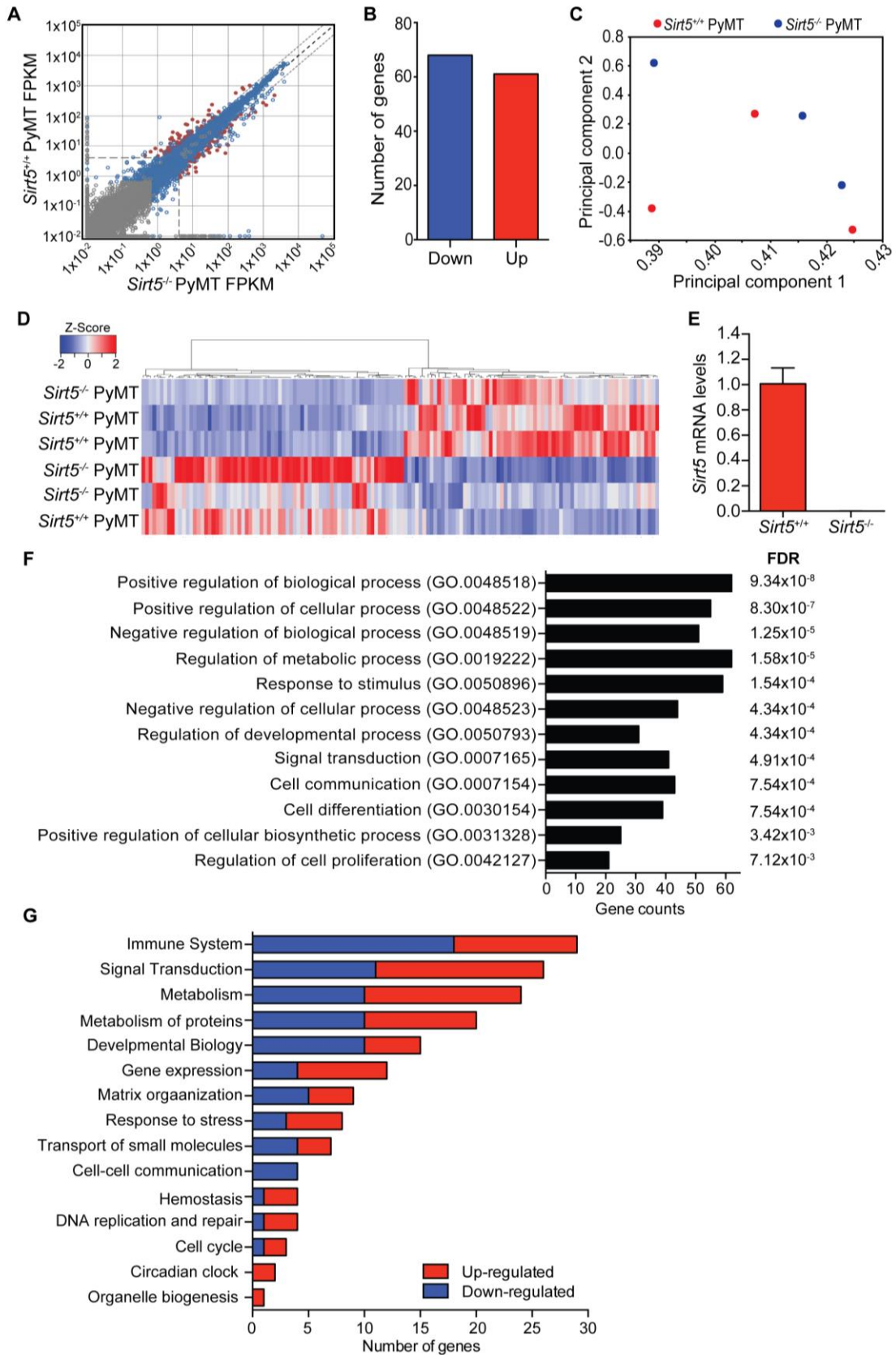


Figure 2.14 *Sirt5* loss affects the expression of genes involved in different metabolic pathways. **(A)** Differential gene expression in between *Sirt5*^{+/+} PyMT and *Sirt5*^{-/-} PyMT mammary tumors. Red dots represent the differential genes. **(B)** Bar graph showing the number of genes that are significantly down-regulated and up-regulated in *Sirt5*^{-/-} PyMT mammary tumors. **(C)** Non-supervised Principal Component Analysis (PCA) showing variability in gene expression between samples. **(D)** Hierarchical clustering analysis of the differential expressed genes between *Sirt5*^{+/+} PyMT and *Sirt5*^{-/-} PyMT mice. Z-Score values and Spearman Rank Correlation Method were used for the generation of the heatmap. **(E)** Expression of *Sirt5* in mammary tumors from *Sirt5*^{+/+} PyMT and *Sirt5*^{-/-} PyMT mice. **(F)** GO analysis of the differentially expressed genes. All enriched GO Biological Processes categories shown showed a P-value and FDR below 0.05. **(G)** Pathways enriched with differentially expressed genes.

Table 2.6 List of differentially expressed genes involved in cellular metabolism.

Gene ID	Average <i>Sirt5</i>^{+/+} PyMT (log2(FPKM))	Average <i>Sirt5</i>^{-/-} PyMT (log2(FPKM))	Fold Change
<i>Cyp3a57</i>	0	3	3.2
<i>Fbp2</i>	5	21	2.2
<i>Slc5a5</i>	2	8	1.9
<i>Fmo2</i>	1	3	1.7
<i>Hal</i>	1	4	1.4
<i>Inpp5j</i>	4	9	1.3
<i>Prkar2b</i>	14	27	1.0
<i>Slc27a1</i>	23	41	0.8
<i>Gpam</i>	7	12	0.8
<i>Ddhd2</i>	16	26	0.7
<i>ldh1</i>	44	69	0.6
<i>Chsy1</i>	32	20	-0.7
<i>Psmb8</i>	169	104	-0.7
<i>Ddah2</i>	117	72	-0.7

<i>Ldhb</i>	140	83	-0.8
<i>Nqo1</i>	62	34	-0.9
<i>Ckb</i>	47	25	-0.9
<i>Ptgs2</i>	4	1	-1.4
<i>Rbp1</i>	104	30	-1.8

including transport of cholesterol, recruitment of immune cells to inflammatory sites and induction of enzymes that degrades extracellular matrix (Malle *et al.* 1993; Ye and Sun 2015). In the context of cancer, increased levels of SAA are often used as a clinical cancer marker. Multiple studies have shown that SAA levels are significantly elevated in the serum of patients with esophageal squamous cell carcinoma, ovarian cancer and lung cancer (Cho *et al.* 2010; Urieli-Shoval *et al.* 2010; Wang *et al.* 2012). Interestingly, previous work revealed that *Saa* expression is down-regulated in liver tissues from *Sirt5*^{-/-} mice treated with high fat diet (Yu *et al.* 2013).

As shown in Table 2.7, *Saa1* and *Saa2* were highly expressed in mammary tumors when compared to other genes. Furthermore, *Saa1* and *Saa2* were significantly down-regulated in *Sirt5*^{-/-} PyMT mice. To validate the data, we conducted RT-qPCR using mammary tumor samples from a bigger cohort of mice. Analysis of serum amyloid A expression confirmed the results obtained in the RNA-sequencing analysis, suggesting that deletion of *Sirt5*^{-/-} significantly reduces serum amyloid A expression (Figure 2.15B).

Given that SAA is secreted during the acute phase of inflammation, we wanted to know whether deletion of *Sirt5*^{-/-} affects the expression of other genes involved in inflammation. No significant differences were observed in the expression of several additional inflammation genes (Figure 2.15C).

2.4.7 Selective inhibition of SIRT5 affects cancer cell growth *in vitro* and mammary tumorigenesis in MMTV-PyMT mice

To further demonstrate that *Sirt5* loss inhibits cancer cell growth we synthesized

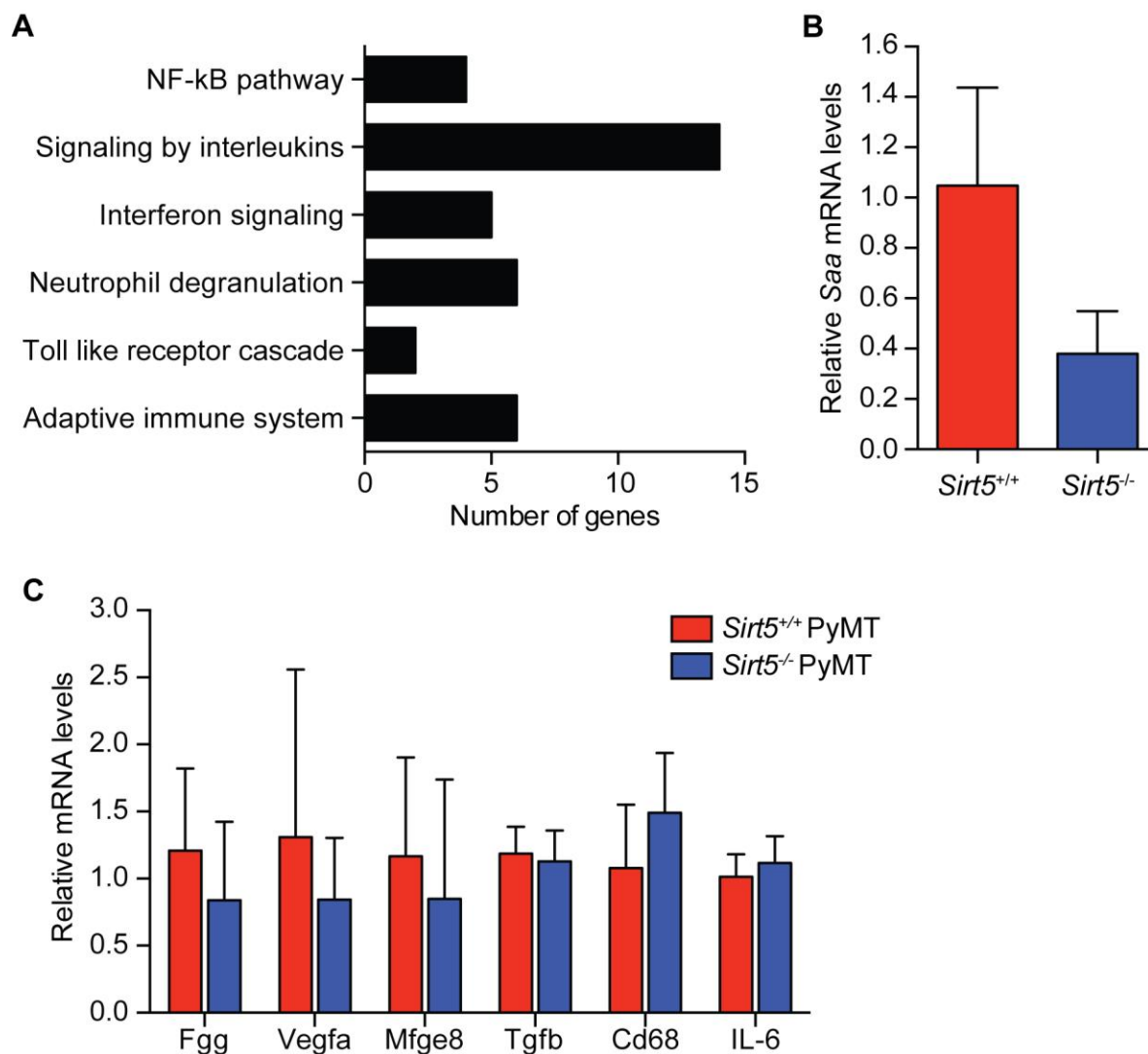


Figure 2.15 Serum amyloid A expression is decreased in *Sirt5*^{-/-} PyMT mammary tumors. (A) Multiple pathways associated to the immune system are enriched with differentially expressed genes. (B) Expression of *Saa* in mammary tumors from *Sirt5*^{+/+} PyMT and *Sirt5*^{-/-} PyMT mice. (C) The expression profile of a selected set of genes associated to inflammation. mRNA level of each gene was normalized to the housekeeping gene *Hprt* and *Rpl13A* and further normalized to the expression level in *Sirt5*^{+/+} PyMT mice.

Table 2.7 List of differentially expressed genes associated to the immune system.

Gene ID	Average <i>Sirt5</i>^{+/+} PyMT (log2(FPKM))	Average <i>Sirt5</i>^{-/-} PyMT (log2(FPKM))	Fold Change
<i>Zbtb16</i>	1	5	2.4
<i>Ctse</i>	1	2	1.8
<i>Cd93</i>	3	5	1.0
<i>Padi2</i>	17	34	1.0
<i>Lama5</i>	9	17	0.9
<i>Sh3kbp1</i>	11	18	0.8
<i>Rap1gap</i>	39	61	0.7
<i>Vegfa</i>	19	31	0.7
<i>Idh1</i>	44	69	0.6
<i>Ifngr2</i>	57	36	-0.7
<i>Psmb8</i>	169	104	-0.7
<i>Ube2f</i>	66	41	-0.7
<i>Atp8a1</i>	8	5	-0.8
<i>Xaf1</i>	16	9	-0.8

<i>Bst2</i>	233	126	-0.9
<i>Nrtn</i>	64	32	-1.0
<i>Tnfrsf1b</i>	8	4	-1.1
<i>Fgf1</i>	15	6	-1.2
<i>Isg15</i>	133	55	-1.3
<i>Ptgs2</i>	4	1	-1.4
<i>Saa1</i>	755	276	-1.5
<i>Saa2</i>	566	169	-1.7
<i>Tnfrsf11b</i>	7	2	-1.9
<i>Fgg</i>	29	7	-2.0

SIRT5-selective inhibitors. To develop SIRT5-selective inhibitors, we used mechanism-based thioacyl lysine compounds, described in Jing *et al.* (Jing *et al.* 2016). Thioacyl lysine peptides react with NAD⁺ in the sirtuin active site and form a stable intermediate that inhibit sirtuin activity. Two thioacyl lysine compounds with different R groups were synthesized, I5-2AM and MY01170 (Figure 2.16A, Supplemental Figure 2.2A).

To test the effectiveness of I5-2AM, we first performed an inhibition assay of recombinant SIRT5 activity using I5-2 (unprotected form of I5-2AM). The IC₅₀ for this compound was 2.05 μM (Figure 2.16B). We next wanted to test the ability of I5-2AM to inhibit the growth of human cancer (MDA-MB 231) and PyMT mammary tumor (AT3) cell lines. Clonogenic assays showed that I5-2AM inhibited the proliferation of MDA-MB-231 and AT3 cancer cells at 100 μM (Figure 2.16C, Supplemental Figure 2.3). We further tested I5-2AM in human embryonic kidney cells, HEK-293T and found that I5-2AM inhibits its proliferation at 50 μM (Supplemental Figure 2.4A). Selective inhibition of SIRT5, also suppressed the anchorage-independent growth of MDA-MB 231 cancer cells and HEK-293T cells (Figure 2.16D-E, Supplemental Figure 2.4B).

To investigate whether SIRT5-selective inhibition affects tumorigenesis *in vivo*, MMTV-PyMT mice received IP injections with either the control vehicle solvent or I5-2AM. Upon treatment, I5-2AM-treated mice had smaller tumors when compared to DMSO-H₂O-treated mice (Figure 2.17A). Total tumor weight was significantly lower in I5-2AM-treated mice (Figure 2.17B). The same trend was observed when only the biggest tumor was weighed (Figure 2.17C). Importantly, I5-2AM treatment did not cause any apparent toxicity or weight loss in mice (Figure 2.17D). We also assessed whether I5-2AM had an effect on the metastatic potential of PyMT mammary tumors. We found

no significant differences. Most PyMT-treated mice did not show lung metastasis (Figure 2.17E). Together, these data suggest that selective inhibition of SIRT5 has anticancer properties.

To test, whether I5-2AM-treatment efficiently reduced SIRT5 activity in tumor samples, we screened global protein succinylation in mammary tumors from I5-2AM- and DMSO-treated mice. Mammary tumors were collected 24 hrs after the last IP injection and processed as described in the Materials and Method section. We found an increment in protein succinylation levels in I5-2AM-treated mice when compared to control groups (Figure 2.17F). Given that SIRT5 regulates CPS1 activity, we further tested blood ammonia levels in treated mice. Blood ammonia was measured in fasted I5-2AM-treated mice 24 hrs post-I5-2AM IP administration. Consistent with the idea that SIRT5 was inhibited in treated mice, we observed that ammonia levels were higher in I5-2AM-treated mice when compared to the control group (Figure 2.17G).

We further analysed I5-2AM content in blood and tissue samples from I5-2AM-treated mice using LC-MS and found the active form of I5-2AM in blood serum and abdominal fat 30 minutes post-I5-2AM IP administration (Figure 2.17H). However, no traces of I5-2AM were detected on mammary tumor samples at this timepoint (Figure 2.17H). We also measured I5-2AM at later endpoints post-I5-2AM IP injection (3 and 24 hrs post-IP administration) and found no traces of this compound in blood or any tissues tested, suggesting that the half-life of I5-2AM is less than 30 minutes.

Given that the half-life of I5-2AM, we tested an additional SIRT5-inhibitor, MY01170 (Supplemental Figure 2.2A). MY01170 is a thioacyl lysine compound with

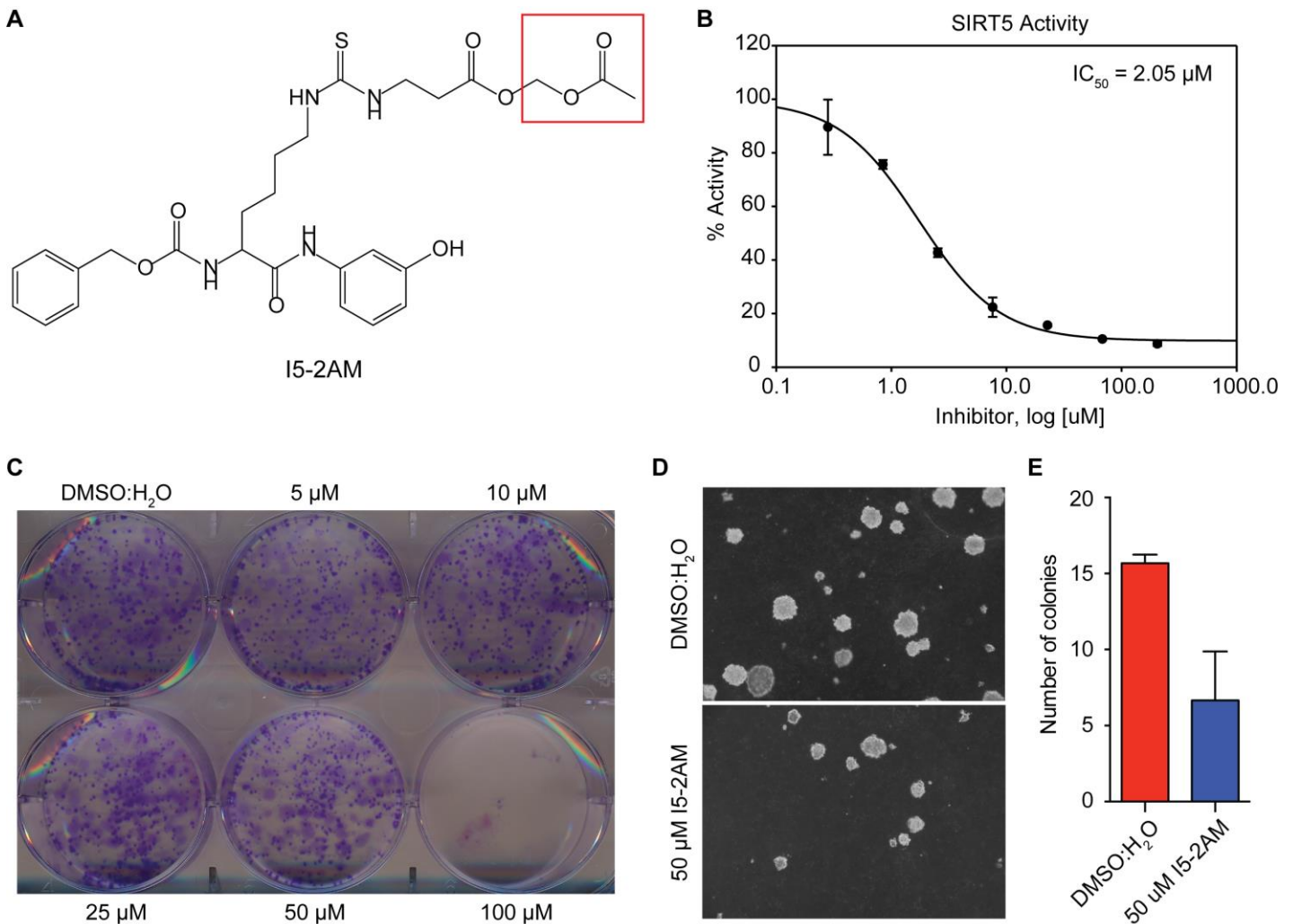
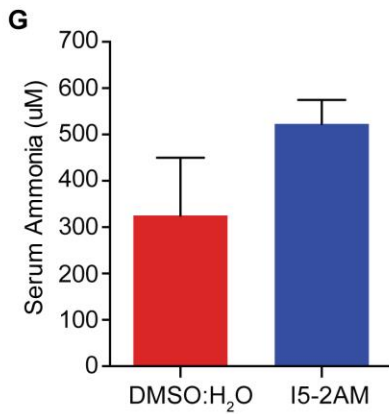
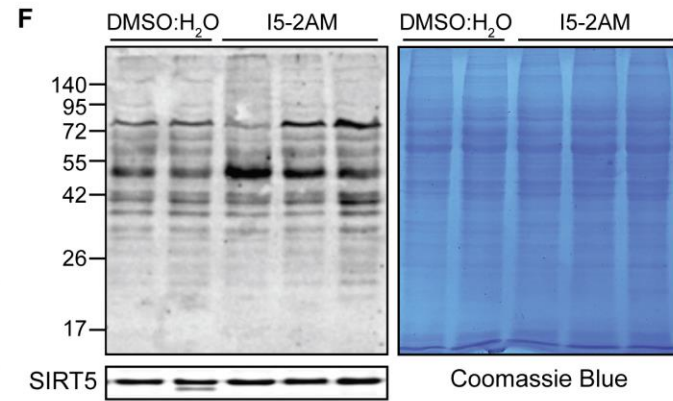
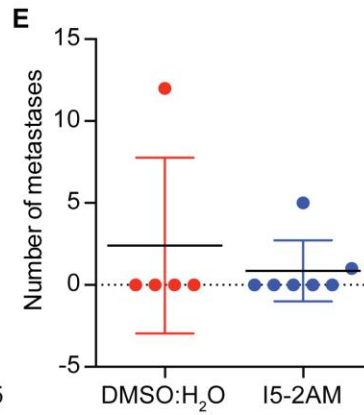
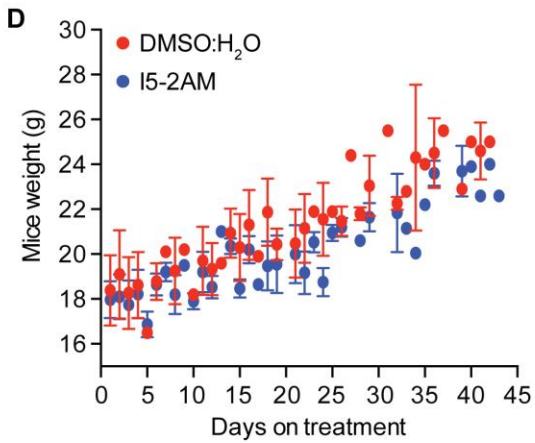
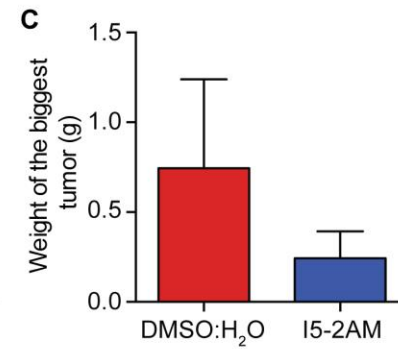
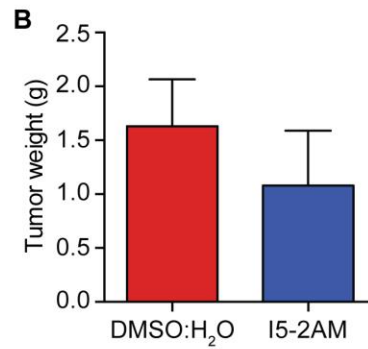
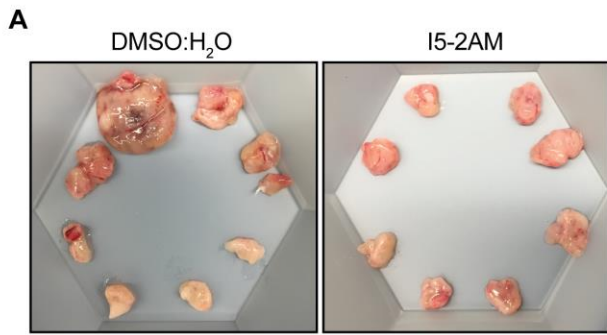


Figure 2.16 SIRT5 inhibition reduces the proliferation of breast cancer cells. (A) Structure of SIRT5-selective inhibitor, I5-2AM. Red box highlights the protective group of I5-2AM when compared to I5-2. **(B)** Graph showing the inhibition of SIRT5 activity with I5-2AM. IC₅₀ for I5-2 on SIRT5 is 2.05 μ M. **(C)** Clonogenic assay performed on MDA-MB 231 cells upon treatment with different concentrations of I5-2AM. **(D)** Soft-agarose assay showing that selective inhibition of SIRT5 with I5-2AM reduced the colony formation of MDA-MB 231 breast cancer cells. **(E)** Quantification of the number of colonies (p-value = 0.0088, T-test).



H

Time Post-injection	Tissue	I5-2AM
30 minutes	Serum	+
	Abdominal Fat	+
	Tumors	-
3 hours	Serum	-
	Abdominal Fat	-
	Tumors	-
24 hrs	Serum	-
	Abdominal Fat	-
	Tumors	-

Figure 2.17 Selective inhibition of SIRT5 reduces tumor load in PyMT mice. **(A)** Gross images of mammary tumors after 6 weeks of treatment with I5-2AM or control vehicle. **(B)** Total tumor weight after treatment ($p = 0.0172$, Mann Whitney test). **(C)** Weight of the biggest tumors after I5-2AM treatment ($p = 0.0111$, Mann Whitney test). **(D)** Average of mice weight through out the 6 weeks treatments with I5-2AM or DMSO:H₂O solution. **(E)** Quantification of the number of lung metastasis in PyMT mice after treatment ($p > 0.999$, Mann Whitney test). **(F)** Western blot of mammary tumors lysates (50 μ g) against Anti-succinyllysine antibody. Tissues from I5-2AM-treated mice showed an increment in succinylation levels when compared to DMSO:H₂O-treated mice. Coomassie blue staining was used as loading control. Tissue lysates were prepared using tumor tissues from PyMT mice that were treated for 6 weeks with I5-2AM or control vehicle, and euthanized 24 hrs after the last injection. **(G)** Serum ammonia levels after 24 hrs of I5-2AM or vehicle administration. PyMT-treated females were treated for 6 weeks with I5-2AM or control vehicle. After the last injection, mice were fasted for 24 hours and sacrificed. Blood was collected by cardiac puncture. Serum was immediately frozen in liquid nitrogen and used for measurement of ammonia levels. N=3 for I5-2AM-treated mice, N=4 for DMSO-H₂O-treated mice. P-value > 0.05 . **(H)** Detection of I5-2AM in mouse serum, abdominal fat, and mammary tumor tissues by LC-MS at different timepoints post-I5-2AM IP administration. Minus and plus signs symbolize no detection and detection of I5-2AM, respectively.

greater stability than I5-2AM. Our preliminary data showed that MY01170 had stronger anti-cancer effect than I52-AM in MCF7. Treatment of MCF7 with different concentrations of MY01170 showed an $IC_{50} < 20 \mu\text{M}$ (Supplemental Figure 2.2B). We further evaluated the anticancer activity of MY01170 using soft agar colony formation assay. MY01170 significantly inhibited anchorage-independent growth of MCF7 when compared to DMSO control vehicle (Supplemental Figure 2.2C). Further experiments are needed to show the potential of MY01170 as a selective-SIRT5 inhibitor with anti-cancer properties.

2.5 DISCUSSION

Lysine succinylation is a major type of protein acylation that plays an important role in regulating the activity of key metabolic enzymes in cancer. Up to now, SIRT5 is the only known enzyme that controls the state of lysine succinylation of mitochondrial proteins. Given that cancer cells rewires their metabolism to sustain their biosynthetic and bioenergetics needs, in part through alteration of lysine succinylation, targeting SIRT5 hold a lot of potential for cancer treatment.

In present work, we investigated the roles of SIRT5 in breast cancer progression. Here, we demonstrated that clinically, overexpression of *SIRT5* has been found in a percentage of breast cancers and its overexpression correlates to poor overall survival of breast cancer patients. Knock-down of *SIRT5* affects the ability of human breast cancer cells, as well as lung cancer cells to exhibit anchorage-independent growth. Furthermore, *Sirt5* loss slowed down the proliferation rate of Kras-transformed MEFs and significantly reduced their ability to growth in soft-agarose,

suggesting that SIRT5 is essential for the proliferation and malignant transformation of cancer cells.

Previous studies have reported that SIRT5 promotes tumorigenesis in human xenograft mouse models, however there are no studies to date that have examined the roles of SIRT5 in a transgenic breast cancer mouse model (Lu *et al.* 2014; Xiangyun *et al.* 2017). To test whether SIRT5 has a fundamental role in mammary tumorigenesis, we used MMTV-PYMT transgenic mice, a genetically engineered model in which the animals develop mammary adenocarcinoma with metastasis to lung and lymph nodes (Guy *et al.* 1992). This model is characterized for recapitulating many aspects of human breast cancer (Lin *et al.* 2003). MMTV-PyMT mice were bred with *Sirt5*^{+/-} to generate MMT-PyMT mice carrying either wild type or deleted *Sirt5* gene. Our data clearly showed that deletion of *Sirt5* slightly delayed mammary tumor development, significantly increased the overall survival of mice and reduced tumor load by affecting the proliferation rate of tumor cells. Together, our data suggested that SIRT5 is essential for the growth of mammary tumors *in vivo*. To further study the effect of *Sirt5* loss in tumor progression to malignancy, we examined lung metastasis in MMTV-PyMT mice. Interestingly, we found that loss of *Sirt5* delays, but does not completely abolishes lung metastasis *in vivo*. Our study shows for the first time, that SIRT5 plays a role in metastasis, however further experiments needs to be performed to underlie the mechanism by which SIRT5 promotes metastasis *in vivo*.

Previous studies have reported that there are several proteins in major metabolic pathways that are targeted by succinylation and regulated by SIRT5 (Park *et al.* 2013; Radin, *et al.* 2013; Zhou *et al.* 2016; Xiangyun *et al.* 2017). Consistent with previous

work, *Sirt5* deficiency led to hypersuccinylation of 132 proteins in mammary tumor tissues, most of which play a role in major metabolic pathways. Among the top identified pathway enriched with hypersuccinylated proteins includes the TCA cycle. In the past years, it has been reported that acquired alterations in some enzymes of the TCA cycle have a pivotal role in carcinogenesis (Sajnani *et al.* 2017). IDH2, for example, has been recognized as a key enzyme that supports cancer cells anchorage independent growth by maintaining redox homeostasis (Jiang *et al.* 2016). Furthermore, recent works have shown that SIRT5 reduces cellular ROS production by activating IDH2 activity (Zhou *et al.* 2016). Here, we showed that depletion of SIRT5 induces hypersuccinylation of IDH2 in mammary tumors. Furthermore, loss of SIRT5 significantly impairs anchorage independent growth of cancer cells. We believe that SIRT5 promotes cancer cell proliferation under such conditions, in part by desuccinylating and activating IDH2. However, it should be pointed out that effects on other SIRT5-regulated pathways might also contribute to the inhibition of cancer growth and tumorigenesis. Other pathways, including, the respiratory electron transport and lipid metabolism, were also enriched with hypersuccinylated proteins. These pathways also contribute as sources of energy and macromolecule production in cells, and deregulation of enzyme involved in these metabolic pathways have been extensively associated with cancer cells malignant proliferation (Phan *et al.* 2014; Jiang *et al.* 2016). These data highlight the potential mechanisms whereby SIRT5 may impact tumorigenesis.

Several studies have also reported that *Sirt5* loss affects the expression levels of genes involved in different cellular processes (Lu *et al.* 2014; Lv *et al.* 2015). However, the mechanism by which SIRT5 regulates expression of these genes is still

undefined. Our RNA-seq data on mammary tumors showed that *Sirt5* depletion induces alteration of multiple genes, several of which are involved in inflammatory response and cytokine signaling. Among the identified genes, *Saa1* and *Saa2* were significantly reduced in *Sirt5*^{-/-} PyMT mammary tumors. *Saa* genes encode for a family of apolipoproteins, known as serum amyloid A (SAA). The SAA proteins are highly expressed in response to inflammation and accumulating evidence suggests that these proteins play an active role in inflammation by activating transcription factors, such as NF- κ B, influencing the lifespan of neutrophils and stimulating different immune cells (e.g. neutrophils and macrophages) to promote cell immunity (Urieli-Shoval *et al.* 2010; Eklund *et al.* 2012; Ye and Sun 2015). The level of SAA proteins in human blood severely increases in cancer and its expression are associated with poor prognosis (Yang, *et al.* 2016). Furthermore, most recent studies have shown that SAA also induces the expression of pro-inflammatory factors that potentiates the tumor growth and invasion (Ye and Sun 2015). Down-regulation of *Saa* upon *Sirt5* deletion has been previously reported in mice liver tissues after fasting (Yu *et al.* 2013). Our data, also supports the reported evidences and opens up the possibility of novel biological functions of SIRT5. Further experiments are needed to establish the mechanism by which *Sirt5* deletion induces down-regulation of *Saa*.

Given that complete *Sirt5* deletion in mice has anti-cancer effects in mammary tumorigenesis and modest effects in whole animals, pharmacological inhibition of SIRT5 represents an attractive therapeutic target. We have developed SIRT5 inhibitors and tested their anti-cancer effects *in vitro* and *in vivo*. SIRT5-selective inhibitor I5-2AM showed inhibition of cell viability and anchorage independent growth of

cancer cells. Furthermore, pharmacological inhibition of SIRT5 with I5-2AM resulted in a reduction of mammary tumor growth in PyMT mice while had no toxicity. Measurements of I5-2AM in blood and tissues showed short half-life, limiting the anti-cancer potential of inhibiting SIRT5 activity. We are currently developing novel SIRT5-selective inhibitors and testing their anticancer potentials.

In conclusion, this work provided strong evidence that SIRT5-mediated post-translational modification of metabolic enzymes regulates the transformed phenotype of cancer cells *in vitro* and mammary tumorigenesis *in vivo*. Together, this data highlights the potential therapeutic value of SIRT5 in cancer treatment.

2.6 SUPPLEMENTAL MATERIALS

Supplemental Materials

Supplemental Figure 2.1

Supplemental Figure 2.2

Supplemental Figure 2.3

Supplemental Figure 2.4

Supplemental Figure 2.5

Supplemental Figure 2.6

Supplemental Table 2.1

Supplemental Table 2.2

Supplemental Table 2.3

Supplemental Table 2.4

Supplemental Materials and Methods

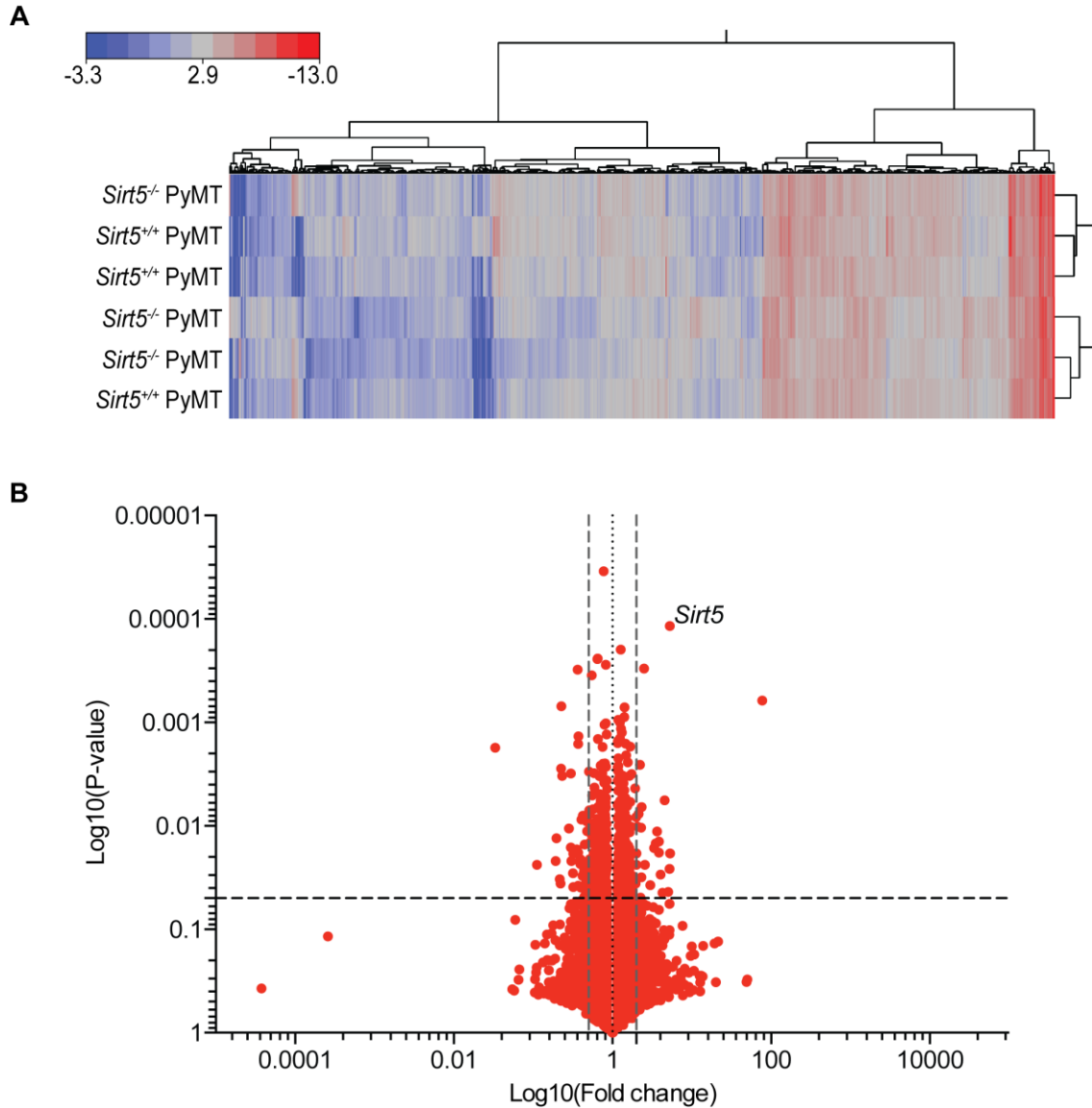
Soft agar assay for Supplemental Figure 2.2

For colony formation in semisolid medium, 10,000 MCF-7 cells were plated in 0.3% low-melting point agarose (LMP, Invitrogen) onto 6-well plate coated with 1.2% LMP mixed with 2X DMEM medium. For treatments, 2X inhibitor (100 μ M final concentration) was added to cells at the time of plating. The medium and inhibitor were replaced with fresh ones every 2-3 days. After 14 days of incubation, colonies were stained and pictured.

Cell viability assay for Supplemental Figure 2.2

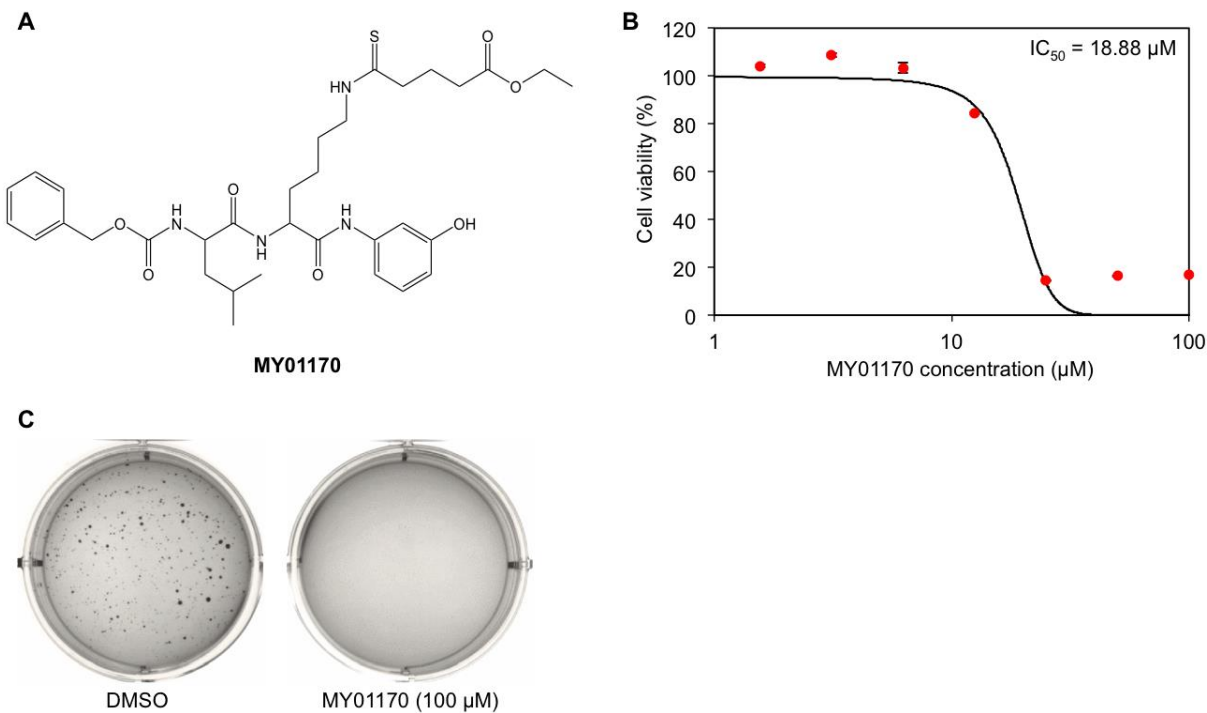
MCF-7 cells were seeded into 96-well plates at 3,000 cells per well. After 24 h, inhibitors were added in triplicates to cells at final concentrations ranging from 1 to 100 μ M. Cells were then incubated for 72 h and cell viability was measured using the CellTiter-Blue viability assay (Promega) following the manufacturer's instructions. Relative cell viability in the presence of the inhibitors was normalized to the control sample (DMSO treated) after background subtraction. GraphPad Prism software was used to determine the IC₅₀ values.

Supplemental Figures

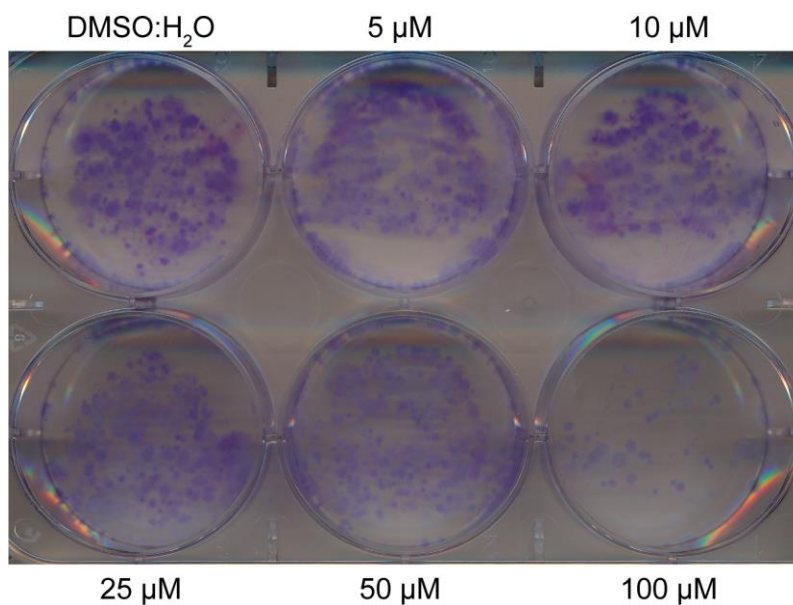


Supplemental Figure 2.1 Hierarchical clustering analysis and volcano plot for genes expressed in *Sirt5*^{+/+} PyMT and *Sirt5*^{-/-} PyMT mammary tumors. (A) Hierarchical clustering analysis of 1,620 variable genes detected in *Sirt5*^{+/+} PyMT and *Sirt5*^{-/-} PyMT mice. Log₂(FPKM) values were and Ward Method were used for the generation of the heatmap. **(B)** Volcano plot of 1,620 variable genes detected in *Sirt5*^{+/+}

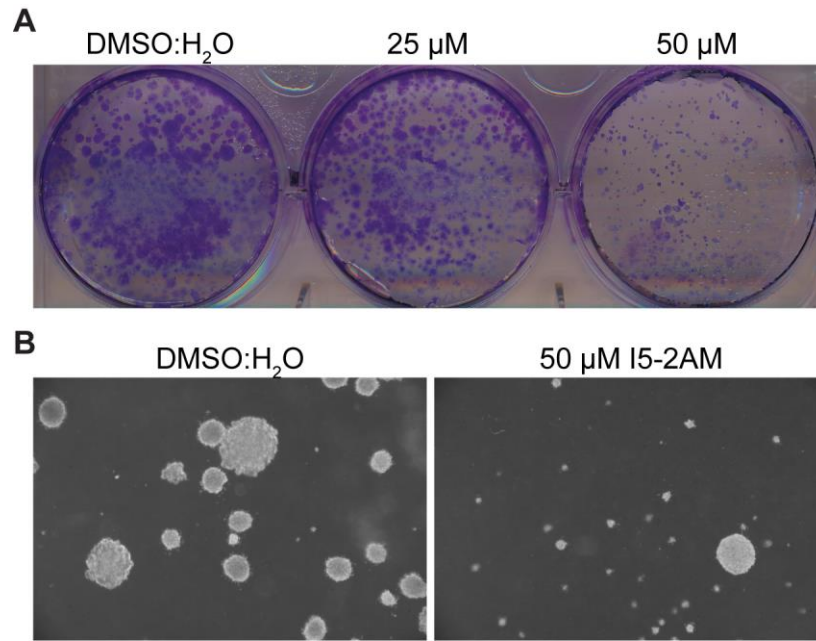
PyMT and *Sirt5*^{-/-} PyMT mice. Genes (red dots) above horizontal line showed p-value > 0.05. Genes to the extreme left and to the extreme right of the gray vertical lines showed a fold change > 2.



Supplemental Figure 2.2 Potential anti-cancer effects of another SIRT5-inhibitor, MY01170. (A) Structure of SIRT5 inhibitor, MY01170. **(B)** Cell viability of MCF-7 cells treated with different concentrations of MY01170 for 3 days. Cells were seeded into 96-well plates at 3,000 cells per well. After 24 h, inhibitors were added in triplicates to cells at final concentrations ranging from 1 to 100 µM. Cells were incubated for 72 hrs and cell viability was measured using the CellTiter-Blue viability assay (Promega) following the manufacturer's instructions. **(C)** Soft-agarose assay showing that inhibition of SIRT5 with MY01170 reduced the colony formation of MCF7 cells. MCF-7 cells were plated in 0.3% low-melting point agarose and coated with 1.2% LMP mixed with 2X DMEM medium. For treatments, 100 µM MY01170 was added to cells at the time of plating. The medium and inhibitor were replaced with fresh ones every 2-3 days. After 14 days of incubation, colonies were stained and pictured. Data provided by Sushabhan Sadhukhan.



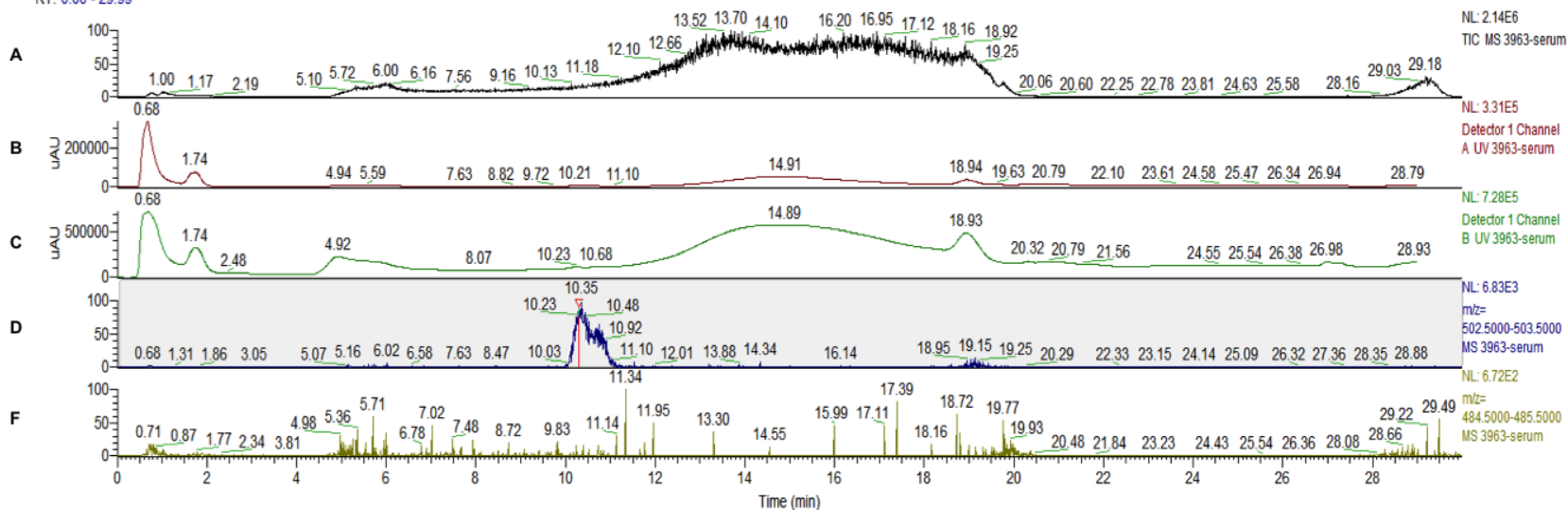
Supplemental Figure 2.3 Clonogenic assay performed on AT3 cells upon treatment with different concentrations of I5-2AM. Cells were seeded in six well plates. A day after, cells were treated with DMSO:H₂O, 5 μM, 10 μM, 25 μM 50 μM or 100 μM of I5-2AM for seven days. Cells were fixed with methanol and stained with Crystal Violet. A reduced number of colonies were observed at 100 μM of I5-2AM.



Supplemental Figure 2.4 Clonogenic assay and soft-agarose assay performed on HEK-293T cells upon treatment with different concentrations of I5-2AM. (A) For long-term survival assay, cells were seeded in six well plates. A day after, cells were treated with DMSO:H₂O, 5 μM, 10 μM, 25 μM 50 μM or 100 μM of I5-2AM for seven days. Cells were fixed with methanol and stained with Crystal Violet. A reduced number of colonies were observed at 50 μM of I5-2AM **(B)** Soft-agarose assay showing that selective inhibition of SIRT5 with I5-2AM reduced the colony formation of HEK-293T cancer cells.

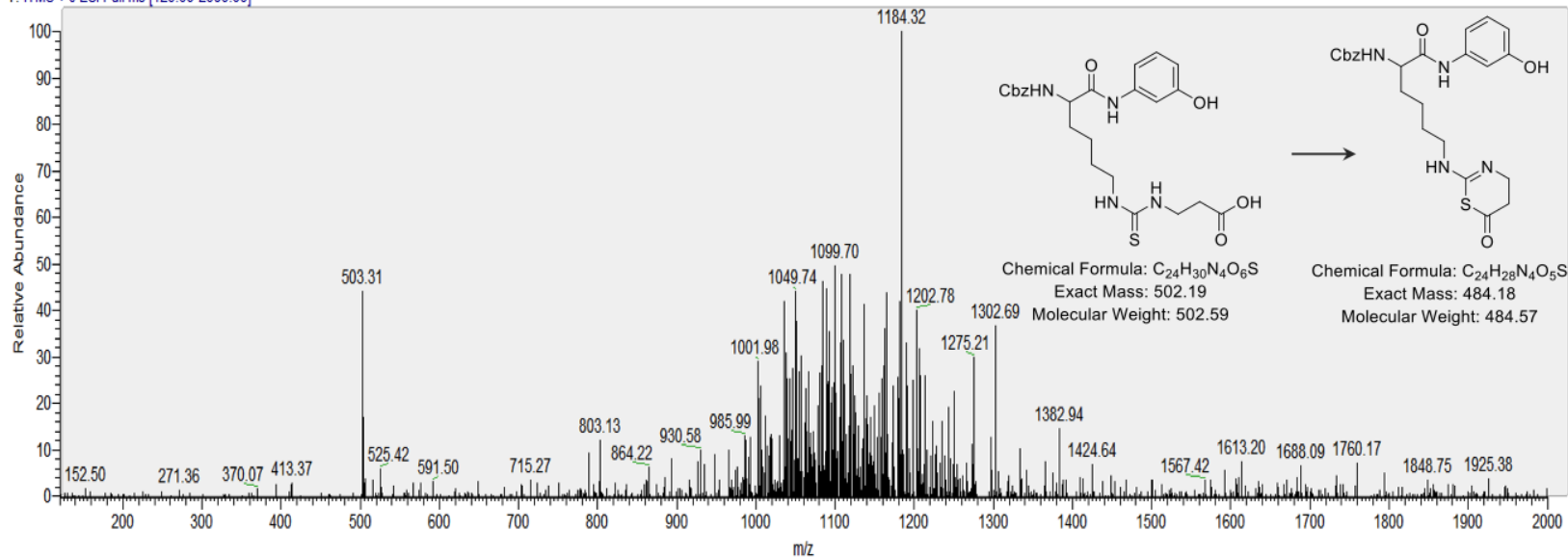
Serum-30 min

RT: 0.00 - 29.99



G 3963-serum #1110 RT: 10.28 AV: 1 NL: 9.22E3

T: ITMS + c ESI Full ms [120.00-2000.00]



Supplemental Figure 2.5 LC-MS data showing the presence of I5-2AM in the serum of I5-2AM-treated mouse after 30 minutes of I5-2AM-IP administration. Treated MMTV-PyMT mice were euthanized 30 minutes after performing the last injection of I5-2AM. Metabolites were extracted from blood serum using methanol. Supernatant was analyzed by LC-MS. **(A)** Mass trace from the whole sample. **(B-C)** UV traces using Channel 1 (254 nm) and Channel 2 (215 nm), respectively. **(D)** Mass trace for I5-2AM (peak observed at 10.35 RT). **(E)** Mass trace for the cyclized form of I5-2AM. **(F)** Chromatogram at 10.28 RT showing the relative abundance of I5-2AM in serum. The structure of I5-2AM (m/z 502.59) and its cyclized form (m/z 484.57) are shown at the bottom of image.

Supplemental Figure 2.6 LC-MS data showing the presence of I5-2AM in the fat of I5-2AM-treated mouse after 30 minutes of I5-2AM-IP administration. Treated MMTV-PyMT mice were euthanized 30 minutes after performing the last injection of I5-2AM. Metabolites were extracted from fat using methanol. Supernatant was analyzed by LC-MS. **(A)** Mass trace from the whole sample. **(B-C)** UV traces using Channel 1 (254 nm) and Channel 2 (215 nm), respectively. **(D)** Mass trace for I5-2AM (peak observed at 10.35 RT). **(E)** Mass trace for the cyclized form of I5-2AM. **(F)** Chromatogram at 10.28 RT showing the relative abundance of I5-2AM in fat. The structure of I5-2AM (m/z 502.59) and its cyclized form (m/z 484.57) are shown at the bottom of image.

Supplemental Tables

Supplemental Table 2.1 Histological classifications of mammary tumors into four distinctly identifiable stages of tumor progression.

Genotype	Tumor	Tumor Area				
		Hyperplasia	MIN	Early	Late	Total
<i>Sirt5</i> ^{+/+} PyMT	1	5	10	80	5	100
	2	5	40	55	0	100
	3	5	20	70	5	100
	4	5	30	65	0	100
	5	5	60	35	0	100
	6	10	70	20	0	100
	7	0	5	10	85	100
	8	5	70	25	0	100
	9	20	70	10	0	100
	10	5	40	30	25	100
	11	5	20	60	15	100
	12	10	85	5	0	100
	13	10	90	0	0	100
	14	5	40	40	15	100
	15	5	80	15	0	100
	16	5	30	40	25	100
	17	5	20	30	45	100

18	5	20	40	35	100
19	5	30	50	15	100
20	10	40	40	10	100
21	10	50	40	0	100
22	5	10	10	75	100
23	5	10	75	10	100
<hr/>					
Mean	7	41	37	16	100
±SD	±4	±26	±23	±24	±0
<hr/>					
1	0	10	30	60	100
2	5	40	55	0	100
3	5	5	5	85	100
4	5	60	35	0	100
5	30	70	0	0	100
6	10	90	0	0	100
7	5	40	50	5	100
8	0	10	10	80	100
9	5	60	35	0	100
10	10	90	0	0	100
11	10	50	40	0	100
12	10	90	0	0	100
13	20	80	0	0	100
14	5	80	15	0	100
15	5	10	40	45	100

Sirt5^{-/-}

PyMT

16	5	15	40	40	100
17	50	50	0	0	100
18	5	30	40	25	100
19	5	20	70	5	100
20	5	30	50	15	100
21	5	95	0	0	100
22	5	35	60	0	100
23	5	10	10	75	100
24	5	50	45	0	100
25	5	60	35	0	100
26	10	90	0	0	100
27	5	55	40	0	100
<i>Mean</i>	9	49	26	16	100
<i>±SD</i>	±10	±30	±23	±28	±0

* Four distinct categories were used to classify areas in the tumors (Lin *et al.* 2003).

Values correspond to the area of the tumor (in percent). Values in bold represent the largest area of the tumor featuring one of the four stages. Mean and standard deviation are shown in Bold-Italic.

Supplemental Table 2.2 List of all the succinylated proteins identified in the LC-MS analysis.

Description	Unique peptides	Peptides only	Peptides only	Peptides
		succinylated in Sirt5 ^{+/+} PyMT	succinylated in Sirt5 ^{-/-} PyMT	succinylated in both
hemoglobin subunit alpha	7	4	0	3
hemoglobin, beta adult s chain	5	2	0	3
10 kDa heat shock protein	8	0	6	2
serum albumin precursor	16	1	6	9
malate dehydrogenase	14	0	6	8
28S ribosomal protein S36	1	0	1	0
ATP synthase subunit d	3	1	1	1
ATP synthase subunit O	6	0	4	2
isocitrate dehydrogenase [NADP]	8	0	6	2
acyl-coenzyme A thioesterase 13	3	0	2	1
electron transfer flavoprotein subunit beta-like partial	3	0	3	0
isocitrate dehydrogenase [NAD]	9	0	8	1

glyceraldehyde-3-phosphate dehydrogenase isoform 2	6	0	4	2
acetyl-CoA acetyltransferase	8	0	7	1
methylglutaconyl-CoA hydratase	8	0	6	2
cytochrome c oxidase subunit 5B	1	0	1	0
aconitate hydratase	17	0	11	6
3-ketoacyl-CoA thiolase	6	0	3	3
dihydrolipoyl dehydrogenase	9	1	4	4
enoyl-CoA delta isomerase 1	5	0	2	3
creatine kinase M-type	6	0	6	0
serine hydroxymethyltransferase	5	0	3	2
peptidyl-prolyl cis-trans isomerase F	4	0	3	1
protein NipSnap homolog 2 isoform X1	5	0	5	0
methylmalonyl-CoA epimerase	2	0	2	0
proline synthase co-transcribed bacterial homolog protein				
isoform c	2	1	1	0
acyl-CoA-binding protein isoform 2	1	1	0	0

citrate synthase	9	2	7	0
hydroxyacyl-coenzyme A dehydrogenase	4	0	2	0
pterin-4-alpha-carbinolamine dehydratase 2	2	1	0	1
aspartate aminotransferase	6	0	2	4
ADP/ATP translocase 1	3	1	2	0
ES1 protein homolog	4	0	3	1
fumarate hydratase	6	0	4	2
succinyl-CoA ligase [ADP/GDP-forming]	5	0	5	0
ATP synthase subunit epsilon	1	0	1	0
ADP/ATP translocase 2	4	0	2	2
60 kDa heat shock protein	8	0	5	3
ATPase inhibitor	2	0	2	0
histidine triad nucleotide-binding protein 2	2	0	2	0
fructose-bisphosphate aldolase A isoform 2	2	0	2	0
stress-70 protein	9	0	7	2
trifunctional enzyme subunit alpha	9	0	9	0

grpE protein homolog 1	3	0	3	0
ATP synthase subunit alpha	8	1	6	1
electron transfer flavoprotein subunit alpha	1	0	1	0
copper transport protein ATOX1	1	0	0	1
elongation factor Tu	4	1	2	1
succinyl-CoA ligase [GDP-forming] subunit beta	2	0	2	0
phosphoglycerate mutase 2	2	0	2	0
single-stranded DNA-binding protein	2	0	2	0
NAD(P)H-hydrate epimerase isoform X1	1	0	0	1
enoyl-CoA delta isomerase 2	4	0	4	0
myoglobin	2	0	2	0
histone H2B type 3-A	1	0	1	0
enoyl-CoA hydratase	3	0	2	1
carbonyl reductase [NADPH] 2 isoform X1	1	0	0	1
citrate lyase beta like isoform X1	3	0	3	0
serotransferrin precursor	3	0	2	1

3-hydroxyacyl-CoA dehydrogenase type-2	2	0	2	0
NADH dehydrogenase	1	0	1	0
succinyl-CoA ligase [ADP-forming] subunit beta	4	0	4	0
peptidyl-prolyl cis-trans isomerase A	1	0	1	0
glutamate dehydrogenase 1	4	0	2	2
carbonic anhydrase 3	1	0	1	0
GTP:AMP phosphotransferase AK3	2	0	2	0
succinyl-CoA:3-ketoacid coenzyme A transferase 1	1	1	1	1
long-chain specific acyl-CoA dehydrogenase	3	0	2	1
trifunctional enzyme subunit beta	2	0	2	0
dihydrolipoyllysine-residue succinyltransferase component of 2-oxoglutarate dehydrogenase complex	5	1	4	0
3-hydroxyisobutyryl-CoA hydrolase	4	0	4	0
acyl-Coenzyme A dehydrogenase family, member 12 isoform X1	3	0	3	0
maleylacetoacetate isomerase isoform 2	1	0	1	0

succinate dehydrogenase [ubiquinone] flavoprotein subunit	4	0	4	0
estradiol 17-beta-dehydrogenase 8	1	0	1	0
39S ribosomal protein L12	3	0	3	0
beta-enolase	1	0	1	0
ATP synthase subunit beta	4	0	1	3
trans-2-enoyl-CoA reductase	1	0	1	0
myosin light chain 1/3, skeletal muscle isoform isoform 3f	1	0	1	0
cytochrome c, somatic	1	0	1	0
alpha-enolase	1	0	0	1
L-lactate dehydrogenase A chain isoform 1	2	0	2	0
protein DJ-1 isoform X1	1	0	1	0
actin, aortic smooth muscle isoform X1	1	0	0	1
28S ribosomal protein S9	1	0	1	0
glutaredoxin-related protein 5	1	0	1	0
lipoamide acyltransferase component of branched-chain	3	0	3	0
alpha-keto acid dehydrogenase complex				

very long-chain specific acyl-CoA dehydrogenase	3	0	3	0
persulfide dioxygenase ETHE1	1	0	1	0
putative RNA-binding protein Luc7-like 2 isoform X10	1	0	1	0
ATP synthase F(0) complex subunit B1	1	1	0	0
carnitine O-palmitoyltransferase 2	0	0	1	0
alpha-1-antitrypsin 1-4 precursor	2	1	1	0
apolipoprotein A-I preproprotein	1	0	0	1
28S ribosomal protein S26	1	0	1	0
pyruvate dehydrogenase E1 component subunit alpha	2	0	2	0
mitochondrial import inner membrane translocase subunit TIM44	1	0	1	0
carnitine O-acetyltransferase isoform X4	1	0	1	0
elongation factor Ts	1	0	1	0
thioredoxin reductase 2	0	0	0	1
aminomethyltransferase	1	0	1	0
2,4-dienoyl-CoA reductase	1	0	1	0

bisphosphoglycerate mutase	1	1	0	0
ubiquinone biosynthesis protein COQ9	0	0	1	0
monofunctional C1-tetrahydrofolate synthase	0	0	3	1
acyl-CoA dehydrogenase family member 9	1	0	1	0
D-2-hydroxyglutarate dehydrogenase	1	0	1	0
pyruvate dehydrogenase protein X component	2	0	2	0
lactamase, beta isoform X2	1	0	0	1
presequence protease	1	0	0	1
NADH dehydrogenase [ubiquinone] flavoprotein 3	1	0	1	0
acyl-CoA synthetase family member 2	1	0	0	1
STAM binding protein like 1 isoform X7	1	0	1	0
short/branched chain specific acyl-CoA dehydrogenase	1	0	1	0
propionyl-CoA carboxylase alpha chain	1	1	0	0
acyl-CoA synthetase family member 3	1	0	1	0
isoleucine--tRNA ligase	1	0	1	0
medium-chain specific acyl-CoA dehydrogenase	1	0	0	1

ubiquinone biosynthesis monooxygenase COQ6 isoform X2	1	0	1	0
ATP synthase subunit gamma	1	1	0	0
dihydrolipoyllysine-residue acetyltransferase component of pyruvate dehydrogenase complex	1	0	0	1
glutaminase kidney isoform	1	0	0	1
cytochrome b-c1 complex subunit 2	1	0	0	1
carbonyl reductase family member 4	1	0	1	0
alpha-aminoadipic semialdehyde dehydrogenase isoform b	1	1	0	0
acyl-coenzyme A thioesterase 9	1	0	1	0
probable arginine--tRNA ligase	1	0	1	0
delta(3,5)-Delta(2,4)-dienoyl-CoA isomerase	1	0	1	0
tyrosine--tRNA ligase	1	0	0	1
glutaryl-CoA dehydrogenase	1	0	1	0
calcium-binding mitochondrial carrier protein SCaMC-1	1	0	0	1
28S ribosomal protein S30	1	0	1	0
keratin, type I cytoskeletal 19	1	0	1	0

pyruvate carboxylase	2	0	2	0
secreted frizzled-related protein 1 precursor	1	1	0	0
spectrin beta chain, erythrocytic	1	0	1	0
cytochrome b-c1 complex subunit 1	1	0	0	1
methylmalonyl-CoA mutase	1	0	1	0
alpha-2-macroglobulin precursor	1	0	1	0
sporulation-specific protein 15	1	0	1	0
glycine--tRNA ligase	1	0	1	0
outer dense fiber protein 2 isoform c	1	0	1	0
axonemal dynein heavy chain isoform X5	1	0	1	0
NAD(P) transhydrogenase	1	1	0	0
fibrillin-1 precursor	1	0	1	0
myosin-4	1	0	1	0

Supplemental Table 2.3 List of significantly differential genes between *Sirt5*^{+/+} PyMT and *Sirt5*^{-/-} PyMT mice.

Entrez gene	Gene ID	Average <i>Sirt5</i> ^{+/+} PyMT (log ₂ (FPKM))	Average <i>Sirt5</i> ^{-/-} PyMT (log ₂ (FPKM))	Fold Change
110187	<i>Scgb2b26</i>	6	86	3.9
622127	<i>Cyp3a57</i>	0	3	3.2
235320	<i>Zbtb16</i>	1	5	2.4
57816	<i>Tesc</i>	6	30	2.4
14120	<i>Fbp2</i>	5	21	2.2
233099	<i>Scgb2b27</i>	467	2117	2.2
235135	<i>Tmem45b</i>	1	4	2.2
18162	<i>Npr3</i>	0	2	2.2
18667	<i>Pgr</i>	0	2	2.1
78284	<i>Creb3l4</i>	3	11	2.0
69387	<i>Dnajb13</i>	2	8	1.9
114479	<i>Slc5a5</i>	2	8	1.9
13034	<i>Ctse</i>	1	2	1.8

270192	<i>Rab6b</i>	1	5	1.7
55990	<i>Fmo2</i>	1	3	1.7
209588	<i>Sectm1a</i>	5	16	1.7
21386	<i>Tbx3</i>	1	2	1.6
433182	<i>Gm5506</i>	13	41	1.6
18227	<i>Nr4a2</i>	3	10	1.6
69863	<i>Ttc39b</i>	4	13	1.6
66805	<i>Tspan1</i>	10	30	1.6
30051	<i>Spdef</i>	11	31	1.5
20249	<i>Scd1</i>	167	472	1.5
18576	<i>Pde3b</i>	2	6	1.5
12023	<i>Barx2</i>	11	30	1.5
207592	<i>Tbc1d16</i>	1	4	1.5
15109	<i>Hal</i>	1	4	1.4
63954	<i>Rbp7</i>	48	127	1.4
19737	<i>Rgs5</i>	4	11	1.3

18627	<i>Per2</i>	5	13	1.3
170835	<i>Inpp5j</i>	4	9	1.3
234797	<i>6430548M08Rik</i>	4	9	1.2
14563	<i>Gdf5</i>	6	13	1.2
227618	<i>Lrrc26</i>	9	21	1.2
30806	<i>Adamts8</i>	3	7	1.2
12580	<i>Cdkn2c</i>	27	59	1.1
81879	<i>Tfcp2l1</i>	7	15	1.1
83397	<i>Akap12</i>	6	13	1.1
17064	<i>Cd93</i>	3	5	1.0
18600	<i>Padi2</i>	17	34	1.0
74413	<i>Tc2n</i>	8	15	1.0
23796	<i>Aplnr</i>	4	8	1.0
1908	<i>Prkar2b</i>	14	27	1.0
76551	<i>Ccdc6</i>	34	66	0.9
17341	<i>Bhlha15</i>	46	88	0.9

16776	<i>Lama5</i>	9	17	0.9
20856	<i>Stc2</i>	12	23	0.9
223775	<i>Pim3</i>	13	24	0.9
235380	<i>Dmxl2</i>	2	3	0.9
214137	<i>Arhgap29</i>	10	19	0.9
20530	<i>Slc31a2</i>	48	86	0.9
232023	<i>Vopp1</i>	15	27	0.9
97998	<i>Deptor</i>	22	41	0.9
13819	<i>Epas1</i>	8	15	0.8
26457	<i>Slc27a1</i>	23	41	0.8
69993	<i>Chn2</i>	13	23	0.8
14732	<i>Gpam</i>	7	12	0.8
58194	<i>Sh3kbp1</i>	11	18	0.8
18626	<i>Per1</i>	18	30	0.8
64209	<i>Herpud1</i>	35	59	0.8
94040	<i>Clmn</i>	12	20	0.7

22339	<i>Vegfa</i>	19	31	0.7
328329	<i>Mast4</i>	4	7	0.7
72108	<i>Ddhd2</i>	16	26	0.7
16529	<i>Kcnk5</i>	24	38	0.7
21413	<i>Tcf4</i>	9	14	0.7
14284	<i>Fosl2</i>	18	29	0.7
110351	<i>Rap1gap</i>	39	61	0.7
15926	<i>Idh1</i>	44	69	0.6
15980	<i>Ifngr2</i>	57	36	-0.7
70350	<i>Basp1</i>	183	116	-0.7
54353	<i>Skap2</i>	62	39	-0.7
269941	<i>Chsy1</i>	32	20	-0.7
67921	<i>Ube2f</i>	66	41	-0.7
16913	<i>Psmb8</i>	169	104	-0.7
51793	<i>Ddah2</i>	117	72	-0.7
12608	<i>Cebpb</i>	216	132	-0.7

20556	<i>Slfn2</i>	63	38	-0.7
56699	<i>Cdc42ep4</i>	46	28	-0.7
70186	<i>Fam162a</i>	156	94	-0.7
16832	<i>Ldhb</i>	140	83	-0.8
108655	<i>Foxp1</i>	8	5	-0.8
54366	<i>Cttnal1</i>	17	10	-0.8
70155	<i>Ogfrl1</i>	75	44	-0.8
108096	<i>Slco1a5</i>	27	15	-0.8
11980	<i>Atp8a1</i>	8	5	-0.8
13197	<i>Gadd45a</i>	57	32	-0.8
54725	<i>Cadm1</i>	19	11	-0.8
327959	<i>Xaf1</i>	16	9	-0.8
13640	<i>Efna5</i>	17	9	-0.8
19401	<i>Rara</i>	15	8	-0.9
16007	<i>Cyr61</i>	60	33	-0.9
18104	<i>Nqo1</i>	62	34	-0.9

225207	<i>Zfp521</i>	7	4	-0.9
385354	<i>Frmd7</i>	8	4	-0.9
69550	<i>Bst2</i>	233	126	-0.9
74319	<i>Mettl23</i>	37	20	-0.9
12709	<i>Ckb</i>	47	25	-0.9
18188	<i>Nrtn</i>	64	32	-1.0
16518	<i>Kcnj2</i>	6	3	-1.0
116701	<i>Fgfr1</i>	48	24	-1.0
19280	<i>Ptprs</i>	19	9	-1.0
83396	<i>Glis2</i>	6	3	-1.0
68957	<i>Paqr6</i>	17	8	-1.1
12587	<i>Mia</i>	90	42	-1.1
329252	<i>Lgr6</i>	18	9	-1.1
64075	<i>Smoc1</i>	63	29	-1.1
21938	<i>Tnfrsf1b</i>	8	4	-1.1
14164	<i>Fgf1</i>	15	6	-1.2

94346	<i>Tmem40</i>	22	10	-1.2
100038882	<i>Isg15</i>	133	55	-1.3
22419	<i>Wnt5b</i>	46	18	-1.3
19225	<i>Ptgs2</i>	4	1	-1.4
20208	<i>Saa1</i>	755	276	-1.5
217682	<i>Plekhd1</i>	15	5	-1.5
30937	<i>Lmcd1</i>	11	4	-1.6
12560	<i>Cdh3</i>	3	1	-1.6
69219	<i>Ddah1</i>	23	7	-1.6
229791	<i>D3Bwg0562e/Plp</i> <i>pr4</i>	7	2	-1.6
72027	<i>Slc39a4</i>	9	3	-1.6
16665	<i>Krt15</i>	7	2	-1.6
68010	<i>Bambi</i>	4	1	-1.6
226245	<i>Plekhs1</i>	8	3	-1.6
17304	<i>Mfge8</i>	847	264	-1.7

20209	<i>Saa2</i>	566	169	-1.7
19659	<i>Rbp1</i>	104	30	-1.8
56279	<i>Fam69b</i>	6	2	-1.8
18383	<i>Tnfrsf11b</i>	7	2	-1.9
434197	<i>Fam169b</i>	3	1	-2.0
99571	<i>Fgg</i>	29	7	-2.0
69938	<i>Scrn1</i>	4	1	-2.0
13406	<i>Dmp1</i>	18	4	-2.1
67573	<i>Loxl4</i>	2	0	-2.3
22373	<i>Wap</i>	148	29	-2.3
21956	<i>Tnnt2</i>	12	2	-2.4
18189	<i>Nrxn1</i>	2	0	-2.4
68346	<i>Sirt5</i>	15	3	-2.4
67547	<i>Slc39a8</i>	16	2	-2.8
192200	<i>Wfdc12</i>	51	7	-2.9
319169	<i>Hist1h2ak</i>	3	0	-10.0

Supplemental Table 2.4 List of GO Biological Pathways enriched with differential genes between *Sirt5*^{+/+} PyMT and *Sirt5*^{-/-} PyMT mice.

#Pathway ID	Pathway description	Gene count	FDR
GO.0048518	positive regulation of biological process	62	9.34E-08
GO.0048522	positive regulation of cellular process	55	8.30E-07
GO.0048519	negative regulation of biological process	51	1.25E-05
GO.0019222	regulation of metabolic process	62	1.58E-05
GO.0009893	positive regulation of metabolic process	44	2.21E-05
GO.0051239	regulation of multicellular organismal process	35	8.72E-05
GO.0050896	response to stimulus	59	1.54E-04
GO.0031325	positive regulation of cellular metabolic process	37	2.08E-04
GO.0009605	response to external stimulus	26	4.34E-04
GO.0031323	regulation of cellular metabolic process	53	4.34E-04
GO.0044700	single organism signaling	43	4.34E-04
GO.0048523	negative regulation of cellular process	44	4.34E-04
GO.0050793	regulation of developmental process	31	4.34E-04

GO.0051716	cellular response to stimulus	50	4.39E-04
GO.0007165	signal transduction	41	4.91E-04
GO.0007154	cell communication	43	7.54E-04
GO.0009892	negative regulation of metabolic process	32	7.54E-04
GO.0030154	cell differentiation	39	7.54E-04
GO.0042221	response to chemical	35	7.54E-04
GO.0044763	single-organism cellular process	78	1.12E-03
GO.0050794	regulation of cellular process	71	1.12E-03
GO.0060591	chondroblast differentiation	3	1.32E-03
GO.0048513	organ development	35	1.62E-03
GO.0009888	tissue development	25	1.97E-03
GO.0044767	single-organism developmental process	49	1.97E-03
GO.0048731	system development	41	1.97E-03
GO.0010646	regulation of cell communication	32	2.95E-03
GO.0031328	positive regulation of cellular biosynthetic process	25	3.42E-03
GO.0060541	respiratory system development	9	3.66E-03

GO.0031324	negative regulation of cellular metabolic process	28	4.30E-03
GO.0001501	skeletal system development	12	4.46E-03
GO.0050789	regulation of biological process	71	5.31E-03
GO.0042127	regulation of cell proliferation	21	7.12E-03
GO.0007275	multicellular organismal development	43	7.64E-03
GO.0048469	cell maturation	7	7.74E-03
GO.0048608	reproductive structure development	11	8.55E-03
GO.0051173	positive regulation of nitrogen compound metabolic process	24	8.75E-03
GO.0061458	reproductive system development	11	8.75E-03
GO.0048583	regulation of response to stimulus	33	9.38E-03
GO.0010033	response to organic substance	26	9.79E-03
GO.0000052	citrulline metabolic process	3	1.02E-02
GO.0031326	regulation of cellular biosynthetic process	37	1.02E-02
GO.0045893	positive regulation of transcription, DNA-templated	21	1.02E-02
GO.0048584	positive regulation of response to stimulus	23	1.02E-02
GO.0051216	cartilage development	7	1.02E-02

GO.0065007	biological regulation	72	1.02E-02
GO.0065009	regulation of molecular function	29	1.02E-02
GO.0030855	epithelial cell differentiation	12	1.09E-02
GO.0010647	positive regulation of cell communication	21	1.10E-02
GO.0023051	regulation of signaling	29	1.10E-02
GO.0080090	regulation of primary metabolic process	46	1.33E-02
GO.2000026	regulation of multicellular organismal development	22	1.33E-02
GO.0044707	single-multicellular organism process	48	1.39E-02
GO.0045944	positive regulation of transcription from RNA polymerase II	17	1.41E-02
GO.0032101	regulation of response to external stimulus	14	1.42E-02
GO.0044092	negative regulation of molecular function	16	1.42E-02
GO.0010605	negative regulation of macromolecule metabolic process	26	1.63E-02
GO.0048856	anatomical structure development	42	1.71E-02
GO.0009653	anatomical structure morphogenesis	26	1.76E-02
GO.0009966	regulation of signal transduction	26	1.76E-02
GO.0006950	response to stress	30	1.86E-02

GO.0032879	regulation of localization	26	1.86E-02
GO.0032269	negative regulation of cellular protein metabolic process	15	2.03E-02
GO.0045935	positive regulation of nucleobase-containing compound	22	2.03E-02
GO.0010604	positive regulation of macromolecule metabolic process	29	2.16E-02
GO.0048468	cell development	21	2.16E-02
GO.1900744	regulation of p38MAPK cascade	3	2.16E-02
GO.0009987	cellular process	84	2.21E-02
GO.0006357	regulation of transcription from RNA polymerase II promoter	22	2.23E-02
GO.0050790	regulation of catalytic activity	24	2.30E-02
GO.0010628	positive regulation of gene expression	22	2.33E-02
GO.0030968	endoplasmic reticulum unfolded protein response	4	2.33E-02
GO.0043086	negative regulation of catalytic activity	13	2.52E-02
GO.0034620	cellular response to unfolded protein	4	2.72E-02
GO.0030324	lung development	7	2.83E-02
GO.0033554	cellular response to stress	19	2.94E-02
GO.0030323	respiratory tube development	7	2.98E-02

GO.0030852	regulation of granulocyte differentiation	3	2.98E-02
GO.0051094	positive regulation of developmental process	17	2.98E-02
GO.0060429	epithelium development	16	2.98E-02
GO.0072358	cardiovascular system development	14	2.98E-02
GO.0072359	circulatory system development	14	2.98E-02
GO.0009991	response to extracellular stimulus	10	3.18E-02
GO.0097167	circadian regulation of translation	2	3.18E-02
GO.0060255	regulation of macromolecule metabolic process	44	3.41E-02
GO.0061448	connective tissue development	7	3.53E-02
GO.0060411	cardiac septum morphogenesis	4	3.72E-02
GO.0009967	positive regulation of signal transduction	17	3.83E-02
GO.0030155	regulation of cell adhesion	11	3.84E-02
GO.0071456	cellular response to hypoxia	5	4.00E-02
GO.0033993	response to lipid	13	4.05E-02
GO.0045444	fat cell differentiation	5	4.08E-02
GO.0001817	regulation of cytokine production	10	4.29E-02

GO.0001525	angiogenesis	8	4.41E-02
GO.0048738	cardiac muscle tissue development	6	4.44E-02
GO.0006082	organic acid metabolic process	13	4.66E-02
GO.0023056	positive regulation of signaling	18	4.66E-02
GO.0044093	positive regulation of molecular function	19	4.66E-02
GO.0051270	regulation of cellular component movement	12	4.66E-02
GO.0030334	regulation of cell migration	11	4.73E-02

2.7 REFERENCES

- Bringman-Rodenbarger LR, Guo AH, Lyssiotos CA, Lombard DB. Emerging roles for SIRT5 in metabolism and cancer. *Antioxid. Redox Signal.* 2017; 46(9):429-438.
- Broad Institute of MIT and Harvard. Retrieved from <https://portals.broadinstitute.org/ccle>.
- Cardiff RD, Anver MR, Gusterson BA, Hennighausen L, Jensen RA, Merino MJ, Rehm S, Russo J, Tavassoli FA, Wakefield LM, Ward JM, Green JE. The mammary pathology of genetically engineered mice: the consensus report and recommendations from the Annapolis meeting. *Oncogene.* 2000; 19:968-988.
- Cho WCS, Yip TT, Cheng WW, Au JSK. Serum amyloid A is elevated in the serum of lung cancer patients with poor prognosis. *Br. J. Cancer.* 2010; 102(12):1731-1735.
- Du J, Zhou Y, Su X, Yu J, Khan S, Jiang H, Kim J, Woo J, Kim J, Choi B, He B, Chen W, Zhang S, Cerione R, Auwerx J, Hao Q, Lin H. Sirt5 is an NAD-dependent protein lysine demalonylase and desuccinylase. *Science.* 2011; 334:806-809.
- Eklund KK, Niemi K, Kovanen PT. Immune functions of serum amyloid A. *Crit. Rev. Immunol.* 2012; 32(4):335-348.
- Ferlay J, Soerjomataram I, Dikshit R, Eser S, Mathers C, Rebelo M, Maxwell Parkin D, Forman D, Bray F. Cancer incidence and mortality worldwide: Sources, methods and major patterns in GLOBOCAN 2012. *Int. J. Cancer.* 2015; 136:E359-E386.
- Gao J, Aksoy BA, Dogrusoz U, Dresdner G, Gross B, Sumer SO, Sun Y, Jacobsen A, Sinha R, Larsson E, Cerami E, Sander C, Schultz N. Integrative analysis of complex cancer genomics and clinical profiles using the cBioPortal. *Sci. Signal.*

2013; 6(269):p11.

Guy CT, Cardiff RD, Muller WJ. Induction of mammary tumors by expression of polyomavirus middle T oncogene: a transgenic mouse model for metastatic disease. *Mol. Cell Biol.* 1992; 12(3):954-961.

Gyorffy B, Lanczky A, Eklund AC, Denkert C, Budczies J, Li Q, Szallasi Z. An online survival analysis tool to rapidly assess the effect of 22,277 genes on breast cancer prognosis using microarray data of 1809 patients. *Breast Cancer Res. Treatment.* 2010; 123(3):725-731.

He W, Newman JC, Wang MZ, Ho L, Verdin E. Mitochondrial sirtuins: regulators of protein acylation and metabolism. *Trends in Endocrinol. and Metabol.* 2012; 23(9): 467-476.

Herschkowitz JI, Simin K, Weigman VJ, Mikaelian I, Usary J, Hu Z, Rasmussen KE, Jones LP, Assefnia S, Chandrasekharan S, Backlund MG, Yin Y, Khramtsov AI, Bastein R, Quackenbush J, Glazer RI, Brown PH, Green JE, Kopelovich L, Furth PA, Palazzo JP, Olopade OI, Bernard PS, Churchill GA, Van Dyke T, Perou CM. Identification of conserved gene expression features between murine mammary carcinoma models and human breast tumors. *Genome Biol.* 2007; 8:R76.

Hirschey MD, Zhao Y. Metabolic Regulation by Lysine Malonylation, Succinylation, and Glutarylation. *Mol. Cell Proteomics.* 2015; 14(9):2308-2315.

Houtkooper RH, Pirinen E, Auwerx J. Sirtuins as regulators of metabolism and healthspan. *Nature Rev. Mol. Cell Biol.* 2012; 13:225-238.

Jackson EL, Willis N, Mercer K, Bronson RT, Crowley D, Montoya R, Jacks T, Tuveson DA. Analysis of lung tumor initiation and progression using conditional

- expression of oncogenic K-ras. *Genes Dev.* 2001; 15:3243-3248.
- Jiang L, Shestov AA, Swain P, Yang C, Parker SJ, Wang QA, Terada LS, Adams ND, McCabe MT, Pietrak B, Schmidt S, Metallo CM, Dranka BP, Schwartz B, DeBerardinis R. Reductive carboxylation supports redox homeostasis during anchorage-independent growth. *Nature.* 2016; 532(7598):255-258.
- Karve TM, Cheema AK. Small Changes Huge Impact: The Role of Protein Posttranslational Modifications in Cellular Homeostasis and Disease. *Journal of Amino Acids.* 2011; 207691.
- Kim D, Pertea G, Trapnell C, Pimentel H, Kelley R, Salzberg SL. TopHat2: accurate alignment of transcriptomes in the presence of insertions, deletions and gene fusions. *Genome Biology.* 2013; 14:R36.
- Kroemer G, Pouyssegur J. Tumor cell metabolism: cancer's Achilles' heel. *Cancer Cell.* 2008; 13:472-482.
- Lee JJ, Herrera KNG, Haigis MC. Sirtuins in Cancer-Emerging Role as Modulators of Metabolic Reprogramming. *Sirtuins. Proteins and Cell Regulation*, Springer, Dordrecht. 2016; 10:171-190.
- Lin EY, Jones JG, Li P, Zhu L, Whitney KD, Muller WJ, Pollard JW. Progression to malignancy in the polyoma middle T oncoprotein mouse breast cancer model provides a reliable model for human diseases. *Am. J. Pathol.* 2003; 163:2113-2126.
- Lu W, Zuo Y, Feng Y, Zhang M. SIRT5 facilitates cancer cell growth and drug resistance in non-small cell lung cancer. *Tumor Biol.* 2014; 35(11):10699-10705.
- Lunt SY, Vander V. Aerobic glycolysis: meeting the metabolic requirements of cell

- proliferation. *Annu. Rev. Cell Dev. Biol.* 2011; 27:441-464.
- Lv XB, Liu L, Cheng C, Yu B, Xiong L, Hu K, Tang J, Zeng L, Sang Y. SUN2 exerts tumor suppressor functions by suppressing the Warburg effect in lung cancer. *Sci. Rep.* 2015; 5:17940.
- Malle E, Steinmetz A, Raynes JG. Serum amyloid A (SAA): an acute phase protein and apolipoprotein. *Atherosclerosis.* 1993; 102(2):131-146.
- Martin M. Cutadapt removes adapter sequences from high-throughput sequencing reads. *EMBnet.journal.* 2011; 17:10-12.
- Ouaissi M, Sielezneff I, Silvestre R, Sastre B, Bernard JP, Lafontaine JS, Payan MJ, Dahan L, Pirrò N, Seitz JF, Mas E, Lombardo D, Ouaisi A. High histone deacetylase 7 (HDAC7) expression is significantly associated with adenocarcinomas of the pancreas. *Ann. Surg. Oncol.* 2008; 15(8):2318-2238.
- Park J, Chen J, Tishkoff D, Peng C, Tan M, Dai L, Xie Z, Zhan Y, Zwaans B, Skinner M, Lombard D, Zhao Y. SIRT5-Mediated Lysine Desuccinylation Impacts Diverse Metabolic Pathways *Mol. Cell.* 2013; 50:919-930.
- Phan LM, Yeung SCJ, Lee MH. Cancer metabolic reprogramming: importance, main features, and potentials for precise targeted anti-cancer therapies. *Cancer Biol. Med.* 2014; 11(1):1-19.
- Plante I, Stewart MK, Laird DW. E valuation of Mammary Gland Development and Function in Mouse Models. *J. Vis. Exp.* 2011; 53:e2828.
- Rardin MJ, He W, Nishida Y, Newman JC, Carrico C, Danielson SR, Guo A, Gut P, Sahu AK, Li B, Uppala R, Fitch M, Riiff T, Zhu L, Zhou J, Mulhern D, Stevens RD, Ilkayeva OR, Newgard CB, Jacobson MP, Hellerstein M, Goetzman ES,

- Gibson BW, Verdin E. SIRT5 regulates the mitochondrial lysine succinylome and metabolic networks. *Cell Metab.* 2013; 18:920-933.
- Sadhukhan S, Liu X, Ryu D, Nelson OD, Stupinski JA, Li Z, Chen W, Zhang S, Weiss RS, Locasale JW, Auwerx J, Lin H. Metabolomics-assisted proteomics identifies succinylation and SIRT5 as important regulators of cardiac function. *Proc. Natl. Acad. Sci. USA.* 2016; 113:4320-4325.
- Sajnani K, Islam F, Smith RA, Gopalan V, Lam AK. Genetic alterations in Krebs cycle and its impact on cancer pathogenesis. *Biochimie.* 2017; 135:164-172.
- Sun JY, Xu L, Tseng H, Ciccarelli B, Fulciniti M, Hunter ZR, Maghsoudi K, Hatjiharissi E, Zhou Y, Yang G, Zhu B, Liu X, Gong P, Ioakimidis L, Sheehy P, Patterson CJ, Munshi NC, O'Connor OA, Treon SP. Histone deacetylase inhibitors demonstrate significant preclinical activity as single agents, and in combination with bortezomib in Waldenstrom's macroglobulinemia. *Clin. Lymphoma Myeloma Leuk.* 2011; 11:152-156.
- Trapnell C, Hendrickson D, Sauvageau M, Goff L, Rinn JL, Pachter L. Differential analysis of gene regulation at transcript resolution with RNA-seq. *Nature Biotechnology.* 2013, 31:46-53.
- Urieli-Shoval S, Finci-Yeheskel Z, Dishon S, Galinsky D, Linke RP, Ariel I, Levin M, Ben-Shachar I, Prus D. Expression of Serum Amyloid A in Human Ovarian Epithelial Tumors: Implication for a Role in Ovarian Tumorigenesis. *J. Histochem. Cytochem.* 2010; 58(11):1015-1023.
- Wang JY, Zheng YZ, Yang J, Lin YH, Dai SQ, Zhang G, Liu WL. Elevated levels of serum amyloid A indicate poor prognosis in patients with esophageal squamous

- cell carcinoma. *BMC Cancer*. 2012; 12:365.
- Warburg O. On the origin of cancer cell. *Science*. 1925; 123:309-314.
- Wise DR, Ward PS, Shay JE, Cross JR, Gruber JJ, Sachdeva UM, Platt JM, De Matteo RG, Simon MC, Thompson CB. Hypoxia promotes isocitrate dehydrogenase-dependent carboxylation of alpha-ketoglutarate to citrate to support cell growth and viability. *Proc. Natl. Acad Sci. USA*. 2011; 108:19611-19616.
- Xiangyun Y, Xiaomin N, Linping G, Yunhua X, Ziming L, Yongfeng Y, Zhiwei C, Shun L. Desuccinylation of pyruvate kinase M2 by SIRT5 contributes to antioxidant response and tumor growth. *Oncotarget*. 2017; 8:6984-6993.
- Yang M, Liu F, Higuchi K, Sawashita J, Fu X, Zhang L, Zhang L, Fu L, Tong Z, Higuchi K. Serum amyloid A expression in the breast cancer tissue is associated with poor prognosis. *Oncotarget*. 2016; 7(24):35843-35852.
- Ye RD, Sun L. Emerging functions of serum amyloid A in inflammation. *J. Leukoc. Biol*. 2015; 98(6):923-929.
- Yu J, Sadhukhan S, Noriega LG, Moullan N, He B, Weiss RS, Lin H, Schoonjans K, Auwerx J. Metabolic Characterization of a Sirt5 deficient mouse model. *Sci.Rep*. 2013; 3:2806.
- Zhou L, Wang F, Sun R, Chen X, Zhang M, Xu Q, Wang Y, Wang S, Xiong Y, Guan KL, Yang P, Yu H, Ye D. SIRT5 promotes IDH2 desuccinylation and G6PD deglutarylation to enhance cellular antioxidant defense. *EMBO Rep*. 2016; 17:811-822.
- Zhu M, Weiss RS. Increased Common Fragile Site Expression, Cell Proliferation Defects, and Apoptosis following Conditional Inactivation of Mouse Hus1 in

Primary Cultured Cells. Mol. Biol. Cell; 2007; 18:1044-1055.

CHAPTER 3. EVALUATING THE EFFECT OF *SIRT5* LOSS IN LYMPHOMAGENESIS

Author Contributions

Yashira L. Negrón Abril generated all or partial data for the following figures of

Chapter 3:

Figure 3.1

Figure 3.2

Figure 3.3

Figure 3.4

Authors Contribution

Figure 3.1A Sushabhan Sadhukhan

3.1 ABSTRACT

Aberrant activation of c-MYC oncogene induces cancer cell dependency on glutamine metabolism for their survival and enhanced proliferation. Clinically, *MYC* overexpression is associated to poor disease outcome in B-cell lymphoma patients, highlighting the need to identify molecular mechanisms that can suppress glutamine usage in these cancers. Recently, it was reported that the mitochondrial sirtuin, SIRT5 modulates ammonia-induced autophagy and survival in cancer cells by controlling glutamine metabolism, suggesting that it might have therapeutic potential for treating glutamine-dependent cancers; such as B-cell lymphoma. To investigate the importance of SIRT5-regulated post-translational modifications in lymphomagenesis, we generated a mouse model in which *Sirt5* is knocked out and c-Myc is constitutive activated. E μ -*Myc* transgenic mice overexpress *Myc* under the control of the immunoglobulin heavy chain gene enhancer (E μ), resulting in the development of pre-B and B-cell lymphoma. Our data revealed that deletion of *Sirt5* had no effect on lymphoma incidence and progression. Both, *Sirt5*^{+/+} E μ -*Myc* and *Sirt5*^{-/-} E μ -*Myc* mice showed signs of illness at similar ages and analysis of tumor tissues did not show any difference in size or histological grade. Interestingly, immunoblotting for succinyl lysine revealed multiple proteins with elevated succinylation in tumors from *Sirt5*^{-/-} E μ -*Myc* mice, and liquid chromatography-mass spectrometry (LC-MS) analysis identified many metabolic enzymes that were highly succinylated in *Sirt5*^{-/-} E μ -*Myc* thymic tumors, including aconitate hydratase, malate dehydrogenase, isocitrate dehydrogenase, fumarate hydratase and multiple subunits of ATP synthase. Together, these data show that

SIRT5-mediated post-translational modification of key metabolic enzymes is not essential for lymphomagenesis.

3.2 INTRODUCTION

B cell lymphoma comprises around 80% of cases of Non Hodgkin's lymphoma and is the seventh leading cancer in females and males in the U.S. (Siegel *et al.* 2012). In recent years, multiple studies have shown that dysregulation of *c-MYC* is essential in the pathogenesis of a number of B-cell lymphomas, including Burkitt lymphoma (BL) and diffuse large B-cell lymphoma (DLBCL) (Green *et al.* 2012; Cattoretti 2013). Dysregulation of *c-MYC*, together with other prognostic factors, confers proliferation and survival advantages in lymphoma cells, and therefore a poor prognosis.

Growing evidence suggest that activation of *c-MYC* oncogene reprograms cancer cell metabolism (Dang 2013). *MYC* regulates multiple metabolic pathways including glycolysis, lipid synthesis and glutamine metabolism (Muñoz-Pinedo *et al.* 2012; Le *et al.* 2012; Boroughs and DeBerardinid 2015). Activation of *c-MYC* in B-cell lymphoma induces cellular dependence on glutamine as an important biosynthetic and bioenergetic source for cell growth and survival (Wise and Thompson 2010; Dang 2013). Furthermore, *MYC*-induced glutaminolysis supports the production of NADPH and glutathione, which are two major antioxidants in the cell (DeBerardinis *et al.* 2007; Gao *et al.* 2010).

Recent reports have shown that generation of ammonia from glutaminolysis could potentially promote autophagy activation (Eng, *et al.* 2010; Cheong *et al.* 2011). Autophagy in cancer seems to have dual role. In some settings, it serves as a tumor suppressive pathway, by limiting oxidative stress-mediated oncogenic mutations (Mathew *et al.* 2009; Takamura *et al.* 2011). In other settings, autophagy supports cancer cell survival by providing nutrients and suppressing apoptosis (Guo *et al.*

2011; Altman *et al.* 2011). Recently, it was reported that one member of the Sirtuin family, SIRT5, modulates ammonia-induced autophagy and survival in cancer cells by controlling glutamine metabolism (Polleta *et al.* 2015). SIRT5 is the only known mitochondrial sirtuin that has strong desuccinylase, demalonylase and deglutarylase activity (Du *et al.* 2011; Tan *et al.* 2014). SIRT5 inactivates glutaminase (GLS2), thereby reducing the levels of glutamate and ammonia production. SIRT5 also promotes ammonia detoxification by activating carbamoyl phosphate synthase 1 (CPS1), the rate-limiting enzyme of the urea cycle. Given the relative contributions of SIRT5 in glutaminolysis, we hypothesized that SIRT5 is essential to tune ammonia-induced autophagy to the specific needs of cancer cells.

In this study, we examined the tumor modulatory role of SIRT5 in lymphomagenesis by using a genetic mouse model in which *Sirt5* is knocked out and *c-Myc* is constitutive activated. Unexpectedly, SIRT5 loss in E μ -*Myc* transgenic mice did not affect lymphoma incidence and mortality, even though it targets multiple key metabolic enzymes. Together, these data suggest that SIRT5-regulated posttranslational modification of metabolic enzymes is not essential for the metabolic reprogramming in *Myc*-induced murine B-cell lymphoma.

3.3 MATERIALS AND METHODS

Animals

Sirt5 transgenic mice were obtained from Johan Auwerx (Yu *et al.* 2013). These mice were backcrossed with C57BL/6 mice. E μ -*Myc* transgenic mice (catalogue name, C57BL/6J-Tg(IghMyc)22Bri/J) were purchased from The Jackson Laboratory (Adams *et*

al. 1985). Eμ-*Myc* transgenic mice were crossed with *Sirt5*^{+/-} mice to obtain *Sirt5*^{+/-} Eμ-*Myc* offspring. *Sirt5*^{+/-} Eμ-*Myc* mice were then bred with *Sirt5*^{+/-} mice to generate littermates that were *Sirt5*^{+/+} Eμ-*Myc* and *Sirt5*^{-/-} Eμ-*Myc*.

Genotyping

Genotyping was performed by polymerase chain reaction (PCR) amplification using allele-specific primers and genomic DNA extracted from mouse-tails. Identification of the Eμ-*Myc* transgene was detected using the following Eμ-*Myc* primers:

(F) 5'-TTAGACGTCAGGTGGCACTT-3'

(R) 5'-TGAGCAAAAACAGGAAGGCA-3'

PCR reaction conditions were 94 °C (5 minutes), followed by 30 cycles of 94 °C (20 seconds), 65 °C (30 seconds), 72 °C (1 minute), and 72 °C (10 minutes). Identification of the *Sirt5* genotype was performed using the following *Sirt5* primers:

5'-CTTGAGCAGAAAACCCACAGAGGAGAGAAC-3',

5'-GTGTATAGTTGTGTGCTGTGTGCTTGTAC-3'

5'-GGGAAAGATCTGGGGTTGGAATTTACC-3'

PCR reaction conditions were 95 °C (5 minutes), followed by 30 cycles of 95 °C (30 seconds), 64.6 °C (30 seconds), 72 °C (1 minute), and 72 °C (7 minutes).

Monitoring tumor development and tissue collection

Sirt5^{+/+} Eμ-*Myc* and *Sirt5*^{-/-} Eμ-*Myc* mice were weighed and monitored twice weekly after birth for tumors and signs of illness. Only mice showing enlarged lymphoid organs at necropsy were designated as having lymphomas. When experimental mice

met the endpoint criteria, mice were euthanized by CO₂ asphyxiation. Enlarged thymus, spleen and lymph nodes were dissected and weighed. Lymph nodes collected include cervical, axillary, brachial and inguinal lymph nodes. Tumors and other tissues were collected, fixed with 4% paraformaldehyde (PFA), embedded in paraffin, sectioned, and stained with hematoxylin and eosin (H&E). H&E-stained sections were scanned using an Aperio ScanScope and analyzed by a veterinarian certified in anatomic pathology by the American College of Veterinary Pathologists blinded to treatment group. Tumor tissues and organs were snap frozen in liquid N₂ and stored at -80 °C for subsequent analyses.

Immunoblot analysis

Tissue extracts were prepared using lysis buffer (50 mM Tris-HCl, pH 8.0, 150 mM NaCl, 1 mM EDTA, 1% Nonidet P-40, 5 mM nicotinamide) supplemented with protease and phosphatase inhibitors. Tissues were homogenized in a tissue homogenizer. The lysates were centrifuged at 20,000 × *g* for 30 min at 4 °C to remove the cell debris. Protein concentration of the supernatant was measured using the Bradford method. Fifty micrograms of protein were loaded and separated on 10% polyacrylamide gel and transferred to PVDF membrane (Perkin Elmer). The membrane was blocked using 5% BSA or milk in TBST (25 mM Tris-HCl, pH 7.4, 150 mM NaCl, and 0.1% Tween-20), incubated with Rabbit pan-specific antisuccinyllysine (PTM-401, PTM Biolabs) or SIRT5 rabbit monoclonal antibody (8782, Cell Signaling) antibody antibodies. Chemiluminescent signal was detected on a VersaDoc Imaging system and quantified using Quantity One software (Bio-Rad Laboratories).

Nano LC/MS-MS

Frozen powdered thymic lymphomas from *Sirt5*^{+/+} E μ -Myc and *Sirt5*^{-/-} E μ -Myc mice were homogenized and lysed as previously described (Sadhukhan *et al.* 2016). One milligram of total protein from *Sirt5*^{+/+} E μ -Myc and *Sirt5*^{-/-} E μ -Myc tumor samples was digested with trypsin and labeled with light and heavy dimethyl groups, respectively. The isotopically labeled peptides were mixed and enriched using antisuccinyllysine antibody as described by Sadhukhan *et al.* (Sadhukhan *et al.* 2016). Identification and quantification of succinyl-lysine peptides were analyzed by Nano LC-MS/MS as described by Sadhukhan *et al.* (Sadhukhan *et al.* 2016).

3.4 RESULTS

3.4.1 Reduced succinylation levels are observed in multiple proteins in thymic lymphoma when compared with normal thymus tissue in mice

Overexpression of *Sirt5* has been reported in multiple cancer types. In Chapter 2, we demonstrated that *Sirt5* deletion reduces breast cancer growth and mammary tumorigenesis. To identify other tumor types that might become susceptible to *Sirt5* deletion, we investigated the status of protein lysine succinylation in a variety of normal and tumor tissues from mice. Western blot analysis for succinyllysine demonstrated that the greatest change in protein succinylation levels was observed in normal thymus (Lane 4) versus thymic lymphoma (Lane 3) (Figure 3.1A). There was higher protein succinylation level in normal thymus compared with lymphoma tumors, supporting the idea that SIRT5 activity is increased and essential for tumor growth. Other tumor types, such as lung tumors (Lane 1) and testis tumors (Lane 5) did not show significant

differences in succinylation levels when compared to normal tissues (Lanes 6-7) (Figure 3.1A). Interestingly, we did not observe significant differences in SIRT5 expression between tumors and normal tissues. To validate these results, we tested protein lysine succinylation status in lymphoma tumor tissues from different mouse strains including, Hus1^{neo/neo}Atm^{-/-} (Lanes 3-4), P53KO^{+/-} (Lane 5), and CHK-HKO^{neo/neo}ATM^{-/-} (Lane 6) mice (Figure 3.1B). Succinylation levels were lower in thymus tumors from different mouse backgrounds when compared to healthy thymus, suggesting that SIRT5 activity is increased in lymphomagenesis (Figure 3.1B).

To investigate the relevance of our results, we analyzed the mRNA expression of *Sirt5* in different blood cancer cell lines using the dataset from Cancer Cell Line Encyclopedia and found that *Sirt5* is overexpressed in some blood cancers cells including Chronic Myeloid Leukemia (CML), B-cell lymphoma (B-cell) and Diffuse Large B Cell Lymphomas (DLBCL) (Figure 3.1C) (Broad Institute of MIT and Harvard). Together, these data suggest that SIRT5 might be essential for lymphomagenesis.

3.4.2 Lymphoma development and progression is not impaired upon genetic deletion of *Sirt5*.

To investigate the roles of SIRT5 in lymphomagenesis, we generated a murine mouse model in which *Sirt5* is knocked out and *c-Myc* is constitutively activated. E μ -*Myc* transgenic mice overexpress *Myc* under the control of the immunoglobulin heavy chain gene enhancer (E μ) and show increased pre-B and B cell lymphomas at 15-20 weeks of age (Adams *et al.* 1985). *Sirt5*^{+/-} mice were crossed with E μ -*Myc* transgenic to generate *Sirt5*^{+/-} E μ -*Myc* mice. These mice were then crossed with *Sirt5*^{+/-}

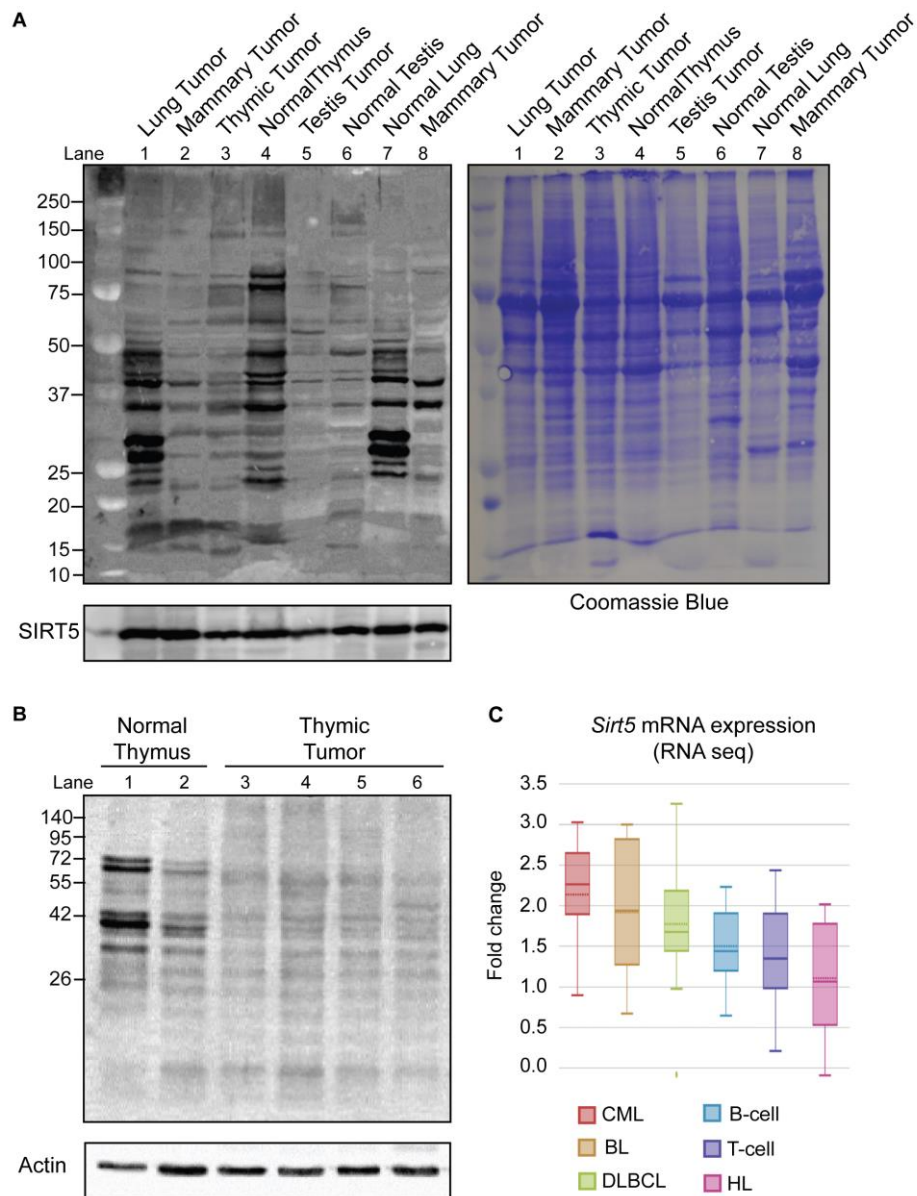


Figure 3.1 Succinylation levels in normal and tumor tissues and *SIRT5* mRNA expression in lymphoma. (A) Succinylation and SIRT5 levels in different normal and tumor tissue lysates. Tissues were collected from different mice strains. Tissues lysates in the following lanes correspond to: (1) *Rrm2^{Tg}*, (2) *Sirt5^{+/+}* PYMT, (3) *Hus1^{neo/neo}Atm^{-/-}*, (4,6,7) WT-129, and (8) *Sirt5^{-/-}* PyMT. **(B)** Western blot comparing succinylation levels in normal thymus and thymic lymphomas from different strains of mice. Tissues lysates in

the following lanes correspond to: (1-2) WT-129, (3-4) *Hus1^{neo/neo}Atm^{-/-}*, (5) *P53KO^{+/-}*, and (6) *CHK-HKO^{neo/neo}ATM^{-/-}*. Fifty micrograms of samples were separated on a 12% SDS gel, transferred to a membrane, and probed with anti-succinyl antibody (1:500) and/or SIRT5. Coomassie blue and actin were used as the loading controls. **(C)** *SIRT5* mRNA expression in multiple blood cancer cell lines. Data retrieved from Cancer Cell Line Encyclopedia.

mice to produce *Sirt5*^{+/+} E μ -Myc and *Sirt5*^{-/-} E μ -Myc littermates. To assess whether the loss of *Sirt5* affects lymphomagenesis we compared the survival of *Sirt5*^{+/+} E μ -Myc (n=12) and *Sirt5*^{-/-} E μ -Myc (n=11) mice. Surprisingly, we found that the loss of *Sirt5* did not affect the survival of E μ -Myc mice (p-value = 0.7420 with the log rank test) (Figure 3.2A). The median survival of *Sirt5*^{+/+} E μ -Myc and *Sirt5*^{-/-} E μ -Myc mice were 86 and 88 days, respectively.

At necropsy, most of these mice had lymphoma invading the thoracic cavity and enlarged lymph nodes and spleen (Figure 3.2B). Some mice had tumors on the thoracic vertebral column. The formation of these tumors was observed at a similar rate in *Sirt5*^{+/+} E μ -Myc and *Sirt5*^{-/-} E μ -Myc mice (Table 3.1). To test whether *Sirt5* loss affected the growth of lymphoma, we evaluated the weight of the thymus, spleen and lymph nodes in these mice. No significant differences were observed in the weight of any of these tissues (Figure 3.2C-E). These data are consistent with the Kaplan Meier survival and indicated that SIRT5 is not essential for lymphomagenesis in this model.

3.4.3 Histological analysis of lymphomas and spleens upon deletion of *Sirt5*.

Although there were no differences in the overall survival of E μ -Myc mice upon *Sirt5* deletion and no significant differences in tumor weight, we wanted to investigate whether there were histological differences among *Sirt5*^{+/+} E μ -Myc and *Sirt5*^{-/-} E μ -Myc tumor tissues. The histology of lymphomas, spleens and livers were evaluated in a blinded fashion. Most lymphomas and spleen tissues from *Sirt5*^{+/+} E μ -Myc and *Sirt5*^{-/-} E μ -Myc were infiltrated and replaced by a population of neoplastic lymphocytes. High mitotic rate was observed, especially in the thymus where there are

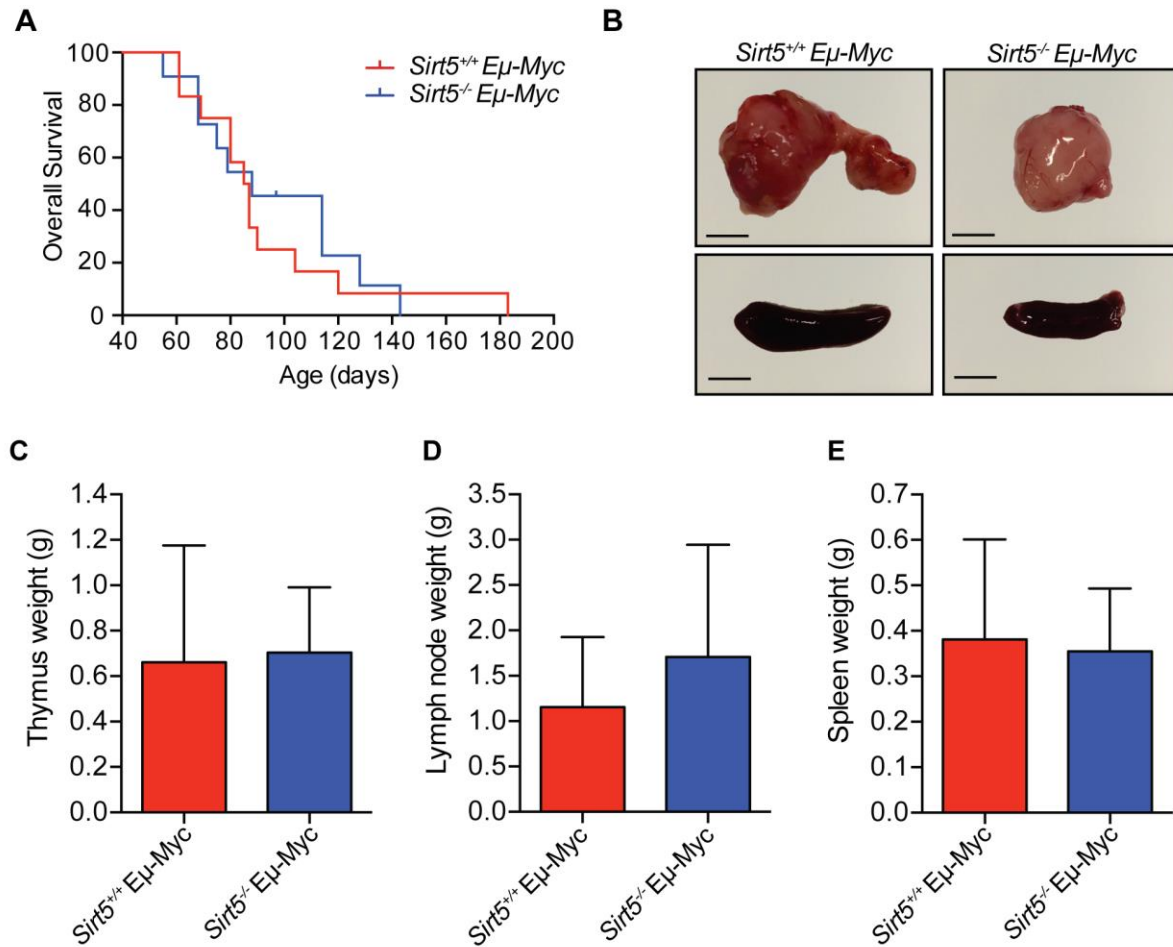


Figure 3.2 *Sirt5* deletion does not significantly affect lymphomagenesis *in vivo*.

(A) Kaplan Meier tumor overall survival curve for *Sirt5*^{+/+} Eμ-Myc and *Sirt5*^{-/-} Eμ-Myc mice ($p = 0.7420$, Logrank (Mantel-Cox test)). **(B)** Representative images of thymic lymphomas and enlarged spleens in *Sirt5*^{+/+} Eμ-Myc and *Sirt5*^{-/-} Eμ-Myc mice. Scale represents 0.25 cm. **(C-E)** Bar graphs showing the weight of thymic lymphomas, lymph nodes and spleens for *Sirt5*^{+/+} Eμ-Myc and *Sirt5*^{-/-} Eμ-Myc mice. No significant differences were observed for the three comparisons ($p > 0.05$, Unpaired t-test).

Table 3.1 Percent of mice with enlarged thymus, spleen and lymph nodes.

Mice	Enlarged Thymus	Enlarged Spleen	Enlarged Lymph nodes*
<i>Sirt5</i> ^{+/+} E μ -Myc	(9/10) 0.90	(8/9) 0.89	(8/11) 0.72
<i>Sirt5</i> ^{-/-} E μ -Myc	(8/8) 1.00	(8/8) 1.00	(7/10) 0.70

* Lymph nodes collected include cervical, axillary, branchial and inguinal lymph nodes.

large chromatin aggregates amongst the tumor. No metastases were observed in liver tissues from *Sirt5*^{+/+} Eμ-*Myc* or *Sirt5*^{-/-} Eμ-*Myc* mice (Figure 3.3).

2.4.4 Prominent increased of succinylated proteins in *Sirt5*^{-/-} Eμ-*Myc* lymphomas.

We screened global protein succinylation in thymic tumors from *Sirt5*^{+/+} Eμ-*Myc* and *Sirt5*^{-/-} Eμ-*Myc* mice. In agreement with the data shown in Chapter 2, we found prominent increases in succinylated proteins in *Sirt5*^{-/-} Eμ-*Myc* mice when compared to *Sirt5*^{+/+} Eμ-*Myc* mice (Figure 3.4A). We next, performed a comparative proteomic analysis using a stable-isotope reductive dimethylation approach, followed by enrichment of succinylated peptides and LC-MS/MS analysis as described by Sadhukhan *et al.* (Sadhukhan *et al.* 2016) to identify proteins that were regulated by SIRT5 in lymphoma. LC-MS/MS analysis identified 235 lysine succinylation sites across 81 proteins in mammary tumors from *Sirt5*^{+/+} Eμ-*Myc* and *Sirt5*^{-/-} Eμ-*Myc* mice. Among these 235 succinylated peptides, 171 peptides were only succinylated in *Sirt5*^{-/-} Eμ-*Myc* lymphomas and 31 were highly abundant in *Sirt5*^{-/-} Eμ-*Myc* when compared to *Sirt5*^{+/+} Eμ-*Myc* (Figure 3.4B). Similarly to what we observed in mammary tumors, most of the identified proteins showed only one unique succinylated site, however, other proteins had between two to seventeen unique succinylated sites (Figure 3.4C).

We investigated pathway enrichment analysis using Reactome (www.reactome.org) to gain an insight into how succinylation and SIRT5 regulate metabolic networks in lymphomas. As expected, most succinylated proteins identified are enzymes involved in cellular metabolism (62%). Detailed analysis of metabolic pathways revealed that the top pathways enriched with succinylation-targeted proteins

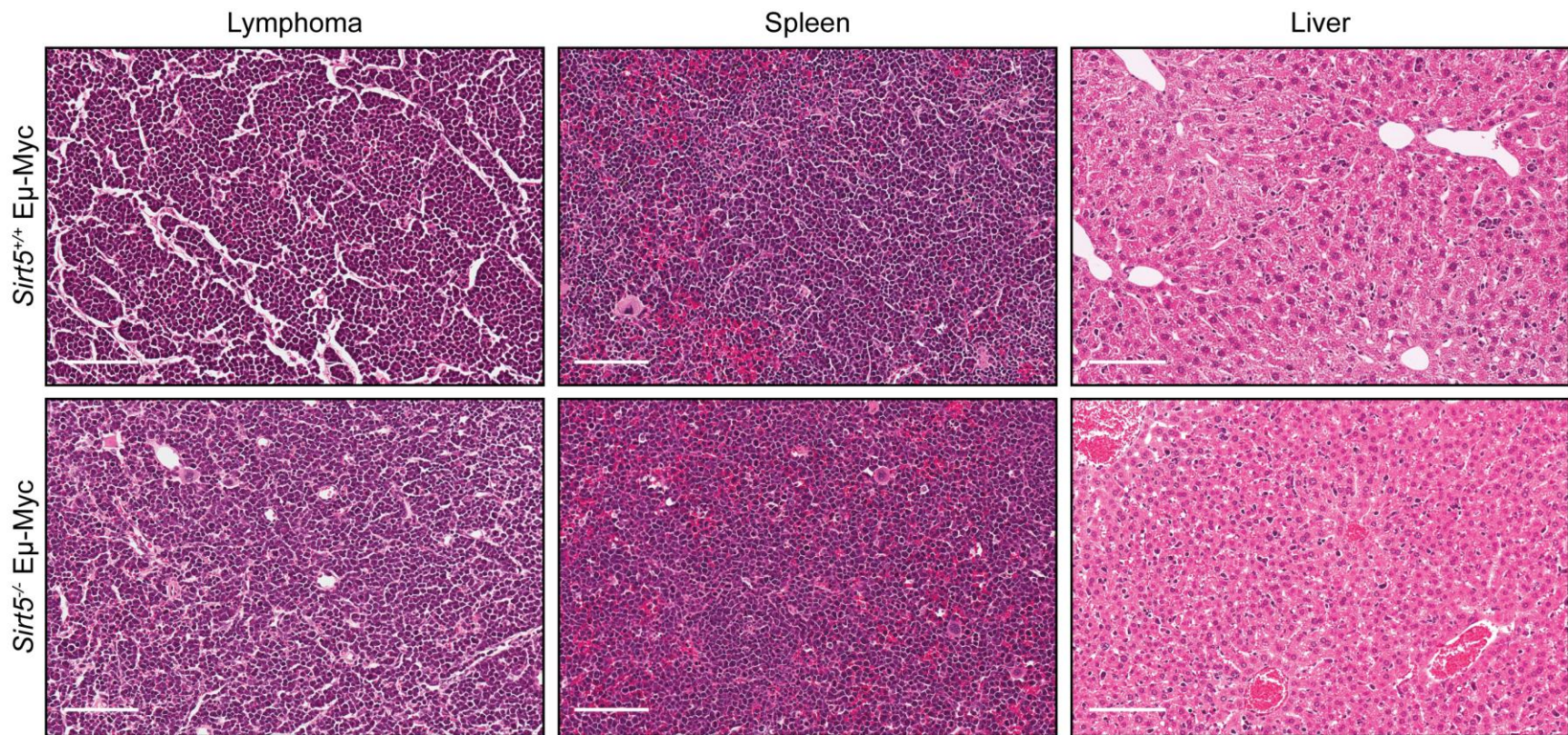


Figure 3.3 Representative images of tumor tissues, spleen and liver tissues from *Sirt5*^{+/+} Eμ-*Myc* and *Sirt5*^{-/-} Eμ-*Myc* mice. Tumors and other tissues were harvested upon necropsy. Analysis of H&E stained tumors and spleens did not show significant histological differences between *Sirt5*^{+/+} Eμ-*Myc* and *Sirt5*^{-/-} Eμ-*Myc* mice. Histology of liver tissues show no presence of metastases. Scale represents 100 μm.

were enzymes involved in the TCA cycle and respiratory electron transport, as well as metabolism of lipids (Figure 3.4D). Among the hypersuccinylated enzymes involved in the TCA cycle were citrate synthase, aconitase hydratase, isocitrate dehydrogenase, succinyl CoA ligase, fumarate hydratase and malate dehydrogenase (Table 3.2). ATP synthases subunits (alpha, beta, delta, F(0) and F(1)) as well as other enzymes involved in ATP transport were also hypersuccinylated in *Sirt5*^{-/-} Eμ-*Myc* thymic tumors (Table 3.3). Another pathway that was highly enriched in hypersuccinylated proteins is lipid metabolism. A total of 19 proteins involved in fatty acid metabolism and ketone body synthesis were hypersuccinylated in *Sirt5*^{-/-} Eμ-*Myc* thymic tumors (Table 3.4). Interestingly, our LC-MS data did not show glutaminase (GLS2) as a SIRT5 target in thymic lymphomas. Together, these results validate our data in mammary tumor tissues and suggest that SIRT5 targets key metabolic enzymes independently of the tumor type.

3.5 DISCUSSION

In Chapter 2, we showed that SIRT5 is essential for the anchorage independent growth of cancer cells and mammary tumor growth. To extend our knowledge on the pro-tumorigenic roles of SIRT5, we screened protein succinylation levels in a variety of tumor tissues and normal tissues. We found that the greatest change in protein succinylation levels was in normal lymph node versus lymphoma. The succinylation states of proteins were significantly reduced in lymphomas when compared to healthy lymph nodes, suggesting increased SIRT5 activity in lymphomas.

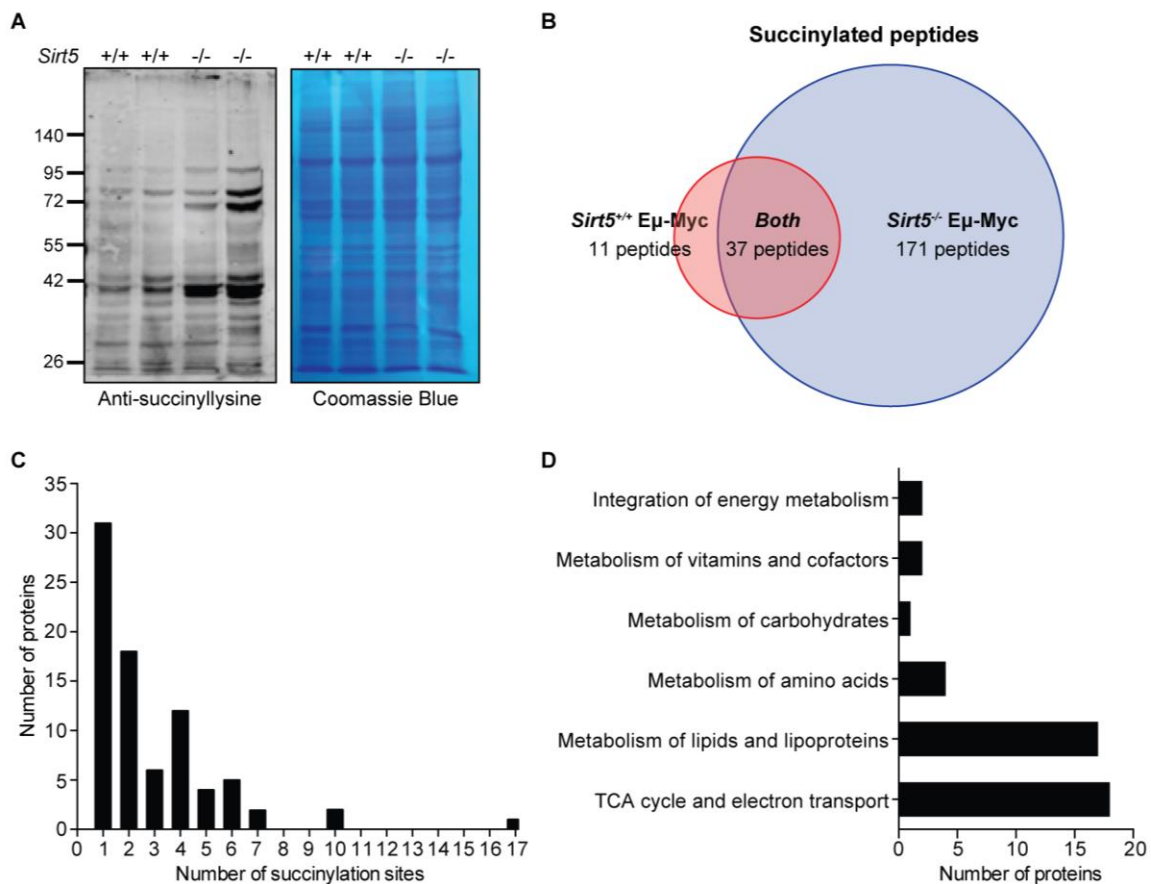


Figure 3.4 Succinylation levels in thymic tumors from *Sirt5*^{+/+} Eμ-Myc and *Sirt5*^{-/-} Eμ-Myc mice and metabolic pathways highly targeted by SIRT5. (A) Western blot of thymic tumors lysates (50 μg) against Anti-succinyllysine antibody. Thymic tumors from *Sirt5*^{-/-} Eμ-Myc mice showed increased succinylation levels when compared to *Sirt5*^{+/+} Eμ-Myc. Coomassie blue staining was used as loading control. (B) Number of unique succinylated peptides identified in *Sirt5*^{+/+} Eμ-Myc and *Sirt5*^{-/-} Eμ-Myc thymic tumors. (C) Distribution of number of lysine succinylation sited per proteins. (D) Metabolic pathways enriched with lysine succinylated proteins.

Table 3.2 List of hyper-succinylated proteins involved in the TCA cycle.

Protein	Unique succinylation sites	Sites in		Sites in <i>Sirt5</i> ^{+/-} and	
		<i>Sirt5</i> ^{+/+} Eμ- <i>Myc</i>	<i>Sirt5</i> ^{-/-} Eμ- <i>Myc</i>	<i>Sirt5</i> ^{-/-} Eμ- <i>Myc</i>	<i>Sirt5</i> ^{+/+} Eμ- <i>Myc</i>
Citrate synthase	6	0	5	1	
Aconitate hydratase	10	0	9	1	
Isocitrate dehydrogenase 2	7	2	3	2	
Isocitrate dehydrogenase 3	4	0	4	0	
Succinyl CoA ligase synthase, subunit α	4	0	3	1	
subunit β	4	0	4	0	
Fumarate hydratase	4	0	3	1	
Malate dehydrogenase	7	0	6	1	

*Data shown in this table was obtained from a comparative proteomic analysis using stable-isotope reductive dimethylation approach, followed by enrichment of succinylated peptides and LC-MS/MS analysis. Unique succinylated sites in *Sirt5*^{+/+} Eμ-*Myc* and *Sirt5*^{-/-} Eμ-*Myc* thymic tumors were quantified manually.

Table 3.3 List of hyper-succinylated proteins involved in the production and transport of ATP.

Protein	Unique succinylation sites	Sites in		Sites in <i>Sirt5</i> ^{+/-} and	
		<i>Sirt5</i> ^{+/+} Eμ- <i>Myc</i>	<i>Sirt5</i> ^{-/-} Eμ- <i>Myc</i>	<i>Sirt5</i> ^{-/-} Eμ- <i>Myc</i>	<i>Sirt5</i> ^{-/-} Eμ- <i>Myc</i>
ATP synthase					
Subunit α	2	0	2	0	0
Subunit β	3	0	3	0	0
Subunit d	1	0	0	1	0
Subunit O	1	0	1	0	0
F(0)	2	0	2	0	0
F(1)	1	0	0	1	0
ADP/ATP translocase 1	5	1	4	0	0
ADP/ATP translocase 2	5	0	5	0	0
ATPase inhibitor	1	0	1	0	0

*Data shown in this table was obtained from a comparative proteomic analysis using stable-isotope reductive dimethylation approach, followed by enrichment of succinylated peptides and LC-MS/MS analysis. Unique succinylated sites in *Sirt5*^{+/+} Eμ-*Myc* and *Sirt5*^{-/-} Eμ-*Myc* thymic tumors were quantified manually.

Table 3.4 List of hyper-succinylated proteins involved in lipid metabolism.

Protein	Unique succinylation sites	Sites in		Sites in <i>Sirt5</i> ^{+/-} and	
		<i>Sirt5</i> ^{+/+}	E μ -Myc	<i>Sirt5</i> ^{-/-}	E μ -Myc
serum albumin precursor	6	0		3	3
trifunctional enzyme subunit alpha	17	0		10	7
trifunctional enzyme subunit beta	2	0		1	2
acetyl-CoA acetyltransferase	4	0		4	0
acyl-CoA synthetase family member 2	2	0		2	0
acyl-coenzyme A thioesterase 2	1	0		1	0

acyl-coenzyme A thioesterase 13	2	0	2	0
hydroxyacyl-coenzyme A dehydrogenase	3	0	3	0
enoyl-CoA delta isomerase 1	2	0	2	0
enoyl-CoA delta isomerase 2b	2	0	2	0
enoyl-CoA hydratase	3	0	3	0
trans-2-enoyl-CoA reductase	2	0	1	1
very long-chain specific acyl-CoA dehydrogenase	2	0	2	0
long-chain specific acyl- CoA dehydrogenase	1	0	1	0

medium-chain specific acyl-CoA dehydrogenase	2	0	2	0
carnitine O- palmitoyltransferase 2	2	0	2	0
3-ketoacyl-CoA thiolase	10	0	9	1
succinyl-CoA:3-ketoacid coenzyme A transferase 1	2	0	2	0
carbonyl reductase family member 2	1	0	1	0

*Data shown in this table was obtained from a comparative proteomic analysis using stable-isotope reductive dimethylation approach, followed by enrichment of succinylated peptides and LC-MS/MS analysis. Unique succinylated sites in *Sirt5*^{+/+} Eμ-*Myc* and *Sirt5*^{-/-} Eμ-*Myc* thymic tumors were quantified manually.

B-cell lymphomas are characterized by displaying a pronounced dependency in glutamine metabolism. Increased glutamine uptake in cancer cells is often driven by alterations in the expression of the transcription factor c-MYC (Le *et al.* 2012). Growing evidences have shown that increased glutamine metabolism is essential for survival and proliferation of Myc-induced Burkitt lymphoma cells, and inhibition of glutaminase, inhibited tumor cell growth *in vivo* (Ogura *et al.* 2010; Le *et al.* 2012; Jeong *et al.* 2014).

Several studies have shown that the mitochondrial sirtuin, SIRT4, functions as a tumor suppressor by regulating glutamine metabolism. SIRT4 negatively regulates glutamate dehydrogenase (GDH) activity through ADP-ribosylation, and represses Myc-induced B-cell lymphomagenesis (Jeong *et al.* 2014). SIRT5, in the other hand, has been reported to regulate glutamine metabolism. A recent report has shown that SIRT5 desuccinylates and inactivates glutaminase (GLS2) activity in breast cancer cells (Polleta *et al.* 2015). Inactivation of GLS2 results in reduced levels of glutamate and ammonia production. Another study revealed that SIRT5 promotes glutamine metabolism in colorectal cancer cells by deglutarylating and increasing the enzymatic activity of GLUD1 (Wang *et al.* 2018). Given the dependency of Myc-induced Burkitt lymphoma in glutamine, the relative contribution of SIRT5 in glutaminolysis, and the great differences in protein succinylation levels between normal thymus and thymic tumors, we set out to investigate the requirements of SIRT5 in lymphomagenesis.

Here, we generated a mouse model in which *Sirt5* is knocked out and *c-Myc* is constitutive activated. E μ -*Myc* transgenic mice overexpress Myc under the control of the immunoglobulin heavy chain gene enhancer (E μ) and show increased pre-B and B cell lymphomas (Adams *et al.* 1985). Unexpectedly, our study revealed that *Sirt5* loss did

not affect Myc-induced lymphomagenesis and mortality in $E\mu$ -*Myc* mice. Furthermore, it did not have any impact on tumor size or histological grade.

While lymphomagenesis in $E\mu$ -*Myc* mice was not affected by *Sirt5* deletion, protein succinylation levels of thymic lymphomas were significantly increased upon *Sirt5* loss. Immunoblotting for succinyl lysine revealed multiple proteins with elevated succinylation in tumors from *Sirt5*^{-/-} $E\mu$ -*Myc* mice when compared to *Sirt5*^{+/+} $E\mu$ -*Myc* littermates. Furthermore, LC-MS analysis identified many metabolic enzymes involved in the TCA cycle and respiratory electron transport, fatty acid metabolism and ketone body synthesis were highly succinylated in *Sirt5*^{-/-} $E\mu$ -*Myc* thymic tumors. To our surprise, the LC-MS data did not identify GLS2 as a SIRT5 target. Although GLS2 was not identified as a SIRT5 target in lymphomas, the LC-MS data collected in lymphomas tissues was very consistent with the LC-MS data collected in mammary tumor tissues (Chapter 2), suggesting that SIRT5 targets the same metabolic enzymes, indistinctively of tumor types. Furthermore, these data suggest that the key metabolic enzymes regulated by SIRT5-mediated post-translational modifications are essential for metabolic reprogramming in mammary tumorigenesis, but not in lymphomagenesis. Further experiments are required to fully understand the molecular mechanism by which SIRT5 loss impairs mammary tumorigenesis, but not lymphomagenesis. However, we might entail that SIRT5 likely impacts cancer in a tissue or oncogen-specific manner.

While studying the roles of SIRT5 in $E\mu$ -*Myc* transgenic mice, we did observe that there was a cohort of mice carrying the $E\mu$ -*Myc* transgene that never became sick and did not develop lymphoma, independently of *Sirt5* status (Supplemental Table 3.1). Recently, it was reported that lymphomas arising in the $E\mu$ -*Myc* transgenic mouse are

heterogeneous and show two distinct gene expression profiles that significantly affect lymphoma onset (Rempel *et al.* 2014). In our study, we observed that lymphoma onset and lymphoma mortality were independent of *Sirt5* status, suggesting that SIRT5 is not essential for lymphomagenesis. However, in our study, we did not discriminate between these two distinct groups. To further investigate the roles of SIRT5 in lymphomagenesis, it is crucial to perform genetic profiling of tumor tissues from *Sirt5*^{+/+} E μ -*Myc* and *Sirt5*^{-/-} E μ -*Myc* mice and determine whether any of these two distinctive groups are susceptible to SIRT5 loss. These data will serve as a stratification method to establish the importance of SIRT5 in different types of B-cell lymphoma.

3.6 SUPPLEMENTAL MATERIALS

Supplemental Table 3.1

Supplemental Table 3.1 List of mice that did not develop lymphoma or show signs of illness at 17 weeks old or older.*

Genotype	Number of mice	Number of females	Number of males
<i>Sirt5</i> ^{+/+} Eμ- <i>Myc</i>	3	1	2
<i>Sirt5</i> ^{+/-} Eμ- <i>Myc</i>	4	1	3
<i>Sirt5</i> ^{-/-} Eμ- <i>Myc</i>	4	0	4

* Autopsy was performed in these mice and they showed no signs of lymphoma development.

3.7 REFERENCES

- Adams JM, Harris AW, Pinkert CA, Corcoran LM, Alexander WS, Cory S, Palmiter RD, Brinster RL. The c-myc oncogene driven by immunoglobulin enhancers induces lymphoid malignancy in transgenic mice. *Nature*. 1985; 318(6046):533-538.
- Altman BJ, Jacobs SR, Mason EF, Michalek RD, MacIntyre AN, Coloff JL, Ilkayeva O, Jia W, He YW, Rathmell JC. Autophagy is essential to suppress cell stress and to allow BCR-Abl-mediated leukemogenesis. *Oncogene*. 2011; 30:1855-1867.
- Boroughs LK, DeBerardinis RJ. Metabolic pathways promoting cancer cell survival and growth. *Nat. Cell Biol.* 2015; 17(4) 351-359.
- Broad Institute of MIT and Harvard. Retrieved from <https://portals.broadinstitute.org/ccle> on December 2, 2017.
- Cattoretti G. MYC expression and distribution in normal mature lymphoid cells. *J. Pathol.* 2013; 229(3):430-440.
- Cheong H, Lindsten T, Wu J, Lu C, Thompson, CB. Ammonia-induced autophagy is independent of ULK1/ULK2 kinases. *Proc. Natl. Acad. Sci. USA*. 2011; 108:11121-11126.
- Dang CV. MYC, metabolism, cell growth, and tumorigenesis. *Cold Spring Harb. Perspect. Med.* 2013; 3(8):a014217.
- Du J, Zhou Y, Su X, Yu J, Khan S, Jiang H, Kim J, Woo J, Kim J, Choi B, He B, Chen W, Zhang S, Cerione R, Auwerx J, Hao Q, Lin H. Sirt5 is an NAD-dependent protein lysine demalonylase and desuccinylase. *Science*. 2011; 334:806-809.
- Eng CH, Yu K, Lucas J, White E, Abraham, RT. Ammonia derived from glutaminolysis is a diffusible regulator of autophagy. *Sci. Signal.* 2010; 3:ra31.

- Green TM, Nielsen O, de Stricker K, Xu-Monette ZY, Young KH, Møller MB. High levels of nuclear MYC protein predict the presence of MYC rearrangement in diffuse large B-cell lymphoma. *Am. J. Surg. Pathol.* 2012; 36(4):612-619.
- Guo JY, Chen HY, Mathew R, Fan J, Strohecker AM, Karsli-Uzunbas G, Kamphorst JJ, Chen G, Lemins JM, Karantza V, Collier HA, Dipaola RS, Gelinas C, Rabinowitz JD, White E. Activated Ras requires autophagy to maintain oxidative metabolism and tumorigenesis. *Genes Dev.* 2011; 25:460-470.
- Wang YQ, Wang HL, Xu J, Tan J, Fu LN, Wang JL, Zou TH, Sun DF, Gao QY, Chen YX, Fang JY. Sirtuin5 contributes to colorectal carcinogenesis by enhancing glutaminolysis in a deglutarylation-dependent manner. *Nat. Commun.* 2018; 9(1):545.
- SM, Lee A, Lee J, Haigis MC. SIRT4 protein suppresses tumor formation in genetic models of Myc-induced B cell lymphoma. *Journal of Biological Chemistry.* 2014; 289(7):4135-4144.
- Le A, Lane A, Hamaker M, Bose S, Gouwn A, Barbi J, Tsukamoto T, Rojas C, Slusher B, Zhang H, Zimmerman L, Liebler D, Slebos R, Lorkiewicz P, Higashi R, Fan T, Dang V. Glucose-Independent Glutamine Metabolism via TCA Cycling for Proliferation and Survival in B Cells. *Cell metabolism.* 2012; 15:110-121.
- Mathew R, Karp CM, Beaudoin B, Vuong N, Chen G, Chen HY, Bray K, Reddy A, Bhanot G, Gelinas C, Dipaola RS, Karantza-Wadsworth V, White E. Autophagy suppresses tumorigenesis through elimination of p62. *Cell.* 2009; 137:1062-1075.

- Muñoz-Pinedo C, El Mjiyad N, Ricci J. Cancer metabolism: current perspectives and future directions. *Cell Death and Disease*. 2012; 3:e248.
- Ogura M, Nakamura Y, Tanaka D, Zhuang X, Fujita Y, Obara A, Hamasaki A, Hosokawa M, Inagaki N. Overexpression of SIRT5 confirms its involvement in deacetylation and activation of carbamoyl phosphate synthetase 1. *Biochem. Biophys. Res. Commun.* 2010; 393:73-78.
- Polletta L, Vernucci E, Carnevale I, Arcangeli T, Rotili D, Palmerio S, Steegborn C, Nowak T, Schutkowski M, Pellegrini L, Sansone L, Villanova L, Runci A, Pucci B, Morgante E, Fini M, Mai A, Russo MA, Tafani M. SIRT5 regulation of ammonia-induced autophagy and mitophagy. *Autophagy*. 2015; 11:253-270.
- Rempel RE, Jiang X, Fullerton P, Tan TZ, Ye J, Lau JA, Mori S, Chi JT, Nevins JR, Friedman DR. Utilization of Eμ-*myc* Mouse to Model Heterogeneity of Therapeutic Response. *Mol. Cancer Ther.* 2014; 13(12):3219-3229.
- Sadhukhan S, Liu X, Ryu D, Nelson OD, Stupinski JA, Li Z, Chen W, Zhang S, Weiss RS, Locasale JW, Auwerx J, Lin H. Metabolomics- assisted proteomics identifies succinylation and SIRT5 as important regulators of cardiac function. *Proc. Natl. Acad. Sci. USA*. 2016; 113:4320- 4325.
- Siegel R, Naishadham D, Jemal A. Cancer statistics 2012. *CA Cancer J. Clin.* 2012; 62:10-29.
- Takamura A, Komatsu M, Hara T, Sakamoto A, Kishi C, Waguri S, Eishi Y, Hino O, Tanaka K, Mizushima N. Autophagy-deficient mice develop multiple liver tumors. *Genes Dev.* 2011; 25:795-800.

- Tan M, Peng C, Anderson KA, Chhoy P, Xie Z, Dai L, Park J, Chen Y, Huang H, Zhang Y, Ro J, Wagner GR, Green MF, Madsen AS, Schmiesing J, Peterson BS, Xu G, Ilkayeva OR, Muehlbauer MJ, Braulke T, Mühlhausen C, Backos DS, Olsen, CA, McGuire PJ, Pletcher SD, Lombard DB, Hirschey MD, Zhao Y. Lysine glutarylation is a protein post-translational modification regulated by SIRT5. *Cell Metab.* 2014; 19:605-617.
- Wise DR, Thompson CB. Glutamine addiction: a new therapeutic target in cancer. *Trends Biochem. Sci.* 2010; 35:427-433.
- Yu J, Sadhukhan S, Noriega LG, Moullan N, He B, Weiss RS, Lin H, Schoonjans K, Auwerx J. Metabolic Characterization of a Sirt5 deficient mouse model. *Sci. Rep.* 2013; 3:2806.

CHAPTER 4

4.1 CONCLUSIONS

Mammalian sirtuins have been implicated in a wide variety of cellular processes, such as gene expression, cell survival, cell death, angiogenesis and regulation of energy metabolism (North and Verdin 2004; Chalkiadaki *et al.* 2015). Among the three-mitochondrial sirtuins, SIRT5 is the only known mitochondrial enzyme that catalyzes NAD⁺-dependent demalonylation, desuccinylation and deglutarylation (Schuetz *et al.* 2007; Du *et al.* 2011; Zhou *et al.* 2012; Roessler *et al.* 2014; Li *et al.* 2015). In recent years, many studies have implicated SIRT5 in regulating a variety of metabolic pathways by targeting key metabolic enzymes. SIRT5 is known to stimulate glycolysis and restrict the TCA cycle as well as the electron transport chain (Park *et al.* 2013; Nashida *et al.* 2015; Zhang *et al.* 2015; Xiangyun *et al.* 2017). SIRT5 has been also implicated in blocking glutaminolysis by inhibiting glutamine metabolism, reducing cellular ROS levels by promoting NADPH production, promoting ammonia detoxification by activating the urea cycle and inducing fatty acid β oxidation by activating VLCAD and ECHA (Nakagawa *et al.* 2009; Radin *et al.* 2013; Polleta *et al.* 2015; Zhou *et al.* 2016). Given the significant roles of SIRT5 in regulating multiple metabolic pathways, increased attention has been given in elucidating the roles of SIRT5 in cancer metabolic reprogramming.

In recent years, multiple studies have implicated SIRT5 in contributing to the malignant phenotype of cancer. The work presented here highlights a novel function of SIRT5-mediated post-translational modification in breast cancer progression. Firstly, we show that *Sirt5* is overexpressed in human breast cancer. Furthermore, we demonstrate

that overexpression of *Sirt5* correlates with poor overall survival of patients with breast cancer.

To test the unique enzymatic activity of SIRT5 in cancer progression, we first examined its importance for the development of transformed phenotypes in cultured cancer cells. Our data demonstrates that SIRT5 is essential for the transformed phenotype of human cancer cells. Loss of SIRT5 in human breast cancer cells and Kras-expressing mouse embryonic fibroblast cells suppresses their transformed properties. We later demonstrated that knock-out of *Sirt5* reduces mammary tumorigenesis and metastasis in PyMT transgenic mice. To extend our knowledge of the pro-tumorigenic roles of SIRT5, we used another *in vivo* model that recapitulates glutamine-dependency of human cancers. Unexpectedly, our study revealed that loss of SIRT5 has no effect on the incidence of lymphomas in E μ -Myc transgenic mice, suggesting that the pro-tumorigenic roles of SIRT5 are tissue or oncogene-specific.

Given the biological functions of SIRT5 and its therapeutic potentials, in recent years, there has been increasing interest in developing novel SIRT5 inhibitors. Several peptides and small molecule inhibitors of SIRT5 have been reported, however, the anti-tumor potential of these compounds has not been reported yet (He *et al.* 2012; Maurer *et al.* 2012; Roessler *et al.* 2014; Zhang *et al.* 2015). Here, we show for the first time the anti-tumor potential of two small molecule SIRT5 inhibitors named, I5-2AM and MY01170. Inhibition of SIRT5 with these small molecules inhibited the anchorage independent growth of cancer cells. Furthermore, treatment with I5-2AM reduced mammary tumor growth in MMTV-PyMT mice. These data recapitulates similar results as when *Sirt5* was knock-out/down and highlights the potential of targeting SIRT5 as a

to treat cancer. To identify SIRT5 cellular targets that might support tumorigenesis we performed LC-MS analysis using mammary and thymic tumor tissues from *Sirt5*^{+/+} and *Sirt5*^{-/-} transgenic mice. Consistent with published works, our data revealed that SIRT5 targets many metabolic enzymes (Park *et al.* 2013; Radin *et al.* 2013). Our data specifically show that SIRT5 targets most enzymes involved in the TCA cycle and ATP production and transport. SIRT5 also targets a number of enzymes involved in fatty acid metabolism. Some of the enzymes identified as SIRT5-targets (e.g. IDH2, SDH, ACAT2) in our study have been implicated in supporting the transformed phenotypes of cancer cells (e.g. anchorage-independent growth and migration/invasiveness) (Phan *et al.* 2014; Jiang *et al.* 2016). These data highlight the potential mechanisms whereby SIRT5 may impact tumorigenesis.

In conclusion, the work presented here provides a novel example of the pro-tumorigenic roles of SIRT5-mediated post-translational modification on key metabolic enzymes.

4.2 FUTURE DIRECTIONS

Our data indicate that SIRT5, a mitochondrial regulator of metabolism, supports the malignant phenotypes of breast cancer cells and promotes mammary tumorigenesis in mice. We also demonstrate that SIRT5 targets many key metabolic enzymes that have been involved in the metabolic reprogramming of cancer cells. However, further experiments are required to identify SIRT5-specific targets that serve as downstream effectors, conferring human breast cancer cells with the ability to grow in soft agarose and promoting mammary tumor growth and metastasis in PyMT transgenic mice.

Recent reports have shown that enhanced production of reactive oxygen species (ROS) is associated with cancer cell detachment from the extracellular matrix. In order to continue growing under these conditions (high ROS levels and no anchorage), cancer cells depend on IDH1/2 activity to support redox homeostasis (Jiang *et al.* 2016). Previously reports have shown that SIRT5 reduces cellular ROS production by activating 6PDG, IDH2 and SOD1 (Lin *et al.* 2013; Zhou *et al.* 2016). Our LC-MS data also identified IDH2 as a SIRT5 target. Therefore, we are currently performing immunoblotting assays to validate IDH2 as a SIRT5 substrate and functional assays to determine whether IDH2 can rescue the defect in anchorage-independent growth in *Sirt5*KD/KO cells. Given the fact that SIRT5 targets many metabolic enzymes, we plan to continue testing other potential targets that are also associated to anchorage independence phenotype of cancer cells.

Comparative analysis of gene expression profiles between *Sirt5*^{+/+} PyMT and *Sirt5*^{-/-} PyMT mice revealed significant dysregulation of genes involved in inflammation. Recent reports have shown that inflammation plays a crucial role in tumor progression, invasion and metastasis (Swann *et al.* 2008; Grivennikov *et al.* 2010). Furthermore, inflammation also affects immune surveillance and response to therapy (Smyth *et al.* 2006; Lin and Karin 2007). Immune cells that infiltrate tumors engage in an extensive and dynamic crosstalk with cancer cells. The most frequently found immune cells within the tumor microenvironment are tumor-associated macrophages (TAMs) and T cells (Condeelis and Pollard 2006; Smyth *et al.* 2006). TAMs are known to promote tumor growth and metastasis by stimulating angiogenesis (Condeelis and Pollard 2006; Grivennikov *et al.* 2010). In this work, we show for the first time that *Sirt5* loss delays

lung metastasis in PyMT transgenic mice, however no mechanism has been fully studied. In order to elucidate the mechanism by which SIRT5 promotes lung metastasis *in vivo*, we are setting out multiple experiments to test the requirements of SIRT5 in regulating cellular events that induces mammary tumor invasion and metastasis. We are currently testing the effect of SIRT5 loss in inflammation, angiogenesis and macrophage infiltration.

Recently, it was reported that SIRT5 controls inflammatory response of macrophages (Wang *et al.* 2017). Wang and co-workers showed that SIRT5 suppresses the pro-inflammatory response in macrophages by desuccinylating and activating PKM2 (Wang *et al.* 2017). SIRT5-dependent hypersuccinylation of PKM2 in LPS-stimulated macrophages promotes PKM2 entry into the nucleus that results in an increased transcriptional expression of IL-1 β and other pro-inflammatory cytokines (Wang *et al.* 2017). Given that macrophages play an important role in modulating the tumor microenvironment, and that SIRT5 regulates the pro-inflammatory response of activated macrophages, we set out to study the roles of SIRT5 in the tumor microenvironment. We are currently generating orthotopic mice by injecting PyMT tumor cells into the mammary fat pad of *Sirt5*^{+/+} and *Sirt5*^{-/-} mice to study whether SIRT5 is essential in the tumor microenvironment to facilitate tumor proliferation and metastasis or whether SIRT5 is only essential for tumor cells. Together, these experiments will help us to further elucidate roles for SIRT5 in the tumor microenvironment that impact mammary tumor progression and metastasis.

Given that complete deletion of *Sirt5* in mice negatively affected mammary tumorigenesis and had modest effects in whole animals, we generated SIRT5 inhibitors

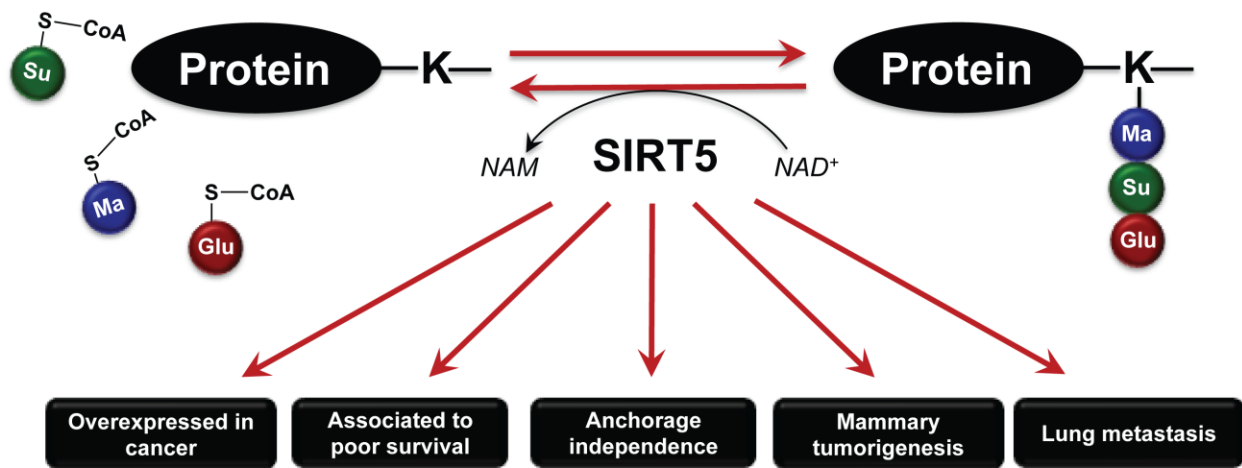
to test its therapeutic potentials. Our SIRT5 inhibitors, I5-2AM and MY01170, effectively inhibited the proliferation and anchorage independent growth of cancer cells. Treatment with I5-2AM showed a reduction in mammary tumor growth in PyMT mice. However, further experiments need to be conducted to test its stability and its potential to inhibit SIRT5 activity in mammary tumor tissues. We are also conducting in vivo treatments with MY01170 to test whether it has stronger anti-tumor potential when compared to I5-2AM.

In Chapter 3, we showed that SIRT5 loss does not affect Myc-induced lymphomagenesis and mortality in E μ -Myc mice. Furthermore, it does not have any impact in tumor size and histological grade. A recent report has shown that lymphomas arising in the E μ -Myc transgenic mouse are heterogeneous and show two distinct gene expression profiles that significantly affect lymphoma onset (Rempel *et al.* 2014). Given the heterogeneity in the gene expression profile of these lymphomas and the effect that these variations impart on the tumor incidence and mortality, it might be necessary to perform gene expression profile on lymphoma tissues from *Sirt5*^{+/+} E μ -Myc and *Sirt5*^{-/-} E μ -Myc mice to determine whether any of these two distinctive groups are susceptible to SIRT5 loss. This data will serve as a stratification method to establish the importance of SIRT5 in different types of B-cell lymphoma.

Together these future experiments will provide an insight on the mechanism of action of SIRT5 in promoting mammary tumorigenesis, and will further highlight the potential of SIRT5 to regulate other factors associated to cancer progression and metastasis. In addition, these experiments have the potential to highlight vulnerabilities

that SIRT5 deletion creates in mammary tumorigenesis but not in lymphomagenesis and therefore, identify novel therapeutic intervention against breast cancer.

Roles of SIRT5 in cancer



Effects of SIRT5 loss in cancer

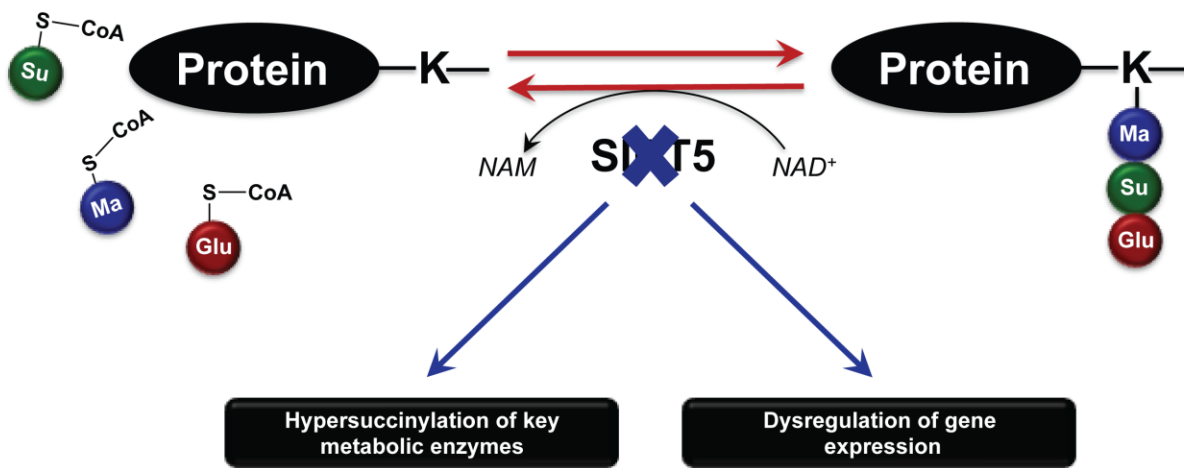


Figure 4.1 Graphical summary model. *SIRT5* is amplified in a subset of breast cancers and other malignancies and it supports the anchorage-independent growth of human cancer cell lines and transformed-Kras MEFs cells. *SIRT5* promotes mammary tumorigenesis and metastasis in PYMT mice. Deficiency of *Sirt5* leads to the hypersuccinylation of multiple mitochondrial proteins and induced dysregulation of genes. *SIRT5* holds promise as a target for cancer therapy.

4.3 REFERENCES

- Chalkiadaki A, Guarente L. The multifaceted functions of sirtuins in cancer. *Nat. Rev. Cancer.* 2015; 15:608-624.
- Condeelis J, Pollard JW. Macrophages: obligate partners for tumor cell migration, invasion, and metastasis. *Cell.* 2006; 124(2):263-266.
- DeBerardinis RJ, Mancuso A, Daikhin E, Nissim I, Yudkoff M, Wehrli S, Thompson CB. Beyond aerobic glycolysis: Transformed cells can engage in glutamine metabolism that exceeds the requirement for protein and nucleotide synthesis. *Proc. Natl. Acad. Sci. USA.* 2007; 104:19345-19350.
- Du J, Zhou Y, Su X, Yu JJ, Khan S, Jiang H, Kim J, Woo J, Kim JH, Choi BH, He B, Chen W, Zhang S, Cerione RA, Auwerx J, Hao Q, Lin H. Sirt5 is a NAD-dependent protein lysine demalonylase and desuccinylase. *Science.* 2011; 334:806-809.
- Gao P, Tchernyshyov I, Chang TC, Lee YS, Kita K, Ochi T, Zeller KI, De Marzo AM, Van Eyk JE, Mendell JT, Dang CV. c-Myc suppression of miR-23a/b enhances mitochondrial glutaminase expression and glutamine metabolism. *Nature.* 2009; 458:762-765.
- Grivennikov SI, Greten FR, Karin M. Immunity, Inflammation, and Cancer. *Cell.* 2010; 140(6): 883-899.
- He B, Du J, Lin H. Thiosuccinyl peptides as Sirt5-specific inhibitors. *J. Am. Chem. Soc.* 2012; 134:1922-1925.
- Jiang L, Shestov AA, Swain P, Yang C, Parker SJ, Wang QA, Terada LS, Adams ND, McCabe MT, Pietrak B, Schmidt S, Metallo CM, Dranka BP, Schwartz B,

- DeBerardinis R. Reductive carboxylation supports redox homeostasis during anchorage-independent growth. *Nature*. 2016; 532(7598):255-258.
- Li F, He X, Ye D, Lin Y, Yu H, Yao C, Huang L, Zhang J, Wang F, Xu S, Wu X, Liu L, Yang C, Shi J, He X, Liu J, Qu Y, Guo F, Zhao J, Xu W, Zhao S. NADP⁺-IDH Mutations Promote Hypersuccinylation that Impairs Mitochondria Respiration and Induces Apoptosis Resistance. *Mol. Cell*. 2015; 60:661-675.
- Lin WW, Karin M. A cytokine-mediated link between innate immunity, inflammation, and cancer. *J. Clin. Invest*. 2007; 117(5):1175-1183.
- Lin ZF, Xu HB, Wang JY, Lin Q, Ruan Z, Liu FB, Jin W, Huang HH, Chen X. SIRT5 desuccinylates and activates SOD1 to eliminate ROS. *Biochem. Biophys. Res. Commun*. 2013; 441:191-195.
- Maurer B, Rumpf T, Scharfe M, Stolfa DA, Schmitt ML, He W, Verdin E, Sippl W, Jung M. Inhibitors of the NAD⁺-dependent protein desuccinylase and demalonylase Sirt5. *ACS Med. Chem. Lett*. 2012; 3:1050-1053.
- Nakagawa T, Lomb DJ, Haigis MC, Guarente L. SIRT5 deacetylates carbamoyl phosphate synthetase 1 and regulates the urea cycle. *Cell*. 2009; 137:560-570.
- Nishida Y, Radin M, Carrico C, He W, Sahu AK, Gut P, Najjar R, Fitch M, Hellerstein M, Gibson BW, Verdin E. SIRT5 Regulates both Cytosolic and Mitochondrial Protein Malonylation with Glycolysis as a Major Target. *Mol. Cell*. 2015; 59:321-332.
- North BJ, Verdin E. Sirtuins: Sir2-related NAD-dependent protein deacetylases. *Genome Biol*. 2004; 5(5):224.
- Park J, Chen Y, Tishkoff DX, Peng C, Tan M, Dai L, Xie Z, Zhang Y, Zwaans BM, Skinner ME, Lombard, DB, Zhao, Y. SIRT5-mediated lysine desuccinylation

- impacts diverse metabolic pathways. *Mol. Cell.* 2013; 50:919-930.
- Phan LM, Yeung SCJ, Lee MH. Cancer metabolic reprogramming: importance, main features, and potentials for precise targeted anti-cancer therapies. *Cancer Biol. Med.* 2014; 11(1): 1-19.
- Polletta L, Vernucci E, Carnevale I, Arcangeli T, Rotili D, Palmerio S, Steegborn C, Nowak T, Schutkowski M, Pellegrini L, Sansone L, Villanova L, Runci A, Pucci B, Morgante E, Fini M, Mai A, Russo MA, Tafani M. SIRT5 regulation of ammonia induced autophagy and mitophagy. *Autophagy.* 2015; 11:253-270.
- Rardin MJ, He W, Nishida Y, Newman JC, Carrico C, Danielson SR, Guo A, Gut P, Sahu AK, Li B, Uppala R, Fitch M, Riiff T, Zhu L, Zhou J, Mulhern D, Stevens RD, Ilkayeva OR, Newgard CB, Jacobson MP, Hellerstein M, Goetzman ES, Gibson BW, Verdin E. SIRT5 regulates the mitochondrial lysine succinylome and metabolic networks. *Cell Metab.* 2013; 18:920-933.
- Rempel RE, Jiang X, Fullerton P, Tan TZ, Ye J, Lau JA, Mori S, Chi JT, Nevins JR, Friedman DR. Utilization of *Eμ-Myc* Mouse to Model Heterogeneity of Therapeutic Response. *Mol. Cancer Ther.* 2014; 13(12):3219-3229.
- Roessler C, Nowak T, Pannek M, Gertz M, Nguyen GTT, Scharfe M, Born I, Sippl W, Steegborn C, Schutkowski M. Chemical probing of the human sirtuin 5 active site reveals its substrate acyl specificity and peptide-based inhibitors. *Angew. Chem. Int. Engl.* 2014; 53:10728-10732.
- Schuetz A, Min J, Antoshenko T, Wang CL, Allali-Hassani A, Dong A, Loppnau P, Vedadi M, Bochkarev A, Sternglanz R, Plotnikov AN. Structural basis of inhibition of the human NAD⁺-dependent deacetylase SIRT5 by suramin. *Structure.* 2007;

15:377-389.

Smyth MJ, Dunn GP, Schreiber RD. Cancer immunosurveillance and immunoediting: the roles of immunity in suppressing tumor development and shaping tumor immunogenicity. *Adv. Immunol.* 2006; 90:1-50.

Swann JB, Vesely MD, Silva A, Sharkey J, Akira S, Schreiber RD, Smyth MJ. Demonstration of inflammation-induced cancer and cancer immunoediting during primary tumorigenesis. *Proc. Natl. Acad. Sci. USA.* 2008; 105(2):652-656.

Wang F, Wang K, Xu W, Zhao S, Ye D, Wang Y, Xu Y, Zhou L, Chu Y, Zhang C, Qin X, Yang P, Yu H. SIRT5 Desuccinylates and Activates Pyruvate Kinase M2 to Block Macrophage IL-1 β Production and to Prevent DSS-Induced Colitis in Mice. *Cell Rep.* 2017; 19(11):2331-2344.

Xiangyun Y, Xiaomin N, Linping G, Yunhua X, Ziming L, Yongfeng Y, Zhiwei C, Shun L. Desuccinylation of pyruvate kinase M2 by SIRT5 contributes to antioxidant response and tumor growth. *Oncotarget.* 2017; 8:6984-6993.

Zang W, Hao Y, Wang Z, Zheng W. Novel thiourea-based sirtuin inhibitory warheads. *Bioorg. Med. Chem. Lett.* 2015; 25:3319-3324.

Zhang W, Zhang SL, Hu X, Tam KY. Targeting Tumor Metabolism for Cancer Treatment: Is Pyruvate Dehydrogenase Kinases (PDKs) a Viable Anticancer Target? *Int. J. Biol. Sci.* 2015; 11(12):1390-1400.

Zhou L, Wang F, Sun R, Chen X, Zhang M, Xu Q, Wang Y, Wang S, Xiong Y, Guan KL, Yang P, Yu H, Ye D. SIRT5 promotes IDH2 desuccinylation and G6PD deglutarylation to enhance cellular antioxidant defense. *EMBO Rep.* 2016; 17:811-822.

Zhou Y, Zhang H, He B, Du J, Lin H, Cerione RA, Hao Q. The bicyclic intermediate structure provides insights into the desuccinylation mechanism of human sirtuin 5 (SIRT5). *J. Biol. Chem.* 2012; 287:28307-28314.

APPENDIX A. A SIRT2-selective inhibitor promotes c-Myc oncoprotein degradation and exhibits broad anticancer activity.

Jing H, Hu J, He B, **Negrón Abril YL**, Stupinski J, Weiser K, Carbonaro M, Chiang YL, Southard T, Giannakakou P, Weiss RS, Lin H.

Cancer Cell. 2016; 29:1-14. <http://dx.doi.org/10.1016/j.ccell.2016.02.007>

Author Contribution

Yashira L. Negrón Abril generated all or partial data for the following figures

Figure 5

Figure 6

Figure S5

SUMMARY

Targeting sirtuins for cancer treatment has been a topic of debate due to conflicting reports and lack of potent and specific inhibitors. We have developed a thiomristoyl lysine compound, TM, as a potent SIRT2-specific inhibitor with broad anticancer effect in various human cancer cells and mouse models of breast cancer. Mechanistically, SIRT2 inhibition promotes c-Myc ubiquitination and degradation. The anticancer effect of TM correlates with its ability to decrease c-Myc level. TM had limited effects on non-cancerous cells and tumor-free mice, suggesting that cancer cells have an increased dependency on SIRT2 that can be exploited for therapeutic benefit. Our studies demonstrate that SIRT2-selective inhibitors are promising anticancer agents and may represent a general strategy to target certain c-Myc-driven cancers.

INTRODUCTION

Oncogenes that drive tumorigenesis have attracted extensive interest as therapeutic targets for treating cancers. MYC, and c-Myc in particular, is one such oncogene. MYC was discovered in studies of fulminant chicken tumors caused by oncogenic retroviruses, which co-opted cellular c-Myc to generate the oncogenic v-Myc (Meyer and Penn, 2008). Subsequently, mouse plasmacytomas and human Burkitt lymphomas were found to be caused by c-Myc activation due to chromosomal translocations that fused c-Myc to the immunoglobulin (Ig) gene loci (Meyer and Penn, 2008). Recent genomic sequencing efforts identified c-Myc as one of the most highly amplified oncogenes in many different human cancers, further highlighting the oncogenic role of c-Myc activation (Beroukhim et al., 2010). The identification of effective therapeutic strategies targeting Myc has been challenging. Recently it was demonstrated that bromodomain inhibitors that target BRD4 could suppress c-Myc transcription and lead to tumor inhibition in vivo (Delmore et al., 2011). This finding underscores the therapeutic value of targeting Myc.

The sirtuin family of NAD-dependent protein lysine deacylases has been shown to play important roles in many physiological processes, including the regulation of transcription, metabolism, and DNA repair (Haigis and Sinclair, 2010; Imai et al., 2000; Imai and Guarente, 2010). Many of these functions are achieved by their ability to deacylate various substrate proteins, including histones, transcription factors, and metabolic enzymes (Du et al., 2011; Haigis and Sinclair, 2010; Imai et al., 2000; Imai and Guarente, 2010; Jiang et al., 2013; Peng et al., 2011; Zhu et al., 2012). Because the functionally related but structurally distinct zinc-dependent histone deacetylases

(HDACs) are established cancer targets (Lee et al., 2012; Marks and Breslow, 2007), there is interest in exploring whether sirtuins can also be important targets for cancers (Fang and Nicholl, 2011; Herranz and Serrano, 2010; Stünkel and Campbell, 2011). However, there is evidence suggesting both tumor suppressor and oncogenic roles of sirtuins (Fang and Nicholl, 2011; Herranz and Serrano, 2010; Stünkel and Campbell, 2011). In the case of SIRT2, genetic studies indicated that aged Sirt2 knockout (KO) mice show increased tumor incidence as compared to wild-type (WT) (Kim et al., 2011a) controls. In contrast, SIRT2 was also observed to have tumor promoting activity in several studies (Chen et al., 2013; Liu et al., 2013; McGlynn et al., 2014; Soung et al., 2014; Yang et al., 2013; Zhao et al., 2014; Zhao et al., 2013). Moreover, several SIRT2 inhibitors have also been reported to have anticancer effects (Cheon et al., 2015; He et al., 2014; Heltweg et al., 2006; Hoffmann et al., 2014; Kim et al., 2011b; Mahajan et al., 2014; McCarthy et al., 2013; Neugebauer et al., 2008; Rotili et al., 2012; Zhang et al., 2009). However, the moderate potency and specificity of the existing sirtuin inhibitors are insufficient to draw conclusions about the anticancer potential of sirtuin inhibition. Thus, whether sirtuin inhibitors are useful anticancer agents is still an open question. Here we set out to develop sirtuin inhibitors with improved potency and selectivity to explore the potential of targeting sirtuins for treating human cancers, especially c-Myc driven cancers.

EXPERIMENTAL PROCEDURES

For more details, see Supplemental Experimental Procedures.

Synthesis of Compounds used in the study

Detailed synthetic routes are presented in Supplemental Experimental Procedures. The NMR spectra of the synthesized compounds are shown in Figure S7.

Inhibition assay for different sirtuins

The assays were carried out using an HPLC-based method with different acyl peptides. The detailed method is described in Supplemental Experimental Procedures.

Cell viability assay

Cells were seeded into 96-well plates at 3000–4000 cells per well. After 24 hr, test compounds were added to cells to final concentrations ranging from 1–50 μM . Cells were then incubated for 72 hr and cell viability was measured using the CellTiter-Blue viability assay (Promega) following the manufacturer's instruction. Relative cell viability in the presence of test compounds was normalized to the vehicle-treated controls after background subtraction. Graphpad Prism software was used to determine the IC50 values.

Knockdown of SIRT1–7 in various cell lines was achieved by lentiviral infection. Lentiviral supernatants were generated as described previously. Cell viability was assessed after 3, 5 or 10 days of infection by using CellTiter-Blue.

Animal experiments

All animals used in this study were handled in accordance with federal and institutional guidelines, under a protocol approved by the Cornell University Institutional

Animal Care and Use Committee (IACUC). For more animal experimental details, please see the Supplemental Experimental Procedures.

Statistical analysis

Quantitative data were expressed as mean \pm sd (standard deviation, shown as error bar) from at least three independent experiments. Differences between two groups were examined statistically as indicated (* $p < 0.05$, ** $p < 0.01$, and *** $p < 0.001$).

RESULTS

Development of a highly selective and potent SIRT2 inhibitor

Most existing sirtuin inhibitors are either not very potent (e.g. with IC₅₀ values in the high micromolar range) or not very selective (i.e. they inhibit several different sirtuins). More potent and more selective sirtuin inhibitors would greatly aid in evaluating the therapeutic potential of targeting sirtuins. To develop potent inhibitors specific for a particular sirtuin, we used mechanism-based thioacyl lysine compounds. Thioacyl lysine peptides can react with NAD in the sirtuin active site, forming a relatively stable intermediate that inhibits sirtuin (Figure 1A) (Fatkins et al., 2006; Hawse et al., 2008; Smith and Denu, 2007). Recent studies suggested that different sirtuins may have different acyl group specificity (Du et al., 2011; Feldman et al., 2013; et al., 2013a; Zhu et al., 2012), which can be utilized to design inhibitors specific for different sirtuins (He et al., 2012; He et al., 2014). To target the sirtuins that can recognize aliphatic acyl groups, we synthesized four thioacyl lysine compounds, TA (thioacetyl) (Suzuki et al., 2009), TB (thiobutyryl), TH (thioheptanoyl), and TM (thiomyrystoyl) (Figure 1B), and then

analyzed their ability to inhibit different sirtuins.

Remarkable differences in the potency and selectivity of these compounds were observed by sirtuin activity assays *in vitro* (Figure 1C, Figure S1A). TA could inhibit SIRT1, SIRT2 and SIRT3, but not very potently. TB was a better SIRT1/SIRT2 inhibitor than TA. The IC₅₀ of TB for SIRT1 (3.8 μ M) and SIRT2 (0.43 μ M) were about 3 fold and >10-fold, respectively, better than those of TA (Figure 1C). Further increasing the size of the thioacyl group by three methylene groups lead to TH, which had even lower IC₅₀ values for SIRT1 (1.2 μ M) and SIRT2 (0.13 μ M). Remarkably, TM, with a 14-carbon thioacyl group, could inhibit SIRT2 with an IC₅₀ value of 0.028 μ M, but inhibited SIRT1 with an IC₅₀ value of 98 μ M and did not inhibit SIRT3 even at 200 μ M (Figure 1C). None of these compounds can efficiently inhibit SIRT5, SIRT6, or SIRT7. Thus, TM is a SIRT2-specific inhibitor *in vitro*. To facilitate later investigations of TM, we also synthesized the corresponding myristoyl lysine compound (M, Figure 1B) as an inactive control for TM. M differs from TM by only one atom (the S atom in TM is changed to an O atom in M). As expected, M did not show sirtuin inhibition even at 200 μ M (Figure 1C).

To further confirm that TM is a mechanism-based inhibitor of SIRT2, we performed substrate competition analyses for TM-mediated SIRT2 inhibition. At saturating NAD concentration, the apparent K_m value for acetyl-H3K9 peptide (acH3K9) increased with increasing TM concentrations, whereas the v_{max} remained relatively constant (Figure 1E). The double-reciprocal plot of 1/v versus 1/[acH3K9] revealed a series of lines that intersect at the 1/v axis (Figure S1C), suggesting that TM is competitive with acH3K9. This is consistent with our recent finding that SIRT2

possesses a large hydrophobic pocket that can accommodate the myristoyl group (Teng et al., 2015). At saturating aH3K9 concentration, both the apparent K_m value for NAD and v_{max} decreased with increasing TM concentrations (Figure 1F), suggesting that TM is uncompetitive with NAD, which is consistent with the fact that formation of the inhibitory covalent intermediate requires NAD. We then used liquid chromatography-mass spectrometry (LC-MS) to examine the formation of the stalled covalent intermediate. Ions with m/z of 1123.33 (the protonated intermediate) and 1145.25 (the sodium adduct of the intermediate) were detected only when TM was incubated with both SIRT2 and NAD (Figure 1D), but not without SIRT2 or NAD (Figure S1B). Overall, these results indicate that TM acts as a mechanism-based inhibitor of SIRT2.

TM exhibited potent anticancer activity

Sirtuin inhibitors have been reported to have anticancer properties. However, most of the inhibitors used are not very selective and thus, inhibiting which sirtuins can provide beneficial effects remains unclear. Having a potent and very selective SIRT2 inhibitor provided a unique opportunity to investigate whether inhibiting SIRT2 can be useful as an anticancer strategy. We initially explored this in several breast cancer cell lines because of the substantial tumor-promoting role of SIRT2 in breast cancer (McGlynn et al., 2014; Soung et al., 2014; Zhao et al., 2014) and the previous studies showing that SIRT2 inhibitors exert anti-proliferative effect against breast cancer cell lines (Di Fruscia et al., 2012; Neugebauer et al., 2008; Rotili et al., 2012; Seifert et al., 2014; Yoon et al., 2014). We assayed the ability of TA, TB, TH, and TM to inhibit three

human breast cancer cell lines, MCF-7, MDA-MB-468 and MDA-MB-231. The cytotoxicity of these compounds correlated with their in vitro SIRT2 inhibitory effects (Figure 2A and Figure S2A). TA, which showed modest SIRT1, SIRT2 and SIRT3 inhibition in vitro, did not inhibit cell viability at 50 μ M. TB had greater inhibitory effect on cell viability than TA, but only showed inhibition at 50 μ M. TH and TM were more potent than TA and TB. Compared with TH, the SIRT2-selective inhibitor TM showed greater inhibition of cell viability. The inactive inhibitor mimic M did not affect cell viability at 50 μ M. Similar result was also obtained in HeLa cells (Figure S2B). Next we treated eight different human normal and breast cancer cell lines with TM. As shown in Figure 2B, different malignant cells showed differential susceptibility to TM. And the two non-cancerous cell lines, MCF-10A and HME1, were much less sensitive to TM, suggesting that the cytotoxicity of TM is relatively selective toward cancer cells. We further evaluated the anticancer activity of TM using soft agar colony formation assay. TM significantly inhibited anchorage-independent growth of various cancer cells tested (Figure 2C and Figure S2C), while the control compound M did not (Figure 2C).

The correlation between the cytotoxic effects of TA, TB, TH, TM and M and their in vitro SIRT2 inhibitory activities suggests that SIRT2 inhibition could have anticancer effects. To further confirm this, we knocked down all seven sirtuins individually in MCF-7, MDA-MB-468, and HeLa cells, which were relatively sensitive to TM (Figure S3A). SIRT2 knockdown (KD) produced the strongest cytotoxicity in all the three cell lines tested (Figure 3A & S3B), which further supported SIRT2 inhibition as a promising anticancer strategy.

We then further examined the effect of SIRT2 KD in the same set of human

breast cancer and non-tumorigenic mammary cell lines in which the cytotoxic effect of TM was tested. SIRT2 KD significantly decreased cell viability in a time-dependent manner in MCF-7, MDA-MB-468, and MDA-MB-231 cells, but did not show much cytotoxicity in BT-549, SK-BR-3, and MDA-MB-453 cells or the non-transformed MCF-10A and HME1 cells (Figure 3B). In MCF-7 and MDA-MB-468 cells, SIRT2 KD resulted in less than 1% cell viability after 10 days of lentiviral infection (Figure S3C). Moreover, colony formation in soft agar by MCF-7 cells was dramatically diminished by SIRT2 KD (Figure 3D–3F). The knockdown data are thus consistent with the small molecule data, indicating that SIRT2 inhibition can effectively suppress cancer cell proliferation and that the anticancer effect of TM is likely through SIRT2 inhibition.

TM inhibits SIRT2 in cells

We next wanted to determine whether TM inhibits cancer cells by targeting SIRT2. We first carried out a number of experiments to validate that SIRT2 is the target of TM in cells. We conjugated biotin to TM and M to generate Biotin-TM and Biotin-M compounds (Figure S4A). We then added these compounds to either total protein extract (Figure 4A) or live cells (Figure 4B) to pull down sirtuins. Biotin-TM was able to pull down SIRT2 but not SIRT1 from the HEK293T cell extract. In contrast, Biotin-M, the inactive control compound, did not pull out SIRT2 (Figure 4A). When assayed using SIRT2 KD cells, the amount of SIRT2 pulled down by Biotin-TM was also decreased (Figure 4B). These data suggest that TM targets SIRT2 but not SIRT1 in cells.

Second, we confirmed that TM inhibits SIRT2 in cells by detecting the acetylation level of known SIRT2 as well as SIRT1 targets. In MCF-7 and MDA-MB-468 cells, TA,

TB, and TH, inhibited SIRT1, based on the acetylation level of a known SIRT1 deacetylation target, p53 (Figure 4D). In contrast, TM showed almost no inhibition of p53 deacetylation. By detecting the acetylation of α -tubulin, a known SIRT2 target, we monitored SIRT2 inhibition. TA or M, which did not inhibit SIRT2 well, did not affect the acetylation of α -tubulin. TB and TH, which have intermediate SIRT2 inhibition potency, slightly increased the acetylation of α -tubulin. TM, the best SIRT2 inhibitor, led to the greatest increase in α -tubulin acetylation (Figure 4C). The effect of TM on α -tubulin acetylation was dose-dependent, whereas M did not affect acetyl- α -tubulin level at 50 μ M (Figure 4E). Similarly, TM, but not M, increased the level of α -tubulin acetylation in MDA-MB-231 cells based on immunofluorescence imaging (Figure 4F). SIRT2 has been reported to be not only a deacetylase, but also a defatty-acylase (He et al., 2014; Liu et al., 2014), so we further examined the effect of TM on the defatty-acylase activity of SIRT2 in cells. Metabolic labeling of fatty-acylated proteins revealed that SIRT2 KD (Figure S4B) but not TM (Figure S4C) was able to elevate the fatty-acylation levels of many proteins, suggesting that in cells TM is a potent inhibitor of SIRT2 deacetylase but not defatty-acylase.

Finally, to confirm that the anticancer effect of TM is due to SIRT2 inhibition, we tested the sensitivity of cells to TM under SIRT2 overexpression or knockdown conditions. If TM inhibits cancer cells by targeting SIRT2, overexpression of SIRT2 would decrease the sensitivity of cells to TM (the increased SIRT2 level would require more TM for inhibition), while partial and transient knockdown of SIRT2 would increase the sensitivity. Indeed, overexpression of SIRT2 (Figure 4H) significantly decreased the cytotoxicity of TM (Figure 4G), while transient and partial knockdown of SIRT2 (Figure

S4E) sensitized cells to TM (Figure S4D). These results support the conclusion that the anticancer effect of TM is through SIRT2 inhibition instead of other off-target effects.

TM inhibits tumor growth in mouse models of breast cancer

To further demonstrate that SIRT2 inhibition can be useful for treating cancers, we tested TM in two mouse models of cancer. The first was a xenograft model in which the triple-negative breast cancer cell line, MDA-MB-231, was injected subcutaneously into immunocompromised mice. When tumor size reached ~200 mm³, the mice were divided into two groups and treated by either direct intratumor (IT) (Figure S5) or intraperitoneal (IP) (Figure 5) injection of the control vehicle solvent (DMSO) or TM (1.5 mg TM in 50 µL DMSO; n = 5) daily. Tumors were collected after 30-days of treatment and analyzed. TM treatment significantly inhibited tumor growth as compared to the control (Figure S5A, S5B, and 5A). Histopathological examination revealed central areas of necrosis in tumors from both DMSO and TM treated mice, but the necrosis was more extensive and the overall tumor size was smaller in the TM treated mice (Figures S5D and 5C). IT TM injection showed a stronger effect in reducing tumor volume and increasing areas of necrosis as compared to IP TM injection. Analysis of TM content in tissue samples from TM-treated mice showed that IP-administered TM reached the tumors, even though the serum concentration of TM was low and a significant amount of TM accumulated in abdominal fat (Figure 5D). TM did not cause significant toxicity in mice (one mouse from each treatment group died, likely due to infection caused by repeated IP injection but not due to TM toxicity) and no significant weight loss was observed in TM-treated mice (Figure S5C and 5B). Immunohistochemistry staining of

Ki-67 was performed to assess the effect of TM on the proliferation of tumor cells in vivo. As shown Figure 5E (upper panel) and 5F, as well as Figure S5F (upper panel) and S5G, a significant decrease in Ki-67+ cells was observed with TM treatment relative to vehicle treatment. To determine whether TM inhibits SIRT2 in vivo, we performed immunofluorescence staining of acetyl- α -tubulin in the xenograft tumors. As shown in Figure 5E (lower panel) and 5G, and Figure S5F (lower panel) and S5H, the acetyl- α -tubulin level was moderately but statistically significantly increased in tumors from TM treated mice compared with those from vehicle-treated mice, suggesting that TM indeed inhibits SIRT2 in vivo.

The second mouse model was the mammary tumor model driven by mammary gland-specific expression of polyoma middle T antigen under the control of mouse mammary tumor virus promoter/enhancer (MMTV-PyMT model) (Guy et al., 1992). The MMTV-PyMT mice received daily IP injections with either the control vehicle solvent (DMSO) or TM (1.5 mg TM in 50 μ L DMSO; n = 10). The Kaplan-Meier tumor-free survival curve showed that TM treatment significantly prolonged the tumor-free survival of mice compared with vehicle-treated mice (Figure 6A). While the average time to tumor onset in the control group was 48 days, the mean latency for TM-treated mice was 54 days. Histopathological examination revealed more extensive areas of necrosis in the neoplasms from TM-treated mice as compared to the control group (Figure 6B). A significant decrease in proliferation of tumor cells was observed with TM treatment relative to vehicle treatment as measured by Ki-67 staining (Figure 6C, upper panel, and 6D). A modest but statistically significant increase in the acetyl- α -tubulin level was observed in tumors from TM-treated mice compared to those from vehicle-treated mice

(Figure 6C, lower panel, and 6E), indicating that SIRT2 was inhibited by TM *in vivo*. The data demonstrate that SIRT2 inhibition with TM delays tumor onset in the MMTV-PyMT model and reduces tumor growth *in vivo*.

COMPARE analysis with the NCI-60 cancer cell panel points to possible mechanism of action for the SIRT2 inhibitor TM

To further investigate the anticancer effects of TM, we first examined whether the level of SIRT2 in different cell lines could be used to predict which cell lines would be more sensitive to SIRT2 inhibitors. We checked the SIRT2 protein level in all the eight human normal and breast cancer cell lines above (Figure 2B & 3B) to see if the sensitivity to TM correlated with SIRT2 level in these cell lines. Compared to MCF-10A and HME1 cells, the cancer cell lines showed relatively high SIRT2 expression. However, we did not see an obvious correlation between SIRT2 level and TM sensitivity (Figure S6A and S6B) among the cancer cell lines, suggesting that other factors account for the SIRT2 inhibitor sensitivity.

To examine the anticancer activity of TM against other malignancies and the molecular mechanisms underlying its activity, we submitted the TM compound to the Developmental Therapeutics Program of the National Cancer Institute (NCI) at the National Institutes of Health for screening against the NCI-60 panel of human cancer cell lines (Shoemaker, 2006) at a single dose of 10 μ M. The screening result showed that TM inhibited 36/56 of the NCI-60 cell lines by >50% at 10 μ M (Figure 7A). In particular, all the leukemia cell lines were very sensitive to TM and most of colon cancer cell lines were sensitive to TM. In contrast, melanoma and ovarian cancer cells were

less sensitive to TM. Consistent with our earlier findings (Figure 2), MCF-7 and MDA-MB-468 cells were very sensitive to TM. One discrepancy was noted for MDA-MB-231 cells, which were very sensitive to TM in the NCI-60 screening, but not very sensitive to TM in our study (IC₅₀ 34 μM). This could be due to differences in the MDA-MB-231 cells or the culture conditions used in NCI-60 screening and our laboratory. To confirm our findings with MDA-MB-231 cells, we purchased a new batch of MDA-MB-231 cells and showed that the sensitivity to TM was similar to that of the cells we tested earlier (Figure S2D). Despite the discrepancy with MDA-MB-231 cells, the screening results suggest that SIRT2 inhibitors can potentially be used to treat many types of cancers.

To investigate how SIRT2 inhibition halts cancer cell proliferation, we took advantage of NCI molecular target COMPARE analysis (Zaharevitz et al., 2002). NCI has accumulated many data sets regarding the properties of the NCI-60 cell lines, including gene expression, DNA methylation, protein expression, and post-translational modifications. The molecular target COMPARE analysis serves to correlate the response of the NCI-60 panel to a small molecule (TM in this case) to known molecular patterns. From this analysis, we found that the sensitivity of NCI-60 cell lines to TM correlated best with c-Myc phosphorylation/protein levels. In other words, cell lines with higher c-Myc phosphorylation/protein levels were more sensitive to TM (Table S1). The correlation between TM sensitivity and c-Myc is intriguing as c-Myc is an oncoprotein that is up-regulated in many cancers.

TM decreases c-Myc oncoprotein level in cancer cells

The correlation between TM efficacy and c-Myc was informative, but the small

correlation value (~ 0.5) was not sufficient to establish a mechanistic relationship. To further understand the connection, we measured c-Myc level in the cells treated with and without TM or M. TM decreased c-Myc protein level in a time-dependent manner in MCF-7 cells, whereas M treatment had no effect on the c-Myc protein level (Figure 7B). Similar effects of TM on c-Myc were also observed in K562 and MDA-MB-468 cells (Figure S6C and S6D). Consistent with the effect of TM, c-Myc abundance was also reduced by SIRT2 KD (Figure 7D), suggesting that TM works through SIRT2 inhibition to decrease c-Myc. To further establish that the reduction in c-Myc protein is important for the anticancer effect of TM, we examined whether the sensitivity of cancer cell lines to TM correlated with the decrease in c-Myc level induced by TM treatment. Among the six breast cancer cell lines in the NCI-60 panel, BT-549 did not respond to treatment with 10 μ M TM. At 10 μ M TM, the viability of BT-549 was close to 100%. This result was in line with our own findings (Figure 2B). Although higher concentrations of TM did decrease the viability of BT-549, the sensitivity was much lower than that of MCF-7 cells. Consistent with the reduced sensitivity to TM, SIRT2 KD in BT-549 cells did not decrease cell viability (Figure 3B and S3C). We therefore examined whether TM could affect c-Myc protein level in BT-549 cells. Consistent with the decreased TM sensitivity, TM treatment did not have a significant effect on c-Myc protein abundance in BT-549 cells (Figure 7C). SIRT2 KD also failed to decrease c-Myc level in BT-549 cells (Figure 7D). These data collectively suggest that the sensitivity of cancer cell lines to TM correlates with the ability of TM to decrease c-Myc level via SIRT2 inhibition in these cell lines. We further measured the IC₅₀ values of TM in six different cancer cell lines and the corresponding decrease in c-Myc level in these cell lines upon TM treatment.

Plotting the IC50 values against the decreases in c-Myc levels indicates that there was an excellent correlation between them (Figure 7E), supporting that the ability of TM to decrease c-Myc is important for its anticancer effect in the cell lines that are very sensitive to TM.

MCF-7 cells were then further analyzed for Myc-specific biological effects. Flow cytometry of TM-treated cells revealed a pronounced increase in cells arrested in G0/G1 phase, with a concomitant decrease of cells in S phase (Figure 8A). Treatment of TM resulted in significant cellular senescence by β -galactosidase staining (Figure 8B). Similar effects of TM on cell cycle progression and cellular senescence were also observed in K562 cells (Figure S6E and S6F), suggesting that the effect of TM-induced c-Myc decrease is not restricted to breast cancer cells. Overall, the phenotypes of G0/G1 cell cycle arrest and cellular senescence are consistent with the anticipated effects of inhibiting cellular c-Myc function (Wu et al., 2007).

To further establish that decreasing c-Myc is important for the anticancer effect of TM, we examined whether forced overexpression of c-Myc in MCF-7 cells is able to reduce TM-mediated cytotoxicity. Cells were transfected with c-Myc for 12 hr before being treated with TM. As shown in Figure 8C and S6G, overexpression of c-Myc significantly reduced the cytotoxicity effect of TM. Together, these results demonstrate TM decreases c-Myc, which is important for the cytotoxicity of TM in tumor cell, although it is likely not the only mechanism that underlies the cytotoxicity.

The c-Myc mRNA level was not affected by TM treatment, suggesting that TM does not affect c-Myc transcription (Figure 8D, Figure S6H). Therefore, the effect of TM on c-Myc protein turnover was tested. The half-life of c-Myc was shortened by TM

treatment, suggesting that TM promoted c-Myc degradation (Figure 8F). Treatment with a proteasome inhibitor, MG132, prevented the TM-induced down-regulation of c-Myc, suggesting that TM promoted the proteasomal degradation of c-Myc (Figure 8E). Increased proteasomal degradation was associated with increased c-Myc ubiquitination (Figure 8G). It was previously reported that SIRT2 can suppress the expression of NEDD4, an E3 ubiquitin ligase for c-Myc (Liu et al., 2013), which could explain why SIRT2 inhibition promotes c-Myc degradation. Indeed, NEDD4 was up-regulated by TM at the transcriptional level (Figure 8H and Figure S6H) and also modestly at the protein level (Figure 8I and Figure S6C) in both MCF-7 and K562 cells. However, this is not a universal mechanism as alteration of NEDD4 level was not detected in TM-treated MDA-MB-468 cells despite the observed reduction in c-Myc protein abundance (Figure S6D & H). As TM regulates the protein stability of c-Myc in all three cell lines, we checked the effect of TM on the transcription levels of several additional known E3 ligases that destabilize c-Myc (Choi et al., 2010; Kim et al., 2003; Liu et al., 2013; Paul et al., 2013; Welcker et al., 2004). As shown in Figure S6H, NEDD4 and TRPC4AP were increased in MCF-7 and K562 cells, but not in MDA-MB-468 cells; FBXW7 and STUB1 were up-regulated only in MDA-MB-468 cells; FBXO32 was increased in all the three cell lines. However, none of the E3 ligase genes was obviously up-regulated by TM in BT-549 cells in which neither cell viability nor c-Myc level was affected by TM. These results suggested that SIRT2 inhibition led to up-regulation of several c-Myc E3 enzymes, which may result in the destabilization of c-Myc by TM.

DISCUSSION

Previous reports have suggested that SIRT1 or SIRT2 inhibitors can have anticancer activity. However, the potency of most of these inhibitors is modest, with IC50 values in the micromolar range at inhibiting purified sirtuins. Most of the sirtuin inhibitors tested for anticancer activity are also not very selective and can inhibit several sirtuins. The modest potency and selectivity make it hard to rule out off-target effects and pinpoint which sirtuin should be targeted for treating cancers. Our SIRT2 inhibitor TM described here has an excellent combination of potency and selectivity that allowed us to conclude that inhibiting SIRT2 produces anticancer effects in a variety of human cancer cell lines. Knocking down of all seven sirtuins also confirmed that SIRT2 is important for the viability of various cancer cell lines while knocking down other sirtuins either had no significant effect or much less effect on cancer cell viability.

C-Myc is an important oncoprotein and is up-regulated in many human tumors. Thus, it has been considered as a promising cancer target. So far, no small molecules can directly target c-Myc in vivo. Recent studies showed that bromodomain inhibitors targeting BRD4 can suppress c-Myc transcription and inhibit tumorigenesis (Delmore et al., 2011). Our studies demonstrate that inhibiting SIRT2 offers a different way to target c-Myc. We show here that our SIRT2 inhibitor TM can effectively decrease the level of c-Myc in various cancer cell lines. Our data suggest that the ability of TM to decrease c-Myc abundance in different cell lines correlates with the sensitivity of the cell lines to TM. We further demonstrate here that decreasing c-Myc protein level is an important mechanism that accounts for hypersensitivity of certain cancer cell lines to TM. However, it should be pointed out that effects on other SIRT2-regulated pathways may also contribute to the activity of TM in cancer cells. This is especially true given that

even cells without TM-induced c-Myc decrease (e.g. MDA-MB-231 and BT-549 cells) can still be inhibited by TM at higher concentrations. This also likely explains why c-Myc overexpression confers some but not complete resistance to TM (Figure 8C). We found that TM promotes the proteolytic degradation of c-Myc without affecting its transcription, which serves as an important but perhaps not the only mechanism by which TM destabilizes c-Myc. Aberrant translational control of the Myc oncoprotein has been implicated in many cancers (Chappell et al., 2000; Wolfe et al., 2014) and might also be involved in TM-induced reduction in c-Myc level. Our work establishes SIRT2 inhibition as a strategy to target the oncoprotein c-Myc, which is effective in many human cancer cell lines. Future detailed mechanistic investigations of the SIRT2/c-Myc regulatory pathway could potentially lead to the identification of additional therapeutic targets.

The roles of sirtuins in cancer have been a topic of debate. Both tumor-promoting and tumor-suppressing roles of SIRT1 have been reported. For SIRT2, Kim et al. reported that SIRT2 is a tumor suppressor because Sirt2 KO mice develop tumors earlier than WT mice (Kim et al., 2011a). Serrano and co-workers did not find a cancer-prone phenotype in unchallenged Sirt2 KO mice that they generated, although they did observe that Sirt2 KO mice had increased tumorigenesis when challenged with carcinogens (Serrano et al., 2013). Contradictory to these genetic studies that pointed to a weak tumor suppressor role of SIRT2, we found that inhibiting SIRT2 with TM has broad anticancer activity in many cancer cell lines.

Different outcomes for mouse genetic studies and pharmacological studies in cancer cells are not without precedent. Similar cases have been well documented in the literature (Weiss et al., 2007). There are several possible explanations. First, there are

several examples of factors that have tumor suppressor activity in normal cells but nevertheless are required for the growth and survival of transformed cells. For example, loss of function for the DNA damage checkpoint kinase ATR causes modest tumor predisposition, but greatly impairs the growth of established tumors (Bartek et al., 2012). SIRT2 has been identified as a regulator of mitotic chromosome segregation (Kim et al., 2011a), a function that could account for the weak tumor predisposition phenotype in Sirt2-deficient mice given the oncogenic consequences of genomic instability. Nevertheless, a greater dependency of transformed cells on SIRT2 due to increased mitotic and other stresses, or because of the regulation of other targets such as c-Myc by SIRT2, result in heightened sensitivity to SIRT2 inhibition in cancer cells. It also should be noted that small molecules may have off target effects, which could contribute to observed pharmacological effects. While it is difficult to completely rule out this possibility for the anticancer effect of TM, our studies using the inactive control compound (M) and the SIRT2 KD studies suggest that the anticancer effect is largely through SIRT2 inhibition.

An alternative explanation relates to the fact that in a genetic knockout, the protein is gone and thus all the enzymatic activities and protein-protein interactions involving the enzyme also are gone. In contrast, when using a small molecule to inhibit the enzyme, the protein is intact and so are the protein-protein interactions that involve the protein. In the case of SIRT2, another layer of complexity is that SIRT2 has multiple enzymatic functions. We and others recently found that sirtuins are not only deacetylases. Some sirtuins, such as SIRT5 (Du et al., 2011) and SIRT6 (Jiang et al., 2013), prefer to hydrolyze other acyl lysine modifications. Perhaps more surprising is

the fact that even the well-studied deacetylases (SIRT1, SIRT2, and SIRT3) can remove long chain fatty acyl groups efficiently (He et al., 2014; Liu et al., 2014). Although the exact substrate proteins for the defatty-acylase activity of SIRT2 remain to be identified, our preliminary studies showed that the fatty-acylation levels of many proteins were elevated when SIRT2 was knocked down (Figure S4B), but not when SIRT2 inhibitor TM was used (Figure S4C). Thus, the small molecule inhibitor may selectively target one of the enzymatic functions of SIRT2, thus contributing to the fact that small molecule inhibitors may produce beneficial pharmacological effects that are different from genetic knockout.

ACKNOWLEDGMENTS

We thank the Development Therapeutic Program at National Cancer Institute (NCI) for screening TM in the NCI60 cell lines. This work is supported in part by an intercampus seed grant from Cornell University and a transformative R01 grant from NIH (CA163255).

REFERENCES

- Bartek J, Mistrik M, Bartkova J. Thresholds of replication stress signaling in cancer development and treatment. *Nat. Struct Mol. Biol.* 2012; 19:5–7. [PubMed: 22218289]
- Beroukhir R, Mermel CH, Porter D, Wei G, Raychaudhuri S, Donovan J, Barretina J, Boehm JS, Dobson J, Urashima M, et al. The landscape of somatic copy-number alteration across human cancers. *Nature.* 2010; 463:899–905. [PubMed: 20164920]
- Chappell SA, LeQuesne JP, Paulin FE, deSchoolmeester ML, Stoneley M, Soutar RL, Ralston SH, Helfrich MH, Willis AE. A mutation in the c-myc-IRES leads to enhanced internal ribosome entry in multiple myeloma: a novel mechanism of oncogene de-regulation. *Oncogene.* 2000; 19:4437–4440. [PubMed: 10980620]
- Chen J, Chan AW, To KF, Chen W, Zhang Z, Ren J, Song C, Cheung YS, Lai PB, Cheng SH, et al. SIRT2 overexpression in hepatocellular carcinoma mediates epithelial to mesenchymal transition by protein kinase B/glycogen synthase kinase-3beta/beta-catenin signaling. *Hepatology.* 2013; 57:2287–2298. [PubMed: 23348706]
- Cheon MG, Kim W, Choi M, Kim JE. AK-1, a specific SIRT2 inhibitor, induces cell cycle arrest by downregulating Snail in HCT116 human colon carcinoma cells. *Cancer Lett.* 2015; 356:637–645. [PubMed: 25312940]
- Choi SH, Wright JB, Gerber SA, Cole MD. Myc protein is stabilized by suppression of a novel E3 ligase complex in cancer cells. *Genes Dev.* 2010; 24:1236–1241. [PubMed: 20551172]

Delmore JE, Issa GC, Lemieux ME, Rahl PB, Shi J, Jacobs HM, Kastiris E, Gilpatrick T, Paranal RM, Qi J, et al. BET bromodomain inhibition as a therapeutic strategy to target c-Myc. *Cell*. 2011; 146:904–917. [PubMed: 21889194]

Di Fruscia P, Ho KK, Laohasinnarong S, Khongkow M, Kroll SH, Islam SA, Sternberg MJ, Schmidtkunz K, Jung M, Lam EW, Fuchter MJ. The Discovery of Novel 10,11-Dihydro-5H-dibenz[b,f]azepine SIRT2 Inhibitors. *Medchemcomm*. 2012

Du J, Zhou Y, Su X, Yu J, Khan SH, Kim J, Woo J, Kim JH, Choi BH, et al. Sirt5 is an NAD-dependent protein lysine demalonylase and desuccinylase. *Science*. 2011; 334:806–809. [PubMed: 22076378]

Fang Y, Nicholl MB. Sirtuin 1 in malignant transformation: Friend or foe? *Cancer Lett*. 2011; 306:10–14. [PubMed: 21414717]

Fatkins DG, Monnot AD, Zheng W. N ϵ -Thioacetyl-lysine: A multi-facet functional probe for enzymatic protein lysine N ϵ -deacetylation. *Bioorg. Med. Chem. Lett*. 2006; 16:3651–3656. [PubMed: 16697640]

Feldman JL, Baeza J, Denu JM. Activation of the protein deacetylase SIRT6 by long-chain fatty acids and widespread deacylation by mammalian sirtuins. *J. Biol. Chem*. 2013; 288:31350–31356. [PubMed: 24052263]

Guy CT, Cardiff RD, Muller WJ. Induction of mammary tumors by expression of polyomavirus middle T oncogene: a transgenic mouse model for metastatic disease. *Mol. Cell Biol*. 1992; 12:954–961. [PubMed: 1312220]

Haigis MC, Sinclair DA. Mammalian Sirtuins: Biological Insights and Disease Relevance. *Annu. Rev. Pathol*. 2010; 5:253–295. [PubMed: 20078221]

Hawse WF, Hoff KG, Fatkins DG, Daines A, Zubkova OV, Schramm VL, Zheng W,

- Wolberger C. Structural insights into intermediate steps in the Sir2 deacetylation reaction. *Structure*. 2008; 16:1368–1377. [PubMed: 18786399]
- He B, Du J, Lin H. Thiosuccinyl peptides as Sirt5-specific inhibitors. *J. Am. Chem. Soc.* 2012; 134:1922–1925. [PubMed: 22263694]
- He B, Hu J, Zhang X, Lin H. Thiomyristoyl peptides as cell-permeable Sirt6 inhibitors. *Org. Biomol. Chem.* 2014; 12:7498–7502. [PubMed: 25163004]
- Heltweg B, Gatbonton T, Schuler AD, Posakony J, Li H, Goehle S, Kollipara R, Depinho RA, Gu Y, Simon JA, Bedalov A. Antitumor activity of a small-molecule inhibitor of human silent information regulator 2 enzymes. *Cancer Res.* 2006; 66:4368–4377. [PubMed: 16618762]
- Herranz D, Serrano M. SIRT1: recent lessons from mouse models. *Nat. Rev. Cancer.* 2010; 10:819–823. [PubMed: 21102633]
- Hoffmann G, Breitenbucher F, Schuler M, Ehrenhofer-Murray AE. A novel sirtuin 2 (SIRT2) inhibitor with p53-dependent pro-apoptotic activity in non-small cell lung cancer. *J. Biol. Chem.* 2014; 289:5208–5216. [PubMed: 24379401]
- Imai, S-i; Armstrong, CM.; Kaeberlein, M.; Guarente, L. Transcriptional silencing and longevity protein Sir2 is an NAD-dependent histone deacetylase. *Nature*. 2000; 403:795–800. [PubMed: 10693811]
- Imai, S-i; Guarente, L. Ten years of NAD-dependent SIR2 family deacetylases: implications for metabolic diseases. *Trends Pharmacol. Sci.* 2010; 31:212–220. [PubMed: 20226541]
- Jiang H, Khan S, Wang Y, Charron G, He B, Sebastian C, Du J, Kim R, Ge E, Mostoslavsky R, et al. SIRT6 regulates TNF-alpha secretion through hydrolysis

of long-chain fatty acyl lysine. *Nature*. 2013; 496:110–113. [PubMed: 23552949]

Kim HS, Vassilopoulos A, Wang RH, Lahusen T, Xiao Z, Xu X, Li C, Veenstra TD, Li B, Yu H, et al. SIRT2 maintains genome integrity and suppresses tumorigenesis through regulating APC/C activity. *Cancer Cell*. 2011a; 20:487–499. [PubMed: 22014574]

Kim SY, Herbst A, Tworkowski KA, Salghetti SE, Tansey WP. Skp2 regulates Myc protein stability and activity. *Mol. Cell*. 2003; 11:1177–1188. [PubMed: 12769843]

Kim WJ, Lee JW, Quan C, Youn HJ, Kim HM, Bae SC. Nicotinamide inhibits growth of carcinogen induced mouse bladder tumor and human bladder tumor xenograft through up-regulation of RUNX3 and p300. *J. Urol*. 2011b; 185:2366–2375. [PubMed: 21511279]

Lee, J-H.; Choy, ML.; Marks, PA. Chapter Two - Mechanisms of Resistance to Histone Deacetylase Inhibitors. In: Steven, G., editor. *Adv. Cancer Res.* Academic Press; 2012. p. 39-86.

Liu PY, Xu N, Malyukova A, Scarlett CJ, Sun YT, Zhang XD, Ling D, Su SP, Nelson C, Chang DK, et al. The histone deacetylase SIRT2 stabilizes Myc oncoproteins. *Cell Death Differ*. 2013; 20:503–514. [PubMed: 23175188]

Liu Z, Yang T, Li X, Peng T, Hang HC, Li XD. Integrative Chemical Biology Approaches for Identification and Characterization of "Erasers" for Fatty-Acid-Acylated Lysine Residues within Proteins. *Angew Chem. Int Ed Engl*. 2014

Mahajan SS, Scian M, Sripathy S, Posakony J, Lao U, Loe TK, Leko V, Thalhofer A, Schuler AD, Bedalov A, Simon JA. Development of pyrazolone and isoxazol-5-one cambinol analogues as sirtuin inhibitors. *J. Med. Chem*. 2014; 57:3283–

3294. [PubMed: 24697269]

Marks PA, Breslow R. Dimethyl sulfoxide to vorinostat: development of this histone deacetylase inhibitor as an anticancer drug. *Nat. Biotechnol.* 2007; 25:84–90. [PubMed: 17211407]

McCarthy AR, Sachweh MC, Higgins M, Campbell J, Drummond CJ, van Leeuwen IM, Pirrie L, Ladds MJ, Westwood NJ, Lain S. Tenovin-D3, a novel small-molecule inhibitor of sirtuin SirT2, increases p21 (CDKN1A) expression in a p53-independent manner. *Mol. Cancer Ther.* 2013; 12:352–360. [PubMed: 23322738]

McGlynn LM, Zino S, MacDonald AI, Curle J, Reilly JE, Mohammed ZM, McMillan DC, Mallon E, Payne AP, Edwards J, Shiels PG. SIRT2: tumour suppressor or tumour promoter in operable breast cancer? *Eur. J. Cancer.* 2014; 50:290–301. [PubMed: 24183459]

Meyer N, Penn LZ. Reflecting on 25 years with MYC. *Nat. Rev. Cancer.* 2008; 8:976–990. [PubMed: 19029958]

Neugebauer RC, Uchiechowska U, Meier R, Hruby H, Valkov V, Verdin E, Sippl W, Jung M. Structure-activity studies on splitomicin derivatives as sirtuin inhibitors and computational prediction of binding mode. *J. Med. Chem.* 2008; 51:1203–1213. [PubMed: 18269226]

Paul I, Ahmed SF, Bhowmik A, Deb S, Ghosh MK. The ubiquitin ligase CHIP regulates c-Myc stability and transcriptional activity. *Oncogene.* 2013; 32:1284–1295. [PubMed: 22543587]

Peng C, Lu Z, Xie Z, Cheng Z, Chen Y, Tan M, Luo H, Zhang Y, He W, Yang K, et al. The first identification of lysine malonylation substrates and its regulatory

- enzyme. *Mol. Cell. Proteomics*. 2011; 10
- Rotili D, Tarantino D, Nebbioso A, Paolini C, Huidobro C, Lara E, Mellini P, Lenoci A, Pezzi R, Botta G, et al. Discovery of salermide-related sirtuin inhibitors: binding mode studies and antiproliferative effects in cancer cells including cancer stem cells. *J. Med. Chem.* 2012; 55:10937–10947. [PubMed: 23189967]
- Seifert T, Malo M, Kokkola T, Engen K, Friden-Saxin M, Wallen EA, Lahtela-Kakkonen M, Jarho EM, Luthman K. Chroman-4-one- and chromone-based sirtuin 2 inhibitors with antiproliferative properties in cancer cells. *J. Med. Chem.* 2014; 57:9870–9888. [PubMed: 25383691]
- Serrano L, Martinez-Redondo P, Marazuela-Duque A, Vazquez BN, Dooley SJ, Voigt P, Beck DB, Kane-Goldsmith N, Tong Q, Rabanal RM, et al. The tumor suppressor SirT2 regulates cell cycle progression and genome stability by modulating the mitotic deposition of H4K20 methylation. *Genes Dev.* 2013; 27:639–653. [PubMed: 23468428]
- Shoemaker RH. The NCI60 human tumour cell line anticancer drug screen. *Nat. Rev. Cancer.* 2006; 6:813–823. [PubMed: 16990858]
- Smith BC, Denu JM. Mechanism-based Inhibition of Sir2 deacetylases by thioacetyl-lysine peptide. *Biochemistry.* 2007; 46:14478–14486. [PubMed: 18027980]
- Soung YH, Pruitt K, Chung J. Epigenetic silencing of ARRDC3 expression in basal-like breast cancer cells. *Sci. Rep.* 2014; 4:3846. [PubMed: 24457910]
- Stünkel W, Campbell RM. Sirtuin 1 (SIRT1): the misunderstood HDAC. *J. Biomol. Screen.* 2011; 16:1153–1169. [PubMed: 22086720]
- Suzuki T, Asaba T, Imai E, Tsumoto H, Nakagawa H, Miyata N. Identification of a cell-

- active non-peptide sirtuin inhibitor containing N-thioacetyl lysine. *Bioorg. Med. Chem. Lett.* 2009; 19:5670–5672. [PubMed: 19700324]
- Teng YB, Jing H, Aramsangtienchai P, He B, Khan S, Hu J, Lin H, Hao Q. Efficient demyristoylase activity of SIRT2 revealed by kinetic and structural studies. *Sci. Rep.* 2015; 5:8529. [PubMed: 25704306]
- Weiss WA, Taylor SS, Shokat KM. Recognizing and exploiting differences between RNAi and small-molecule inhibitors. *Nat. Chem. Biol.* 2007; 3:739–744. [PubMed: 18007642]
- Welcker M, Orian A, Jin J, Grim JE, Harper JW, Eisenman RN, Clurman BE. The Fbw7 tumor suppressor regulates glycogen synthase kinase 3 phosphorylation-dependent c-Myc protein degradation. *Proc. Natl. Acad. Sci. U S A.* 2004; 101:9085–9090. [PubMed: 15150404]
- Wolfe AL, Singh K, Zhong Y, Drewe P, Rajasekhar VK, Sanghvi VR, Mavrakis KJM, Roderick JE, Van der Meulen J, et al. RNA G-quadruplexes cause eIF4A-dependent oncogene translation in cancer. *Nature.* 2014; 513:65–70. [PubMed: 25079319]
- Wu CH, van Riggelen J, Yetil A, Fan AC, Bachireddy P, Felsner DW. Cellular senescence is an important mechanism of tumor regression upon c-Myc inactivation. *Proc. Natl. Acad. Sci. U S A.* 2007; 104:13028–13033. [PubMed: 17664422]
- Yang MH, Laurent G, Bause AS, Spang R, German N, Haigis MC, Haigis KM. HDAC6 and SIRT2 regulate the acetylation state and oncogenic activity of mutant K-RAS. *Mol. Cancer Res.* 2013; 11:1072–1077. [PubMed: 23723075]

- Yoon YK, Ali MA, Wei AC, Shirazi AN, Parang K, Choon TS. Benzimidazoles as new scaffold of sirtuin inhibitors: green synthesis, in vitro studies, molecular docking analysis and evaluation of their anti-cancer properties. *Eur. J. Med. Chem.* 2014; 83:448–454. [PubMed: 24992072]
- Zaharevitz DW, Holbeck SL, Bowerman C, Svetlik PA. COMPARE: a web accessible tool for investigating mechanisms of cell growth inhibition. *J. Mol. Graph Model.* 2002; 20:297–303. [PubMed: 11858638]
- Zhang Y, Au Q, Zhang M, Barber JR, Ng SC, Zhang B. Identification of a small molecule SIRT2 inhibitor with selective tumor cytotoxicity. *Biochem. Biophys. Res. Commun.* 2009; 386:729–733. [PubMed: 19559674]
- Zhao D, Mo Y, Li MT, Zou SW, Cheng ZL, Sun YP, Xiong Y, Guan KL, Lei QY. NOTCH-induced aldehyde dehydrogenase 1A1 deacetylation promotes breast cancer stem cells. *J. Clin Invest.* 2014; 124:5453–5465. [PubMed: 25384215]
- Zhao D, Zou S-W, Liu Y, Zhou X, Mo Y, Wang P, Xu Y-H, Dong B, Xiong Y, Lei Q-Y, Guan K-L. Lysine-5 acetylation negatively regulates lactate dehydrogenase A and is decreased in pancreatic cancer. *Cancer cell.* 2013; 23:464–476. [PubMed: 23523103]
- Zhu AY, Zhou Y, Khan S, Deitsch KW, Hao Q, Lin H. Plasmodium falciparum Sir2A preferentially hydrolyzes medium and long chain fatty acyl lysine. *ACS Chem. Biol.* 2012; 7:155–159. [PubMed: 21992006]

FIGURE LEGENDS

Figure 1. Development of mechanism-based inhibitor of sirtuins. (A) The enzymatic reaction mechanism of sirtuin-catalyzed NAD-dependent deacylation (upper panel). Thioacyl lysine compounds act as suicide substrates to inhibit sirtuins (lower panel). (B) Structures of four different thioacyl lysine sirtuin inhibitors, TA, TB, TH, and TM. M, which differs from TM by just one atom (highlighted by yellow color), is an inactive control of TM. (C) IC₅₀ (μM) values of the TA, TB, TH, TM and M against SIRT1–7. IC₅₀ values derived from Graphpad Prism are presented as mean values from three independent experiments. (D) Mass spectrometry detection of the stable covalent intermediate formed by TM and NAD. (E, F) Henri-Michaelie-Menten plots showing acH3K9 (E) and NAD (F) competition analyses of TM-mediated SIRT2 inhibition. Error bars represent mean ± sd. See also Figure S1.

Figure 2. TM inhibits human cancer cells. (A) Cell viability of MCF-7 and MDA-MB-468 cells treated with the indicated inhibitors for 72 hr. (B) Cell viability of the indicated human normal and breast cancer cells treated with TM for 72 hr. IC₅₀ values were means from 3 independent experiments. (C) Soft agar colony formation of MCF-7 cells treated with ethanol, TM (25 μM in ethanol) or M (25 μM in ethanol). Representative images of colonies were shown on the left panel. Quantification of the colony numbers was shown on the right panel. The y axis represents percent colony number relative to ethanol-treated cells. Statistics, two-tailed Student's t-test. Error bars represent mean ± sd. ***p < 0.001. See also Figure S2.

Figure 3. SIRT2 KD decreases the viability of various cancer cell lines. (A) Cell viability of MCF-7 and MDA-MB-468 cells infected with lentivirus carrying luciferase shRNA (Ctrl) or SIRT1–7 shRNAs for 72 hr. The heat map presents average relative cell viability compared to Ctrl shRNA-infected cells from three independent experiments. (B) Cell viability of various human normal and breast cancer cells infected with lentivirus carrying luciferase (Ctrl) or SIRT2 shRNAs. (C) Representative Western blots showing the knockdown efficiency of SIRT2 in MCF-7 and BT-549 cells. (D) Soft agar colony formation of MCF-7 cells transfected with scrambled siRNA or SIRT2 siRNA. (E) Quantification of the colony numbers in (D). The y axis represents percent colony number relative to scrambled siRNA-transfected cells. Statistics, two-tailed Student's t-test. (F) Representative Western blots showing the knockdown efficiency of SIRT2 by siRNAs in MCF-7 cells. Error bars represent mean \pm sd. *** $p < 0.001$. See also Figure S3.

Figure 4. TM specifically inhibits SIRT2 in cells. (A) Pull-down assay to detect the binding of Biotin-M (10 μ M) and Biotin-TM (10 μ M) to SIRT1 and SIRT2 in HEK293T total cell lysate. (B) Pull-down assay to detect the binding of Biotin-TM (50 μ M) to SIRT2 in MCF-7 cells. D-Biotin (50 μ M) was used as a negative control. (C) Immunoblot for the acetyl- α -tubulin (K40) levels in SIRT2-overexpressing MCF-7 cells treated with indicated inhibitors (25 μ M) for 6 hr. (D) Immunoblot for the acetylation of p53 (K382) in MCF-7 or MDA-MB-468 cells treated with TSA (200 nM) and the indicated inhibitors (25 μ M) for 6 hr. (E) Immunoblot for acetyl- α -tubulin (K40) levels in MCF-7 cells treated with TM or M for 6 hr. (F) Immunofluorescence detection of the acetyl- α -tubulin (K40) level in MDA-

MB-231 cells treated with ethanol, M or TM (25 μ M in ethanol) for 6 hr. **(G)** Effect of SIRT2 overexpression on the cytotoxicity effect of TM. MCF-7 cells were transfected with pCMV vector or pCMV-SIRT2 for 12 hr before being treated with 25 μ M of TM for 12 or 24 hr. The y axis represents relative cell viability compared to ethanol-treated controls. Statistics, two-tailed Student's t-test. **(H)** SIRT2 overexpression in **(G)** was confirmed by Western blot. Error bars represent mean \pm sd. *** $p < 0.001$. See also Figure S4.

Figure 5. Analysis of tumor growth and histopathological findings of xenografted mice treated by intraperitoneal TM injection. Mice bearing MDA-MB-231 human breast cancer xenograft were divided into two groups and treated by IP injection with either the vehicle (DMSO) or TM (1.5 mg TM in 50 μ L DMSO; $n = 5$) daily. Tumors were collected after 30-day treatment. **(A)** Tumor growth chart. Arrows indicate time point when an animal was found dead (1 untreated, 1 treated). Statistics, paired Student's t -test. **(B)** Mouse body weight chart. **(C)** Hematoxylin and eosin staining of tumor tissues after 30 days of treatment with DMSO or TM. **(D)** Detection of TM in mouse serum, fat and tumor tissues by mass spectrometry. **(E)** Representative images of Ki-67 immunohistochemistry staining and acetyl- α -tubulin (K40) immunofluorescence staining of tumor tissues after 30 days of treatment with DMSO or TM. **(F)** Quantification of Ki-67+ cells in **(E)**. The y axis represents Ki-67+ cells per high power field (10 HPFs/tumor for all the tumors analyzed, $n = 3$ for DMSO, $n = 4$ for TM). Statistics, unpaired Student's t-test. **(F)** Quantification of acetyl- α -tubulin fluorescence intensity in **(E)** by ImageJ. The y axis represents integrated intensity per cell. (10 HPFs/tumor for all the

tumors analyzed, n = 3 for DMSO, n = 4 for TM). Statistics, unpaired Student's t-test. Error bars represent mean \pm sd. *p < 0.05, **p < 0.01. See also Figure S5.

Figure 6. Mammary tumorigenesis in MMTV-PyMT female mice following intraperitoneal TM injection. (A) Kaplan-Meier tumor-free survival curve of MMTV-PyMT mice treated by IP injection with either the vehicle (DMSO) or TM (1.5 mg TM in 50 μ L DMSO; n = 10) daily. The x-axis shows mice age; the y-axis shows proportion of mice remaining tumor-free. Statistics, log-rank test. (B) Hematoxylin and eosin staining of mammary tumors after 30 days of treatment with either DMSO or TM. (C) Representative images of Ki-67 immunohistochemistry staining and acetyl- α -tubulin (K40) immunofluorescence staining of tumor tissues after 30 days of treatment with either DMSO or TM. (D) Quantification of Ki-67+ cells in (C). The y axis shows Ki-67+ cells per high power field (10 HPFs/tumor for all the tumors analyzed, n = 4 for DMSO, n = 4 for TM). Statistics, unpaired Student's t-test. (E) Quantification of acetyl- α -tubulin fluorescence intensity in (C) by ImageJ. The y axis shows integrated intensity per cell. (10 HPFs/tumor for all the tumors analyzed, n = 8 for DMSO, n = 8 for TM). Statistics, unpaired Student's t-test. Error bars represent mean \pm sd. *p < 0.05, **p < 0.01.

Figure 7. TM inhibits various types of human cancer cell lines and decreases c-Myc protein level. (A) NCI-60 cell line screening of TM. NCI-60 cell lines were cultured with and without 10 μ M TM for 24 hr. The percent growth of TM-treated cells compared to the controls is shown. The horizontal dotted red line shows 50% growth. (B) The c-Myc protein levels in MCF-7 cells treated with TM (25 μ M) or M (25 μ M). (C) The c-Myc

protein levels in BT-549 cells treated with TM (25 μ M). **(D)** The levels of c-Myc, SIRT2 and α -tubulin in MCF-7 or BT-549 cells infected with luciferase or SIRT2 shRNAs for 72 hr. **(E)** The correlation between the ability of TM to inhibit cancer cell lines and its ability to decrease c-Myc level. The x axis shows IC50 values of TM in different cell lines. The y axis shows the TM-induced decreases in c-Myc level. Relative c-Myc level was obtained by comparing the c-Myc protein level in cells treated with TM for 24 hr to that in vehicle-treated control cells. Error bars represent mean \pm sd. See also Figure S6.

Figure 8. Decreasing c-Myc protein abundance contributes to the anticancer effect of TM. **(A)** Cell cycle distribution (assessed by propidium iodide staining-coupled flow cytometry) of MCF-7 cells treated with TM (25 μ M) for 0, 24, 48 or 72 hr. **(B)** Acidic β -gal (β -gal) staining in MCF-7 cells treated with TM (25 μ M) for 5 days. Representative images were shown in the upper panel, quantification was shown as percentage of β -gal+ cells in the lower panel. Statistics, two-tailed Student's t-test. **(C)** Effect of c-Myc overexpression on the cytotoxicity effect of TM. MCF-7 cells were transfected with pCDH vector or pCDH-c-Myc for 12 hr before being treated with TM for 72 hr. Statistics, two-tailed Student's t-test. **(D)** The mRNA levels of c-Myc in MCF-7 cells treated with TM (25 μ M) or M (25 μ M) analyzed by RT-PCR. **(E)** Effect of MG132 on TM-mediated decrease in c-Myc protein level in MCF-7 cells. Cells were treated with ethanol or TM (25 μ M in ethanol) for 4 hr and then MG132 (10 μ M) for 2 hr. **(F)** Effect of TM on c-Myc degradation in MCF-7 cells. Cells were incubated ethanol or TM (25 μ M in ethanol) for 4 hr and then with CHX (10 μ g/mL) for 0, 0.5, 1, or 2 hr. Loading was normalized based on the level of the internal control, actin. The relative c-Myc protein levels at different

time point of CHX treatment were calculated by normalizing to the corresponding level without CHX treatment. The relative c-Myc levels were plotted against the time of treatment with CHX. **(G)** Effect of TM (25 μ M) on the polyubiquitination of c-Myc in MCF-7. **(H)** The mRNA level of NEDD4 in MCF-7 cells treated with TM (25 μ M) for 12 hr. **(I)** Western blot analysis of NEDD4 protein level in MCF-7 cells treated with TM (25 μ M). Error bars represent mean \pm sd. **p < 0.01, ***p < 0.001. See also Figure S6

Figure 1

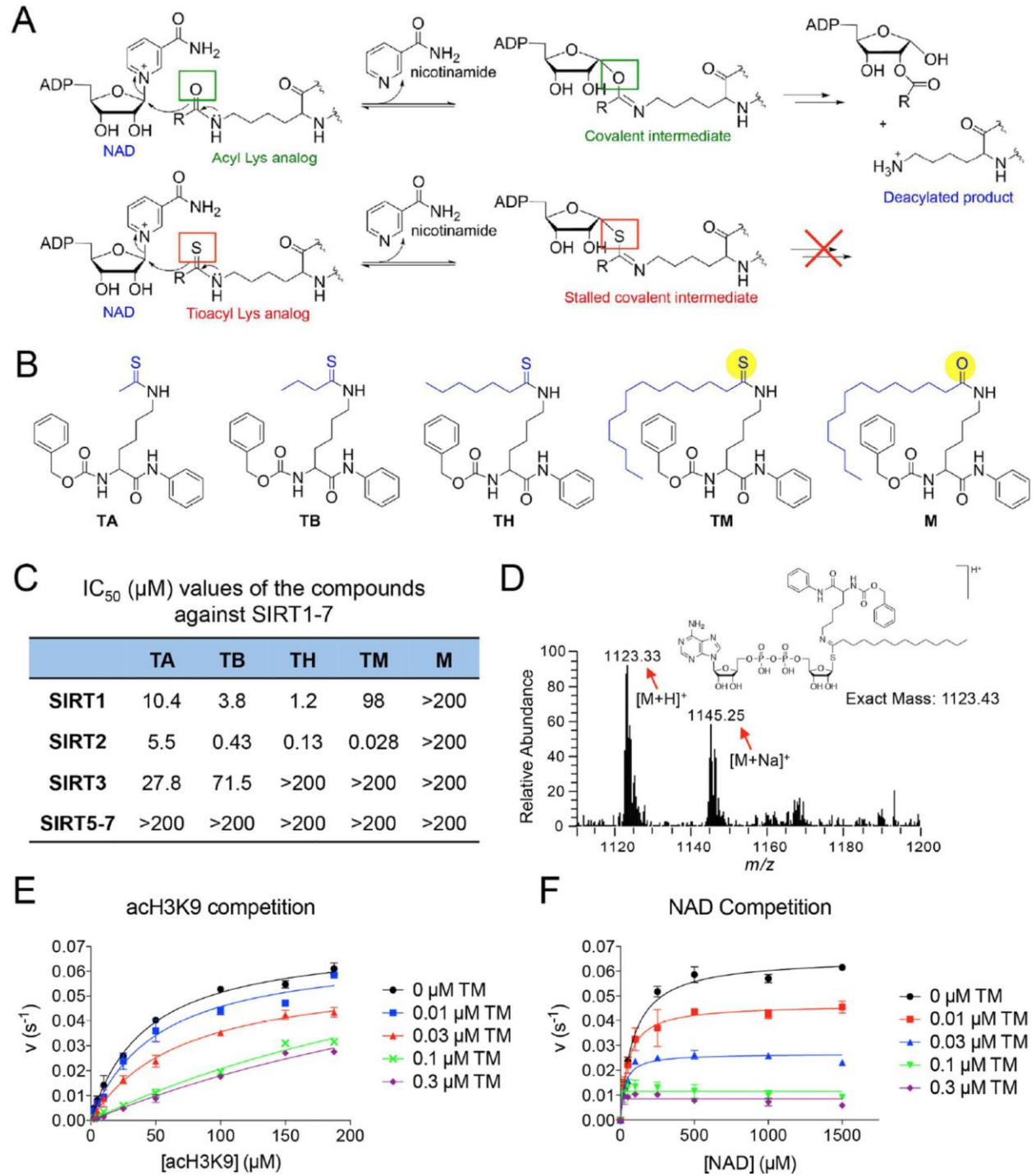


Figure 2

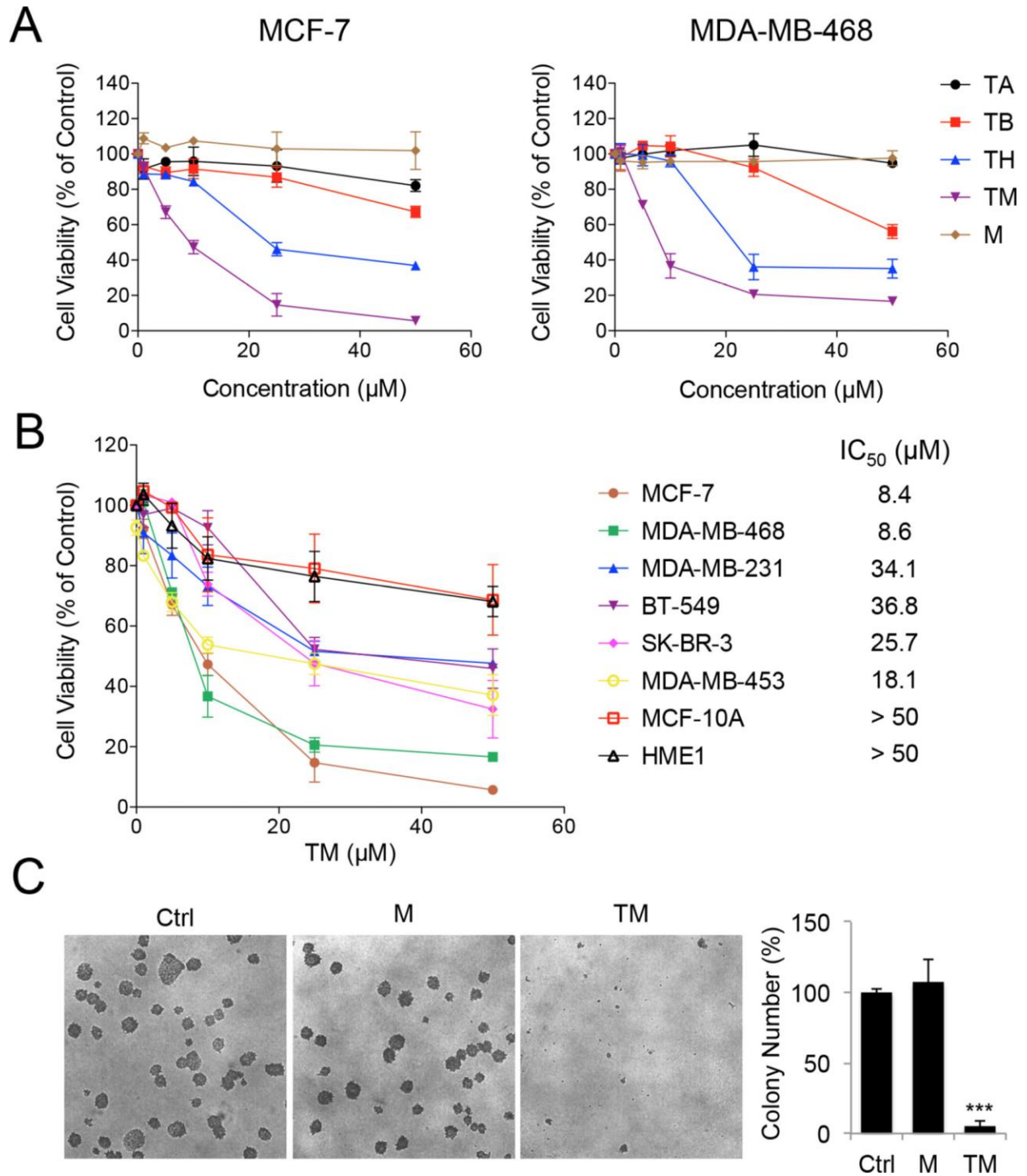
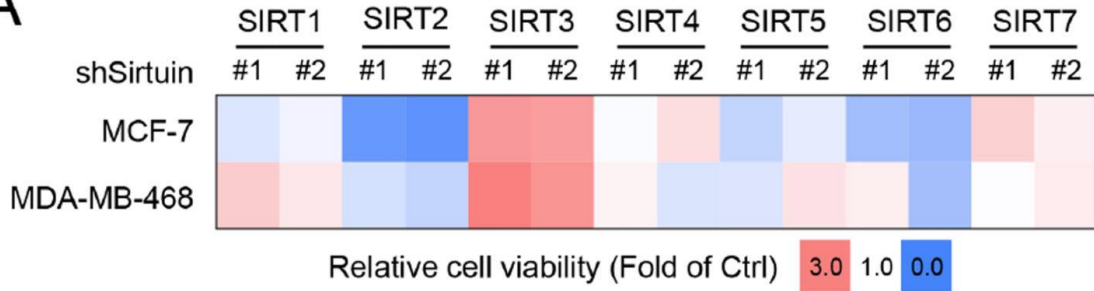
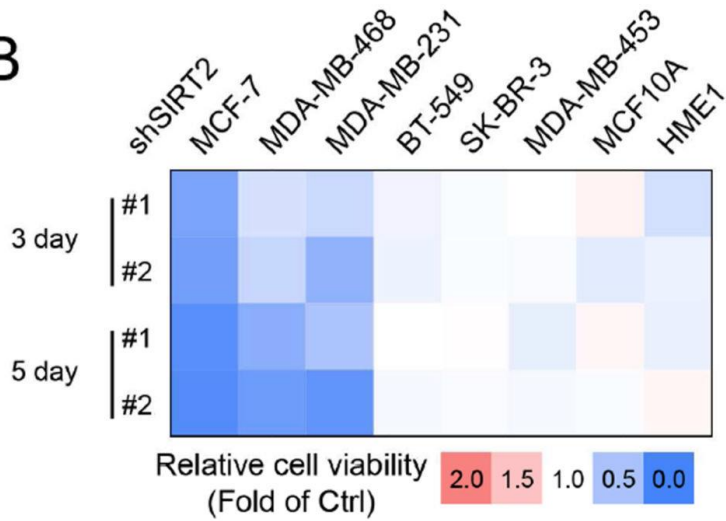


Figure 3

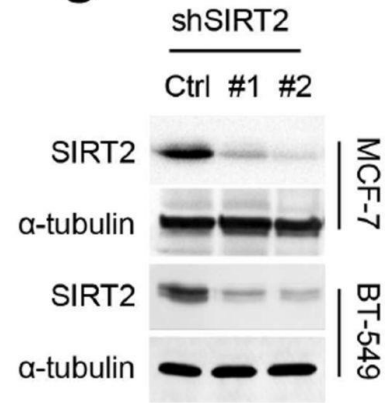
A



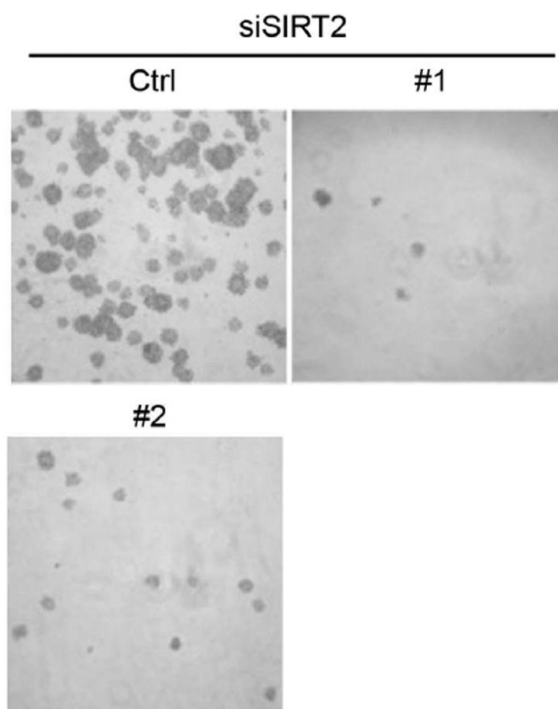
B



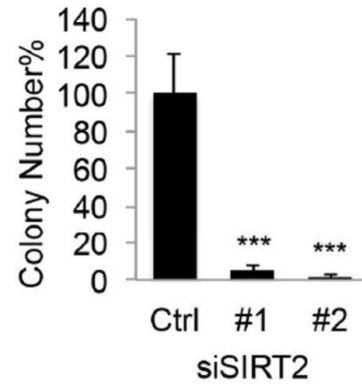
C



D



E



F

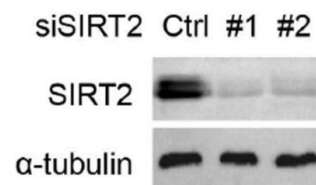


Figure 4

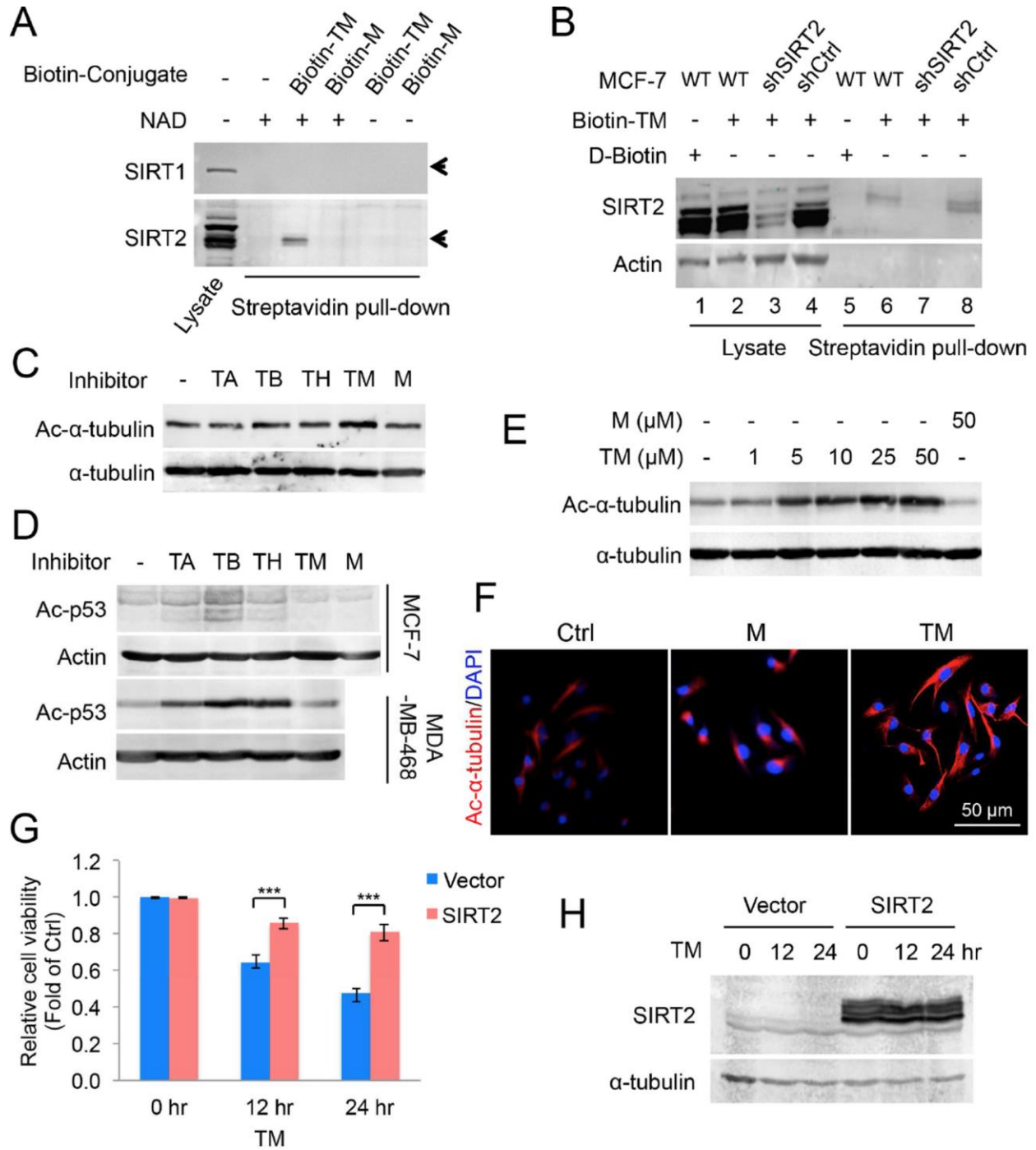


Figure 5

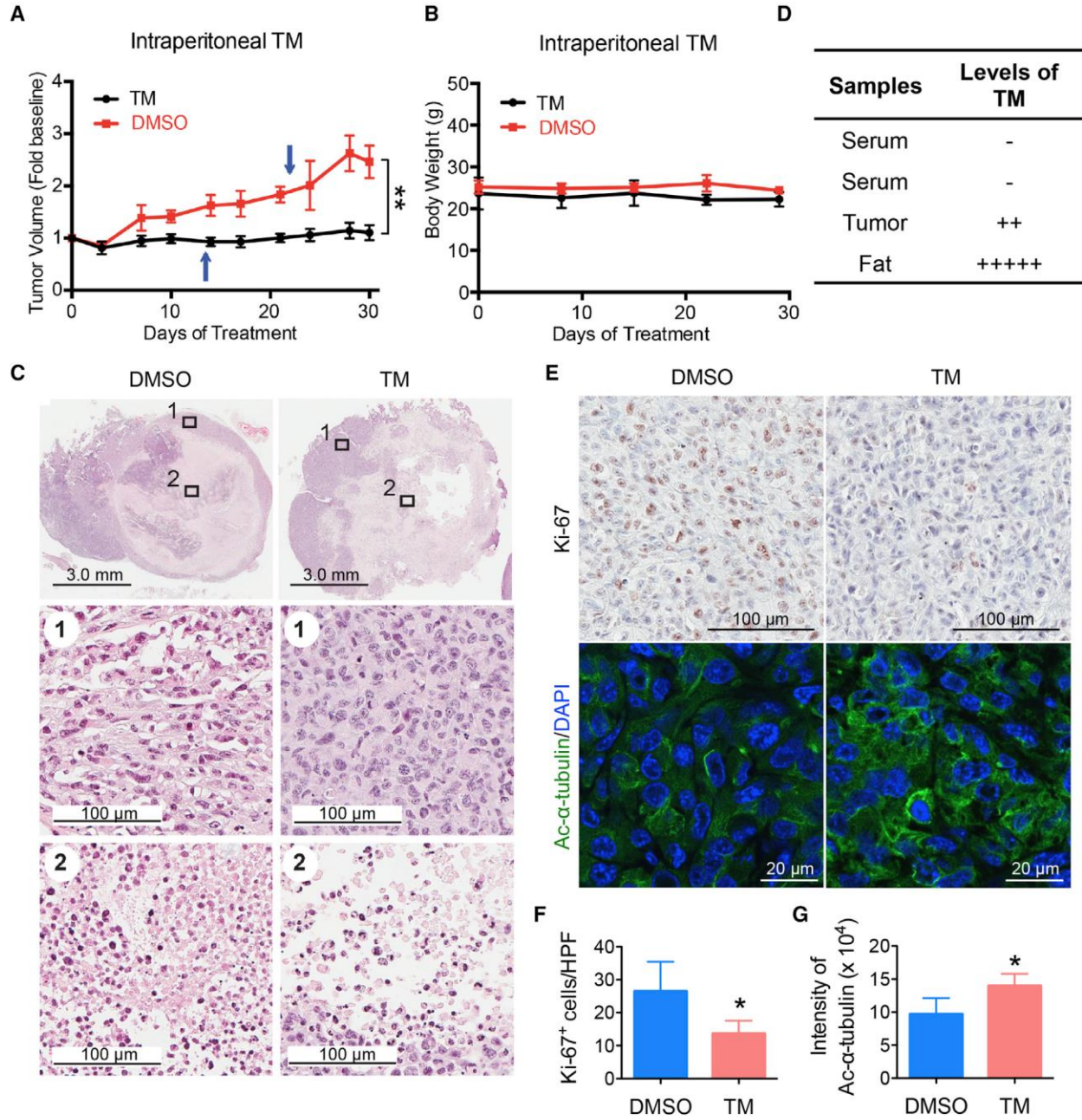


Figure 6

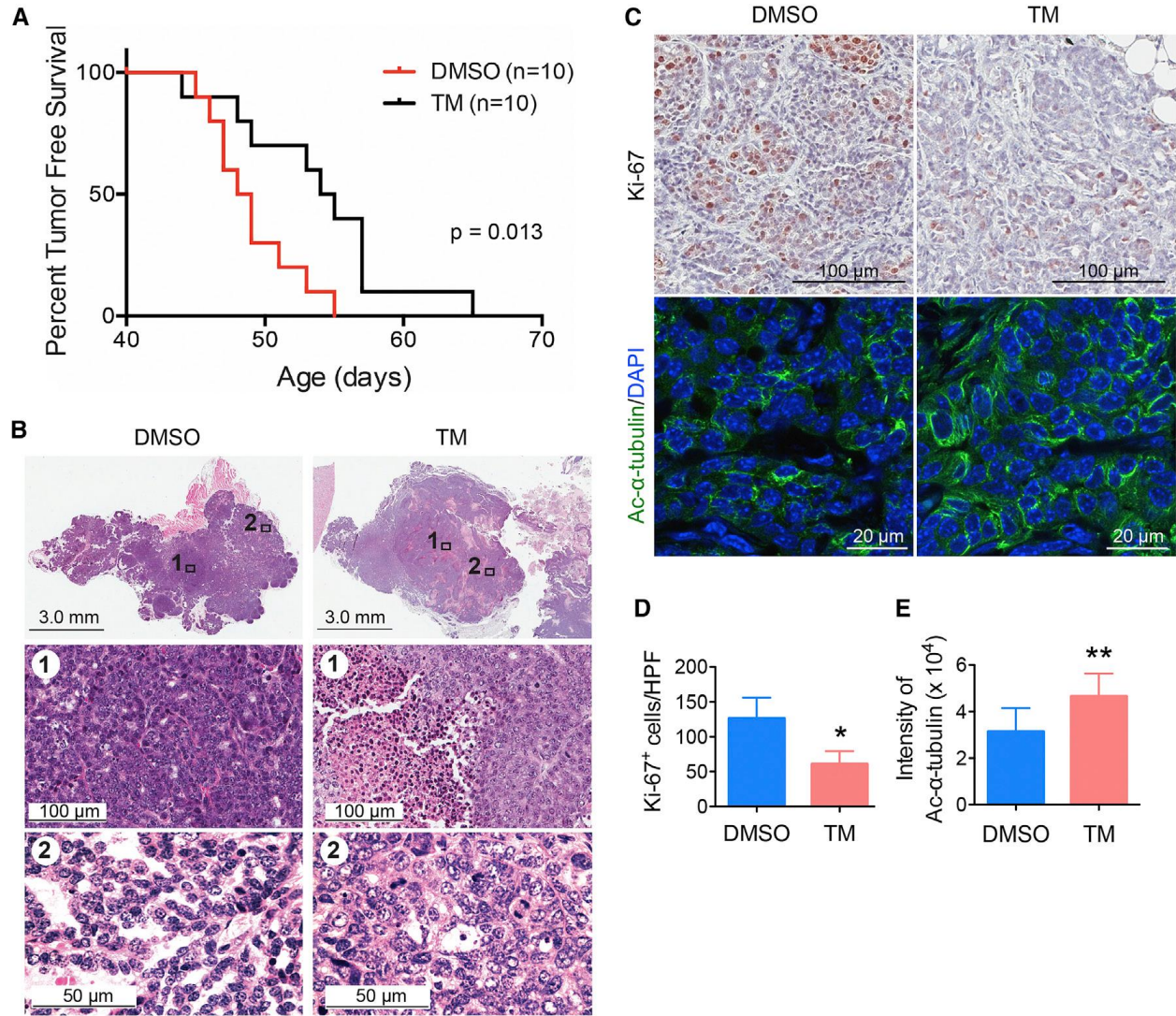
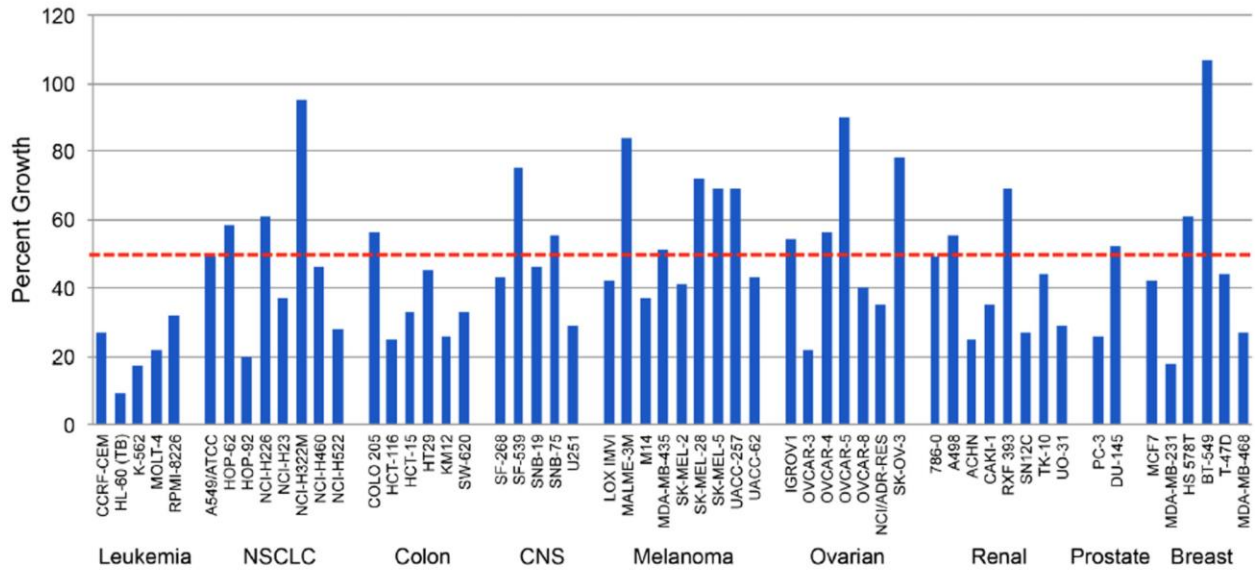
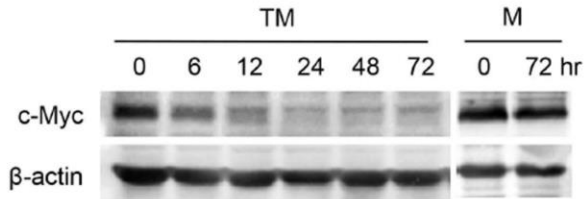


Figure 7

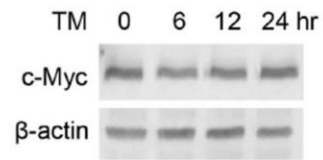
A



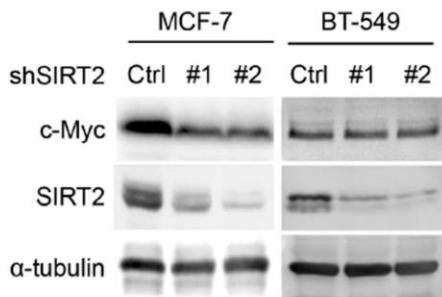
B



C



D



E

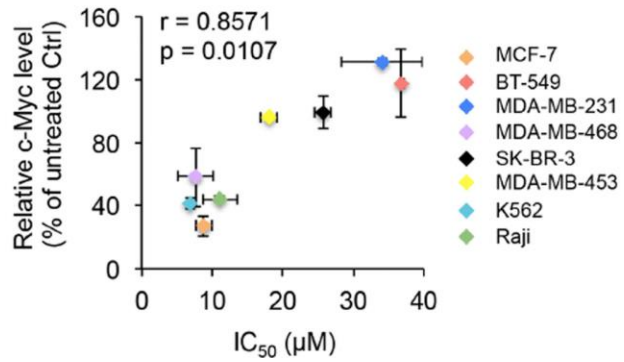
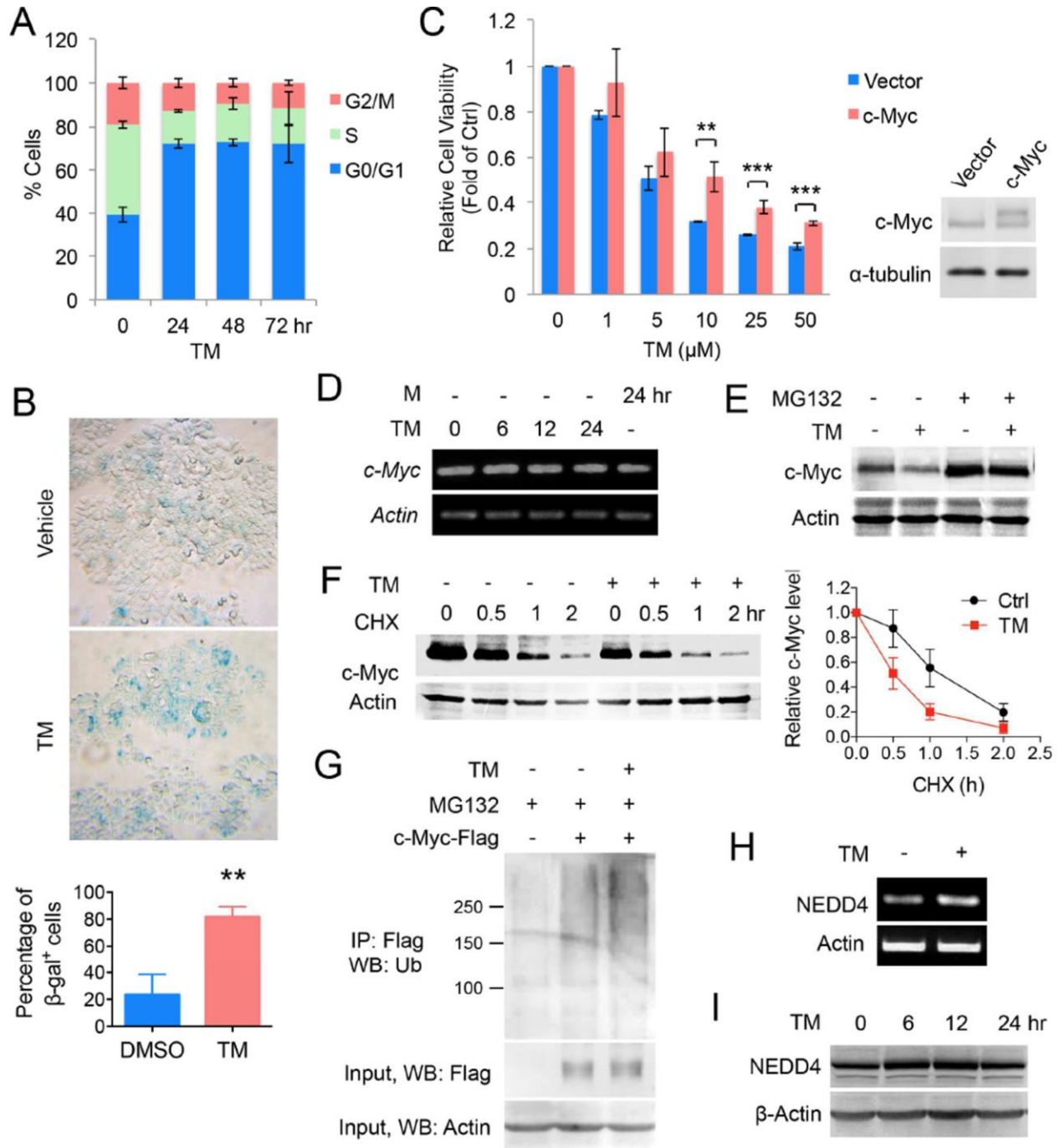


Figure 8



A SIRT2-Selective Inhibitor Promotes c-Myc Oncoprotein Degradation and Exhibits Broad Anticancer Activity

Hui Jing, Jing Hu, Bin He, Yashira L. Negrón Abril, Jack Stupinski, Keren Weiser, Marisa Carbonaro, Ying-Ling Chiang, Teresa Southard, Paraskevi Giannakakou, Robert S. Weiss, and Hening Lin

SUPPLEMENTAL INFORMATION

Supplemental Experimental Procedures

Supplemental Table (S1)

Supplemental Figures (S1-S7)

Supplemental References

SUPPLEMENTAL EXPERIMENTAL PROCEDURES

Cloning, expression and purification of human sirtuins.

Human SIRT1, SIRT3, SIRT5 and SIRT6 were expressed as previously described (Du et al., 2009; Jiang et al., 2013). Human SIRT2 (aa38-356) was cloned and inserted into pET28a vector for the expression of N-terminal His6-SUMO fusion protein. Then SIRT2 expression vector was introduced into an *E. coli* BL21. Successful transformation were selected by plating the cells on kanamycin (50 $\mu\text{g mL}^{-1}$) and chloramphenicol (20 $\mu\text{g mL}^{-1}$) luria broth (LB) plates. Single colonies were selected and grown in LB with kanamycin (50 $\mu\text{g mL}^{-1}$) and chloramphenicol (20 $\mu\text{g mL}^{-1}$) overnight at 37 °C. On the following day the cells were subcultured (1:1000 dilution) into 2 L of LB with kanamycin (50 $\mu\text{g mL}^{-1}$) and chloramphenicol (20 $\mu\text{g mL}^{-1}$). The cells were induced with 20 μM of isopropyl β -D-1-thiogalactopyranoside (IPTG) at an OD600 of 0.6 and grown overnight at 15 °C, 200 rpm. The cells were harvested by centrifugation at 8000 rpm for 5 min at 4 °C (Beckman Coulter refrigerated floor centrifuge) and passed through an EmulsiFlex-C3 cell disruptor (AVESTIN, Inc.) 3 times. Cellular debris was removed by centrifuging at 20,000 rpm for 30 min at 4 °C (Beckman Coulter). The supernatant was loaded onto a nickel column (HisTrap, Ge Healthcare) pre-equilibrated with 20 mM Tris-HCl pH 8.0 with 500 mM NaCl. The protein was eluted with a linear gradient of imidazole (0-500 mM). The desired fractions were pooled, concentrated and buffer exchanged. The His6-SUMO tag was removed by overnight incubation at 4 °C with ULP1, followed by Ni-affinity column purification to remove any undigested SIRT2. The tag-free SIRT2 was further purified on a Superdex 75 column (Bio-Rad, Hercules, CA). The protein was eluted with 20 mM Tris-HCl, pH

8.0, 500 mM NaCl. After concentration, the target protein was frozen at -80 °C.

Reagents, antibodies and plasmids.

All chemicals were obtained in the highest purity available. MG132 was from Cayman Chemical Co. (Ann Arbor, MI). Cycloheximide was purchased from Amresco (Euclid, OH). Trichostatin A (TSA) and AGK2 (2-Cyano-3-[5-(2,5-dichlorophenyl)-2-furanyl]-N-5-quinolinyl-2-propenamide) were obtained from Sigma-Aldrich (St. Louis, MO). The anti-human SIRT1 antibody (3H10.2) was from EMD Chemicals Inc. (San Diego, CA). The anti-human SIRT2 (EPR1667), SIRT6 antibodies were from Abcam (Cambridge, MA). The anti-human SIRT3 (C73E3), acetyl-p53 (Lys382) antibodies were obtained from Cell Signaling Technology (Danvers, MA). The anti-SIRT7 (C-3), c-Myc (9E10), NEDD4 (H-135), ubiquitin (P4D1), β -actin (C4) and the goat anti-mouse/rabbit IgG-horseradish peroxidase-conjugated antibodies were purchased from Santa Cruz Biotechnology (Santa Cruz, CA). The anti-SIRT4 (LS-C100490) antibody was purchased from LSBio, Inc. (Seattle, WA). The anti-SIRT5 antibody (Center) was from Abgent (San Diego, CA). The anti-acetyl- α -tubulin (6-11B-1), α -tubulin (B-5-1-2) antibodies, the anti-Flag M2 antibody conjugated with horseradish peroxidase and the anti-Flag M2 affinity gel were from Sigma-Aldrich.

The pLKO.1-puro lentiviral shRNAs constructs toward Luciferase and SIRT1-7 were purchased from Sigma-Aldrich. Luciferase shRNA (SHC007), SIRT1 shRNA1 (TRCN0000018980), SIRT1 shRNA2 (TRCN0000018981), SIRT2 shRNA1 (TRCN0000040221), SIRT2 shRNA (TRCN0000310335), SIRT3 shRNA1 (TRCN0000038890), SIRT3 shRNA2 (TRCN0000038893), SIRT4 shRNA1

(TRCN0000018948), SIRT4 shRNA2 (TRCN0000232894), SIRT5 shRNA1 (TRCN0000018544), SIRT5 shRNA2 (TRCN0000018545), SIRT6 shRNA 1 (TRCN0000378253) and shRNA 2 (TRCN0000232528), SIRT7 shRNA1 (TRCN0000359663), and SIRT7 shRNA2 (TRCN0000020254) were used. The scrambled siRNA and Stealth Select RNAi™ siRNA targeting SIRT2 (HSS117928 and HSS177042) were purchased from Invitrogen (Carlsbad, CA). To generate human SIRT2 with C-terminal Flag-tag expression vector, full-length human SIRT2 cDNA was amplified by PCR and inserted into pCMV-tag-4a vector between BamHI and XhoI sites. A human c-Myc expression vector with N-terminal Flag-tag was obtained by PCR amplification of Flag-c-Myc and subcloning via BamHI and XhoI sites into pCMV-tag-4a vector.

Inhibition assay for SIRT1, SIRT2, SIRT3, SIRT5.

Different concentrations (0.0064, 0.032, 0.16, 0.8, 4.0, 20, 100 and 200 μ M) of TA~TM, and M were pre-incubated with 0.1 μ M of SIRT1, 0.2 μ M of SIRT2, 1 μ M of SIRT3 or 1 μ M of SIRT5, respectively, and 1 mM NAD in 20 mM Tris-HCl buffer (pH 8.0) with 1 mM dithiothreitol (DTT) at 37 °C for 15 min. Then 10 μ M of acyl peptide (acetyl-H3K9 for SIRT1, SIRT2 and SIRT3; succinyl-H3K9 for SIRT5) was added to initiate the reactions. Then reactions were incubated at 37 °C in a total volume of 60 μ L (5 min for SIRT1, 5 min for SIRT2, 20 min for SIRT3, and 10 min for SIRT5). The reactions were stopped by adding 60 μ L of an aqueous solution of 50% methanol containing 200 mM HCl and 320 mM acetic acid.

After quenching the sirtuin reactions, centrifugation was used to remove precipitated

proteins and the supernatant was analyzed by HPLC with a reverse phase C18 column (Kinetex XB-C18 100A, 100 mm × 4.60 mm, 2.6 μm, Phenomenex) with a gradient of 0 % in 2 min, 0% to 20% in 2min, 20% to 40% B in 13 min and then 40% to 100% for 2 min at 0.5 mL/min. Product quantification was based on the area of absorbance monitored at 280 nm. The peak areas were integrated and the conversion rate was calculated from the peak areas as the fraction of the free H3K9 peptide from the total peptide. All reactions were done in duplicate.

Determination of kinetic parameters for TM.

For SIRT2 inhibition kinetics of TM, a mixture of acetyl-H3K9 (acH3K9) peptide substrate (2.5, 5, 10, 25, 50, 100, 187.5 μM), NAD (25, 50, 100, 250, 500, 1000, 1500 μM), TM (0, 0.01, 0.03, 0.1, and 0.3 μM), 20 mM Tris-HCl (pH 8.0) and 1 mM DTT was incubated at 37 °C. 1 mM NAD was used for determining the kinetic parameters for acH3K9 peptide, 100 μM of acH3K9 peptide was used for the determination of kinetic parameters for NAD. The reaction was started by adding 0.2 μM of SIRT2, and stopped after 5 min by adding 60 μL of an aqueous solution of 50% methanol containing 200 mM HCl and 320 mM acetic acid. The samples were analyzed by HPLC as described above and the initial velocity was calculated. The K_m and v_{max} were obtained from Michaelie-Menten plots using Graphpad Prism software.

Mass spectrometry detection of the stalled intermediate formed by TM and NAD.

Reactions containing 50 μM SIRT2, 100 μM NAD, 100 μM TM, 1 mM DTT, and 20 mM pyridinium formate (pH 7.0) was reacted for 5 min at 37 °C. Controls were run in

which NAD or SIRT2 was removed from the reaction mixture. Reactions were quenched with 1 volume of acetonitrile and the mixture was centrifuged to remove the precipitated protein. The supernatant was then analyzed by LCMS using water and acetonitrile as solvents.

Inhibition assay for SIRT6.

Different concentrations (0.0125, 0.05, 0.2, 0.8, 3.2, 12.8, 51.2, 204.8 μM) of TA~TM were pre-incubated with 1 μM of SIRT6 and 1 mM NAD in 20 mM Tris-HCl buffer (pH 8.0) with 1 mM DTT at 37 °C for 20 min. Then 50 μM of myristoyl-H3K9 peptide (myrH3K9) was added to initiate the reactions. The reactions were incubated at 37 °C in a total volume of 60 μL for 1 hr. The reactions were stopped by adding 60 μL of an aqueous solution of 50% methanol containing 200 mM HCl and 320 mM acetic acid.

Inhibition assay for SIRT7.

Different concentrations (0.0125, 0.05, 0.2, 0.8, 3.2, 12.8, 51.2, 204.8 μM) of TA~TM were pre-incubated with 1 μM of SIRT7 and 1 mM NAD in 150mM NaCl and 50 mM KH_2PO_4 buffer (pH 8.0) with 1 mM DTT at 37 °C for 20 min. Then 10 μM myrH3K9 peptide and 0.083mg/mL tRNA were added to initiate the reactions. Then reactions were incubated at 37 °C in a total volume of 60 μL for 110 min. The reactions were stopped by adding 60 μL of an aqueous solution of 50% methanol containing 200 mM HCl and 320 mM acetic acid.

Cell culture and transfection.

All cell culture media contained 10% (vol/vol) heat-inactivated fetal bovine serum (FBS; Invitrogen, Carlsbad, CA) and 1% penicillin-streptomycin (Invitrogen) unless otherwise specified. Human MCF-7, MDA-MB-231, MDA-MB-468, HeLa, HME1 cells were grown in DMEM media (Invitrogen). Human BT-549, SK-BR-3, MDA-MB-453 and K562 cells were grown in RPMI-1640 media (Invitrogen). The MCF-10A cells were cultured in mammary epithelial cell growth medium (MEGM; Lonza, Walkersville, MD) with supplements according to manufacturer's instruction.

To overexpress SIRT2 or c-Myc in cells, the pCMV-tag-4a vector containing SIRT2 or c-Myc, or pCDH vector containing c-Myc were transfected into cells using FuGene 6 (Promega, Madison, WI) according to manufacturer's protocol. Empty vector was transfected as negative control.

Soft agar colony formation assay.

For colony formation in semisolid medium, 1.0×10^4 cells were plated in 0.3% low-melting point agarose (LMP, Invitrogen) onto 6-well plate coated with 1.2% LMP mixed with 2 × complete medium. For treatments, 2 × inhibitor was added to cells at the time of plating. The medium and inhibitor were replaced with fresh ones every 3 days. For colony formation of the SIRT2 KD cells, cells were transfected with the scrambled siRNA or SIRT2 siRNAs for 48 hr before plating in 6-well plate. Similarly, cell media was replaced every 3 days. After 14 days of incubation, colonies were photographed and counted with ImageJ.

Western blot analysis.

Western blot analysis was performed as described previously (Jiang et al., 2013). The proteins of interest were detected using enzyme-linked chemiluminescence (ECL; Pierce Biotechnology Inc.) and visualized using the Storm Imager (GE Healthcare, Piscataway, NJ). Quantification of Western blots was done using the Quantity One software (Bio-Rad).

Biotin-TM/M pull-down assay.

HEK293T cells were collected and lysed in lysis buffer containing 25 mM Tris, pH 7.4, 150 mM NaCl, 10% glycerol, 1% Nonidet P-40 and 1 × protease inhibitor cocktail (Sigma-Aldrich). The cell extract supernatant was collected after centrifugation at 14,000 g for 20 min at 4 °C. Cell lysates were incubated with 10 μM Biotin-TM or Biotin-M in the absence or presence of 1 mM NAD at 4 °C for 1 hr. The high capacity streptavidin resin (Pierce Biotechnology, Rockford, IL) was added to the mixture and incubated at 4 °C for another 1 hr. After centrifugation at 500 g for 2 min at 4 °C, the streptavidin resin was washed 3 times with 1 mL washing buffer (25 mM Tris, pH 7.4, 150 mM NaCl, 10% glycerol, 0.2% Nonidet P-40). The resinbound proteins were then separated with SDS-PAGE and immunoblotted with anti-SIRT1 or anti-SIRT2 antibodies. To assess the binding of TM to SIRT2 in cells, MCF-7 parental cells, Luciferase KD and SIRT2 KD cells were treated with 50 μM D-Biotin or Biotin-TM as indicated for 6 hr and then lysed in lysis buffer containing 1 mM NAD. Cell extract was collected, streptavidin pull-down and western blot analysis was performed as described above.

SIRT1 inhibition in cells.

MCF-7 or MDA-MB-468 cells were treated with indicated test compounds in the presence of 200 nM TSA for 6 hr. The acetylation level of p53 protein was determined by western blot using anti-acetyl-p53 (K382) antibody. β -actin served as a loading control. SIRT2 inhibition in cells. MCF-7 cells were treated with indicated inhibitors at for 6 hr after being transfected with pCMV-tag-4a-SIRT2 for 18 hr. Cells were collected and lysed in lysis buffer containing 25 mM Tris, pH 7.4, 150 mM NaCl, 10% glycerol, 4 mM MgCl₂, 0.2 mM DTT, 100 mM NAD, 1% Nonidet P-40 and 1 \times protease inhibitor cocktail. And the cell lysates were subjected to western blot for the analysis of acetyl- α -tubulin (K40) and α -tubulin levels.

TM treatment of mice bearing human breast cancer xenotransplants.

Two million MDA MB-231 cells suspended in 100 μ L 1 \times PBS and 100 μ L Matrigel were injected subcutaneously on the flanks of female Ncr Nu/Nu mice. Following the injections, mice were permitted to recover and monitored biweekly, including tumor measurement using calipers. Once the majority of tumors reached a threshold size of 200 mm³, mice with intraperitoneal (IP) or intra-tumor (IT) injections of vehicle alone (DMSO) or inhibitor (TM in DMSO) over one month. IP injections of 1.5 mg TM in 50 μ L DMSO were given daily. IT injections of 0.75 mg TM in 50 μ L DMSO per tumor were given 3 days per week. After one month of treatment or if mice met humane endpoint criteria, mice were euthanized by CO₂ asphyxiation. Tissues were collected, fixed with 10% neutral-buffered formalin, embedded in paraffin, sectioned, and stained with hematoxylin and eosin (H&E). H&E-stained sections were scanned

using an Aperio ScanScope and analyzed by a veterinarian certified in anatomic pathology by the American College of Veterinary Pathologists blinded to treatment group. Serum, tumor tissues and organs were snap frozen in liquid N₂ and stored at -80 °C for subsequent analyses.

TM treatment of MMTV-PyMT mice.

MMTV-PyMT transgenic female mice on a pure FVB/N background were obtained from the Jackson Laboratory and treated beginning at 6 weeks of age with daily IP injections of vehicle (DMSO) or 1.5 mg TM in 50 μ L DMSO over one month. Mice were monitored daily for tumor development and health status, and tumor size was measured twice per week. After one month of treatment or if mice met humane endpoint criteria, mice were euthanized by CO₂ asphyxiation and necropsied. Tissues were collected and analyzed as described above.

Ubiquitination assay.

MCF-7 cells were transfected with pCMV-tag-4a or pCMV-tag-4a-c-Myc, respectively. 18 hours after transfection, cells were treated with 25 μ M TM for 6 hr in the presence of proteasome inhibitor MG132 (10 μ M). Immunoprecipitation was performed with the cell lysates by anti-Flag M2 affinity gel as described previously (He et al., 2014). The gel-bound proteins were resolved on SDS-PAGE and detected with anti-ubiquitin antibody. The c-Myc level in total cell lysates was used as input control.

Reverse transcription (RT)-PCR analysis of mRNA levels.

Total RNA was extracted from vehicle-, TM- or M-treated cells using RNeasy Mini Kit (Qiagen, CA, USA) according to the manufacturer's instructions. The concentration and purity of total RNA were determined by using the NanoDrop (Thermo Fisher Scientific Inc, Wilmington, DE). cDNA was synthesized using SuperScript III reverse transcriptase (Invitrogen). Amplification of genes of interest was performed using Herculase II Fusion DNA Polymerase (Agilent Technologies, Santa Clara, CA) with the gene-specific primers shown below. 10 µl of each PCR product were analyzed by gel electrophoresis on a 2% agarose gel.

Primer	Direction	Sequence
<i>c-Myc</i>	Forward	GGCTCCTGGCAAAGGTCAGAGT
<i>c-Myc</i>	Reverse	CTGCGTAGTTGTGCTGATGTGT
<i>NEDD4</i>	Forward	TCAGGACAACCTAACAGATGCT
<i>NEDD4</i>	Reverse	TTCTGCAAGATGAGTTGGAACAT
<i>Actin</i>	Forward	CATGTACGTTGCTATCCAGGC
<i>Actin</i>	Reverse	CTCCTTAATGTCACGCACGAT
<i>STUB1</i>	Forward	AGCAGGGCAATCGTCTGTTC
<i>STUB1</i>	Reverse	CAAGGCCCGGTTGGTGTAAATA
<i>SKP2</i>	Forward	ATGCCCAATCTTGTCCATCT
<i>SKP2</i>	Reverse	CACCGACTGAGTGATAGGTGT
<i>TRPC4AP</i>	Forward	ACAAGCACACGCTTCTTGC
<i>TRPC4AP</i>	Reverse	CTGACACCTTTTCGAGTCGCC
<i>FBXW7</i>	Forward	CGACGCCGAATTACATCTGTC

<i>FBXW7</i>	Reverse	CGTTGAAACTGGGGTTCTATCA
<i>FBXO32</i>	Forward	GCCTTTGTGCCTACAACCTG
<i>FBXO32</i>	Reverse	CTGCCCTTTGTCTGACAGAAT

Immunofluorescence of cultured cells.

MDA-MB-231 cells were treated with ethanol, M (25 μ M) or TM (25 μ M) for 6 hr. Immunostaining was performed and images were acquired by confocal microscopy as previously described (Mabjeesh et al., 2003). Flow cytometry. For cell cycle analyses, MCF-7 or K562 cells were treated with 25 μ M for 0, 24, 48 and 72 hr. Cells were spun down, washed with PBS, fixed with 70% ethanol overnight, and then washed with PBS. RNA was degraded with RNase A and DNA was stained with propidium iodide (Invitrogen). Samples were analyzed on a BD LSR-II. Cell cycle analysis was performed with FlowJo flow cytometry analysis software (Tree Star, Inc., Ashland, OR).

Cellular senescence staining.

MCF-7 or K562 cells were treated with ethanol or 25 μ M TM. After 5 days of treatment, cells were stained for senescence as previously described (Debacq Chainiaux et al., 2009).

Immunofluorescence and Immunohistochemistry of tumor sections.

Formalin-fixed, paraffin-embedded (FFPE) tumors were sectioned, dewaxed and submitted to heat mediated antigen retrieval in 0.01 M citrate buffer for 50 min. For immunofluorescence, sections were incubated with anti-acetyl- α -tubulin, followed by

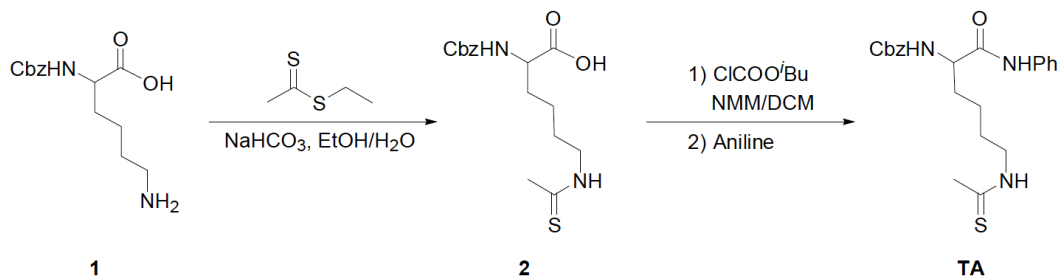
Alexa Fluro-488 conjugated secondary antibodies from Invitrogen and cell nuclei counterstaining with DAPI Fluoromount-G® from SouthernBiotech. Fluorescent images were taken using Zeiss LSM880 inverted confocal microscopy (Carl Zeiss Inc., Thornwood, NY). For immunohistochemistry, sections were incubated with anti-Ki67 Clone MM1 (Vector Laboratories) antibody followed by biotinylated polyclonal rabbit anti-mouse (DAKO). Color was developed using 3,3'-Diaminobenzidine tetrahydrochloride substrate from Invitrogen and counterstained with hematoxinilin. Images were scanned using an Aperio ScanScope.

Synthesis of compounds used in the study

General methods.

Reagents were obtained from Aldrich or Acros in the highest purity available and used as supplied. ¹HNMR was performed on INOVA 400/500 spectrometer. LCMS was carried out on a SHIMADZU LC and Thermo LCQ FLEET MS with a Sprite TARGA C18 column (40 × 2.1 mm, 5 μm, Higgins Analytical, Inc.) monitoring at 215 and 260 nm. Solvents used in LCMS were water with 0.1% acetic acid and acetonitrile with 0.1% acetic acid.

1. Synthetic Route for TA

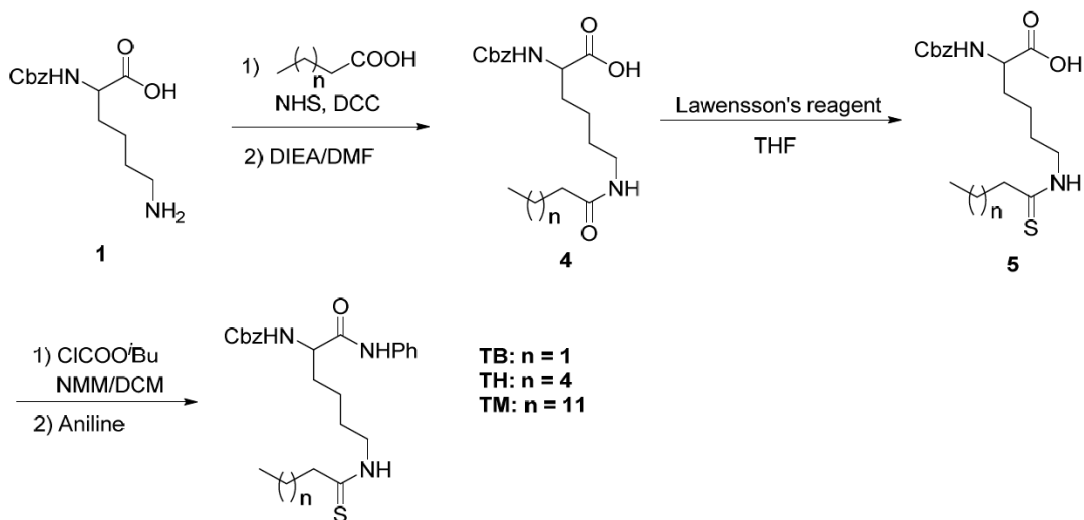


Synthesis of compound 2. To a solution of Z-Lys-OH (2.8 g, 10 mmol) in ethanol (100

mL) was added 20 mL of 10% (w/v) Na₂CO₃ aqueous solution at 0°C. The reaction mixture was allowed to warm to room temperature (rt) while stirred extensively. Ethyl dithioacetate (1.32 g, 11 mmol) was added and the reaction mixture was stirred overnight at rt. Solvent was evaporated and then the crude product was acidified to pH = 2 with 3 M HCl on ice and extracted with DCM (3 x 100 mL). The organic phase was washed with brine (2 x 30 mL), dried with Na₂SO₄, and evaporated to obtain compound 2, which was directly used in the next step without further purification.

Synthesis of compound TA. To a solution of compound 2 (3.38 g, 10 mmol) and Nmethylmorpholine (1.1 ml, 10 mmol) in dry dichloromethane (100 mL) at 0 °C was added dropwisely iso-butylchloroformate (1.3 ml, 10 mmol). The reaction mixture was stirred for 30 min at 0°C. Aniline (1.09 ml, 12 mmol) was added at 0 °C and the reaction mixture was stirred overnight at room temperature. The solvent was removed under reduced pressure and the resulting residue was purified by flash chromatography on silica gel (Hexane/ethyl acetate = 2/1) to afford the expected compound 3 (3.95 g, 95.5% yield). ¹H NMR (400 MHz, CD₃OD): δ 7.53-7.51 (m, 2H), 7.34-7.22 (m, 7H), 7.08-7.04(t, J =7.2Hz, 1H), 5.06 (q, J=8.0Hz, 2H), 4.26-4.22 (m, 1H), 3.54 (t, J=7.1Hz, 2H), 2.39 (s, 3H), 1.89-1.76(m, 1H), 1.78-1.70 (m, 1H), 1.66-1.58 (m, 2H), 1.55-1.35 (m, 2H). ¹³C NMR (126 MHz, CDCl₃): δ 200.88, 170.34, 156.79, 137.34, 135.87, 129.01, 128.62, 128.35, 127.93, 124.78, 120.23, 120.13, 67.34, 55.19, 45.74, 33.97, 32.04, 27.00, 22.70.LCMS (ESI) calcd. for C₂₂H₂₈N₃O₃S [M+H]⁺ 414.2, obsd. 414.3.

2. Synthetic Route for TB, TH, and TM



Synthesis of compound 4. To the solution of acid (30 mmol) in anhydrous N, N'-dimethylformamide (DMF, 20 mL) was added N-hydroxysuccinimide (NHS, 3.45 g, 30 mmol) with stirring at rt. Then N, N'-dicyclohexylcarbodiimide (DCC, 6.19 g, 30 mmol) in anhydrous DMF (20 mL) was added to the reaction. After stirring for 2 hr, the reaction mixture was filtered. The filtrate was added to a solution of Z-Lys-OH (8.4 g, 30 mmol) with N, N-diisopropylethylamine (DIEA, 5.2 mL, 30 mmol) in anhydrous DMF (50.0 mL) at room temperature. The resulting reaction mixture was stirred overnight. Then 44 mL water and 26 mL 1 M HCl was added to the reaction mixture to adjust pH to 2~3. The mixture was extracted ethyl acetate (3 x 200 mL) and washed brine (2 x 100 mL). The organic layer was dried over anhydrous sodium sulfate. After removal of the solvents in vacuum, the residue was purified by flash chromatography on silica gel (DCM/MeOH = 20:1) to afford the expected compound 4 (85% yield).

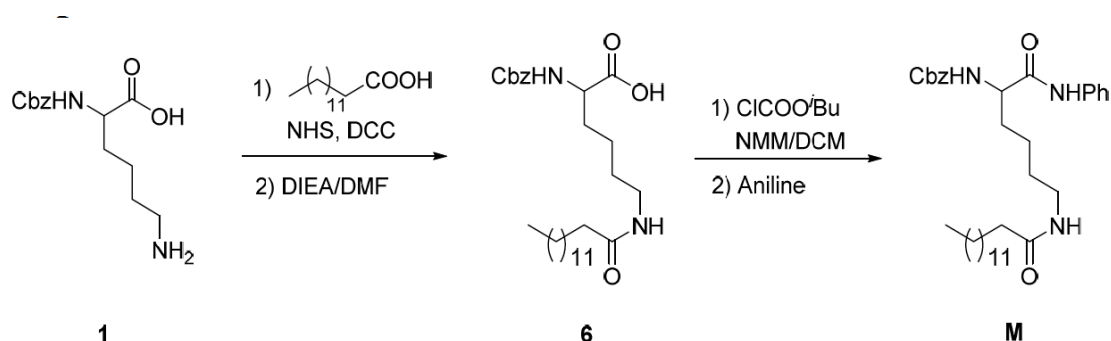
Synthesis of compound 5. To a solution of compound 4 (20 mmol) in THF (100 mL) was added Lawesson's reagent (8.0 g, 20 mmol) at room temperature. The reaction mixture was stirred overnight under nitrogen (monitored by LCMS). After removal of

THF using a rotary evaporator, the residue was purified by silica gel column (DCM/MeOH = 20:1) to give the product as a white solid (76% yield).

Synthesis of compound TB, TH and TM. To a solution of compound 5 (10 mmol) and Nmethylmorpholine (1.1 ml, 10 mmol) in dry dichloromethane (100 mL) at 0 °C was added dropwisely iso-butylchloroformate (1.3ml, 10 mmol). The reaction mixture was stirred for 30 min at 0 °C. Aniline (1.09 ml, 12 mmol) was then added at 0 °C and the reaction mixture was stirred overnight at room temperature. The solvent was removed under reduced pressure and the resulting residue was purified by flash chromatography on silica gel (Hexane/ethyl acetate= 2/1) to afford the expected compound TB, TH, and TM. TB (91% yield) ¹H NMR (400 MHz, CD₃OD): δ 7.57-7.45 (m, 2H), 7.39-7.12 (m, 7H), 7.12-6.99 (m, 1H), 5.05 (q, J = 12.5 Hz, 2H), 4.27-4.23 (m, 1H), 3.55 (q, J = 12.5 Hz, 2H), 2.51 (t, J = 7.2Hz, 2H), 1.91-1.78 (m, 1H), 1.78-1.57 (m, 5H), 1.55-1.33 (m, 2H), 0.86 (t, J = 7.2 Hz, 3H). ¹³C NMR (126 MHz, CDCl₃): δ 205.60, 170.19, 156.74, 137.36, 135.88, 128.99, 128.60, 128.33, 127.96, 124.72, 120.16, 120.06, 119.98, 67.34, 55.19, 48.93, 45.30, 31.89, 27.07, 22.78, 22.63, 13.36. LCMS (ESI) calcd. for C₂₄H₃₂N₃O₃S [M+H]⁺ 442.2, obsd. 442.3; TH (89% yield) ¹H NMR (500 MHz, CDCl₃): δ 8.54 (s, 1H), 7.73 (s, 1H), 7.49 (d, J = 7.5 Hz, 2H), 7.41-7.20 (m, 7H), 7.11 (t, J = 7.4 Hz, 1H), 5.79 (d, J = 7.5 Hz, 1H), 5.19 -5.03 (m, 2H), 4.45-4.31 (m, 1H), 3.70-3.62 (m, 2H), 2.60(t, J = 7.5 Hz, 2H), 1.98-1.91 (m, 1H), 1.81-1.60 (m, 5H), 1.54-1.41 (m, 2H), 1.36-1.18 (m, 6H), 0.87 (t, J = 7.0 Hz, 3H). ¹³C NMR (126 MHz, CDCl₃): δ 205.84, 170.21, 156.75, 137.38, 135.88, 128.99, 128.60, 128.33, 127.95, 124.71, 120.16, 67.34, 55.19, 47.16, 45.34, 31.91, 31.52, 29.47, 28.66, 27.07, 22.65, 22.53, 14.06. LCMS (ESI) calcd. for C₂₇H₃₈N₃O₃S [M+H]⁺ 484.3, obsd. 484.3; TM (91%

yield) ¹H NMR (400 MHz, CD₃OD): δ 7.53 (d, J = 8.0 Hz, 2H), 7.41-7.12 (m, 7H), 7.08 (t, J = 7.4 Hz, 1H), 5.22-4.97 (m, 2H), 4.22 (dd, J = 8.8, 5.4 Hz, 1H), 3.57 (t, J = 7.1 Hz, 2H), 2.54 (t, J = 7.6 Hz, 2H), 1.90-1.79(m, 1H), 1.79-1.61 (m, 5H), 1.55-1.37 (m, 2H), 1.26 (s, 20H), 0.87 (t, J = 6.7 Hz, 3H). ¹³C NMR (126 MHz, CDCl₃): δ 205.84, 170.18, 156.75, 137.37, 135.88, 128.99, 128.60, 128.33, 127.95, 124.71, 120.16, 67.35, 55.19, 47.21, 45.35, 31.93, 29.70, 29.67, 29.65, 29.55, 29.40, 29.37, 29.06, 27.08, 22.70, 22.65, 14.15. LCMS (ESI) calcd. for C₃₄H₅₂N₃O₃S [M+H]⁺ 582.4, obsd. 582.4;

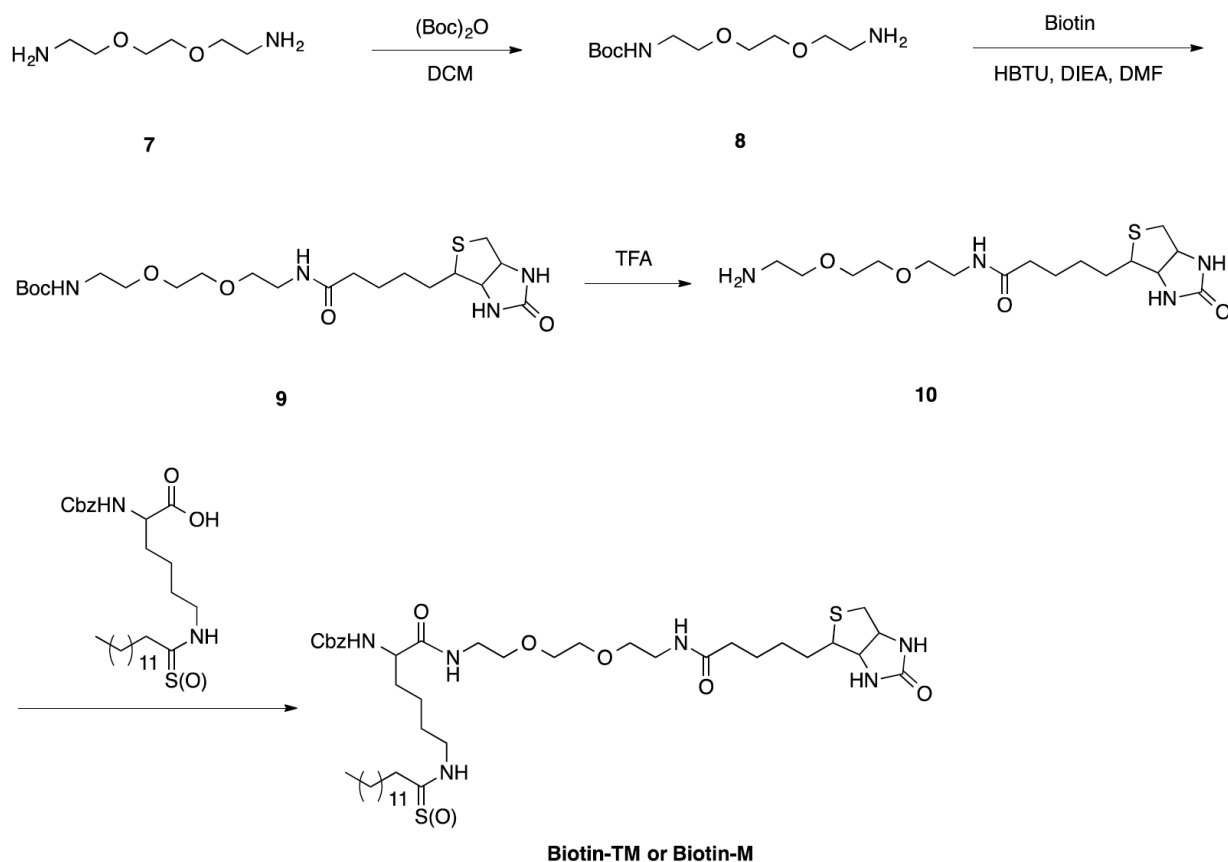
3. Synthesis of compound M



The synthesis of compound 6 followed the method using in the synthesis of compound 4. To a solution of compound 6 (4.9 g, 10 mmol) and N-methylmorpholine (1.1 ml, 10 mmol) in dry dichloromethane (100 mL) at 0 °C was added dropwisely iso-butylchloroformate (1.3 ml, 10 mmol). The reaction mixture was stirred 30 min at 0 °C. Aniline (1.09 ml, 12 mmol) was added at 0 °C and the reaction mixture was stirred overnight at rt. The solvent was removed under reduced pressure and the resulting residue was purified by silica gel chromatography (DCM/MeOH = 50:1) to afford the expected compound M (5.14 g, 91% yield). ¹H NMR (400 MHz, CD₃OD): δ 7.53 (d, J = 7.9 Hz, 2H), 7.40-7.13 (m, 7H), 7.08 (t, J = 7.4 Hz, 1H), 5.13-5.02 (m, 2H), 4.20 (dd, J =

8.5, 5.5 Hz, 1H), 3.15 (t, J = 6.7 Hz, 2H), 2.11 (t, J = 7.6 Hz, 2H), 1.88-1.64 (m, 2H), 1.62-1.34 (m, 6H), 1.32-1.21 (s, 20H), 0.87 (t, J = 7.0 Hz, 3H). ¹³C NMR (126 MHz, DMSO-d₆): δ 172.35, 171.54, 156.53, 139.43, 137.46, 129.11, 128.77, 128.22, 128.14, 123.67, 119.66, 65.87, 55.85, 38.61, 35.92, 31.98, 31.76, 29.53, 29.50, 29.48, 29.41, 29.35, 29.24, 29.18, 29.15, 25.77, 23.48, 22.56, 14.41. LCMS (ESI) calcd. for C₃₄H₅₂N₃O₄ [M+H]⁺ 566.4, obsd. 566.5;

4. Synthetic Route for Biotin-TM and Biotin-M



Synthesis of Compound 8. To a solution of compound **7** (14.8 g, 100 mmol) in DCM (200 mL) was added 100 mL of di-tert-butyl dicarbonate (2.18 g, 10mmol) in DCM at 0°C. The reaction mixture was allowed to warm to rt and stirred extensively overnight.

The organic phase was washed with water, until all the unreacted compound 7 was extracted. After drying over Na₂SO₄ and concentration under vacuum the Boc-protected compound 8 was quantitatively obtained.

Synthesis of Compound 9. To a solution of Biotin (2.2 g, 9 mmol) and HBTU (3.41 g, 9 mmol) in DMF (30 mL) was added DIEA (3.6 mL, 20 mmol) at room temperature with stirring for 30 min. Then compound 8 was added to the resulting mixture. The reaction mixture was stirred extensively overnight. After removal of the solvents under reduced pressure, the residue was purified by flash chromatography on silica gel (DCM/MeOH = 20:1 then 10:1) to afford the expected compound 9 (3.5 g, 81% yield).

Synthesis of Compound 10. To 20 mL of TFA was added the compound 9 (2 g, 4.2 mmol) and the resulting mixture was stirred for 30 min at room temperature. After removing the solvent under vacuum the deprotected compound 10 was quantitatively obtained and used in the next step without further purification.

Synthesis of Compound Biotin-TM and Biotin-M. The synthesis followed the method using in the synthesis of TM. The solvent used to dissolve the compound 10 is DMF instead of DCM. Biotin-TM (81% yield) ¹H NMR (500 MHz, CD₃OD): δ 7.41-7.29 (m, 5H), 5.18-5.05 (m, 2H), 4.49 (dd, J = 7.8, 4.8 Hz, 1H), 4.30 (dd, J = 7.9, 4.5 Hz, 1H), 4.10 (dd, J = 8.7, 5.4 Hz, 1H), 3.66-3.52 (m, 10H), 3.44 -3.34 (m, 4H), 3.21 (dt, J = 9.9, 5.6 Hz, 1H), 2.93 (dd, J = 12.7, 5.0 Hz, 1H), 2.71 (d, J = 12.7 Hz, 1H), 2.59 (t, J = 7.4 Hz, 2H), 2.22 (t, J = 7.4 Hz, 2H), 1.86-1.55 (m, 10H), 1.48-1.38 (m, 4H), 1.35-1.25(m,

20H), 0.91 (t, J = 6.9 Hz, 3H). ¹³C NMR (126 MHz, CD₃OD): δ 205.01, 174.72, 173.54, 164.68, 156.99, 136.77, 128.10, 127.64, 127.42, 69.92, 69.21, 69.09, 66.29, 61.95, 60.21, 55.61, 55.06, 45.68, 45.16, 39.66, 38.91, 35.35, 31.68, 29.44, 29.41, 29.37, 29.33, 29.24, 29.08, 28.57, 28.37, 28.10, 26.92, 25.45, 22.95, 22.34, 13.06. LCMS (ESI) calcd. for C₄₄H₇₅N₆O₇S₂ [M+H]⁺ 863.5, obsd. 863.6. Biotin-M (83% yield) ¹H NMR (400 MHz, CD₃OD): δ 7.39-7.22 (m, 5H), 5.10-5.04 (m, 2H), 4.46 (dd, J = 7.9, 4.9 Hz, 1H), 4.27 (dd, J = 7.8, 4.5 Hz, 1H), 4.05 (dd, J = 8.8, 5.3 Hz, 1H), 3.58 (s, 4H), 3.52 (q, J = 5.2 Hz, 4H), 3.37-3.32 (m, 4H), 3.19-3.11 (m, 3H), 2.89 (dd, J = 12.7, 5.0 Hz, 1H), 2.68 (d, J = 12.7 Hz, 1H), 2.19 (t, J = 7.5 Hz, 2H), 2.13 (t, J = 7.5 Hz, 2H), 1.80-1.34 (m, 14H), 1.26 (s, 20H), 0.88 (t, J = 6.8 Hz, 3H). ¹³C NMR (126 MHz, DMSO): δ 172.58, 172.50, 172.35, 163.15, 156.36, 137.49, 128.77, 128.21, 128.10, 69.98, 69.62, 69.42, 65.79, 61.48, 59.64, 55.88, 55.06, 38.97, 38.88, 38.65, 35.90, 35.55, 32.14, 31.76, 29.53, 29.49, 29.41, 29.31, 29.25, 29.18, 29.15, 28.66, 28.49, 25.78, 25.72, 23.36, 22.56, 14.43. LCMS (ESI) calcd. For C₄₄H₇₅N₆O₈S [M+H]⁺ 847.5, obsd. 847.8.

SUPPLEMENTAL TABLE

Table S1. Related to Figure 7. Top four correlated genes from molecular target Compare analysis of the NCI-60 assay data of TM. The data set used is the MT series.

Rank	Mol. Target ID	Gene	Correlation value	Target pattern description
1	MT18283	MYC	0.503	c-Myc phosphorylation level at T58 and S62
2	MT18332	MYC	0.493	c-Myc protein level
3	MT11065	FGFR2	0.477	Fraction of DNA methylation at FGFR2 5' UTR
4	MT1125	CDC25A	0.465	Relative mRNA levels of CDC25A

SUPPLEMENTAL FIGURES

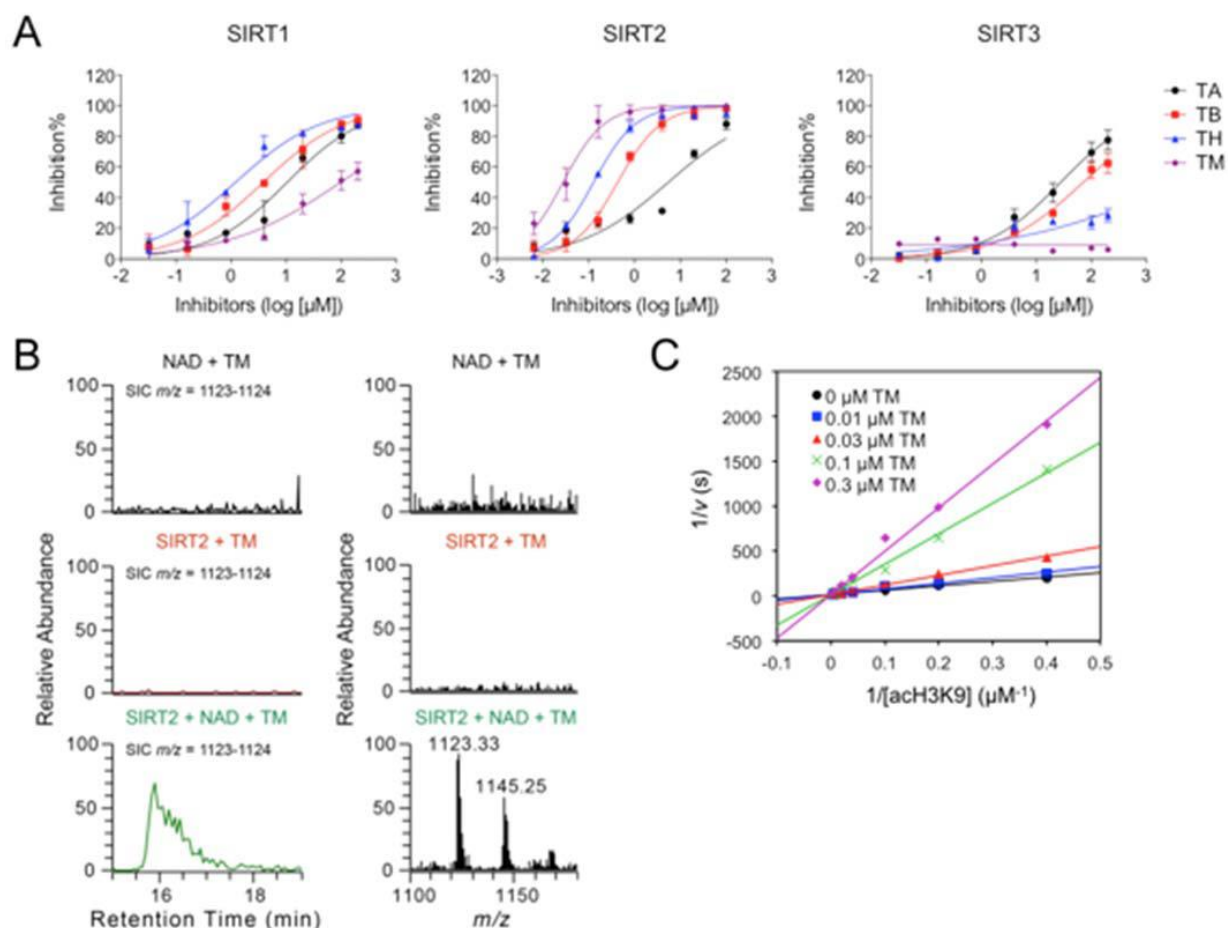


Figure S1. Related to Figure 1. (A) Dose-responsive curve for TA, TB, TH, TM and M against SIRT1-3. **(B)** LC-MS detection of the covalent intermediate formed by TM and NAD. The selected ion chromatogram (SIC) ($m/z = 1123-1124$) was shown on the left, the mass spectrum was shown on the right. The data from the reaction mixture containing 100 μM NAD, 100 μM TM, 1 mM DTT, and 20 mM pyridinium formate (pH 7.0) or the mixture containing 50 μM SIRT2, 100 μM TM, 1 mM DTT, and 20 mM Pyridinium formate (pH 7.0) were shown as negative controls. **(C)** Double reciprocal plot with varied TM and acH3K9 concentrations. Data was fit to competitive inhibition using Graphpad Prism. Error bars represent mean \pm sd.

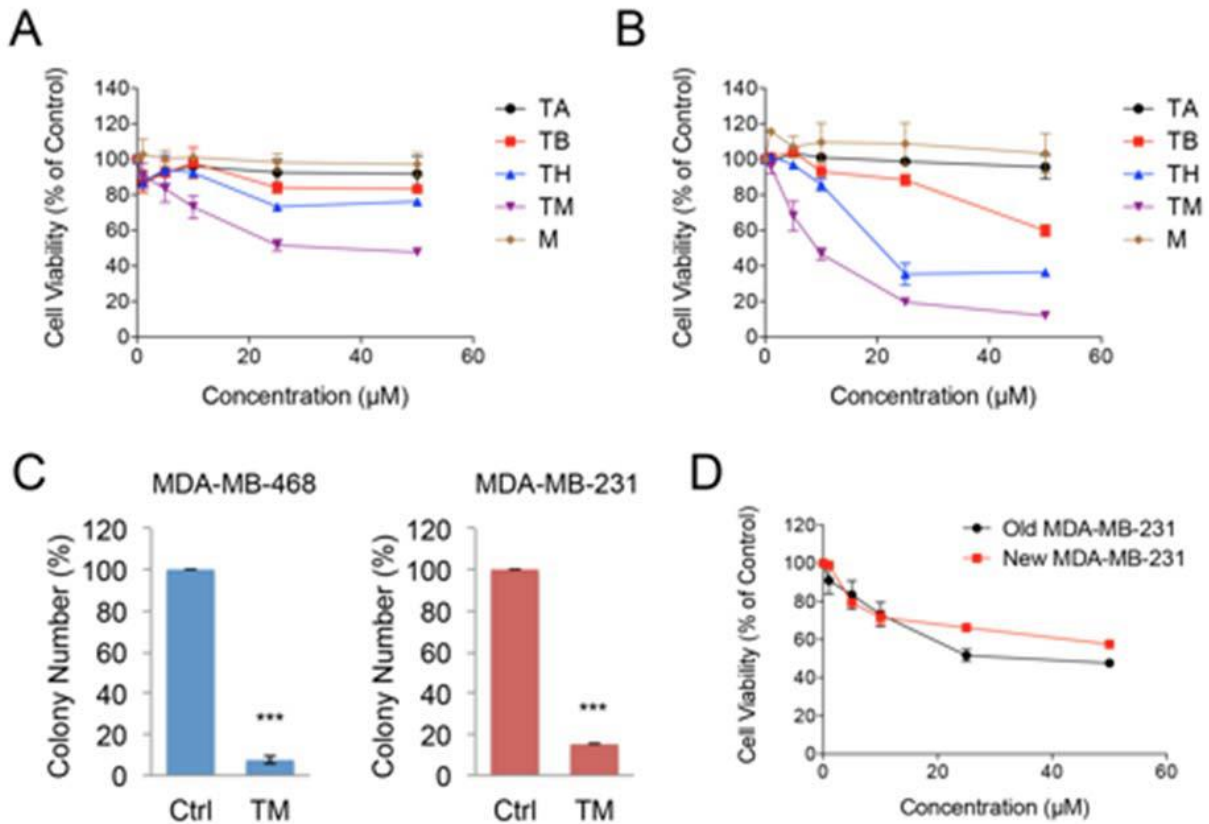


Figure S2. Related to Figure 2. (A and B) Cell viability of MDA-MB-231 (A) and HeLa (B) cells treated with ethanol or indicated inhibitors (1, 5, 10, 25, 50 μM) for 72 hr. (C) Soft agar colony formation of MDA-MB-468 and MDA-MB-231 cells treated with ethanol or TM (25 μM). The y axis represents percent colony number relative to ethanol-treated cells. Statistics, two-tailed Student's t-test. (D) Comparison of the sensitivity of two batches of MDA-MB-231 cells to TM treatment. The old MDA-MB-231 cell line has been maintained in our laboratory for over 2 years; while the new MDAMB-231 cell line has been recently purchased from ATCC. Cells were seeded in 96-well plate one day before TM treatment at a density of 3,000/well. On the day of treatment, cells were incubated with media containing 0, 1, 5, 10, 25, and 50 μM for TM for 3 days. CellTiter-Blue® assay was performed to assess the cell viability. Error bars represent mean \pm sd. *** $p < 0.001$.

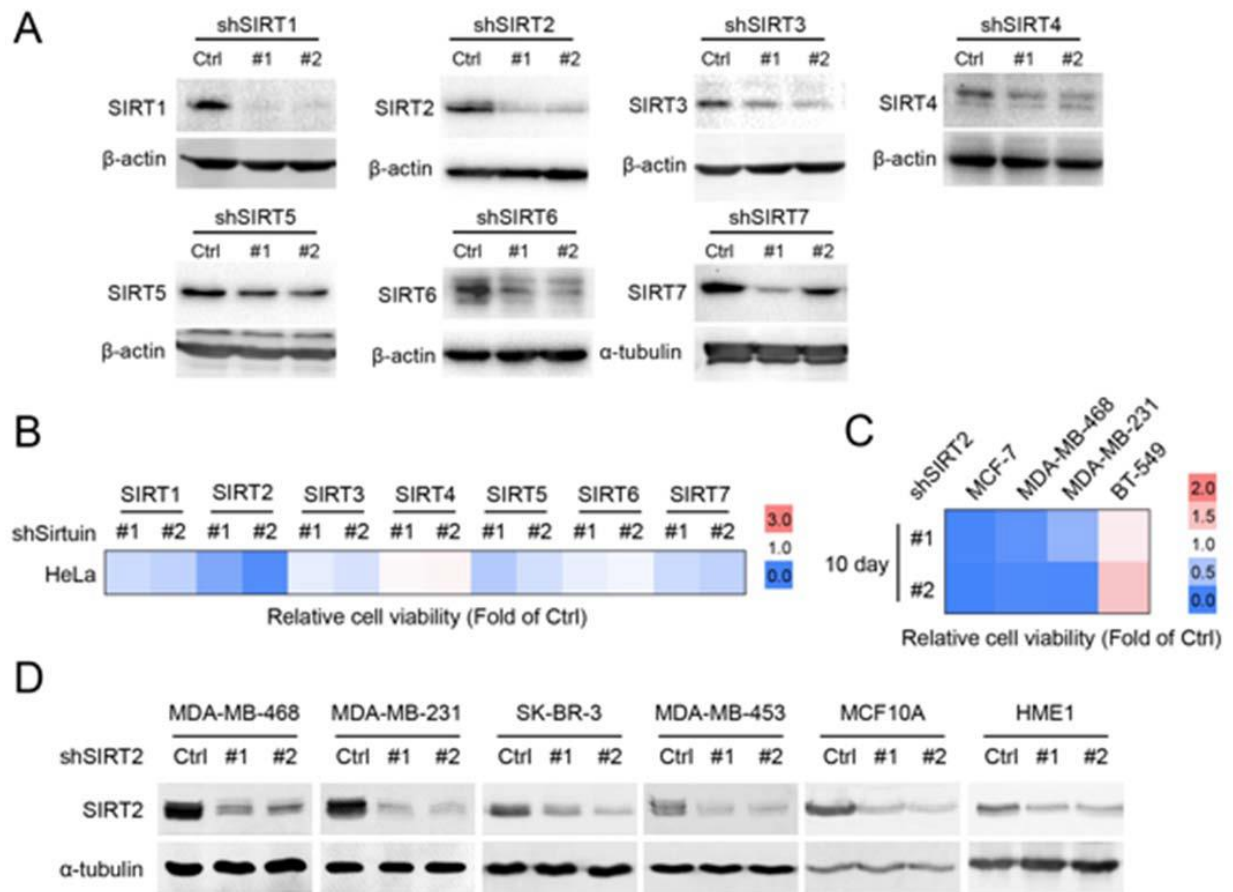


Figure S3. Related to Figure 3. (A) Representative results showing the knockdown efficiency of SIRT1-7 in HeLa cells. Cells were infected with lentivirus carrying Luciferase shRNA and shRNAs against SIRT1-7 for 72 hr before analyzed by Western blot for sirtuin levels. **(B)** Cytotoxicity effects of knocking down SIRT1-7 in HeLa cells after 72 hr of lentiviral infection. **(C)** Cytotoxicity effects of SIRT2 knockdown in MCF-7, MDA-MB-468, MDA-MB-231 and BT-549 cells at day 10 after the infection. **(D)** SIRT2 knockdown efficiency in Figure 3B and Figure S3C was confirmed by Western blot (the first row). The α-tubulin level was used as internal standard of total protein amount.

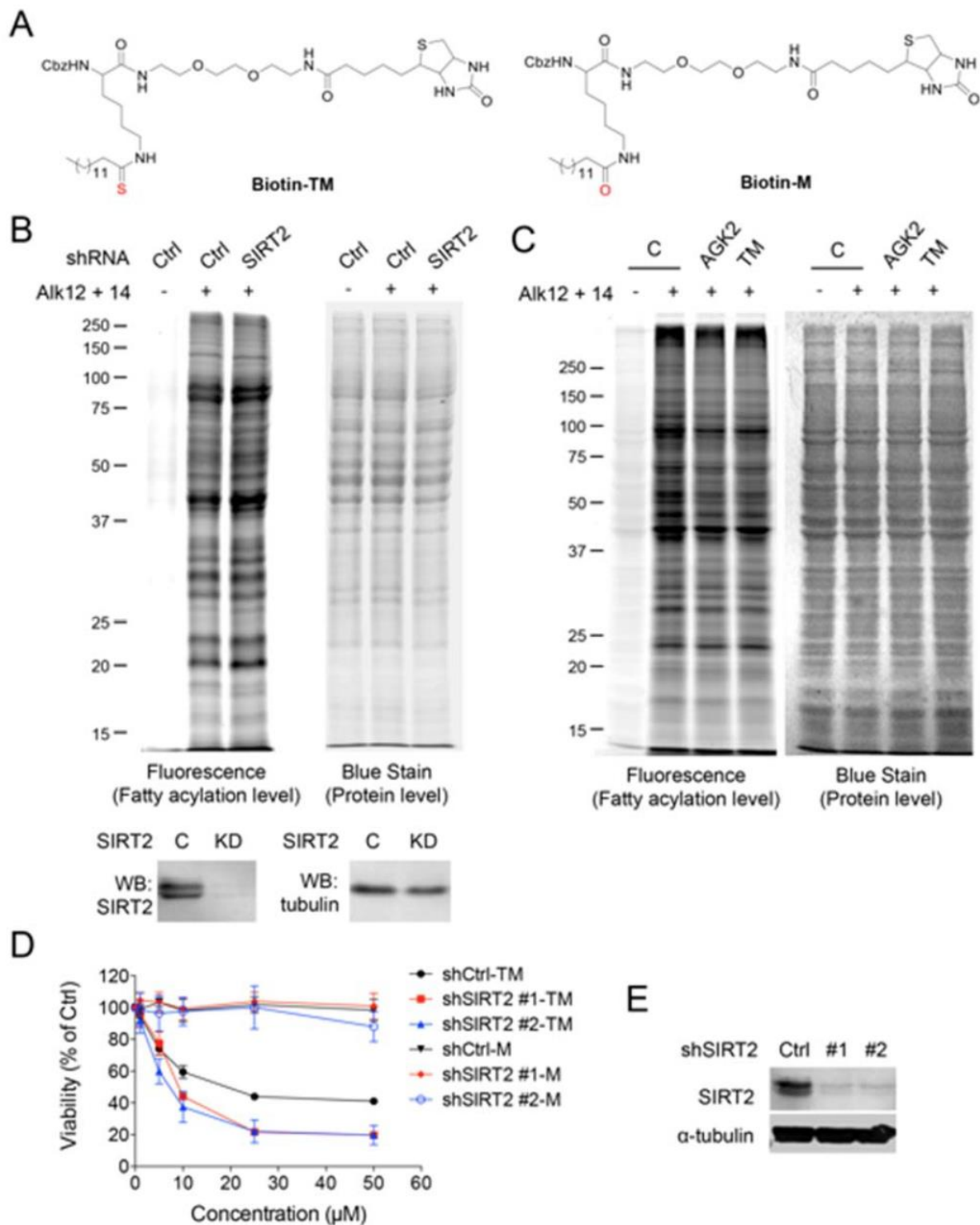


Figure S4. Related to Figure 4. (A) Structures of Biotin-TM and Biotin-M. **(B)** Global protein fatty-acylation in HEK293T cells with Ctrl and SIRT2 knockdown. Protein fatty

acylation was detected by a metabolic labeling method using alkyne-tagged fatty acid analogs Alk12 (50 μ M) and Alk14 (50 μ M) as previously reported (Jiang et al., 2013). **(C)** Global protein fatty acylation in HEK293T cells treated with the ethanol, AGK2 (25 μ M) or TM (25 μ M) for 6 hr in the presence of Alk12 (50 μ M) and Alk14 (50 μ M). **(D)** Effect of SIRT2 knockdown on the sensitivity of MDA-MB-231 cells to TM. MDA-MB-231 cells were infected with lentiviral Luciferase shRNA and SIRT2 shRNAs, respectively, for 24 hr before being treated with different concentrations of TM for another 72 hr. Cell viability was measured by CellTiter-Blue® assay. **(E)** SIRT2 knockdown in **(D)** was confirmed after 72 hr of infection by Western blot. Error bars represent mean \pm sd.

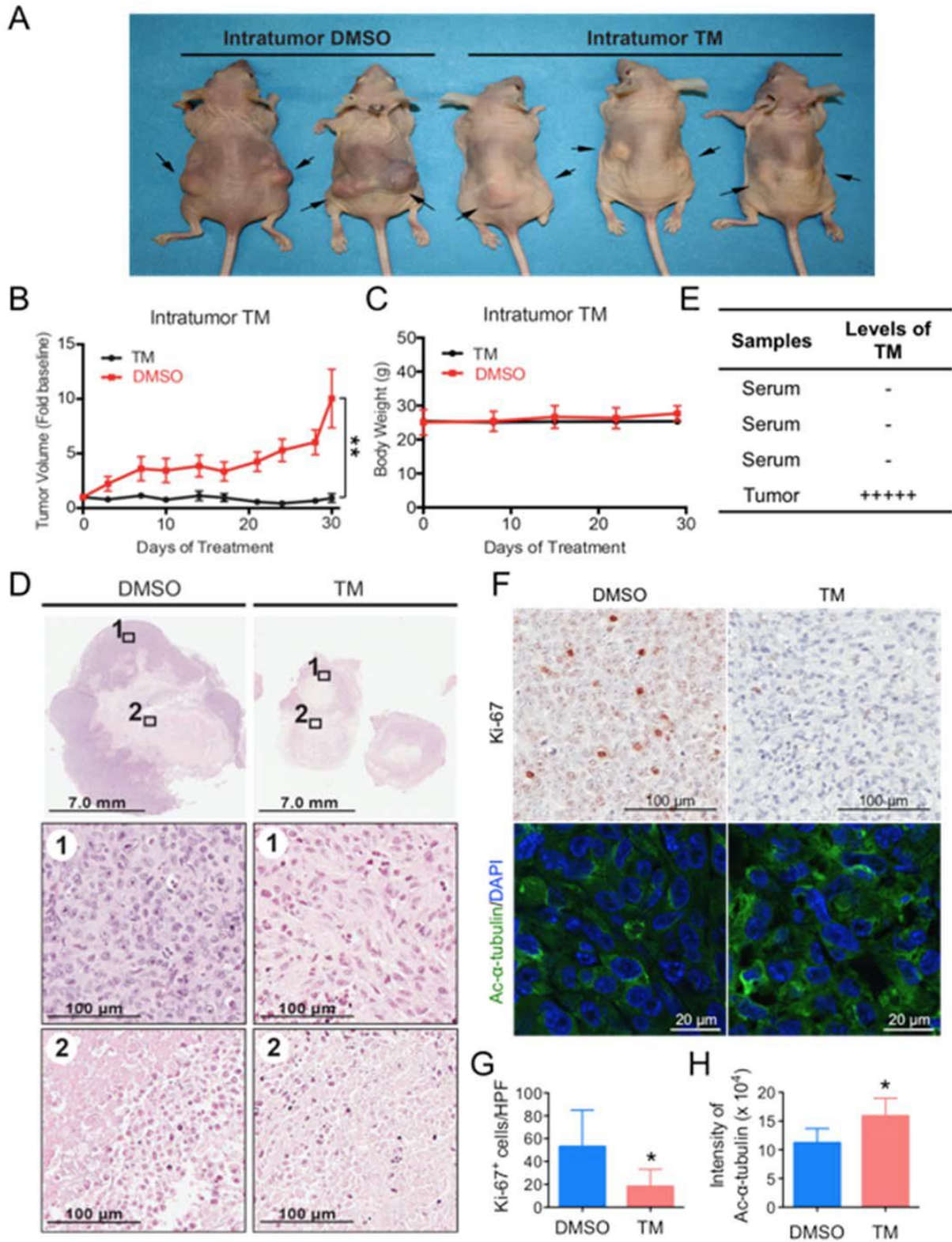


Figure S5. Related to Figure 5. Analysis of tumor growth and histopathological findings of xenografted mice treated by intratumor TM injection. Mice bearing MDA-MB-231 human breast cancer xenograft were divided into two groups and treated by direct intratumor injection with either the control vehicle solvent (DMSO) or TM (0.75 mg TM in 50 μ L DMSO; n = 5) three times per week. Tumors were collected after 30-day treatment. **(A)** Gross findings at necropsy after 30 days of intratumor treatment with either DMSO or TM. **(B)** Tumor growth chart. Statistics, paired Student's ttest. **(C)** Mouse body weight chart. **(D)** Hematoxylin and eosin staining of tumor tissues after 30 days of treatment with either DMSO or TM. **(E)** Detection of TM in mouse serum and tumor tissues by mass spectrometry. **(F)** Representative images of Ki-67 immunohistochemistry staining and acetyl- α - tubulin (K40) immunofluorescence staining of tumor tissues after 30 days of treatment with either DMSO or TM. **(G)** Quantification of Ki-67+ cells in **(F)**. The y axis represents Ki-67+ cells per high power field (10 HPFs/tumor for all the tumors analyzed, n = 4 for DMSO, n = 6 for TM). Statistics, unpaired Student's t-test. **(H)** Quantification of acetyl- α -tubulin fluorescence intensity in **(F)**. The y axis represents integrated intensity per cell. (10 HPFs/tumor for all the tumors analyzed, n = 4 for DMSO, n = 6 for TM). Statistics, unpaired Student's t-test. Error bars represent mean \pm sd. *p < 0.05, **p < 0.01.

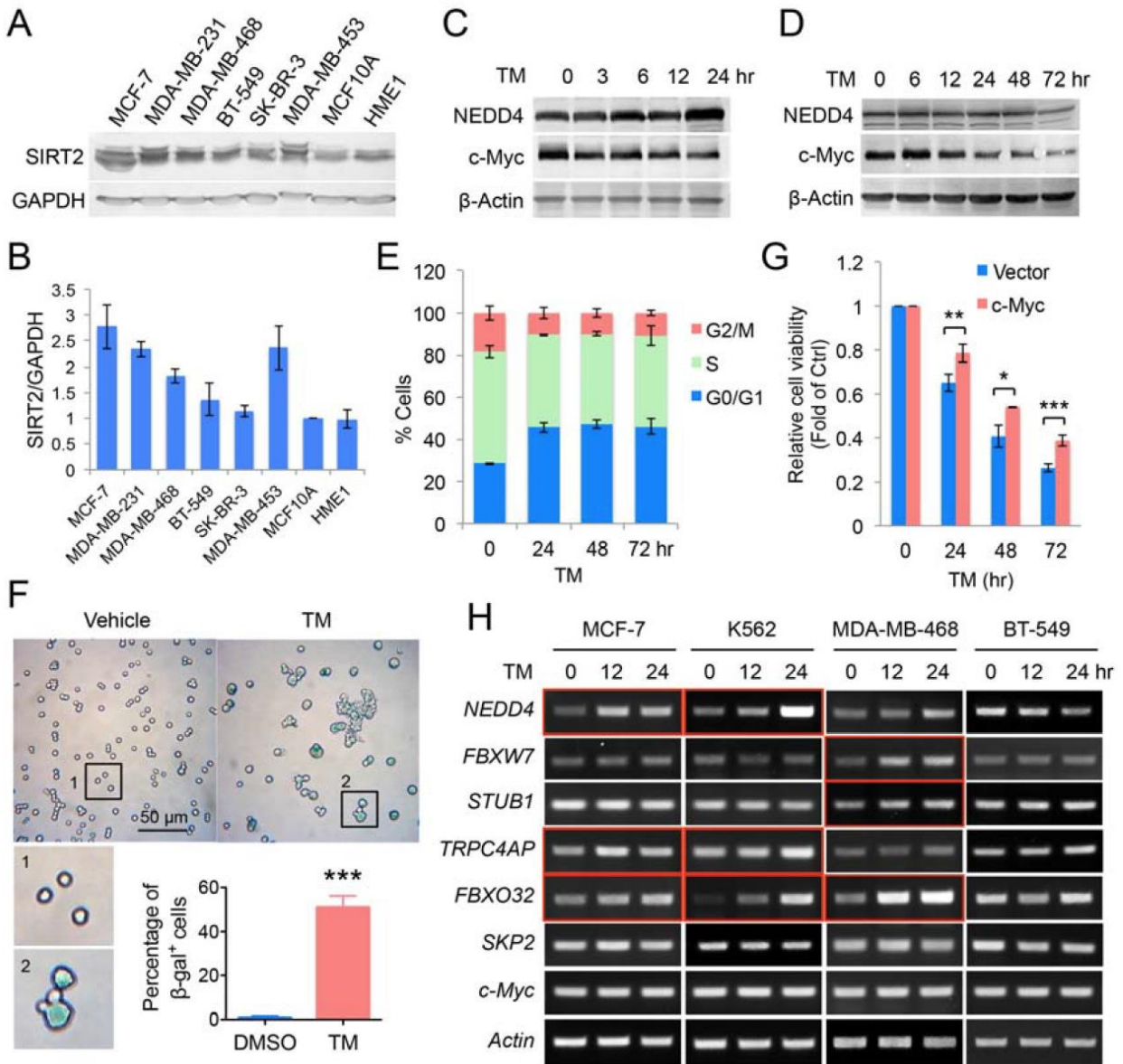
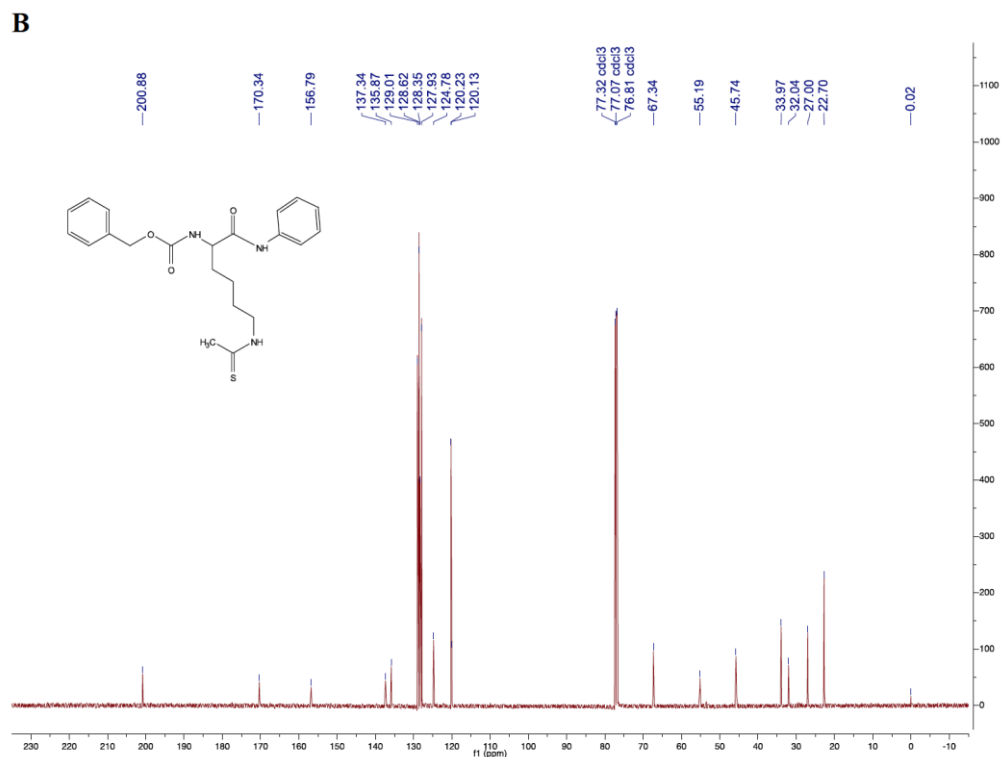
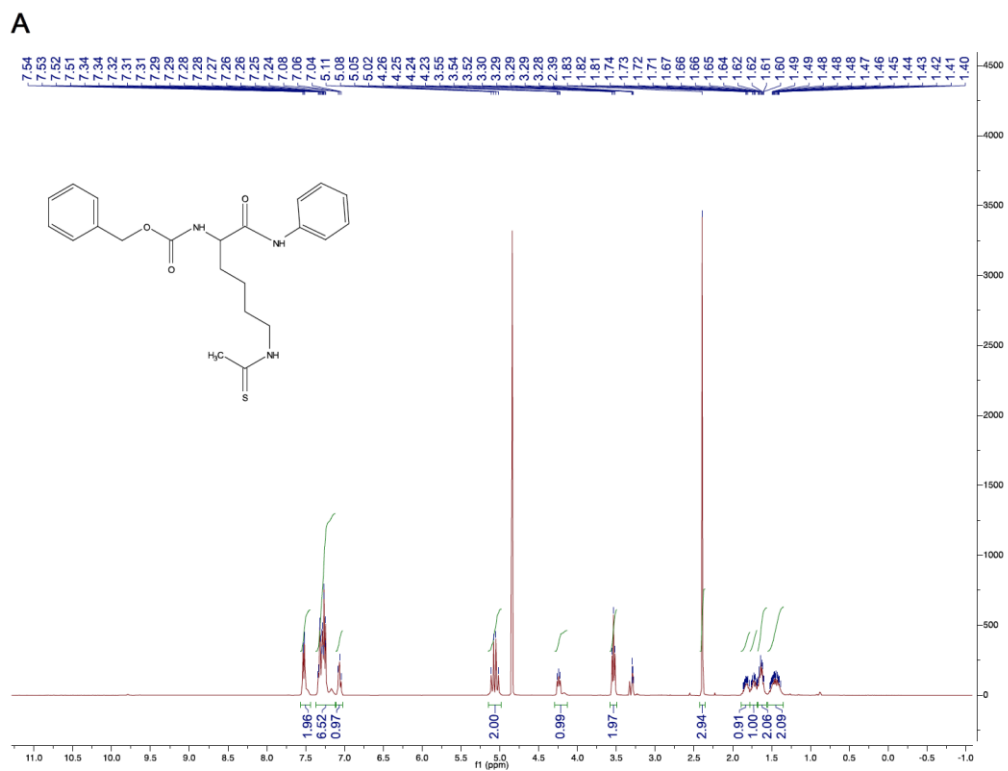
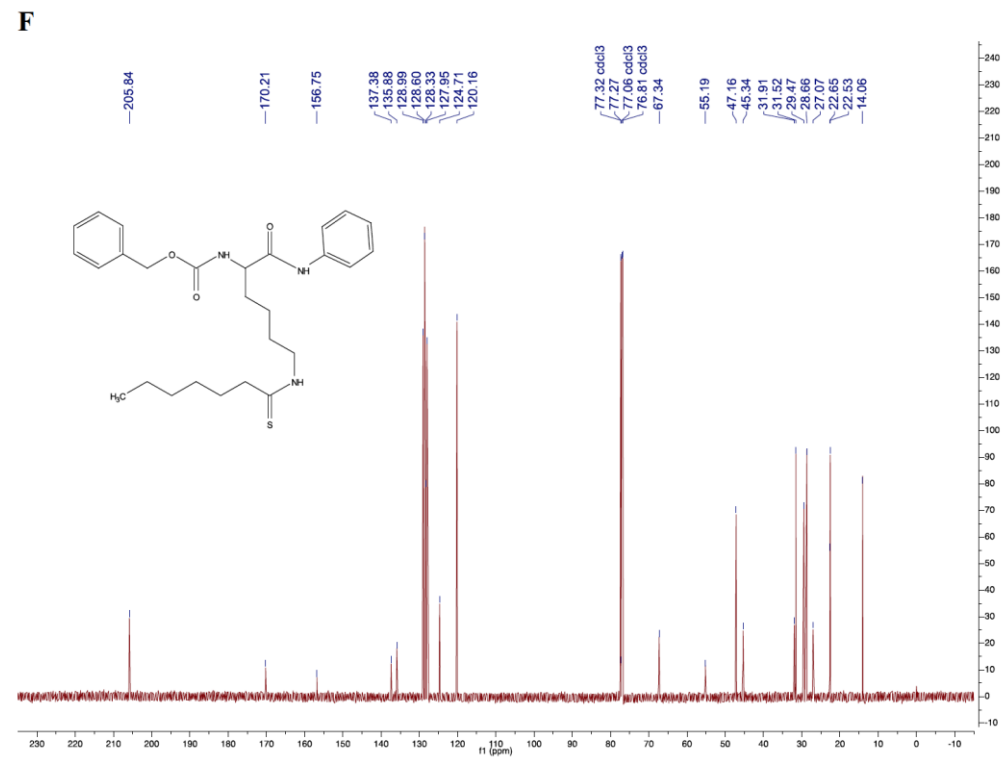
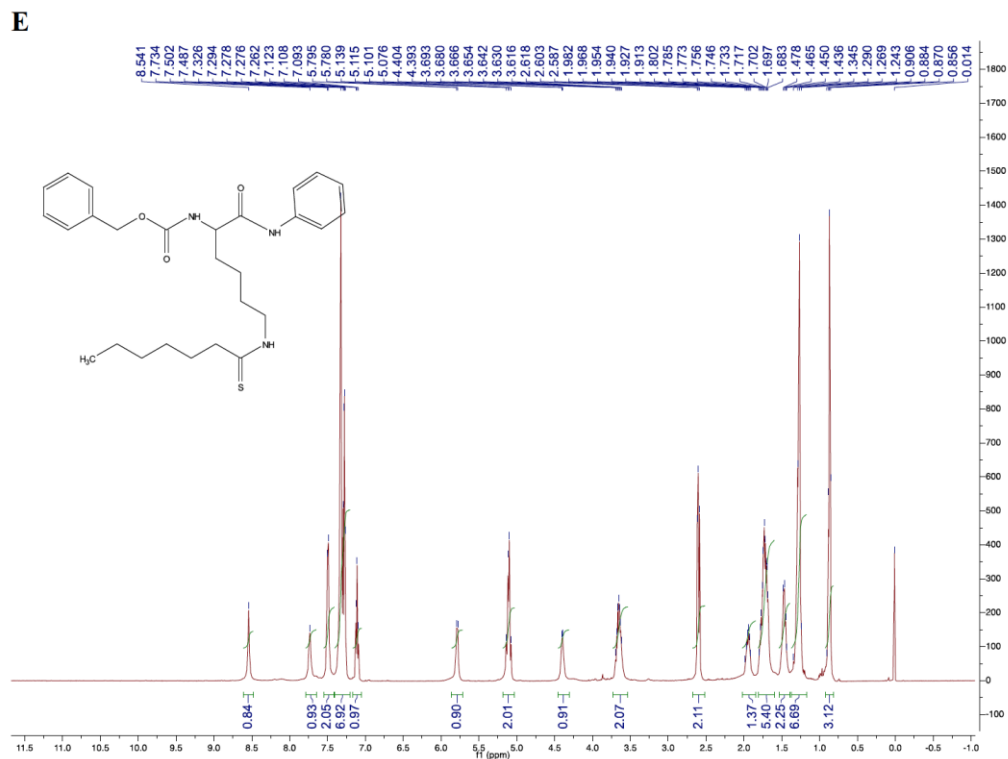


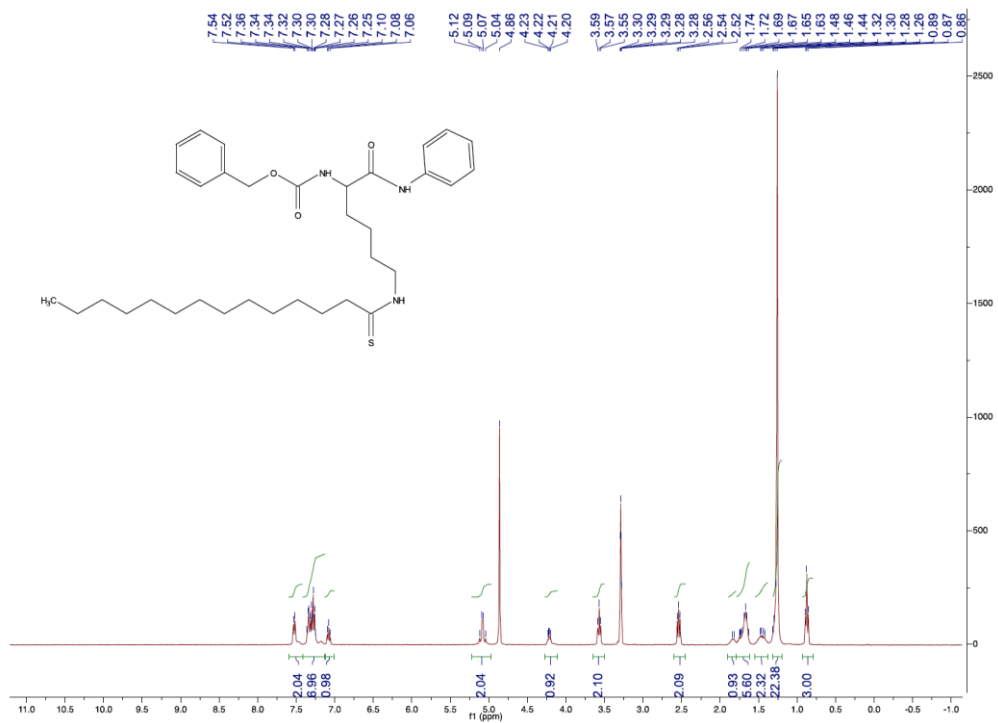
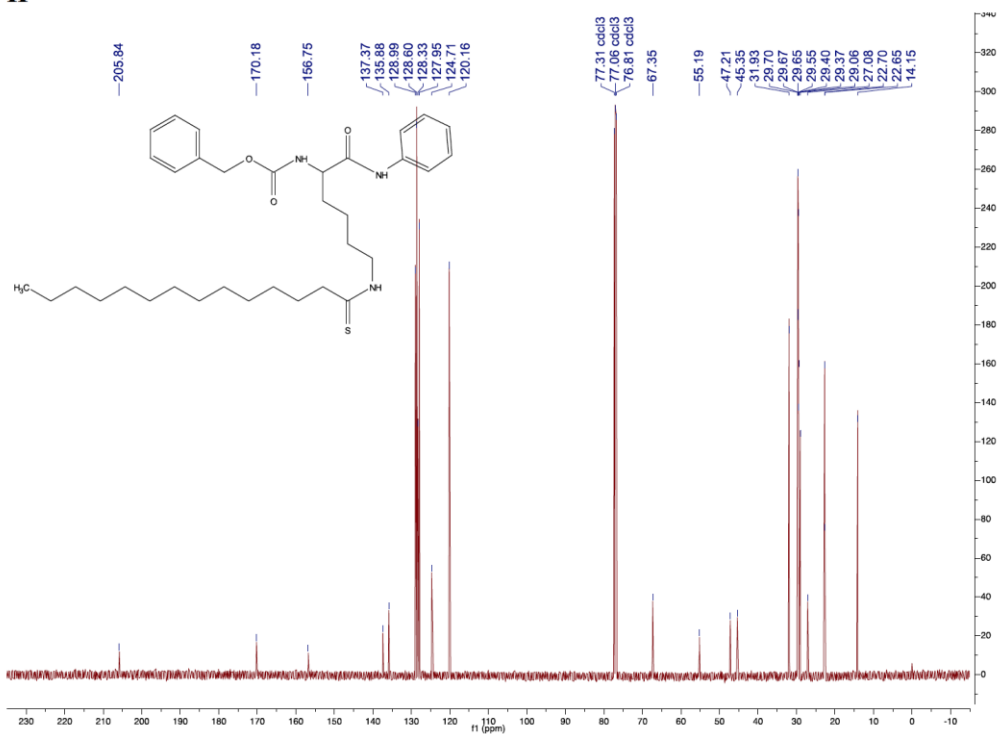
Figure S6. Relate to Figure 8. (A, B) SIRT2 levels in different human normal and breast cancer cell lines. Western blot analysis of SIRT2 level (A) and semi-quantification of SIRT2 level relative to GAPDH level (B). (C, D) Effects of TM on c-Myc and NEDD4 protein levels in K562 (C) and MDAMB-468 (D) cells. Cells were treated as indicated. (E) Cell cycle distribution of K562 cells treated with TM (25 μM) for 0, 24, 48 or 72 hr. The graph shows the percentage of cells for each cell cycle phase as assessed by propidium iodide (PI) staining-coupled flow cytometry. (F) Acidic β-gal (β-

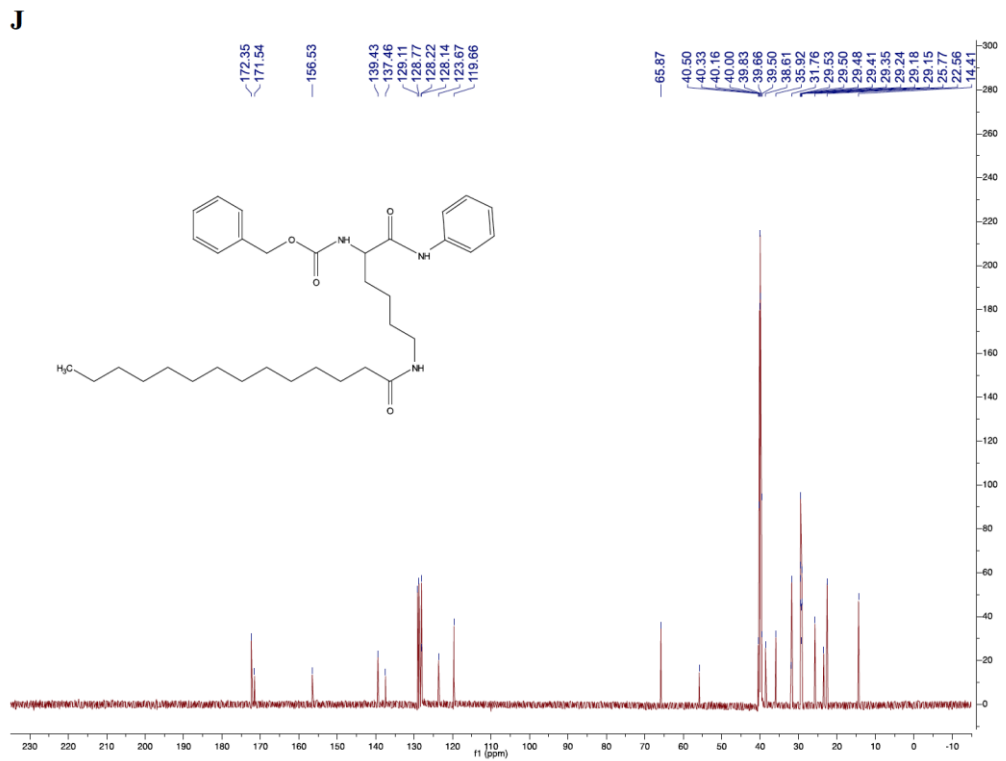
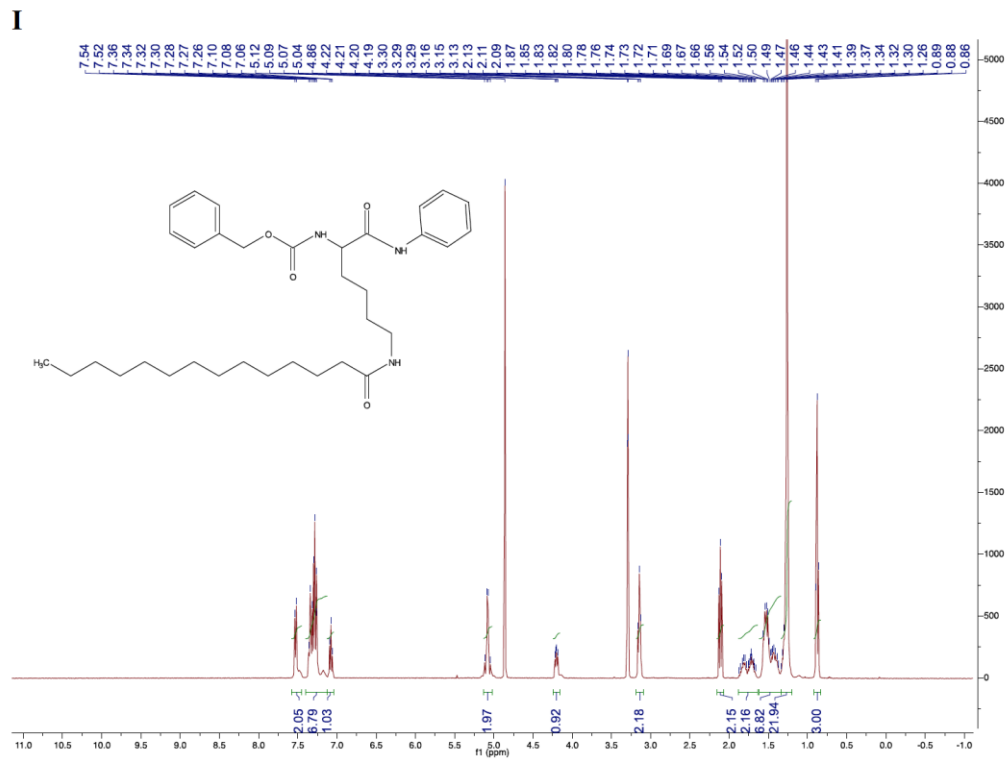
gal) staining in K562 cells treated with TM (25 μ M) for 5 days. Quantification (right panel) was shown as percentage of β -gal⁺ cells. Statistics, two-tailed Student's t-test.

(G) Effect of c-Myc overexpression on the cytotoxicity effect of TM. MCF-7 cells transfected with pCDH vector or pCHD-c-Myc for 12 hr were treated with TM (25 μ M) for another 0, 24, 48 or 72 hr, followed by CellTiter-Blue® assay. **(H)** Effect of TM on the transcript levels of various E3 ligases of c-Myc. MCF-7, K562, MDA-MB-468 or BT-549 cells were treated with TM (25 μ M) for the indicated time. PCR was performed for the assessment of transcript levels of E3 ligases (NEDD4, FBXW7, STUB1, TRPC4AP, FBXO32, SKP2), c-Myc and Actin. Statistics, two-tailed Student's t-test. Error bars represent mean \pm sd. *p < 0.05, **p < 0.01, ***p < 0.001.

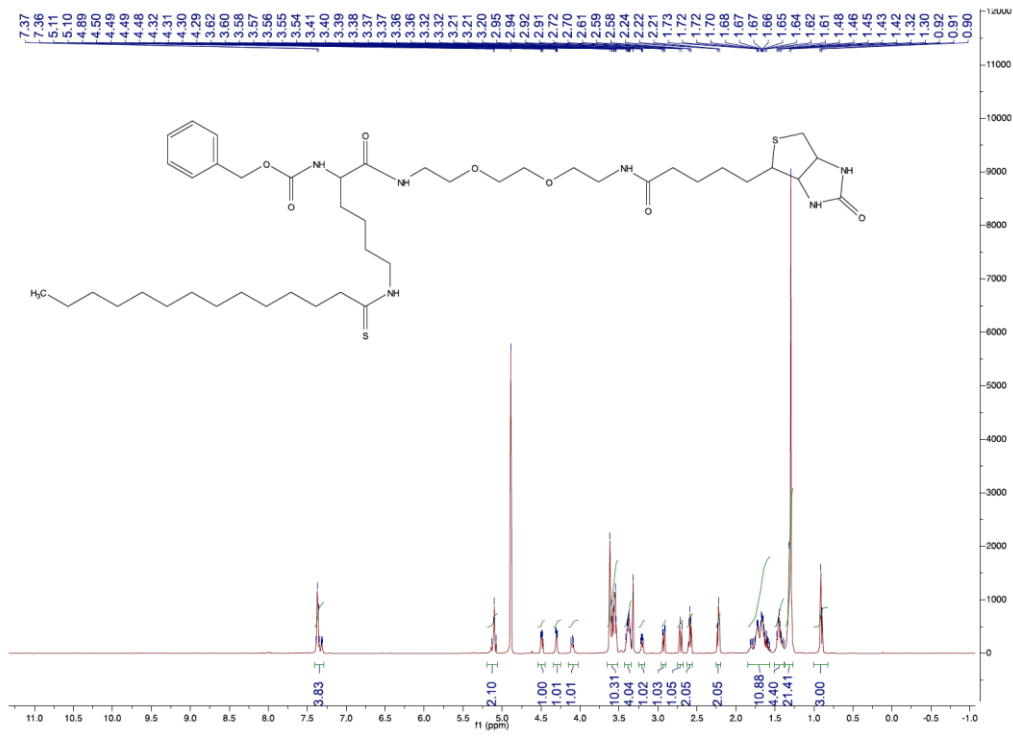




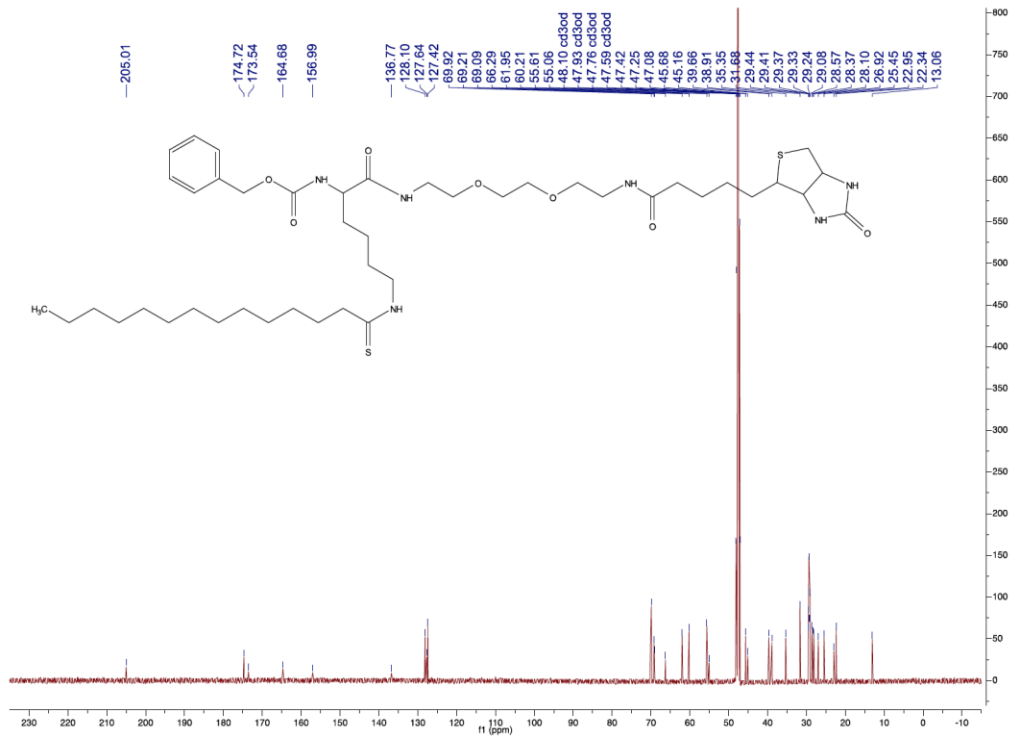
G**H**



K



L



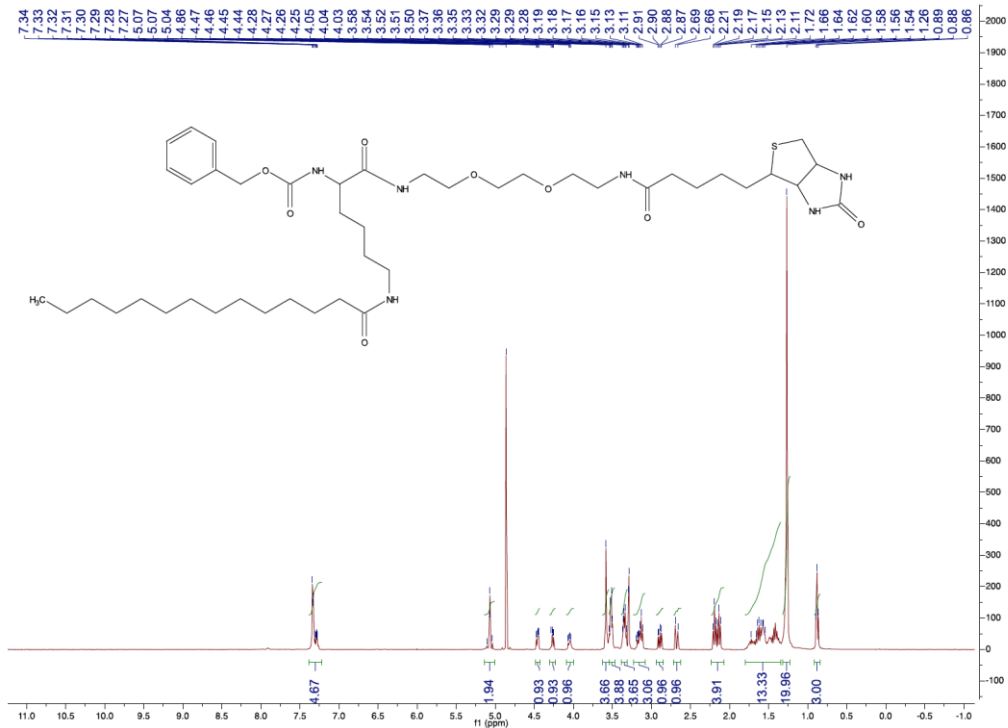
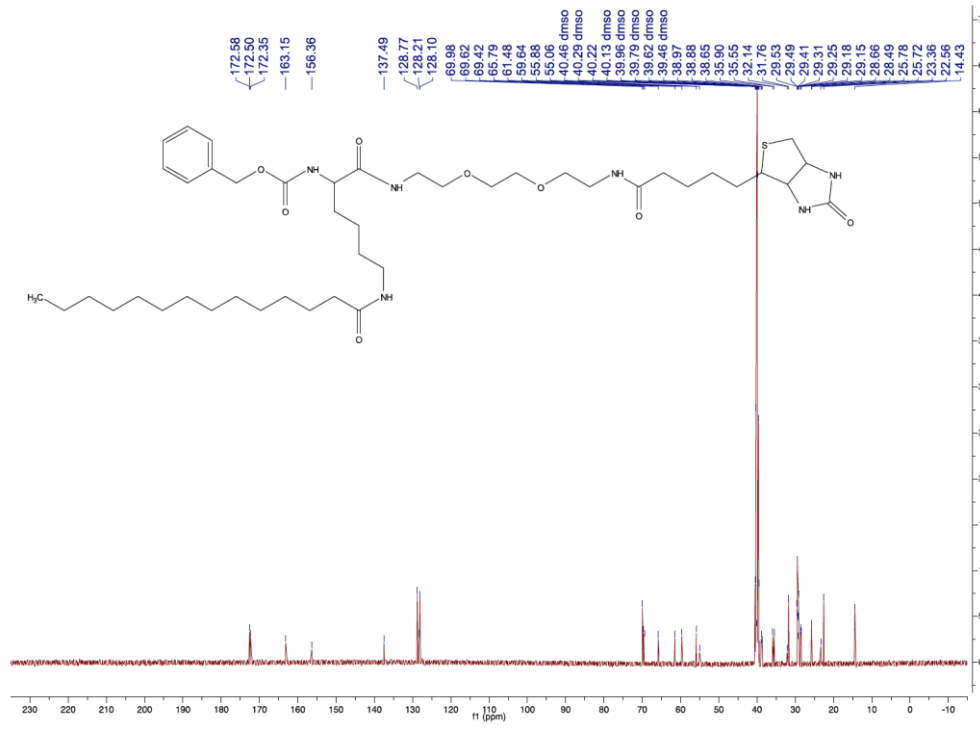
M**N**

Figure S7. Relate to Synthesis of Compounds used in the study in the section of Experimental Procedures. NMR spectra of the synthesized compounds. **(A)** ¹H NMR spectrum of Compound TA. **(B)** ¹³C NMR spectrum of Compound TA. **(C)** ¹H NMR spectrum of Compound TB. **(D)** ¹³C NMR spectrum of Compound TB. **(E)** ¹H NMR spectrum of Compound TH. **(F)** ¹³C NMR spectrum of Compound TH. **(G)** ¹H NMR spectrum of Compound TM. **(H)** ¹³C NMR spectrum of Compound TM. **(I)** ¹H NMR spectrum of Compound M. **(J)** ¹³C NMR spectrum of Compound M. **(K)** ¹H NMR spectrum of Compound Biotin-TM. **(L)** ¹³C NMR spectrum of Compound Biotin-TM. **(M)** ¹H NMR spectrum of Compound Biotin-M. **(N)** ¹³C NMR spectrum of Compound Biotin-M.

SUPPLEMENTAL REFERENCES

- Debacq-Chainiaux, F., Erusalimsky, J. D., Campisi, J., and Toussaint, O. (2009). Protocols to detect senescence-associated beta-galactosidase (SA-beta-gal) activity, a biomarker of senescent cells in culture and in vivo. *Nat. Protoc.* 4, 1798-1806.
- Du, J., Jiang, H., and Lin, H. (2009). Investigating the ADP-ribosyltransferase activity of sirtuins with NAD analogues and ³²P-NAD. *Biochemistry* 48, 2878-2890.
- He, B., Hu, J., Zhang, X., and Lin, H. (2014). Thiomyristoyl peptides as cell-permeable Sirt6 inhibitors. *Org. Biomol. Chem.* 12, 7498-7502.
- Jiang, H., Khan, S., Wang, Y., Charron, G., He, B., Sebastian, C., Du, J., Kim, R., Ge, E., Mostoslavsky, R., et al. (2013). SIRT6 regulates TNF-alpha secretion through hydrolysis of longchain fatty acyl lysine. *Nature* 496, 110-113.
- Mabjeesh, N. J., Escuin, D., LaVallee, T. M., Pribluda, V. S., Swartz, G. M., Johnson, M. S., Willard, M. T., Zhong, H., Simons, J. W., and Giannakakou, P. (2003). 2ME2 inhibits tumor growth and angiogenesis by disrupting microtubules and dysregulating HIF. *Cancer Cell* 3, 363-375.

**APPENDIX B. Simultaneous Disruption of Ribonucleotide Reductase
Regulatory Mechanism Causes Synthetic Lethality in Mice**

Page JL, **Negrón Abril YL**, Li M, Balmus G, Ylikallio E, Jeon Y, Warmoes MO, Oxford E, Parvez S, Zerrad Y, Xu X, Levy J, Tynismaa H, Peters RM, Southard T, Kelly K, Suomalainen A, Aye Y, Locasale JW, Weiss RS.

Manuscript in preparation

Author Contribution

Yashira L. Negrón Abril is a first co-author of this manuscript. She updated the manuscript and generated all or partial data for the following figures

Figure 2

Figure 3

Figure 6

Figure S4

Figure S5

ABSTRACT

A balanced supply of the four deoxyribonucleotide triphosphates (dNTPs) is essential for genomic integrity in mammalian cells. The rate-limiting step in *de novo* dNTP biosynthesis is catalyzed by Ribonucleotide Reductase (RNR). RNR is composed of two non-identical homodimeric subunits, α and β , encoded by the *Rrm1* and *Rrm2/p53R2* genes respectively. Regulation of RNR activity is crucial to maintaining balanced dNTP pools. In mammals, RNR activity is regulated in part by β subunit availability and negative feedback control of the α subunit via an allosteric site termed the activity site. We previously showed that β subunit overexpression in mice induces lung neoplasms. Disruption of the α subunit activity site by the D57N mutation results in an enzyme that cannot be inhibited by dATP, leading to elevated dNTP pools. Here we report on a mouse model featuring loss of RNR feedback control, the *Rrm1-D57N^{Tg}* mouse. Despite loss of dATP feedback inhibition, *Rrm1-D57N^{Tg}* mice were grossly normal. However, simultaneous overexpression of *Rrm1-D57N* and either β subunit caused synthetic lethality associated with dramatically elevated dNTP pools. *Rrm1-D57N^{Tg} + Rrm2^{Tg}* mice survived gestation, but rapidly developed multiple organ dysfunction, including cardiac dilation, kidney degeneration and hepatocellular swelling, that ultimately resulted in death. Together, these data suggest that simultaneous disruption of two main RNR regulatory mechanisms induces lethal imbalances of dNTP pools.

INTRODUCTION

Ribonucleotide reductase (RNR) is a key enzyme for the biosynthesis of the four deoxyribonucleotide triphosphates (dNTPs). RNR catalyzes the rate-limiting step in *de novo* dNTP synthesis by converting ribonucleotides to 2'-deoxyribonucleotides (Nordlund and Reichard 2006). Mammalian RNR enzyme is composed of two non-identical homodimeric subunits, α and β , encoded by the *Rrm1* and *Rrm2/p53R2* genes respectively (Tanaka *et al.* 2000; Nordlund and Reichard 2006). The α subunit of RNR contains the catalytic site and two allosteric sites that regulate the substrate specificity and the enzyme activity. The β subunit contains an iron center that is used for the generation of a tyrosyl radical that is essential for RNR activity.

Regulation of RNR activity is crucial for maintaining balanced dNTP pools (Aye, *et al.* 2015). In mammals, RNR activity is primarily controlled through two main mechanisms; limitation of β subunit availability and allosteric feedback control. The availability of the α and β subunits is regulated in a cell cycle-dependent manner by S phase-specific transcription of *Rrm1* and *Rrm2* genes and the degradation of RRM2 protein at the end of S-phase. While the protein expression of the RRM1 (α subunit) remains relatively constant throughout the cell cycle, the protein expression of RRM2 (β subunit) increases to maximal levels in S-phase and is rapidly degraded by the anaphase-promoting complex (APC^{Cdh1}) in late mitosis, limiting RNR activity (Engström *et al.* 1985; Chabes *et al.* 2003; Chabes *et al.* 2004). The alternative β subunit induced by p53 (p53R2) is expressed at low levels throughout the cell cycle and can complex with the

RRM1 protein to provide dNTPs for mitochondrial replication and DNA repair (Guittet *et al.* 2001; Hakansson *et al.* 2006). We have previously shown that overexpression of either *Rrm2* or *p53R2* in mice induced lung neoplasm (Xu *et al.* 2008). Furthermore, disruption of RNR cell cycle regulation by overexpressing individual RNR subunits or combined overexpression of both wild-type RNR subunits induces modest dNTP pool alterations in mice and age-dependent mtDNA depletion (Xu *et al.* 2008; Ylikallio *et al.* 2010).

In addition to control of RNR protein levels, a second regulatory mechanism governing RNR activity is allosteric feedback control. This involves the binding of effectors to two distinct allosteric sites in the α subunit of RNR: the specificity and the activity site (Nordlund and Reichard 2006). Binding of ATP, dATP, dTTP or dGTP to the specificity site determines substrate specificity. Binding of ATP or dATP to the activity site can respectively stimulate or inhibit RNR activity (Fairman *et al.* 2011). It has been reported that mutation in residue Asp57 to Asn (D57N) results in conformational changes of RNR and consequently affects its ability to discriminate between dATP and ATP (Weinberg *et al.* 1981; Eriksson *et al.* 1981; Caras and Martin 1988). Disruption of the allosteric feedback control by *Rrm1*^{D57N} mutation was shown to be mutagenic in yeast and in mammalian cell culture models (Weinberg *et al.* 1981; Caras and Martin 1988; Chabes *et al.* 2003). Furthermore, dATP feedback inhibition of RNR is essential in developing embryos (Song *et al.* 2017).

To date, no studies have been performed to test the physiological effect of the *Rrm1*^{D57N} mutation in mice. Here we report on the first model of loss of

allosteric feedback control of RNR in mice, as well as the effect of simultaneous disruption of multiple regulatory modes of RNR. Whereas mice that overexpressed *Rrm1-D57N* alone were grossly normal, combined overexpression of *Rrm1-D57N* with either small subunit caused synthetic lethality and unbalanced dNTP pools. These manipulations will allow us to study the effects of various degrees of RNR deregulation in mice, and more completely understand the complex control of this critical enzyme.

MATERIALS AND METHODS

Plasmids

An expression plasmid encoding mouse *Rrm1* was constructed in the pCaggs expression vector as described previously (Ylikallio *et al.* 2010). The *Rrm1-D57N* mutation was inserted in the pCaggs-*Rrm1* plasmid by site-directed mutagenesis as described in Supplemental Materials and Methods.

Experimental mice

Transgenic mice were generated by microinjection of linear plasmid DNA into the male pronucleus of FVB/N zygotes as described in the Supplemental Materials and Methods. *Rrm1-D57N(high/low)^{Tg}* mice were crossed with either *Rrm2^{Tg}* or *p53R2^{Tg}* mice to generate bitransgenic mice. All mice were maintained following guidelines approved by the Cornell University Institutional Laboratory Animal Use and Care Committee.

Southern blot analysis

DNA extracted from tails of adult mice or yolk sacs of embryos was subjected overnight to transgene-specific restriction digest and separated on 0.8% agarose gel. The *Rrm1* and *Rrm1-D57N* transgenes were detected by digestion with *Bam*HI (Fermentas) and the p53R2 transgene was detected by digestion with *Eco*RV (Fermentas). Following alkaline transfer to a nylon membrane (GeneScreen Plus, Perkin Elmer), the presence of transgene DNA was detected with a transgene-specific radiolabeled probe. To determine mtDNA copy number total DNA was isolated from tissues by proteinase K digestion and standard phenol-chloroform extraction. Southern blotting was performed essentially as described (Tynismaa *et al.* 2005).

Northern blot analysis

Total RNA was extracted from mouse cells with RNASat-60 (TelTech, Inc) and separated on agarose/formaldehyde gel. RNA was transferred to a nylon membrane (GeneScreen, Perkin Elmer) and detected with *Rrm1*- or *Gapdh*-specific radiolabeled probe.

Immunoblot analysis

Tissue extracts were prepared as described in Supplemental Materials and Methods. *Rrm1* protein was detected by AD203, mouse monoclonal anti-R1 (InRo Biomedtek), and loading was assessed by detection of α -tubulin with

mouse monoclonal anti- α -tubulin (Sigma). To quantify overexpression in *Rrm1-D57N* transgenic mice, serial dilutions were prepared in RIPA buffer.

Measurement of Ribonucleotide Reductase activity

The activity of RNR was assayed by measuring the formation of radioactive dCDP from [5-³H] CDP. The assay mixture (+/- 0.3 mM dATP) was pre-incubated in a 37 °C water bath for 1 minute after which reconstituted human Rrm2 (3 μ M) was added and the assay mixture was incubated. Aliquots, 30 μ L each, were removed at the indicated time points, quenched with 30 μ L of 2% HClO₄ and neutralized with 30 μ L of 0.4M NaOH. Radioactivity was measured using a scintillation counter (Beckman Coulter, LS6500), subsequent to dephosphorylation with Alkaline Phosphatase as described in the Supplemental Materials and Methods. To measure the activity of RNR in tissue lysates, 400-600 mg of frozen mouse skeletal muscle tissue was ground to a fine powder using a pestle and mortar and transferred to an Eppendorf tube. The tissue powder was suspended in 50 μ L of assay buffer and subjected to 3 cycles of rapid freeze-thaw followed by centrifugation at 18,000 x g for 8 min in a pre-chilled (4°C) centrifuge. The reaction mixture was initiated after adding clarified tissue lysate and 6 μ M reconstituted human Rrm2 to the assay buffer (+/- 0.3 mM dATP). 30 μ L of the reaction mixture was removed at the indicated time points, quenched and neutralized. Same procedure as discussed above was used for the dephosphorylation, separation of the [5-³H]-dCDP product and quantification.

Neonate survival assays

Rrm1-D57N(low)^{Tg} mice were set up in timed mating with *Rrm2^{Tg}* or *p53R2^{Tg}* mice. Females were monitored until pups were born, at which time the pups were counted and weighed. Mice were counted and weighed daily until P21. Pups were genotyped by Southern blot at weaning or when found dead. Only litters in which the fate of all pups was known and in which all control littermates survived the full 21 days or died naturally were used in this analysis. Survival plots were generated with GraphPad Prism software.

Pathological assessment of the heart

Neonates (mice ages P14 and younger) were euthanized by decapitation. Hearts were excised, gently washed in sterile 1X Phosphate Buffer Saline (PBS), fixed in 10% buffered formalin overnight at room temperature and transferred to 70% ethanol. Gross heart morphology pictures were taken through a dissecting microscope within 48 hours of neonate sacrifice. Hearts were cut in either the coronal and transverse plane and embedded for histological analysis.

Histological analysis

Adult and neonate tissues were fixed in 10% buffered formalin overnight at room temperature and embedded in paraffin. Tissues were sectioned at 5µm thickness, mounted onto slides and subjected to hematoxylin and eosin (H&E), Masson's trichrome stain (MT), Periodic Acid Schiff's stain (PAS), Phospho-histone H3 (PH3) (Abcam), mtDNA-encoded complex IV (COX) (Abcam) or the nDNA-

encoded complex II (SDH) (Abcam) staining. Stained slides were digitalized using the Amperio ScanScope (CS0 and CS2) and viewed through Amperio ImageScope program. Detailed description of immunohistological stainings are provided in the Supplemental Materials and Methods.

Extraction of nucleotides from neonate skeletal muscle and embryos

Total nucleotides were extracted from neonatal skeletal muscle using the method described in Ylikallio *et al.* (Ylikallio *et al.* 2010). Modifications to this method are described in the Supplemental Materials and Methods.

qRT-Real time PCR

Twenty-five nanograms of DNA were used as template. *mt-Cytb* gene amplification level was normalized against the amplification level of *Rbm15*, which was used as a nuclear DNA control. Samples were run on an Abi Prism SDS 7000 machine (Applied Biosystem). QPCR data were analysed using 7000 System Sequence Detection Software version 1.2.3 (Applied Biosystems). Refer to the Supplemental Materials and Methods for primer sequences.

Long PCR

Long PCR to amplify the entire mitochondrial genome or selectively deleted mtDNA molecules was done using the Expand Long Template PCR System (Roche). Twenty-five nanograms of DNA were used as template. PCR products

were separated by electrophoresis on 1% agarose gels. Cycling conditions and primer sequences are described in the Supplemental Materials and Methods.

Serum sample preparation and liquid-chromatography mass-spectrometry

For sample preparation and liquid-chromatography mass-spectrometry analysis (LC-MS), all solvents used were HPLC grade, unless otherwise specified. For metabolite extraction 10 μL of serum was added to 90 μL ice cold water. Next, 400 μL of methanol was added and the mixture was vortexed rigorously and subsequently left on ice for 10 minutes. Samples were centrifuged at 20.000 g for 10 minutes at 4 $^{\circ}\text{C}$. The supernatants were completely dried using a vacuum centrifugal evaporator. For LC-MS analysis, the pellets were reconstituted by first adding 15 μL water and next 15 μL of a 1:1 mixture methanol and acetonitrile (v/v). After centrifugation for 20 minutes at 20.000 g and 4 $^{\circ}\text{C}$, supernatants were transferred to LC vials. LC-MS was performed as described earlier by Liu *et al.* (Liu *et al.* 2014)

Peak extraction for LC-MS metabolites, statistical evaluation and pathway analysis

LC-MS raw files were analyzed using Sieve (Thermo Fisher, version 2.0). Both a targeted and untargeted approach was used. For the targeted approach, a pre-defined list with metabolite names together with associated MZ-values and retention times was used to extract high confidence peaks that passed a visual check for quality and interference. For the untargeted approach, Sieve software

selects potential peaks within certain retention time windows and performs a database search for identification. Untargeted metabolite peaks already identified in the targeted analysis were not included again. All statistical evaluations were performed using R (version 3.2.1) (Team R 2013). For data normalization, zero values were substituted with a background noise level of 1000. Significant peaks ($p < 0.05$ and FDR < 0.05) were identified using t-statistics and the false discovery rate method by Benjamini and Hochberg (Benjamini, and Hochberg 1995). The combined targeted and untargeted peaks yielded 219 significant peaks that mapped to 186 unique metabolites associated with a Human Metabolome Database (HMDB) Identifier (some peaks have multiple identifications while some do not have an associated HMDB identifier). The 219 significant peaks were used for principal component analysis and hierarchical clustering. The 186 metabolites were mapped to HMDB identifier numbers and used for pathway analysis using Metaboanalyst (version 3) (Xia, *et al.* 2012).

Data availability

Rrm1^{Tg}, *Rrm2^{Tg}*, *p53R2^{Tg}* and *Rrm1-D57N^{Tg}* mice are available upon request. The level of *Rrm1-D57N* overexpression in skeletal and heart muscles are shown in Figure S1. The frequencies of mice and embryos obtained for each strain are shown in Table S1-S3. Figures S2-S3 show representative images of muscle, kidney and liver of *Rrm1-D57N(low)^{Tg} + Rrm2^{Tg}* bitransgenic mice. Summary of body weight, heart weight, and heart to body weight ratio for wild type and *Rrm1-D57N(low)^{Tg} + Rrm2^{Tg}* mice are shown in Table S4. M-mode

echocardiographic images and measurements for wild type and *Rrm1-D57N(low)^{Tg} + Rrm2^{Tg}* bitransgenic mice are shown in Figure S4 and Table S5. Hierarchical cluster analysis of metabolites identified using mass spectrometry is shown in Figure S5. Table S6 and S7 show the list of differential metabolites in the purine and pyrimidine metabolism, and differential metabolites associated with various heart conditions, respectively.

RESULTS

Generation of *Rrm1-D57N* transgenic mice and expression analyses

To assess the effect of loss of RNR allosteric feedback control, we generated mice that overexpress a mutant form of the α subunit by modifying the pCaggs-*Rrm1* construct previously described by Xu, X. (Xu, *et al.* 2008). Two independent transgenic founder animals were obtained (Figure 1A, lanes 6 and 12). The founder animal in lane 12 showed greater transgene signal and the presence of two different transgene bands whereas the founder in lane 6 showed a single band of lower relative intensity; the resulting strains are referred to hereafter as *Rrm1-D57N(low)^{Tg}* (lane 6) and *Rrm1-D57N(high)^{Tg}* (lane 12). Both strains were maintained on a pure FVB/N background.

Endogenous and transgenic expression was assessed in a variety of tissues in *Rrm1-D57N(high)^{Tg}* and wild-type FVB mice by Northern blot analysis (Figure 1B). In wild type FVB mice, *Rrm1* was detected most strongly in the most proliferative tissues, the testis and thymus. Northern blot analysis of *Rrm1-D57N(high)^{Tg}* mice revealed two bands corresponding to *Rrm1* transcript, the

upper band from the endogenous locus was the predominant band in the spleen and thymus, while the lower band from the transgene predominated in lung, liver, kidney, and skeletal muscle.

The expression results obtained by Northern blot analysis were confirmed by immunoblot (Figure 1C). We assessed total Rrm1 protein levels in tissues obtained from wild type FVB mice (Wt), *Rrm1-D57N(low)^{Tg}* mice (L), and *Rrm1-D57N(high)^{Tg}* (H) mice. In agreement with the Southern blot in Figure 1A, *Rrm1-D57N(high)^{Tg}* mice showed higher Rrm1 protein levels than *Rrm1-D57N(low)^{Tg}* mice, which were intermediate between wild type and *Rrm1-D57N(high)^{Tg}* levels. To obtain a more precise value for *Rrm1-D57N* overexpression in tissues from transgenic mice, we utilized the serial dilution method reported previously (Ylikallio *et al.* 2010). Because pCaggs drives the greatest expression in skeletal and cardiac muscle, we assessed the level of *Rrm1-D57N* overexpression in these two tissues (Figure S1). We found that the *Rrm1-D57N(low)^{Tg}* was expressed roughly 94-fold (93.99x) in the skeletal muscle while the *Rrm1-D57N(high)^{Tg}* was expressed over 600-fold (608.41x).

To assess whether the *Rrm1-D57N^{Tg}* mice were defective for feedback control, we performed a radioactivity assay that measures the formation of radioactive dCDP from [5-³H] CDP previously described by Aye and Stubbe (Aye and Stubbe 2011). We first measured the specific activity of recombinant RNR in the presence or absence of dATP. As shown in Figure 1D, the specific activity of wild type enzyme was completely inhibited in the presence of dATP. However, the opposite trend is observed in the activity of the mutant enzyme bearing the

D57N mutation. In the presence of dATP, the activity of the mutant enzyme increases dramatically. This increase in activity is due to the deficiency of the mutant enzyme to discriminate between ATP and dATP. We next measured the catalytic activity of RNR in skeletal muscle lysates from *Rrm1-D57N(high)^{Tg}* mice using the same radioactive assay (Figure 1E). As expected, the addition of dATP did not inhibit the activity of mutant RNR overtime. Together these data strongly suggest that D57N mutation desensitize RNR to the feedback inhibition of dATP and *Rrm1-D57N* mutant mice lack RNR allosteric control.

We next wanted to address whether overexpression of *Rrm1-D57N* in mice would cause changes to the dNTP pools. We previously reported that mice that overexpress either of the β RNR subunits, *Rrm2* or *p53R2*, show elevated and unbalanced dNTP pools in the skeletal muscle, the tissue with the highest level of overexpression. We therefore measured dNTPs from the skeletal muscle of wild type, *Rrm1^{Tg}*, and *Rrm1-D57N(high)^{Tg}* aged 3-6 months (Figure 1F). We found no dNTP pool elevations in the *Rrm1^{Tg}* mice compared to wild type mice, consistent with our findings from a previous study (Ylikallio *et al.* 2010). We found a statistical significant elevation of dATP levels in the skeletal muscles from *Rrm1-D57N(high)^{Tg}* when compared to wild type mice. No statistical differences were observed for the other three nucleotides (dGTP, dCTP and dTTP).

Even with the high levels of *Rrm1-D57N* overexpression, mice harboring the transgenes appeared grossly normal and were obtained at expected frequencies (Table S1). In crosses between wild type FVB mice and *Rrm1-D57N(low)^{Tg}* mice, 256 wild type and 231 transgenic mice were obtained

($P=0.26$, χ^2). Likewise, crosses between wild type FVB and *Rrm1-D57N(high)^{Tg}* mice yielded 275 wild type and 246 transgenic mice ($P=0.20$, χ^2). In order to assess the phenotypic effects of loss of RNR allosteric regulatory control in mice, we generated a cohort of *Rrm1-D57N(low)^{Tg}*, *Rrm1-D57N(high)^{Tg}*, and transgene-negative control mice and aged them to a maximum age of 18 months. Necropsy of these mice revealed that mice harboring either D57N transgene were grossly normal relative to wild type control animals. We found a modest increase in the lung tumor incidence in both *Rrm1-D57N(low)^{Tg}* (36.73%, $n=49$) and *Rrm1-D57N(high)^{Tg}* (34.62%, $n=26$) mice compared to wild type mice (27.27%, $n=44$). Mean tumor size, tumor multiplicity, and histopathological grade were not altered by overexpression of *Rrm1-D57N*.

Simultaneous overexpression of Rrm1-D57N and either small RNR subunit causes synthetic lethality

To assess the effect of simultaneous disruption of multiple RNR regulatory mechanisms, we crossed mice overexpressing *Rrm1-D57N* (high or low) with mice overexpressing either small RNR subunit. We found that mice with high levels of *Rrm1-D57N* overexpression and either small RNR subunit were not viable (Table 1). Specifically, of a total of 30 *Rrm1-D57N(high)^{Tg} + p53R2^{Tg}* bitransgenic mice expected, 0 were obtained. Likewise, 26.5 *Rrm1-D57N(high)^{Tg} + Rrm2^{Tg}* bitransgenic mice were expected and 0 were observed.

To determine the exact stage of lethality, we dissected embryos from *Rrm1-D57N(high)^{Tg} x p53R2^{Tg}* cross and *Rrm1-D57N(high)^{Tg} x Rrm2^{Tg}* cross

(Figures 2A-B). Through embryonic day 10.5 (e10.5), *Rrm1-D57N(high)^{Tg} + p53R2^{Tg}* embryos were observed at the expected frequencies, and most were grossly normal (Table S2). After e12.5, only dead *Rrm1-D57N(high)^{Tg} + p53R2^{Tg}* embryos were observed, and were fewer than expected. These embryos lacked blood within the vessels of the yolk sac (Figure 2A). The frequency of resorbed embryos increased over the time frame analyzed, with few resorptions being observed before e10.5, but 8, 19 and 9 resorptions at e10.5, e11.5 and e12.5, respectively. *Rrm1-D57N(high)^{Tg} + Rrm2^{Tg}* embryos derived from crosses between *Rrm1-D57N(high)^{Tg}* and *Rrm2^{Tg}* mice displayed great variability in lifespan (Figure 2B). As early as e10.5, abnormal bitransgenic embryos were observed. Normal bitransgenic embryos were observed through e17.5 but at lower than expected frequencies, and two bitransgenic mice were observed that had survived gestation but died immediately after birth (Table S3).

Mice bearing low levels of *Rrm1-D57N* overexpression and either small RNR subunit overexpression showed distinct survival. Of an expected 51.25 *Rrm1-D57N(low)^{Tg} + p53R2^{Tg}* mice at weaning, 0 were observed (Table 1). *Rrm1-D57N(low)^{Tg} + p53R2^{Tg}* mice who survived gestation developed normally through approximately 4 days. However, survival of these mice decreased progressively at P5; none lived beyond P8 (Figure 2C). Interestingly, of 69.75 expected *Rrm1-D57N(low)^{Tg} + Rrm2^{Tg}* bitransgenic mice expected at weaning, 5 were obtained that survived to adulthood. Of the five surviving bitransgenic adults, two survived 21 days and one 25 days. The last two mice survived 90 and

120 days. With the exception of these five mice, most *Rrm1-D57N(low)^{Tg}* + *Rrm2^{Tg}* bitransgenic mice died between P6 to P11 (Figure 2D).

Overall, higher levels of expression of *Rrm1-D57N* caused shorter lifespan, while overexpression of *p53R2* had more severe effects when combined with *Rrm1-D57N* than does overexpression of *Rrm2*.

***Rrm1-D57N(low)^{Tg}* + *Rrm2^{Tg}* bitransgenic mice exhibit altered morphology and histology of the heart**

Rrm1-D57N(low)^{Tg} + *Rrm2^{Tg}* bitransgenic mice that survived to weaning were runt compared to littermates (Figure 2E). Throughout life, bitransgenic mice were hunched, inactive, and displayed small muscles and alopecia. Bitransgenic mice that survived 90 days or longer exhibited severe skeletal and cardiac muscle degeneration (Figure S2). However the aforementioned muscle defects in bitransgenic mice do not account for the earlier lethality observed in this and the other synthetic lethal crosses. To determine the primary cause of death in these mice, we monitored and weighted daily the neonates and performed necropsy in the entire litter when the bitransgenic neonate was about to die. Upon necropsy, we noticed that *Rrm1-D57N(low)^{Tg}* + *Rrm2^{Tg}* bitransgenic mice, but not control mice, showed pleural effusion. Fluid accumulation affected the entire pleural cavity, and in mice surviving 8 days or later, was also observed within the abdomen. To determine the cause of the pleural effusion, we analyzed multiple tissues via H&E staining. *Rrm1-D57N(low)^{Tg}* + *Rrm2^{Tg}* bitransgenic exhibited degeneration of renal tubules, edema, dilated tubules, and fibrosis (Figure S3).

These mice also displayed hepatocellular swelling. Periodic acid Schiff's (PAS) staining on liver samples showed lipid and glycogen accumulation (Figure S3).

Necropsy of mice also revealed that the hearts from wild-type and *Rrm1-D57N(low)^{Tg} + Rrm2^{Tg}* bitransgenic mice were morphologically different. The heart of *Rrm1-D57N(low)^{Tg} + Rrm2^{Tg}* bitransgenic mice were significantly enlarged when compared with wild type and single transgenic littermates (Figures 3 A-B). Analysis of heart weight/body weight ratio showed that all bitransgenic mice had significantly ($P=0.0031$, Unpaired t-test) higher heart to body weight proportions as compared with age-matched wild type controls (Figure 3C and Table S4).

To assess the possibility of dilated cardiomyopathy (DCM) in bitransgenic mice, we measured ventricular size and wall thickness. DCM is characterized by ventricular chamber enlargement and depressed myocardial contractility (Hershberger *et al.* 2010). Histological examination of the cardiac cross sections showed a significant enlargement of ventricular chambers in *Rrm1-D57N(low)^{Tg} + Rrm2^{Tg}* bitransgenic mice (Figure 3 D-G). The left ventricular chamber was significantly larger in bitransgenic mice compared to wild type littermates. There was also a trend towards increased right ventricular size and thinner ventricular walls in *Rrm1-D57N(low)^{Tg} + Rrm2^{Tg}* bitransgenic mice. Intracardiac thrombi was apparent in the left atrium or ventricle of *Rrm1-D57N(low)^{Tg} + Rrm2^{Tg}* bitransgenic mice but not wild type mice (Figures 3 E and G). The presence of intracardiac thrombi was confirmed histologically in 6 of 13 bitransgenic mice ($P=0.005$, Fisher's exact test). The occurrence of cardiac thrombi was related to

age. Six out of seven *Rrm1-D57N(low)^{Tg} + Rrm2^{Tg}* bitransgenic mice 7 days old or older had thrombi. In contrast, only one of six mice 6 days old and younger had thrombi.

Abnormal myocardial architecture, such as cardiomyocyte size and increased interstitial space were also observed in *Rrm1-D57N(low)^{Tg} + Rrm2^{Tg}* bitransgenic mice (Figure 3 H-I). Histological analysis of the heart revealed lower number of cells in bitransgenic mice. To corroborate this observation we arbitrary counted the number of cells in ten high power fields (HPF) and found that bitransgenic mice had significant lower number of cells when compared to wild type (P=0.0019, Unpaired t-test with Welch's correction) (Figure 3J). To test whether the reduced number of cells was due to abnormal proliferation of cells, we performed phospho-histone H3 (PH3) staining in heart tissues from bitransgenic and wild type littermates. PH3 staining showed significantly fewer mitotic cells in *Rrm1-D57N(low)^{Tg} + Rrm2^{Tg}* bitransgenic hearts as compared to wild type mice (P=0.0026, Unpaired t-test with Welch's correction) (Figures 3 K-M).

We performed echocardiograms in a cohort of mice to determine whether the morphologic and structural changes in the heart were associated with functional deficits. M-Mode echocardiographic measurements from the right parasternal short axis view revealed a depression in fractional shortening between wild type and *Rrm1-D57N(low)^{Tg} + Rrm2^{Tg}* bitransgenic mice (Figure S4 and Table S5).

Taken together, these results suggest that simultaneous disruption of multiple regulatory modes of RNR affects proper cell proliferation and promotes DCM that lead to synthetic lethality in mice.

Altered dNTP pools in the skeletal muscle of *Rrm1-D57N(low)^{Tg} + Rrm2^{Tg}* bitransgenic mice

We hypothesized that simultaneously disruption of both main regulatory mechanisms governing RNR activity would lead to elevated and/or unbalanced nucleotide pools, which may have consequences for genomic stability and survival. To test whether RNR deregulation in mice caused lethality through alterations to dNTP pools, we extracted total nucleotides from the skeletal muscle of *Rrm1-D57N(low)^{Tg} + Rrm2^{Tg}* bitransgenic mice at P5. The total amount of each dNTP was measured using the indirect enzymatic assay described by Sherman and Fyfe with modifications (Sherman and Fyfe 1989; Ferraro *et al.* 2010). The levels of each nucleotide in *Rrm1-D57N(low)^{Tg} + Rrm2^{Tg}* bitransgenic muscle tissue were increased relative to wild type (Figure 4A). Level of dATP was increased 335-fold, dGTP was increased 2.55-fold, dCTP was increased 8.78-fold, and dTTP was increased 12.57-fold. We also extracted and measured nucleotides from the skeletal muscle from *Rrm1-D57N(low)^{Tg} + p53R2^{Tg}* mice and found dNTP pools were also elevated in *Rrm1-D57N(low)^{Tg} + p53R2^{Tg}* mice compared to wild type littermates (Figure 4B).

To determine whether the timing of lethality is dictated in part by dNTP pool alterations during embryonic development, we extracted and measured

dNTPs from whole embryos derived from the *Rrm1-D57N(low)^{Tg}* x *Rrm2^{Tg}* and the *Rrm1-D57N(high)^{Tg}* x *p53R2^{Tg}* cross at e10.5. We found no difference in any of the dNTPs between the genotypes in embryos derived from the *Rrm1-D57N(low)^{Tg}* x *Rrm2^{Tg}* cross. (Figure 4C). For our surprise, dNTP pools were only moderately altered in *Rrm1-D57N(high)^{Tg}* + *p53R2^{Tg}* bitransgenic embryos relative to wild type embryos (Figure 4D).

Extreme RNR hyperactivity could not only elevate dNTP pools to toxic levels, but could conceivably also deplete the pools of precursors. In order to test whether this was occurring in our *Rrm1-D57N(low)^{Tg}* + *Rrm2^{Tg}* bitransgenic mice, we measured the levels of the NDPs (CDP, UDP, GDP, and ADP) by HPLC (Figure 4E). We found no differences between genotypes. These data suggest that elevated RNR activity causes increased and unbalanced dNTP pools, especially after gestation, but do not deplete precursor pools.

Mitochondrial genome instability does not cause synthetic lethality in *Rrm1-D57N(low)^{Tg}* + *Rrm2^{Tg}* bitransgenic mice

We previously reported age-dependent mtDNA depletion in wild-type *Rrm1^{Tg}* + *Rrm2^{Tg}* and *Rrm1^{Tg}* + *p53R2^{Tg}* mice, to levels of approximately 40% compared to wild-type (Ylikallio *et al.* 2010). MtDNA depletion to <1-10 % in mice is known to be lethal during embryonic development (Larsson *et al.* 1998) and after birth (Bourdon *et al.* 2007). Furthermore, mtDNA mutations have been associated to several forms of cardiomyopathy (DiMauro and Schon 2003; Zhang *et al.* 2003). Therefore, we asked if the synthetic lethality of *Rrm1-D57N^{Tg}* +

Rrm2^{Tg} or *p53R2^{Tg}* bitransgenic mice was caused by mtDNA instability. We measured mtDNA copy number in *Rrm1-D57N(low)^{Tg} + Rrm2^{Tg}* bitransgenic mice at juvenile (P4 and P8), young adult (P19 and P25), and aged adult (P90 and P102) mice (Figure 5A). We found that bitransgenic mice had normal mtDNA copy numbers in the skeletal muscle at P4 and P8. However, while mtDNA copy number in skeletal muscle of control mice increased with age, mtDNA copy number in the skeletal muscle of bitransgenic mice failed to expand to the same level throughout development. At P19, mtDNA copy number in bitransgenic mice was ~50% of the wild type level. In the two mice that survived to 90 and 102 days, mtDNA copy numbers in skeletal muscle were 30% and 62% of the wild-type levels, respectively. Therefore, as the mice aged beyond P19, the mtDNA levels remained lower in the *Rrm1-D57N(low)^{Tg} + Rrm2^{Tg}* bitransgenic mice than in wild-type mice, but the depletion did not appear to progress below the levels present at P19. These results suggest that simultaneous overexpression of *Rrm1-D57N(low)^{Tg}* and *Rrm2^{Tg}* delays the developmental amplification of mtDNA, but the residual mtDNA is higher than the minimum threshold reported to escape pathogenic mtDNA depletion in mice.

In addition to quantitative mtDNA defects, alterations to dNTP pools have been suggested to cause mtDNA point mutations and large scale mtDNA deletions in humans (Nishino *et al.* 1999; Nishigaki *et al.* 2003; Tyynismaa *et al.* 2009). We sequenced mtDNA in the hypervariable control region and the cytochrome *b* gene regions but found no increase in mtDNA point mutations in skeletal muscle of *Rrm1-D57N(low)^{Tg} + Rrm2^{Tg}* bitransgenic mice at P25 (data

not shown). To determine whether mtDNA deletions were present, we performed long PCR to assess the total size of the mtDNA in P25 bitransgenic mice. In both wild type and *Rrm1-D57N(low)^{Tg} + Rrm2^{Tg}* bitransgenic mice, we detected only the full-length mtDNA (16kb) in skeletal muscle (Figure 5B), kidney and heart (data not shown), indicating that no deletions were formed in the mtDNA of *Rrm1-D57N(low)^{Tg} + Rrm2^{Tg}* bitransgenic mice.

A clinically significant defect of mtDNA maintenance leads to dysfunction of respiratory chain complex IV (cytochrome *c* oxidase, COX) that is partially encoded by mtDNA. Compensatory hyperproliferation of mitochondria, which can be observed as increased activity of the nuclear encoded complex II (succinate dehydrogenase, SDH), is also frequently observed. COX/SDH assay on frozen skeletal muscle from the P25 bitransgenic mice showed normal COX activity and no increase in SDH signal (Figure 5C).

Taken together, these results showed that extreme upregulation of dNTP pools in *Rrm1-D57N(low)^{Tg} + Rrm2^{Tg}* bitransgenic mice caused age-dependent mtDNA depletion in skeletal muscle, but no point mutations or deletions. The mice were born with normal mtDNA copy numbers, suggesting that mtDNA maintenance was not impaired during embryonic development. Finally, the mtDNA depletion was not deep enough to impair respiratory chain function, as determined by the COX/SDH activity assay.

Metabolic alterations in *Rrm1-D57N(low)^{Tg} + Rrm2^{Tg}* bitransgenic mice

To investigate systemic effects of RNR hyperactivity on metabolism, we

analyzed serum samples from *Rrm1-D57N(low)^{Tg} + Rrm2^{Tg}* bitransgenic and wild type littermates (P6-P8). The LC-MS analysis showed gross metabolite differences, with a hierarchical clustering analysis showing complete separation between the two conditions (Figure S5). A statistical analysis identified 219 differential peaks that were used in a principal component analysis (PCA) that resulted in two separate groups using only the first principal component (Figure 6A). Pathway analysis showed purine and pyrimidine metabolism had a large number of differential metabolites, in concordance with a hyperactive enzyme active in both of these pathways (Figure 6B, Table S6). In addition, the LC-MS analysis revealed altered levels of metabolites associated to heart conditions in bitransgenic mice (Table S7). These data together, showed alteration of multiple metabolites in bitransgenic mice.

DISCUSSION

Regulation of RNR activity is essential for maintaining balanced pools of dNTPs. Malfunction of RNR regulatory mechanisms can result in genomic instability, enhanced mutagenesis and cell death (Kunz *et al.* 1994). In mammals, RNR activity is regulated primarily through the availability of the β subunit and negative feedback control of the activity site in the α subunit. We previously showed that disruption of RNR cell cycle regulatory mechanism by overexpressing either β subunit induces dNTP pool alteration and increases the incidence of lung neoplasms in mice (Xu *et al.* 2008). Here we report on the first mouse model featuring the loss of allosteric feedback control of RNR.

Additionally, the data presented here demonstrates that simultaneous overexpression of *Rrm1-D57N* and either β subunit causes synthetic lethality associated with dramatically elevated dNTP pools.

Previous studies have shown that defects in RNR allosteric regulation is mutagenic in yeast and mammalian cells. Analysis of *Rrm1-D57N* mutants, which are defective to feedback inhibition by dATP, showed increase dNTP levels and high mutation rates as compared to the corresponding wild type cell lines (Weinberg *et al.* 1981; Chabes *et al.* 2003). Despite loss of dATP feedback inhibition, mice bearing either, high or low expression of *Rrm1-D57N* transgene were grossly normal and did not show increased dNTP pools. The limited effect of deregulating RNR allosteric feedback control in mice could be due to the fact that other RNR regulatory mechanisms are still intact.

Unlike the disruption of a single regulatory mechanism of RNR, simultaneous disruption of the two main regulatory mechanisms is synthetic lethal in mice. Overexpression of *Rrm1-D57N*(*high*)^{Tg} and either β subunit causes embryonic lethality. Mice carrying low expression of *Rrm1-D57N* transgene and either *Rrm2* or *p53R2* transgene survived through gestation, but the lifespan was significantly shortened.

To understand the synthetic lethality of RNR deregulation, we further characterized mice derived from the least severe combination, the *Rrm1-D57N*(*low*)^{Tg} x *Rrm2*^{Tg} cross. *Rrm1-D57N*(*low*)^{Tg} + *Rrm2*^{Tg} bitransgenic mice showed pronounced growth retardation and weight loss starting at postnatal day 5. These phenotypes were accompanied by a progressive deterioration of

skeletal muscles, accumulation of pleural effusion, kidney degeneration and hepatocellular swelling. Further characterization revealed that the lethality observed in *Rrm1-D57N(low)^{Tg} + Rrm2^{Tg}* bitransgenic mice was mainly caused by heart failure. Cardiac pathology in these mice showed similar patterns to those described for human DCM; ventricular dilation with thinner walls and depression in fractional shortening (Van Vleet and Ferrans 1986; Schönberger and Seidman 2001; Hershberger *et al.* 2010). Furthermore, our histological analysis revealed a reduction of cell proliferation in *Rrm1-D57N(low)^{Tg} + Rrm2^{Tg}* bitransgenic hearts. The reduced number of proliferating cells within the heart could possibly contribute to the development of DCM and it is likely to be caused by increased replication stress that results from RNR-mediated dNTP pool alteration. Together, these data suggest that balance supply of dNTP pools through RNR regulation is essential for survival.

Data presented here, also demonstrates that RNR deregulation induces unbalance pool of dNTPs. *Rrm1-D57N(low)^{Tg} + Rrm2^{Tg}* bitransgenics mice showed dramatic elevation of dNTP pools in the skeletal muscles, resulting in 300-fold increase in dATP, 10 fold increase of dCTP and dTTP and 50% increase in dGTP. This was consistent with our previous findings that both the *Rrm1-D57N(low)^{Tg}* and *Rrm2^{Tg}* transgenes are highly overexpressed within the skeletal muscle. These significant changes support a role for RNR hyperactivity in causing synthetic lethality.

Altered dNTP pools are thought to underlie mtDNA instability in several mitochondrial disorders in humans and mice. Mutation of thymidine kinase 2

(TK2), a mitochondrial kinase that plays an important role in the salvage pathway, induces mitochondrial DNA depletion syndrome with progressive encephalopathy and myopathy in humans (Saada *et al.* 2001; Götz *et al.* 2008). In our previous work, we reported that mice overexpressing *Rrm1^{Tg}* and *Rrm2^{Tg}* or *p53R2^{Tg}* displayed age-dependent mtDNA depletion, which was associated with altered dNTP pools in the skeletal muscle (Ylikallio *et al.* 2010). Mutations in mtDNA have also been linked to cardiomyopathy (Zhang *et al.* 2003; DiMauro and Schon 2003; Kujoth *et al.* 2005; Wallace *et al.* 2013). Mice expressing a knock-in inactivation of the POLG show mtDNA mutagenesis that results in anemia, kyphosis and heart enlargement (Trifunovic *et al.* 2004; Kujoth *et al.* 2005). Mice lacking *p53R2* developed post-natal mtDNA depletion that resulted in early myopathy (Bourdon *et al.* 2007). Despite the dramatic alteration of dNTP, *Rrm1-D57N(low)^{Tg} + Rrm2^{Tg}* mice did not show mtDNA depletion, nor signs of increased rate of mtDNA point mutations or deletions. The normal result from the COX/SDH activity assay confirmed that mitochondrial dysfunction is not a cause of muscle degeneration in these mice. Therefore, mtDNA depletion is unlikely to account for the lethal phenotype in these mice.

To investigate systemic effects of RNR hyperactivity on metabolism, we performed global metabolomics analysis on serum from *Rrm1-D57N(low)^{Tg} + Rrm2^{Tg}* mice and wild type littermates. The LC-MS analysis showed gross metabolite differences, with a hierarchical clustering analysis already showing complete separation between the two conditions. Pathway analysis showed purine and pyrimidine metabolism had a large number of differential metabolites,

in concordance with RNR hyperactivity. Moreover, several intermediates of nucleotide metabolism and other pathways that were differential in our analysis have been linked to various heart conditions.

In many cardiovascular diseases, including DCM, the heart undergoes “metabolic shift” causing impairment of myocardial energetics manifested as decreased phosphocreatine to ATP ratio and depletion in ATP content, that ultimately results in malfunction of the heart. Studies in animal models have shown that loss of ATP depletion in heart failure (HF) is caused in part by total adenine pool (Shen *et al.* 1999). The loss of total adenine pool in HF is believed to result from excessive purine degradation. In concordance with this, metabolic profile in our *Rrm1-D57N(low)^{Tg} + Rrm2^{Tg}* bitransgenic mice revealed significant decrease of several intermediates of purine metabolism, including AMP, GMP, inosine and hypoxanthine. We also observed mild elevation of uric acid, the final oxidation product of purine catabolism. Serum uric acid levels are frequently elevated in heart and renal failure (Cicoira *et al.* 2002; Johnson *et al.* 2003), which are observed in *Rrm1-D57N(low)^{Tg} + Rrm2^{Tg}* bitransgenic mice. Lower levels of AMP, GMP, inosine and hypoxanthine and accumulation of uric acid, may reflect increase purine degradation as a defense mechanism against unbalanced dNTP levels that results from RNR hyperactivity (Shen *et al.* 1999; Gironès *et al.* 2014). In addition to loss of total adenine pools, we see reduced serum levels of several acyl carnitines in *Rrm1-D57N(low)^{Tg} + Rrm2^{Tg}* bitransgenic mice. Carnitine/acylcarnitine exchange is essential for transporting long chain fatty acids into mitochondria. This pathway is the major source of

energy for myocardium (Palmieri 2008). Previous studies have shown progressive inhibition of fatty acid metabolism in hypertrophic and failing heart (Regitz *et al.* 1990; Maekawa *et al.* 2013; Sansbury *et al.* 2014). Therefore, deficiency of acyl carnitines in *Rrm1-D57N(low)^{Tg} + Rrm2^{Tg}* bitransgenic mice could limit the energy production in the heart and contribute to the development of DCM. Collectively, these results show that RNR hyperactivity has profound effects myocardial energetics that ultimately results in DCM.

All together, these findings illustrate the need for tight control of RNR activity. Severe deregulation of RNR in multicellular organisms leads to significant changes of in dNTPs that ultimately results in systemic organ failure and death.

ACKNOWLEDGEMENTS

We would like to thank Dr. Patrick Stover for allowing use of the UPLC and for technical advice. We would also like to thank Christina Cota for valuable suggestions regarding embryonic phenotypes. This work was supported by Cornell University Center for Vertebrate Genomics Scholar Awards [J.P. and X.X.]; and National Institutes of Health training grant T32GM07617 [J.P.].

REFERENCES

- Aye, Y., J. Stubbe, 2011 Clofarabine 5'-di and -triphosphates inhibit human ribonucleotide reductase by altering the quaternary structure of its large subunit. *Proc. Natl. Acad. Sci. USA.* 108(24): 9815-9820.
- Aye, Y., M. Li, M. J. C. Long, R. S. Weiss, 2015 Ribonucleotide reductase and cancer: biological mechanisms and targeted therapies. *Oncogene.* 34: 2011-2021.
- Benjamini, Y., Y. Hochberg, 1995 Controlling the false discovery rate: A practical and powerful approach to multiple testing. *J. R. Stat. Soc. Ser. B.* 57(1): 289-300.
- Bourdon, A., L. Minai, V. Serre, J. P. Jais, E. Sarzi, *et al.*, 2007 Mutation of RRM2B, encoding p53-controlled ribonucleotide reductase (p53R2), causes severe mitochondrial DNA depletion. *Nat. Genet.* 39(6): 776-780.
- Caras, I. W., D. W. Jr. Martin, 1988 Molecular cloning of the cDNA for a mutant mouse ribonucleotide reductase M1 that produces a dominant mutator phenotype in mammalian cells. *Mol. Cell Biol.* 8(7): 2698-2704.
- Chabes, A. L., S. Bjorklund, L. Thelander, 2004 S Phase-specific transcription of the mouse ribonucleotide reductase R2 gene requires both a proximal repressive E2F-binding site and an upstream promoter activating region. *J. Biol. Chem.* 279(11): 10796-10807.
- Chabes, A. L., C. M. Pflieger, M. W. Kirschner, L. Thelander, 1985 Mouse ribonucleotide reductase R2 protein: a new target for anaphase-promoting

- complex-Cdh1-mediated proteolysis. *Proc. Natl. Acad. Sci. USA.* 100: 3925-3929.
- Chabes, A., B. Georgieva, V. Domkin, X. Zhao, R. Rothstein, *et al.*, 2003 Survival of DNA damage in yeast directly depends on increased dNTP levels allowed by relaxed feedback inhibition of ribonucleotide reductase. *Cell.* 112(3): 391-401.
- Cicoira, M., L. Zanolla, A. Rossi, G. Golia, L. Franceschini, *et al.*, 2002 Elevated serum uric acid levels are associated with diastolic dysfunction in patients with dilated cardiomyopathy. *Am. Heart J.* 143(6): 1107-1111.
- DiMauro, S., E. A. Schon, 2003 Mitochondrial respiratory-chain diseases. *N. Engl. J. Med.* 348: 2656-2668.
- Engström, Y., S. Eriksson, I. Jildevik, S. Skog, L. Thelander, *et al.*, 1985 Cell cycle-dependent expression of mammalian ribonucleotide reductase. Differential regulation of the two subunits. *J. Biol. Chem.* 260: 9114-9116.
- Eriksson, S., L. Gudas, S. M. Clift, I. W. Caras, B. Ullman, *et al.*, 1981 Evidence for genetically independent allosteric regulatory domains of the protein M1 subunit of mouse ribonucleotide reductase. *J. Biol. Chem.* 256(19): 10193-10197.
- Fairman, J. W., S. R. Wijerathna, M. F. Ahmad, H. Xu, R. Nakano, *et al.*, 2011 Structural basis for allosteric regulation of human ribonucleotide reductase by nucleotide-induced oligomerization. *Nat. Struct. Mol. Biol.* 18: 316-322.

- Ferraro, P., E. Franzolin, G. Pontarin, P. Reichard, V. Bianchi, 2010 Quantitation of cellular deoxynucleoside triphosphates. *Nucleic Acids Res.* 38(6): 85.
- Gironès, N., S. Carbajosa, N. A. Guerreo, C. Poveda, C. Chillón-Marinas, *et al.*, 2014 Global metabolomic profiling of acute myocarditis caused by trypanosoma cruzi Infection. *PLoS Negl. Trop. Dis.* 8(11): e3337.
- Götz, A., P. Isohanni, H. Pihko, A. Paetau, R. Herva, *et al.*, 2008 Thymidine kinase 2 defects can cause multi-tissue mtDNA depletion syndrome. *Brain.* 131(11): 2841-50.
- Guittet, O., P. Hakansson, N. Voevodskaya, S. Fridd, A. Graslund, *et al.*, 2001 Mammalian p53R2 protein forms an active ribonucleotide reductase *in vitro* with the R1 protein, which is expressed both in resting cells in response to DNA damage and in proliferating cells. *J. Biol. Chem.* 276: 40647-40651.
- Hakansson, P., A. Hofer, L. Thelander, 2006 Regulation of mammalian ribonucleotide reduction and dNTP pools after DNA damage and in resting cells. *J. Biol. Chem.* 281(12): 7834-7841.
- Hershberger, R. E., A. Morales, J. D. Siegfried, 2010 Clinical and genetic issues in dilated cardiomyopathy: A review for genetics professionals. *Genet. Med.* 12: 655-667.
- Johnson, R. J., D. Kang, D. Feig, S. Kivlighn, J. Kanellis, *et al.*, 2003 Is there a pathogenetic role for uric acid in hypertension and cardiovascular and renal disease? *Hypertension*, 41(6): 1183-1190.

- Kochanowski, N., F. Blanchard, R. Cacan, F. Chirat, E. Guedon, *et al.*, 2006
Intracellular nucleotide and nucleotide sugar contents of cultured CHO cells determined by a fast, sensitive, and high-resolution ion-pair RP-HPLC. *Anal. Biochem.* 348(2): 243-251.
- Kujoth, G. C., A. Hiona, T. D. Pugh, S. Someya, K. Panzer, *et al.*, 2005
Mitochondrial DNA mutations, oxidative stress, and apoptosis in mammalian aging. *Science.* 309(5733): 481-484.
- Kunz, B. A., S. E. Kohalmi, T. A. Kunkel, C. W. Mathews, E. M. McIntosh, *et al.*, 1994
International Commission for Protection Against Environmental Mutagens and Carcinogens. Deoxyribonucleoside triphosphate levels: a critical factor in the maintenance of genetic stability. *Mutat. Res.* 318: 1-64.
- Larsson, N. G., J. Wang, H. Wilhelmsson, A. Oldfors, P. Rustin, *et al.*, 1998
Mitochondrial transcription factor A is necessary for mtDNA maintenance and embryogenesis in mice. *Nat. Genet.* 18(3): 231-236.
- Liu, X., Z. Ser, J. W. Locasale, 2014
Development and quantitative evaluation of a high resolution metabolomics technology. *Anal. Chem.* 86(4): 2175-2184.
- Maekawa, K., A. Hirayama, Y. Iwata, Y. Tajima, T. Nishimaki-Mogami, *et al.*, 2013
Global metabolomic analysis of heart tissue in a hamster model for dilated cardiomyopathy. *J. Mol. Cell. Cardiol.* 59: 76-85.

- Nishigaki, Y., R. Martí, W. C. Copeland, M. Hirano, 2003 Site-specific somatic mitochondrial DNA point mutations in patients with thymidine phosphorylase deficiency. *J. Clin. Invest.* 111(12): 1913-1921.
- Nishino, I., A. Spinazzola, M. Hirano, 1999 Thymidine phosphorylase gene mutations in MNGIE, a human mitochondrial disorder. *Science.* 283(5402): 689-692.
- Nordlund, P., P. Reichard, 2006 Ribonucleotide reductases. *Annu. Rev. Biochem.* 75: 681-706.
- Palmieri, F. 2008 Diseases caused by defects of mitochondrial carriers: a review. *Biochim. Biophys. Acta.* 1777: 564-578.
- Regitz, V., A. L. Shug, E. Fleck, 1990 Defective myocardial carnitine metabolism in congestive heart failure secondary to dilated cardiomyopathy and to coronary, hypertensive and valvular heart diseases. *Am. J. Cardiol.* 65(11): 755-760.
- Saada, A., A. Shaag, H. Mandel, Y. Nevo, S. Eriksson, *et al.*, 2001 Mutant mitochondrial thymidine kinase in mitochondrial DNA depletion myopathy. *Nat Genet.* 29(3): 342-4.
- Sansbury, B. E., A. M. DeMartino, Z. Xie, A. C. Brooks, R. E. Brainard, *et al.*, 2014 Metabolomic analysis of pressure-overloaded and infarcted mouse hearts. *Circ. Heart Fail.* 7(4): 634-642.
- Schönberger, J., C. E. Seidman, 2001 Many roads lead to a broken heart: the genetics of dilated cardiomyopathy. *Am. J. Hum. Genet.* 69: 249-260.

- Shen, W., K. Asai, M. Uechi, M. A. Mathier, R. P. Shannon, *et al.*, 1999 Progressive loss of myocardial ATP due to a loss of total purines during the development of heart failure in dogs: a compensatory role for the parallel loss of creatine. *Circulation*. 100(20): 2113-2118.
- Sherman, P. A., J. A. Fyfe, 1989 Enzymatic assay for deoxyribonucleoside triphosphates using synthetic oligonucleotides as template primers. *Anal. Biochem*. 180(2): 222-226.
- Song, Y., R. A. Marmion, J. O. Park, D. Biswas, J. D. Rabinowitz, 2017 Dynamic Control of dNTP Synthesis in Early Embryos. *Dev. Cell* 42: 301-308.
- Tanaka, H., H. Arakawa, T. Yamaguchi, K. Shiraishi, S. Fukuda, *et al.*, 2000 A ribonucleotide reductase gene involved in a p53-dependent cell-cycle checkpoint for DNA damage. *Nat*. 404(6773): 42-49.
- Team, R., 2013 R Development Core Team. *RA Lang. Environ. Stat. Comput.*
- Trifunovic, A., A. Wredenberg, M. Falkenberg, J. N. Spelbrink, A. T. Rovio, *et al.*, 2004 Premature ageing in mice expressing defective mitochondrial DNA polymerase. *Nat*. 429: 417-423.
- Tyynismaa, H., K. Peltola Mjosund, S. Wanrooij, I. Lappalainen, E. Ylikallio, *et al.*, 2005 Mutant mitochondrial helicase Twinkle causes multiple mtDNA deletions and a late-onset mitochondrial disease in mice. *Proc. Natl. Acad. Sci. USA* 102(49): 17687-17692.
- Tyynismaa, H., E. Ylikallio, M. Patel, M. J. Molnar, R. G. Haller, *et al.*, 2009 A heterozygous truncating mutation in RRM2B causes autosomal-dominant

- progressive external ophthalmoplegia with multiple mtDNA deletions. *Am. J. Hum. Genet.* 85(2): 290-295.
- Van Vleet, J. F., V. J. Ferrans, 1986 Myocardial diseases of animals. *Am. J. Pathol.* 124: 98-178.
- Wallace, D. C., M. T. Lott, V. Procaccio, 2013 Emery and Rimoin's Principles and Practice of Medical Genetics, Mitochondrial Medicine: The Mitochondrial Biology and Genetics of Metabolic and Degenerative Diseases, Cancer, and Aging, edited by D. L. Rimoin, R. E. Pyeritz, B. R. Korf. Churchill Livingstone Elsevier, Philadelphia.
- Weinberg, G., B. Ullman, D. W. Jr. Martin, 1981 Mutator phenotypes in mammalian cell mutants with distinct biochemical defects and abnormal deoxyribonucleoside triphosphate pools. *Proc. Natl. Acad. Sci. USA.* 78: 2447-2451.
- Xu, X., J. L. Page, J. A. Surtees, H. Liu, S. Lagedrost, *et al.*, 2008 Broad overexpression of ribonucleotide reductase genes in mice specifically induces lung neoplasms. *Cancer Res.* 68: 2652-2660.
- Xia, J., R. Mandal, I. V. Sinelnikov, D. Broadhurst, D. S. Wishart, 2012 MetaboAnalyst 2.0-a comprehensive server for metabolomic data analysis. *Nucleic Acids Res.* 40(W1): 127-133.
- Ylikallio, E., J. L. Page, X. Xu, M. Lampinen, G. Bepler, *et al.*, 2010 Ribonucleotide reductase is not limiting for mitochondrial DNA copy number in mice. *Nucleic Acids Res.* 38(22): 8208-8218.

Zhang, D., J. L. Mott, P. Farrar, J. S. Ryerse, S. Chang, *et al.*, 2003
Mitochondrial DNA mutations activate the mitochondrial. *Cardiovas. Res.*
57: 147-157.

FIGURE LEGENDS

Figure 1. Generation of *Rrm1-D57N* overexpressing mice. (A) Southern blot analysis of DNA from potential *Rrm1-D57N^{Tg}* founder animals. Tail DNA was subjected to hybridization with a *Rrm1*-specific radiolabeled probe. Arrows indicate bands corresponding to the endogenous *Rrm1* gene and the *Rrm1-D57N* transgene. Note that the founder in lane 12 [referred to as *Rrm1-D57N(high)*] shows greater signal intensity and an additional transgene band, indicating higher transgene copy number than in the founder in lane 6 [*Rrm1-D57N(low)*]. **(B)** Northern blot analysis of *Rrm1* expression in wild type and *Rrm1-D57N(high)^{Tg}* mice. Total RNA was extracted from the indicated tissues of wild type FVB and *Rrm1-D57N(high)^{Tg}* mice and subjected to Northern blot analysis with a radiolabeled *Rrm1*-specific probe. Positions of the wild type and *Rrm1-D57N*-derived transcripts are indicated. Total RNA is shown as a loading control. Note that skeletal muscle was intentionally underloaded. **(C)** Immunoblot analysis of RRM1 protein expression in the indicated tissues of wild type (Wt), *Rrm1-D57N(low)^{Tg}* (L), and *Rrm1-D57N(high)^{Tg}* (H) mice. Total protein from the indicated tissues was immunoblotted with a RRM1-specific antibody. The same membrane was probed with an antibody specific to α -tubulin as a loading control. **(D)** Specific activity of recombinant RNR (Wild type and *Rrm1-D57N*) in the presence or absence of dATP. The specific activity (25,000 cpm/nmol) of RNR was measured using [5-³H]-CDP for the formation of dCDP over time in the presence or absence of dATP. [5-³H]-CDP, ATP, hRNR1 (Wild type/*Rrm1-*

D57N), and hRNR2 were incubated in a 37 °C water bath in the presence and absence of dATP. **(E)** Measurement of RNR specific activity (25,000 cpm/nmol) in *Rrm1-D57N^{Tg}* skeletal muscle in the presence or absence of dATP. Frozen mouse skeletal muscle tissue was powdered, suspended in assay buffer and freeze thawed three times. Reaction was initiated after adding tissue lysate to the reaction mixture containing [5-³H]-CDP, ATP, hRNR2 and +/- dATP. **(F)** Measurement of dNTP levels in the skeletal muscle of adult wild type, *Rrm1^{Tg}* and *Rrm1-D57N(high)^{Tg}* mice. Total nucleotides were extracted from the skeletal muscle of mice of the indicated genotypes and were quantified using the indirect enzymatic method. Stars above the bars denote presence of a significant difference: * indicates $0.01 < p \leq 0.05$; **** $p \leq 0.0001$, determined using *t*-test.

Figure 2. Simultaneous overexpression of Rrm1-D57N and either beta subunit causes synthetic lethality. **(A)** Images of embryos derived from the *Rrm1-D57N(high)^{Tg} x p53R2^{Tg}* breedings. Bitransgenics are grossly normal through 10.5 dpc. At 11.5 dpc, dead bitransgenic embryos are distinguishable from controls. **(B)** Images of *Rrm1-D57N(high)^{Tg} + Rrm2^{Tg}* bitransgenic embryos and controls. Bitransgenics are found dead as early as 13.5 dpc. **(C)** Kaplan-Meier survival curve for mice derived from *Rrm1-D57N(low)^{Tg} + p53R2^{Tg}* breeding. $p < 0.0033$, log rank test. **(D)** Kaplan-Meier survival curve for mice derived from *Rrm1-D57N(low)^{Tg} + Rrm2^{Tg}* breeding. $p < 0.0001$, log rank test. **(E)** Gross morphology of *Rrm1-D57N(low)^{Tg} + Rrm2^{Tg}* bitransgenic mice. Bitransgenic mice are runted and show alopecia and decreased activity. Pups

were counted on P0 (day of birth) and monitored daily. Pups were genotyped by Southern blot analysis of tail DNA at 21 days of age or when found dead. Bitransgenics surviving past 21 days of age were housed with sex-matched littermates and monitored frequently, and euthanized when moribund.

Figure 3. Characterization of cardiac defects in *Rrm1-D57N^{Tg}* + *Rrm2^{Tg}* bitransgenic mice. Heart tissue from bitransgenic and wild type control mice was excised, gently washed in sterile 1xPBS, weighed, fixed in 10% formalin overnight, moved to 70% ethanol, sectioned, and stained. **(A-B)** Gross heart morphology in wild type and bitransgenic mice. Scale bars, 1 cm. **(C)** Analysis of heart to body weight ratio for wild type and *Rrm1-D57N(low)^{Tg}* + *Rrm2^{Tg}* littermates. Unpaired t-test $P = 0.0031$. **(D-G)** Representative H&E sections of heart tissue from wild type and bitransgenic mice cut in the coronal or transverse plane. Most bitransgenics developed a thrombus (black arrow) in their right atrium or left ventricle. Scale bars, 1 mm. **(H-I)** Representative images of H&E sections of hearts from wild type and *Rrm1-D57N^{Tg}* + *Rrm2^{Tg}* littermates. Scale bars, 50 μm . **(J)** Quantification of the total number of cells in H&E sections of hearts from wild type and *Rrm1-D57N^{Tg}* + *Rrm2^{Tg}* mice. Bitransgenics showed a significantly decreased number of cells when compared to wild type mice. Unpaired t-test with Welch's correction $P = 0.0019$. **(K-L)** Phospho-histone H3 (PH3) staining of the heart tissues from wild type and *Rrm1-D57N^{Tg}* + *Rrm2^{Tg}* mice. Black arrows indicate phospho-histone H3 positive cells. Scale bars, 50 μm . **(M)** Quantification of the total number of phospho-histone H3 positive cells.

Rrm1-D57N^{Tg} + *Rrm2^{Tg}* showed significantly fewer mitotic cells as compared to wild type mice. Unpaired t-test with Welch's correction $P=0.0026$. Data shown are the mean \pm SD, $n = 7$.

Figure 4. dNTP pool alterations in bitransgenic embryos and neonates.

Each dNTP was measured by an indirect enzymatic assay. Results are normalized for total amount of tissue used. **(A)** dNTP pools in *Rrm1-D57N(low)^{Tg}* + *Rrm2^{Tg}* bitransgenic mice. Total nucleotides were extracted from the skeletal muscle of bitransgenic and control littermates at P5. One-way ANOVA $P < 0.0001$ for dATP, $P = 0.0026$ for dGTP, $P = 0.0078$ for dCTP and $P = 0.0007$ for dTTP. **(B)** dNTP pools in *Rrm1-D57N(low)^{Tg}* + *p53R2^{Tg}* bitransgenic mice at P3 or P5. One-way ANOVA $P = 0.0003$ for dATP, $P = 0.0159$ for dCTP and $P = 0.0059$ for dTTP. **(C-D)** dNTP pools from whole embryos derived from the *Rrm1-D57N(low)^{Tg}* x *Rrm2^{Tg}* and *Rrm1-D57N(high)^{Tg}* x *p53R2^{Tg}* breeding at e10.5. One-way ANOVA for Figure D $P < 0.0001$ for dATP and $P = 0.0058$ for dGTP. **(E)** NDP pools in *Rrm1-D57N(low)^{Tg}* + *Rrm2^{Tg}* bitransgenic mice skeletal muscle. Nucleotides are measured by HPLC and compared to standard curves. No statistical difference observed for NDP pools. Data shown are the mean \pm SD. Stars above the bars denote presence of a significant difference after calculating exact P values using Turkey's multiple comparisons tests: * indicates $0.01 < p \leq 0.05$; ** $p \leq 0.01$; *** $p \leq 0.001$; **** $p \leq 0.0001$.

Figure 5. mtDNA integrity in bitransgenic mice. (A) mtDNA copy number in bitransgenic mice from *Rrm1-D57N(low)^{Tg}* x *Rrm2^{Tg}* breedings. Total DNA was extracted from skeletal muscle of bitransgenic and control mice at different stages of development: Juvenile = P4, P8; Young adult = P19, P25; Adult = P90, P102. mtDNA is quantified by qPCR and normalized to the nuclear 18S rRNA. Number of mice varies among genotype and age (Juvenile: Wild type = 2, *Rrm1-D57N(low)^{Tg}* = 5, *Rrm2^{Tg}* = 6, *Rrm1-D57N(low)^{Tg}* + *Rrm2^{Tg}* = 4; Young adults: Wild type = 3, *Rrm1-D57N(low)^{Tg}* = 1, *Rrm2^{Tg}* = 3, *Rrm1-D57N(low)^{Tg}* + *Rrm2^{Tg}* = 2; Adults: Wild type = 2, *Rrm1-D57N(low)^{Tg}* = 2, *Rrm2^{Tg}* = 0, *Rrm1-D57N(low)^{Tg}* + *Rrm2^{Tg}* = 2). One-way ANOVA P = 0.0301 for Juvenile. Data shown are the mean ± SD. Stars above the bars denote presence of a significant difference: * indicates $0.01 < p \leq 0.05$, determined using *t*-test. **(B)** Long PCR on mtDNA from skeletal muscle of *Rrm1-D57N(low)^{Tg}* + *Rrm2^{Tg}* bitransgenic and wild type littermate at P25. Only the full length 16 kb mtDNA is detected. **(C)** Activity of respiratory chain complexes in skeletal muscle of *Rrm1-D57N(low)^{Tg}* + *Rrm2^{Tg}* bitransgenic and wild type littermate at P25. Tissues were stained for activity of the mtDNA-encoded complex IV (COX, brown), the nDNA-encoded complex II (SDH, blue), or both.

Figure 6. Metabolome analysis of serum from *Rrm1-D57N^{Tg}* + *Rrm2^{Tg}* bitransgenic mice and wild type control littermates. (A) Principal component analysis. Differential metabolites identified using mass spectrometry readily distinguished the two groups (*Rrm1-D57N^{Tg}* + *Rrm2^{Tg}* vs Wild type) in the first

principal component (explaining 76.9% of the variation) highlighting profound differences in serum metabolite profiles. **(B)** Pathway analysis. The number and fraction of differential metabolites ($p < 0.05$, $fdr < 0.05$) that participate in the depicted KEGG pathway modules. Only KEGG pathway modules with 4 or more differential metabolites are depicted. **(C)** Nucleotide biosynthesis pathway. Arrows show downregulated (blue) and upregulated (red) nucleotides in the serum of bitransgenic mice.

Figure 1

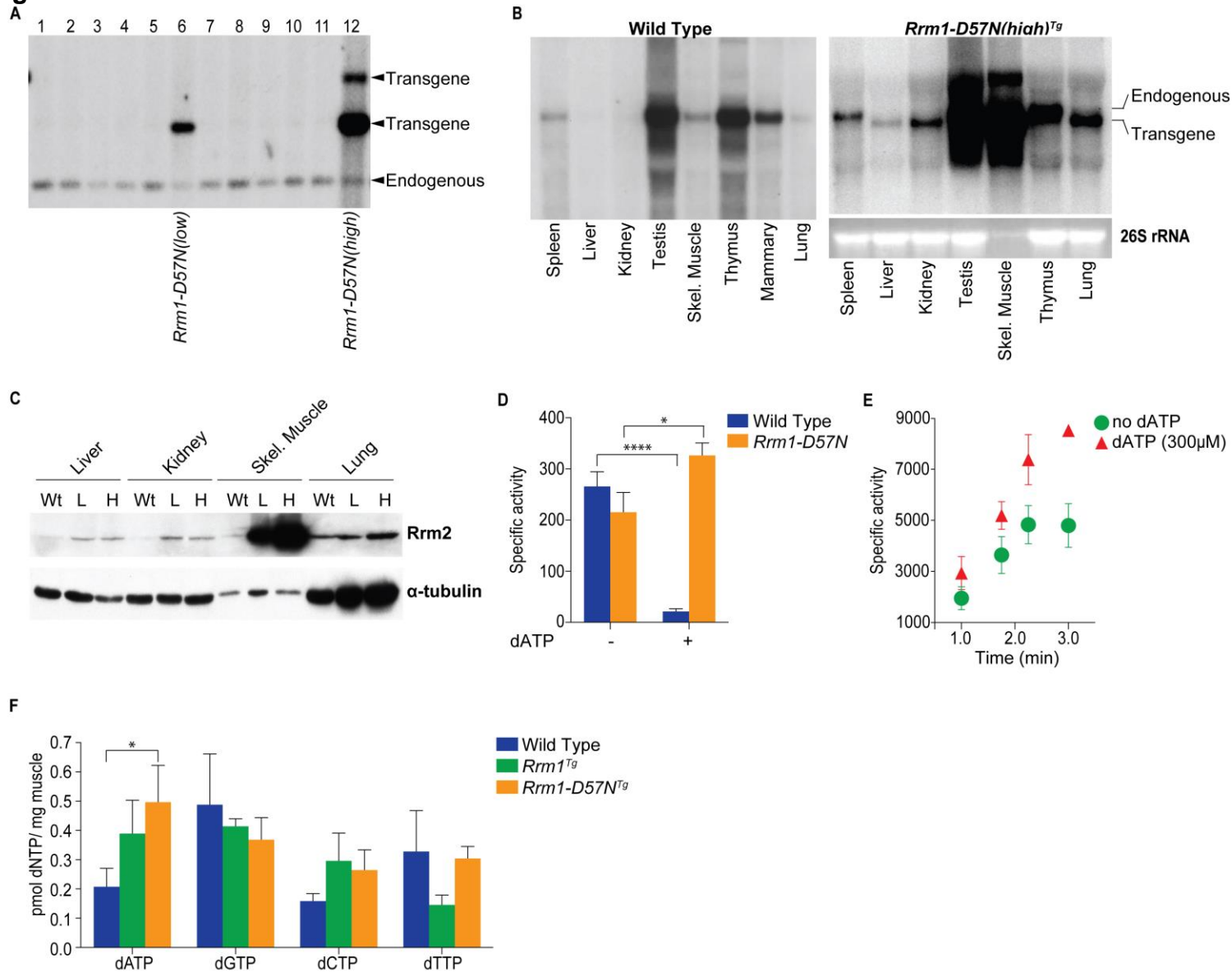


Figure 2

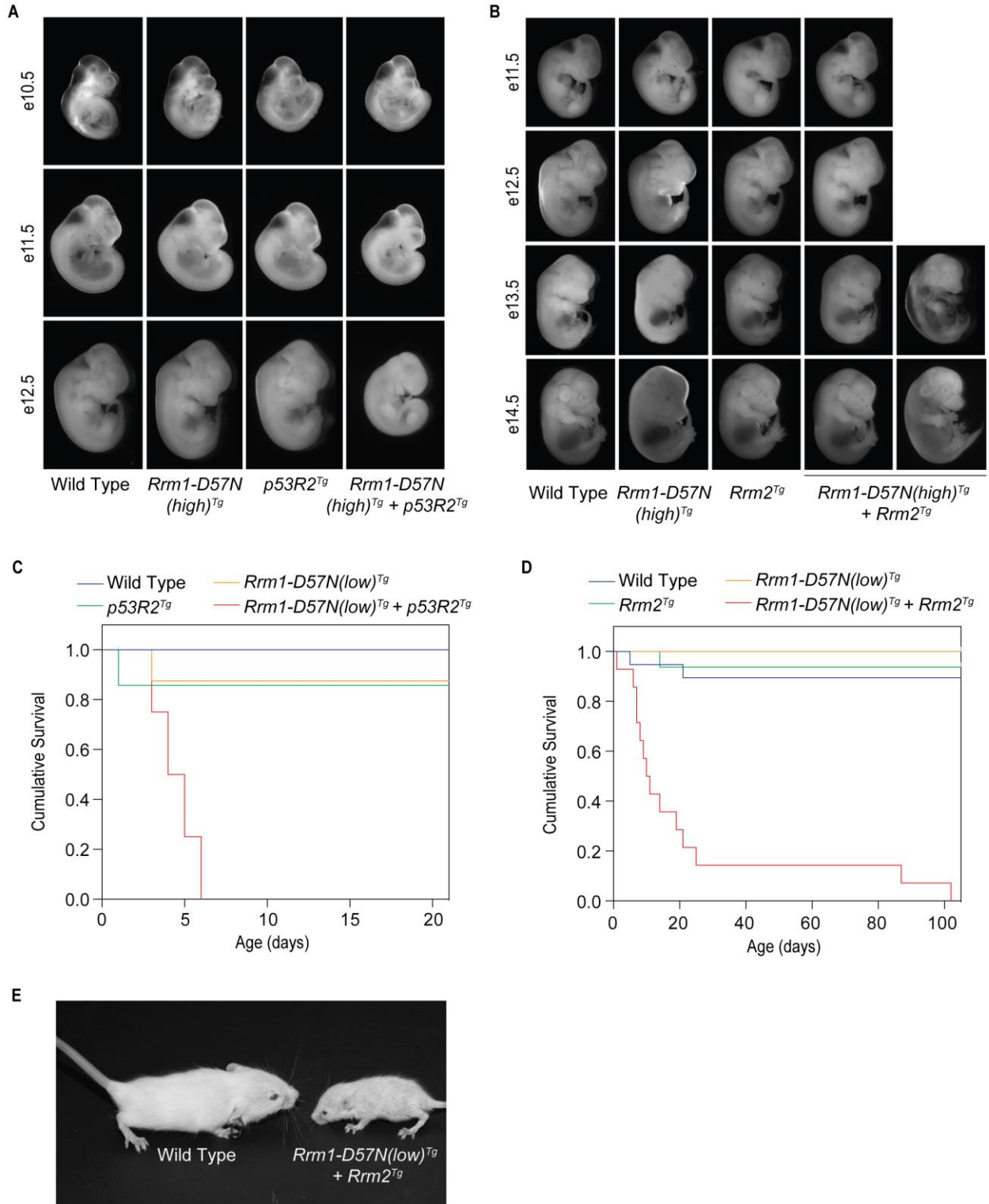


Figure 3

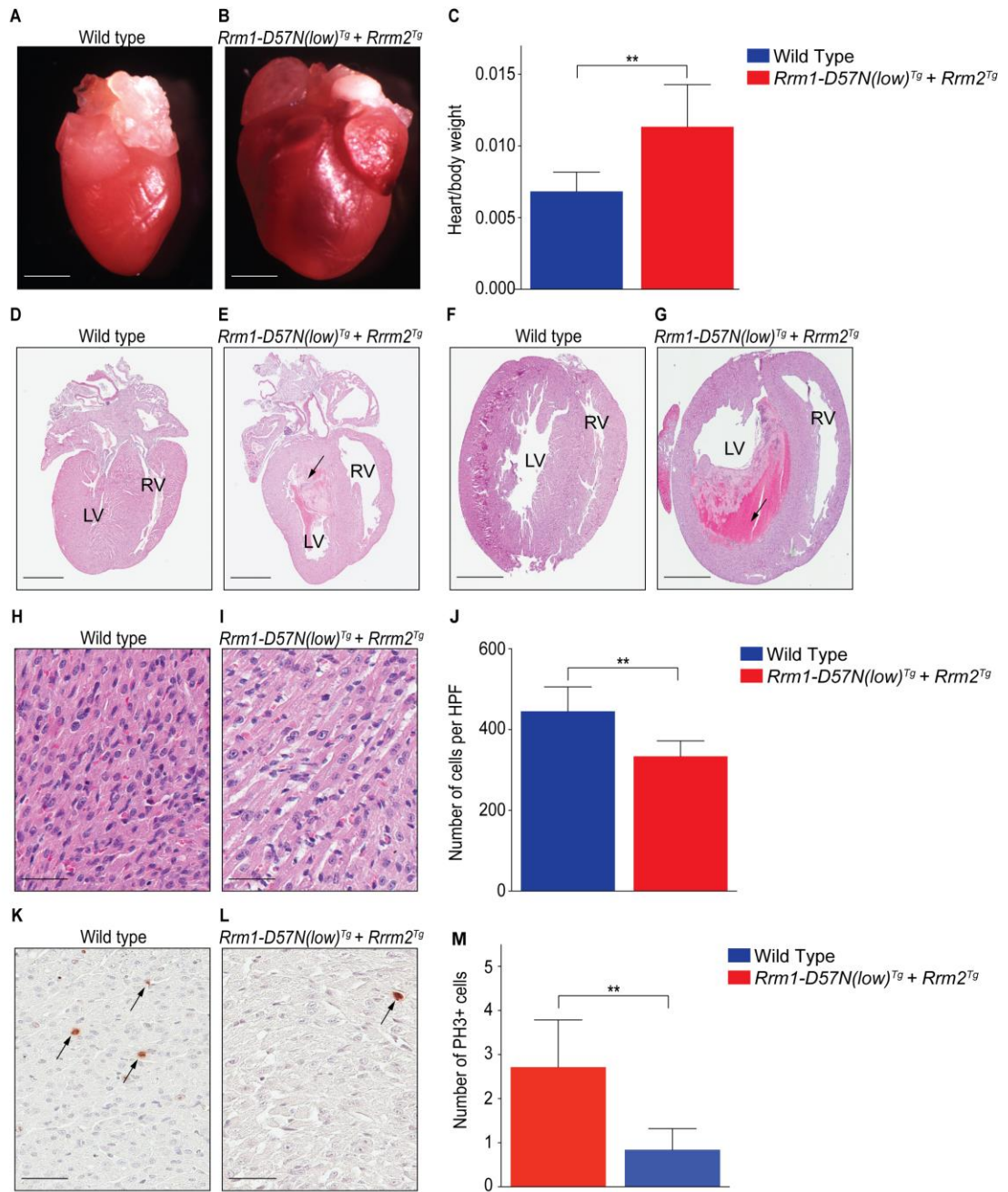


Figure 4

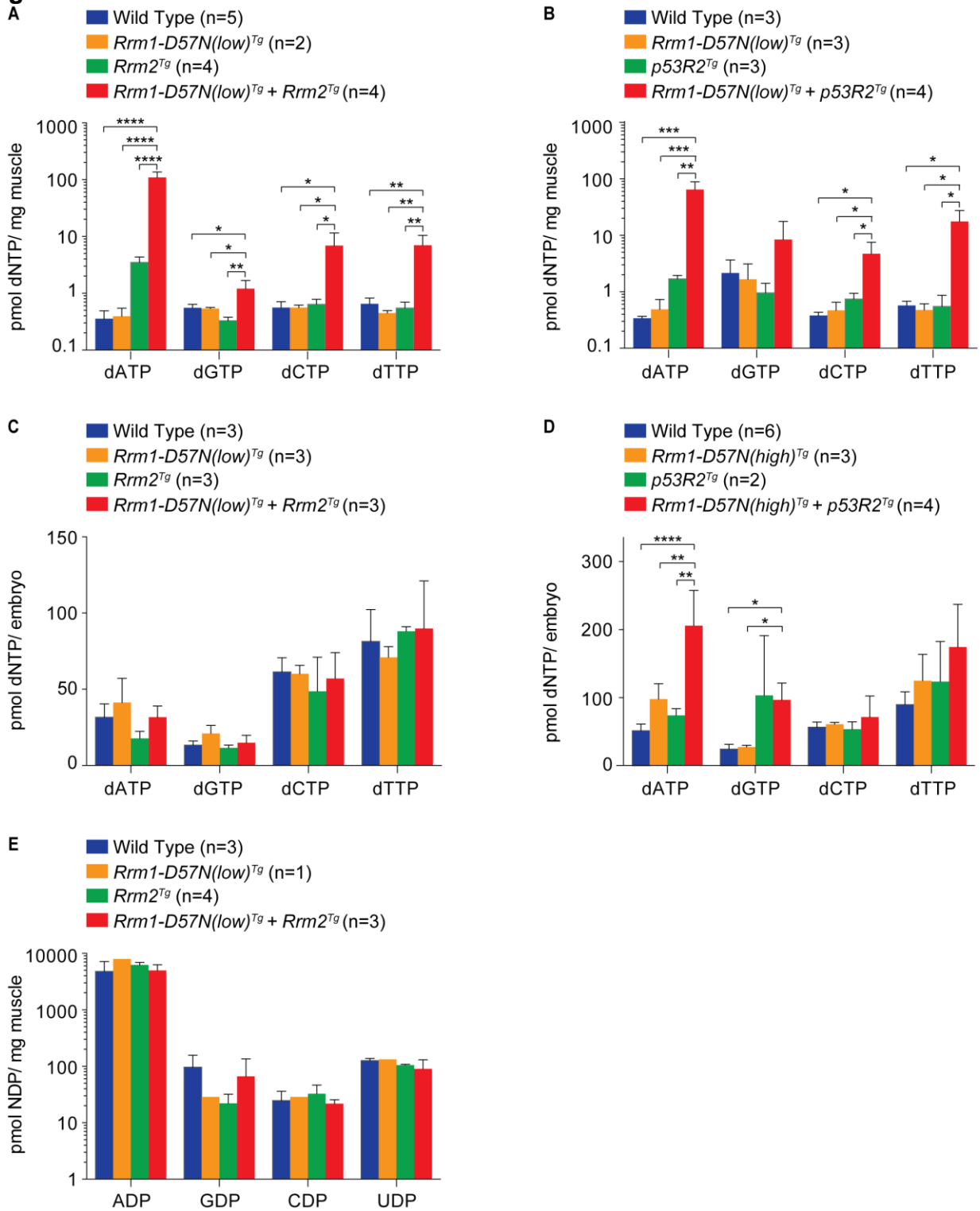


Figure 5

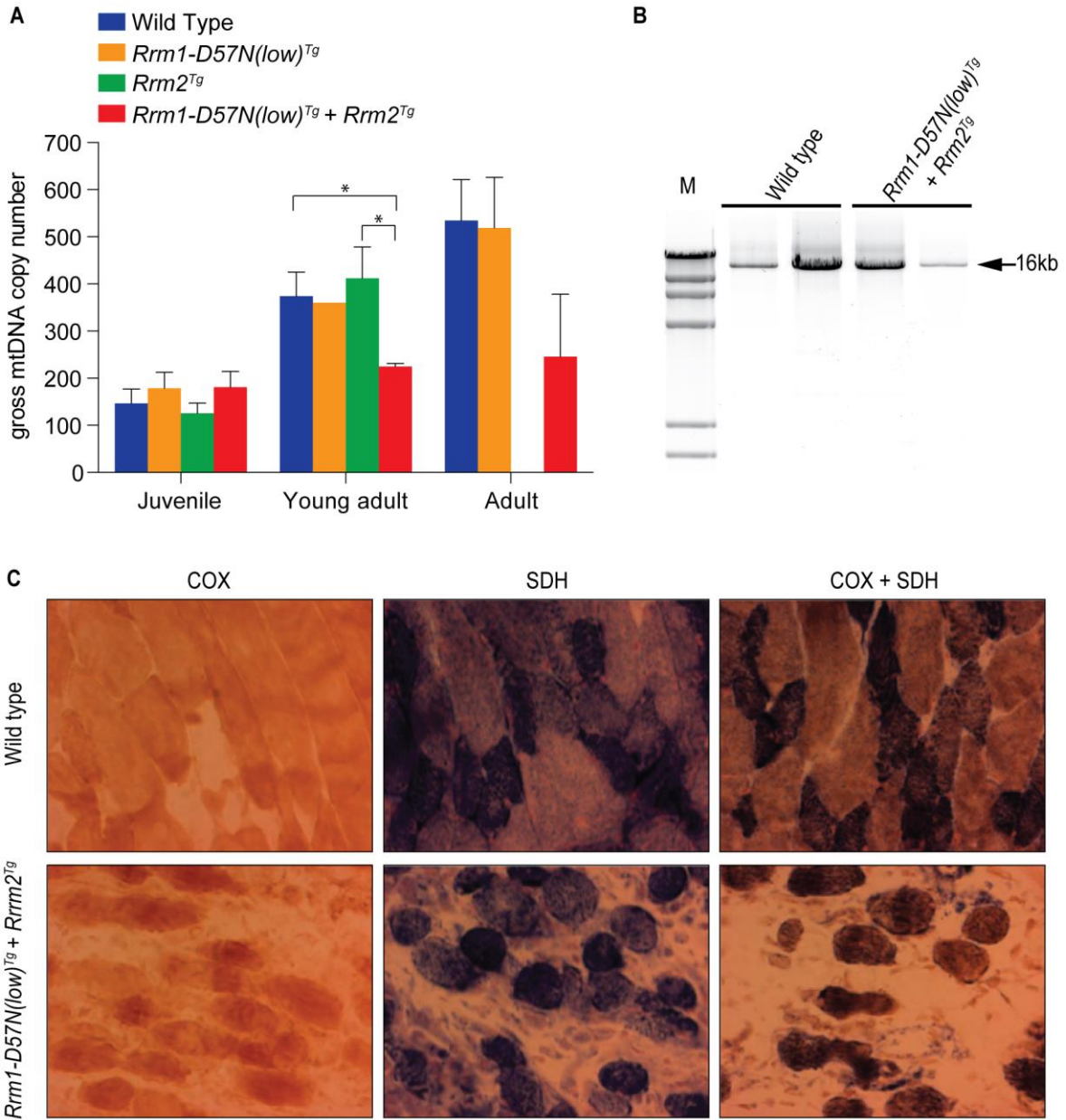


Figure 6

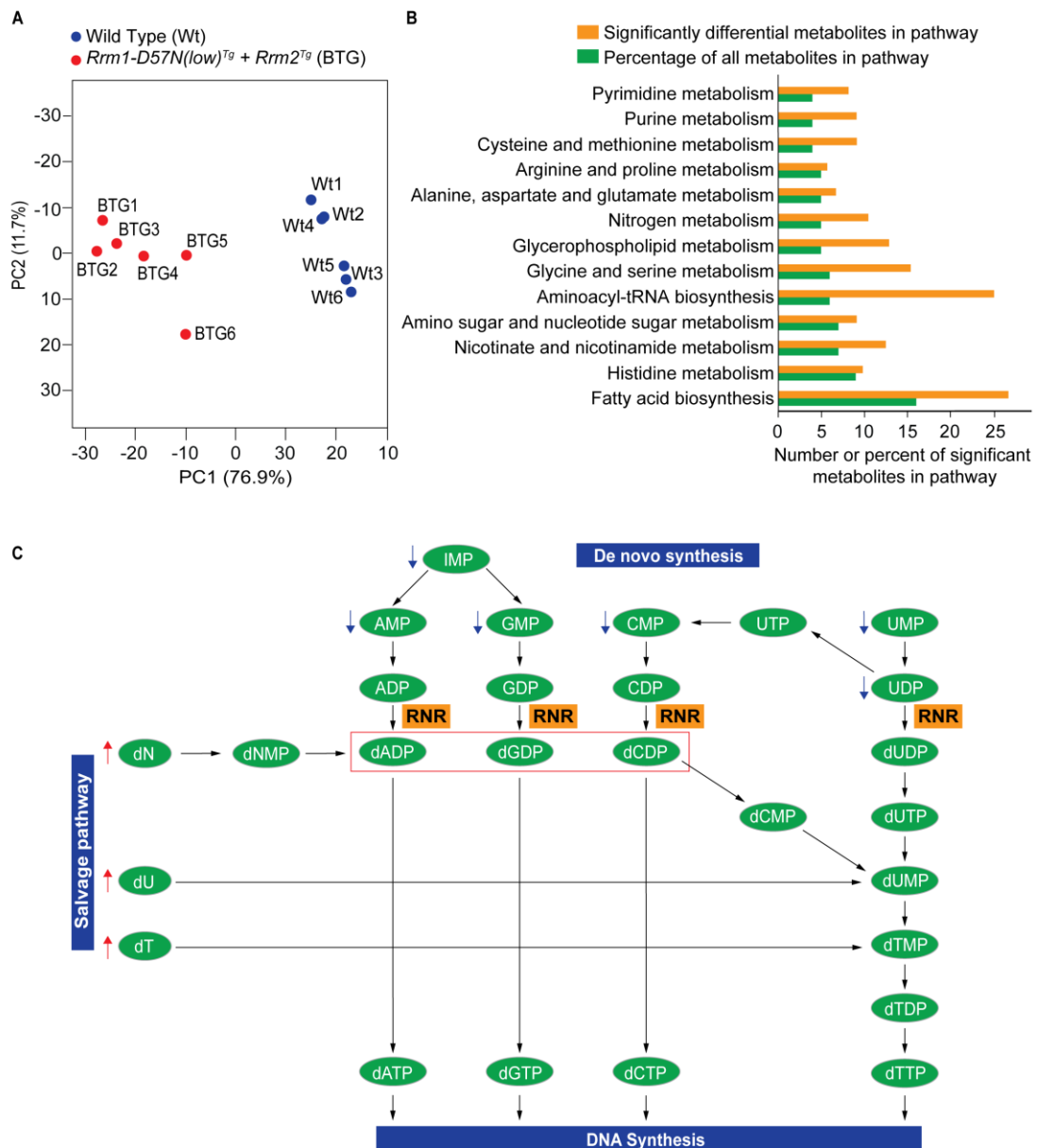


Table 1. Synthetic lethality upon simultaneous overexpression of *Rrm1*-D57N and either small RNR subunit.

CROSS	GENOTYPE	# OFFSPRING
<i>Rrm1^{Tg} x p53R2^{Tg}</i>	Wild type	29 (37.25)
	<i>Rrm1^{Tg}</i>	52 (37.25)
	<i>p53R2^{Tg}</i>	35 (37.25)
	<i>Rrm1^{Tg} + p53R2^{Tg}</i>	33 (37.25)
<i>Rrm1-D57N(high)^{Tg} x p53R2^{Tg}</i>	Wild type	51 (30)
	<i>Rrm1^{Tg}</i>	40 (30)
	<i>p53R2^{Tg}</i>	29 (30)
	<i>Rrm1-D57N(high)^{Tg} + p53R2^{Tg}</i>	0 (30)*
<i>Rrm1-D57N(low)^{Tg} x p53R2^{Tg}</i>	Wild type	77 (51.25)
	<i>Rrm1^{Tg}</i>	68 (51.25)
	<i>P53R2^{Tg}</i>	60 (51.25)
	<i>Rrm1-D57N(low)^{Tg} + p53R2^{Tg}</i>	0 (51.25)*
<i>Rrm1^{Tg} x Rrm2^{Tg}</i>	Wild type	57 (48.75)
	<i>Rrm1^{Tg}</i>	54 (48.75)
	<i>Rrm2^{Tg}</i>	38 (48.75)
	<i>Rrm1^{Tg} + Rrm2^{Tg}</i>	46 (48.75)
<i>Rrm1-D57N(high)^{Tg} x Rrm2^{Tg}</i>	Wild type	33 (26.5)
	<i>Rrm1^{Tg}</i>	35 (26.5)
	<i>Rrm2^{Tg}</i>	38 (26.5)
	<i>Rrm1-D57N(high)^{Tg} +Rrm2^{Tg}</i>	0 (26.5)*
<i>Rrm1-D57N(low)^{Tg} x Rrm2^{Tg}</i>	Wild type	96 (69.75)
	<i>Rrm1^{Tg}</i>	93 (69.75)
	<i>Rrm2^{Tg}</i>	85 (69.75)
	<i>Rrm1-D57N(low)^{Tg} + Rrm2^{Tg}</i>	5 (69.75)*

Note: Mice harboring *Rrm1*^{Tg}, *Rrm1-D57N(low)*^{Tg}, or *Rrm1-D57N(high)*^{Tg} were crossed to mice carrying either the *Rrm2* or *p53R2* transgene. Progeny were genotyped at weaning by Southern blot. Observed numbers of animals of each genotype are indicated with expected number in parentheses. * $p < 0.05$, χ^2 test.

Simultaneous Disruption of Ribonucleotide Reductase Regulatory Mechanism Causes Synthetic Lethality in Mice

Jennifer L. Page^{*,1}, **Yashira L. Negrón Abril^{*,†,1}**, Minxing Li^{*}, Gabriel Balmus^{*}, Emil Ylikallio[‡], Yejoo Jeon^{*}, Marc O. Warmoes[§], Eva Oxford^{*}, Saba Parvez[†], Yasmine Zerrad^{*}, Xia Xu^{*}, Joshua Levy^{*}, Henna Tynismaa[‡], Rachel M. Peters^{*}, Teresa Southard^{*}, Katie Kelly^{*}, Anu Suomalainen[‡], Yimon Aye[†], Jason W. Locasale[§] and Robert S. Weiss^{*,2}

SUPPLEMENTAL INFORMATION

Supplemental Materials and Methods

Supplemental Tables (S1-S7)

Supplemental Figures (S1-S5)

Supplemental References

SUPPLEMENTAL MATERIALS AND METHODS

Plasmids

An expression plasmid encoding mouse *Rrm1* was constructed in the pCaggs expression vector as described previously by Xu, *et al.* (Xu, *et al.* 2008). Relative to the previously reported *Rrm1* transgene construct, UTR sequences were removed in order to improve expression. The *Rrm1* open reading frame (ORF) was amplified from pCaggs-*Rrm1* with primers F: 5'-CTCGTCGACATGCATGTGATCAAGCGAGATGGC-3' and R: 5'-TCAGGATCCACACATCAGGCACTC-3'. The PCR product was cloned into pCR2.1 with the Topo-TA cloning kit (Stratagene). Following sequencing analysis of the insertion fragment ends to confirm the absence of PCR-induced mutations, the PCR-amplified *Rrm1* sequence was digested out with *Stu*I and replaced by the non-amplified *Stu*I fragment from pCaggs-*Rrm1*. Fragment orientation was confirmed by *Sph*I and *Eco*RI digestion. The *Rrm1* ORF was then excised from pCR2.1 with *Sal*I/*Xho*I and ligated into *Xho*I-linearized pCaggs. Fragment orientation was confirmed by *Bam*HI and *Sal*I/*Xho*I digests. The *Rrm1*-D57N mutation was inserted by site-directed mutagenesis. Briefly, primers D57N (5'-CCACAGTGGAACTGAACACCCTGGCTGCT-3') and D57N-AS (5'-AGCAGCCAGGGTCAGTTCCACTGTGG-3') were used to amplify the entire pCaggs-*Rrm1* plasmid. Following *Dpn*I digestion, products were transformed into DH5a and cultured on NZY⁺ medium. The presence of the mutation was confirmed by *Xcm*I digest, as the D57N mutation destroys an *Xcm*I site. The

pCaggs-*Rrm1*-D57N clone was confirmed to be free of other mutations by sequencing.

Generation of transgenic mice

Transgenic mice were generated by microinjection of linear plasmid DNA into the male pronucleus of FVB/N zygotes. The pCaggs-*Rrm1*-D57N plasmid was linearized by Sall digestion. Transgenic founder mice were identified by Southern blot analysis. Transgenic mice were maintained as hemizygotes on the FVB/N inbred background strain. Genotyping of mice expected to carry a single RNR transgene was performed as previously described by Xu *et al.* (Xu *et al.* 2008).

Pathological assessment of the heart

Fixed hearts were cut in either the coronal and transverse plane. Hearts cut in the coronal plane were positioned with forceps so that one auricle was positioned above the opposite auricle. The longitudinal cut was made vertically down through the two auricles to reveal all four chambers (right and left atrium, right and left ventricles). To observe ventricle cavity and wall thickness, transverse cuts were made by making a horizontal cut right below the auricles of each heart. To quantify ventricle morphology, transversely cut hearts embedded in paraffin and stained with H&E stain were scanned using Amperio ScanScope. The area of the whole heart cross-section, the left ventricle, and right ventricle were measured using Amperio ImageScope program. The diameter of the heart was obtained by measuring the length of the cross sectional area. The diameter line

was drawn such that it cut halfway through the right ventricle and the left ventricle. Along this same line, the right ventricle wall thickness was obtained by measuring the distance from the right ventricle exterior to the adjacent outer wall of the heart. The interventricular septum wall thickness was measured between the left and right ventricle wall. The left ventricle exterior (edge farther from the interventricular septum) to the adjacent outer wall of the heart was measured as the left ventricle wall. The proportion of each length to the whole diameter was quantified. Only hearts cross sections that did not seem to show artifacts from the atrial area were measured. Significance was evaluated through JMP by the Student's T- test with $\alpha = 0.05$ and when applicable, $\alpha = 0.005$.

Immunohistochemistry on tissue sections

Tissue sections (5 μ m thickness) were deparaffinized, rehydrated in graded alcohols. Antigen retrieval was performed by microwaving the slides in 0.01M sodium citrate (40 minutes). After incubation in 30% hydrogen peroxide and BSA blocker, sections were incubated with Phospho-histone H3 primary antibody (Millipore, 06-570) overnight at 4°C. Immunoreactivity of PH3 was visualized using Histostain bulk kit from Invitrogen. Slides were scanned and viewed as previously described. Ten HPF images per mouse were used to quantify PH3 positive cells. Unpaired t-test with Welch's correction was used to evaluate the significance. COX/SDH staining was performed as described by Tyynismaa *et al.* (Tyynismaa *et al.* 2005).

Echocardiography

Neonatal mice (6-8 days of age) were anesthetized with isoflurane and echocardiograms were performed using a Visual Sonics Vevo-2100 ultrasound fitted with an MS-700 ultrasound probe. The body temperature was maintained at 36-37°C. M-mode measurements were obtained from a right parasternal short axis view of the heart at the level of the papillary muscles.

Immunoblot analysis

Tissue extracts were prepared by lysis in RIPA buffer (150mM NaCl, 50mM NaF, 1% NP-40, 0.8% DOC, 0.1% SDS, 50 mM Tris pH 8.0, and 50 mM EDTA) supplemented with protease inhibitors (apropinin, 2µg/mL; leupeptin 2µg/mL, and PMSF, 20 µg/mL) and sodium orthovanadate (400 µM) as a phosphatase inhibitor. Extracts were separated on 10% polyacrylamide gel and transferred to PVDF membrane (Perkin Elmer). R1 protein was detected by AD203, mouse monoclonal anti-R1 (InRo Biomedtek), and loading was assessed by detection of α -tubulin with mouse monoclonal anti- α -tubulin (Sigma). To quantify overexpression in *Rrm1-D57N* transgenic mice, serial dilutions were prepared in RIPA buffer. The same sample volume necessary for 25 µg of total protein from undiluted lysate was used for the dilution samples. Chemiluminescent signal was detected on a VersaDoc Imaging system and quantified using Quantity One software (Bio-Rad Laboratories). Band intensity was determined for each dilution series sample and plotted following subtraction of background signal. The measured intensity for each undiluted wild-type band was fitted to the generated

line for the corresponding *Rrm1-D57N^{Tg}* dilution series. Fold overexpression values were corrected for loading by standardization based on α -tubulin signal.

Measurement of Ribonucleotide Reductase activity

To measure the activity of recombinant RNR, assay buffer in a final volume of 130 μ L, containing, in final concentrations, 50 mM Hepes (pH 7.6), 15 mM MgCl₂, 3 mM ATP, 2mM NADPH, 0.1 mM TR, 1 μ M TRR, 0.3 μ M hRNR1 (WT/D57N), +/- 0.3 mM dATP, and 0.5 mM [5-³H]-CDP (Specific activity: 25,000 cpm/ nmol) was incubated in a 37 °C water bath for 1 min after which 3 μ M reconstituted human RNR2 was added and the assay mixture was incubated. 30 μ L of the reaction mixture was removed at the indicated time points and quenched with 30 μ L of 2% HClO₄ and then neutralized with 30 μ L of 0.4M NaOH. Dephosphorylation, separation of the [5-³H]-dCDP product, and liquid scintillation counting were performed as follow: To the reaction mix, 1 mM dC, 10U Calf Alkaline Phosphatase in dephosphorylation buffer [100 mM Tris-HCl (pH 8.5)] was added in a final volume of 500 μ L and incubated at 37 °C for 2 hours. 450 μ L of the dephosphorylated sample was then loaded onto a borate resin, washed first with 550 μ L ddH₂O and twice subsequently with 3.5 mL ddH₂O. One milliliter of the flow through was added with 9 mL of scintillation solution (Perkin-Elmer, 6013389) and the radioactivity was measured using a scintillation counter (Beckman Coulter, LS6500). To measure the activity of RNR in tissue lysates, 400-600 mg of frozen mouse skeletal muscle tissue was ground to a fine powder using a pestle and mortar and transferred to an Eppendorf tube. The tissue

powder was suspended in 50 μ L of assay buffer [50 mM Hepes buffer (pH 7.6) containing 15 mM $MgCl_2$ and protease inhibitor (Roche, 11836170001)]. The suspension was subject to 3 cycles of rapid freeze-thaw followed by centrifugation at 18,000 x g for 8 min in a pre-chilled (4°C) centrifuge. Meanwhile, assay buffer in a final volume of 130 μ L, containing, in final concentrations, 50 mM Hepes (pH 7.6), 15 mM $MgCl_2$, 3 mM ATP, 10 mM DTT, 10 mM NaF, +/- 0.3 mM dATP and 0.5 mM [5- 3H]-CDP (Specific activity: 25,000 cpm/ nmol) was incubated in a 37 °C water bath for 1.5 min after which 6 μ M reconstituted human RNR2 was added and the assay mixture was incubated for an additional 30 s. The reaction was initiated by the addition of clarified tissue lysate (i.e., the supernatant collected post centrifugation above) and assay buffer such that the total assay volume was brought up to 130 μ L. (Around 5 μ L lysate was flash frozen and saved for the subsequent determination of protein concentration using Bradford assay). 30 μ L of the reaction mixture was removed at the indicated time points, quenched and neutralized. Same procedure as discussed above was used for the dephosphorylation, separation of the [5- 3H]-dCDP product and quantification.

qRT-PCR

For mtDNA quantification, qRT-PCR reactions were done with 25 ng total DNA used as template and normalizing the *mt-Cytb* gene amplification level (primer sequences: 5'-GCTTTCCACTTCATCTTACCATTTA-3' and 5'-TGTTGGGTTGTTTGATCCTG-3') against the amplification level of *Rbm15*,

which was used as a nuclear DNA control (primer sequences: 5'-GGACACTTTTCTTGGGCAAC-3' and 5'-AGTTTGGCCCTGTGAGACAT-3'). Samples were run on an Abi Prism SDS 7000 machine (Applied Biosystem). Amplification conditions were: 95°C for 7 minutes followed by 35 cycles of 95°C for 10 seconds and 60°C for 30 seconds. Dissociation curves were checked to ensure the existence of a single PCR product. Each sample was run in duplicate, and samples with significant variation between duplicates were excluded. QPCR data were analyzed using 7000 System Sequence Detection Software version 1.2.3 (Applied Biosystems).

Long PCR

Long PCR to amplify the entire mitochondrial genome or selectively deleted mtDNA molecules was done using the Expand Long Template PCR System (Roche). 25 ng total DNA was used as template. Cycling conditions were: 92°C for 2 minutes followed by 30 cycles of 92°C for 10 seconds and 68°C for 12 minutes. PCR products were separated by electrophoresis on 1% agarose gels and visualized with a Typhoon 9400 scanner (Amersham Biosciences). Primers hybridized to the control region of mtDNA located at nucleotide positions 1953-1924 and 2473-2505 (primer sequences 5'-GAGGTGATGTTTTTGGTAAACAGGCGGGGT-3' and 5'-GGTTCGTTTGTTC AACGATTAAAGTCCTACGTG -3').

Extraction of nucleotides from neonate skeletal muscle and embryos

Total nucleotides were extracted from neonatal skeletal muscle using the method described by Ylikallio *et al.* (Ylikallio, *et al.* 2010) with the following modifications: Neonates were euthanized by decapitation and immediately dissected in order to prevent nucleotide degradation. Skeletal muscle harvested from all four limbs was pooled together and immediately chilled on dry ice. The sample was weighed and snap-frozen in liquid nitrogen. Samples were stored at -80 °C until nucleotides were extracted. Samples were homogenized in cold 10% trichloroacetic acid+15mM MgCl₂ for 1 minute in a Qiagen TissueLyser. Halfway through, samples were incubated on ice for 30 sec. Embryos at e10.5 were removed from the uterus and yolk sac in cold 1x PBS and immediately ground in 100 µL of cold 0.4N perchloric acid using a microcentrifuge tube-fitting pestle. Following homogenization, samples were incubated on ice for 20 minutes. The rest of the extraction was performed as previously described by Ylikallio, *et al.* (Ylikallio, *et al.* 2010).

Measurement of nucleotide pools

dNTPs were measured using an indirect enzymatic assay as reported by Ferraro *et al.* (Ferraro *et al.* 2010). Standard curves were prepared from concentrated stocks of pure individual dNTPs (Fermentas). Reactions in 50 µL total volume were incubated for 1 hour and then 30µL was spotted to Whatman DE81 paper discs and dried. Discs were washed three times in 5%Na₂HPO₄, and once each in dH₂O and 95% EtOH. Discs were dried and counted on a Beckman Coulter LS6500 scintillation counter. Measurement of ribonucleosides was performed as

in N. Kochanowski *et al.* (Kochanowski *et al.* 2006) with modifications. Analyses were carried out on a Shimadzu UHPLC system. Samples were separated on a Supelco LC-18T column in 30mM KH_2PO_4 and 10mM tetrabutylammonium hydrogen sulfate, pH 6.5 : methanol (A=91.7:8.3, B=71.6:28.4) over a 40 minute time period. The program ran 0%-100%B from 0-24 minutes, 1 minute at 100% B, and 100%-0% B from 25-30 minutes at a flow rate of 1 mL/minute. Identities of analytes were confirmed both by comparison of elution time to known standards and by wavelength of maximum absorbance (λ_{max}). Sample extracts in which ATP comprised less than 65% of the total adenine nucleotides were excluded from further analysis.

SUPPLEMENTAL TABLES

Table S1 (related to Figure 1). *Rrm1*-D57N transgenic mice are obtained at expected frequencies^a

Cross	Genotype	# offspring
Wild type FVB x <i>Rrm1</i> -D57N(low) ^{Tg}	Wild type	256 (243.5)
	<i>Rrm1</i> -D57N(low) ^{Tg}	231 (243.5)
Wild type FVB x <i>Rrm1</i> -D57N(high) ^{Tg}	Wild type	275 (260.5)
	<i>Rrm1</i> -D57N(high) ^{Tg}	246 (260.5)

^a Mice harboring *Rrm1*-D57N(low)^{Tg} or *Rrm1*-D57N(high)^{Tg} mice were crossed to wild type FVB mice. Progeny were genotyped at weaning by PCR. Observed numbers of animals of each genotype are indicated with expected number in parentheses.

Table S2 (related to Figure 2). Lifespan of *Rrm1*-D57N(high)^{Tg} + *p53R2*^{Tg} bitransgenic embryos^a

Rrm1-D57N(high) ^{Tg} x p53R2 ^{Tg}									
	Wild type		Rrm1-D57N ^{Tg}		p53R2 ^{Tg}		Rrm1-D57N(high) ^{Tg} + p53R2 ^{Tg}		
stage	# obs	(#exp)	# obs	(#exp)	# obs	(#exp)	# obs	(#exp)	resorptions
9.5	5	4.5	6	4.5	3	4.5	4(1)	4.5	2
10.5	37(3)	26.75	24	26.75	14	26.75	32(1)	26.75	8
11.5	54	30.5	29	30.5	36	30.5	13(3)	30.5	19
12.5	25	16.5	14	16.5	16	16.5	11(11)	16.5	9
13.5	12	10.25	17(2)	10.25	10(1)	10.25	2(2)	10.25	1
14.5	7	4	5	4	4	4	0	4	0

^a Females harboring the *Rrm1*-D57N(high) transgene were mated to males harboring the *p53R2* transgene. At the indicated timepoints (in days post coitus or dpc) females were euthanized by CO₂ asphyxiation and the embryos analyzed. DNA isolated from the yolk sacs was genotyped by Southern blot analysis. Total numbers of embryos of each genotype observed are indicated with expected numbers in parentheses.

Table S3 (related to Figure 2). **Lifespan of *Rrm1-D57N*(high)^{Tg} + *Rrm2*^{Tg} bitransgenic embryos^a**

Rrm1-D57N(high) ^{Tg} x Rrm2 ^{Tg}									
	Wild type		Rrm1-D57N ^{Tg}		Rrm2 ^{Tg}		Rrm1-D57N(high) ^{Tg} + Rrm2 ^{Tg}		
stage	# obs	(#exp)	# obs	(#exp)	# obs	(#exp)	# obs	(#exp)	resorptions
9.5	3	4	5	4	3	4	5	4	0
10.5	7	7.25	3	7.25	11	7.25	8(1)	7.25	3
11.5	6	6	6	6	7	6	5	6	9
12.5	8	10	7(1)	10	16	10	9(1)	10	2
13.5	2	8.25	7	8.25	13(1)	8.25	11(6)	8.25	1
14.5	2	4	2	4	7	4	5(3)	4	1
15.5	7	9.25	9(1)	9.25	11(1)	9.25	10(7)	9.25	1
16.5	1	4	3	4	7	4	5(1)	4	0
17.5	7	7	6	7	12(1)	7	4(3)	7	0
18.5	11(1)	8.75	7	8.75	17	8.75	0	8.75	7
19.5	4	2.75	4(1)	2.75	3	2.75	0	2.75	0
P0	9	4.5	3	4.5	4	4.5	2(2)	4.5	0

^a Females harboring the *Rrm1*-D57N(high) transgene were mated to males harboring the *Rrm2* transgene. At the indicated timepoints in days post coitus or dpc) females were euthanized by CO₂ asphyxiation and the embryos analyzed. DNA isolated from the yolk sacs was genotyped by Southern blot analysis. Total numbers of embryos of each genotype observed are indicated with expected numbers in parentheses.

Table S4 (related to Figure 3). **Summary of body weight, heart weight, and heart to body weight ratio for wild type and Rrm1-D57N(low)^{Tg} + Rrm2^{Tg} mice^a**

Genotype	Mouse ID	Age	Heart/body weight	Mean \pm SEM
Wild type	WT1	P6	0.0089	0.0068 \pm 0.0005
	WT2	P6	0.0070	
	WT3	P6	0.0056	
	WT4	P6	0.0078	
	WT5	P8	0.0058	
	WT6	P8	0.0052	
	WT7	P8	0.0075	
Rrm1-D57N(high)^{Tg} + Rrm2^{Tg}	BTG1	P6	0.0091	0.0113 \pm 0.0011*
	BTG2	P6	0.0076	
	BTG3	P6	0.0093	
	BTG4	P6	0.0134	
	BTG5	P8	0.0116	
	BTG6	P8	0.0122	
	BTG7	P8	0.0162	

^aBody and heart weight were measured for seven pairs of bitransgenic and control mice from the same litter (1-7). Heart to body weight ratio was calculated. * Bitransgenic mice had significantly increased heart to body weight compared to their control littermates (p=0.0031, Unpaired T-test)

Table S5 (related to Figure 3 and Figure S4). **M-mode (right parasternal short axis) echocardiographic measurements^a**

AVG Measurements	Wild type (n=4)	<i>Rrm1-D57N(low)^{Tg} + Rrm2^{Tg} (n=3)</i>
IVS Diastole (mm)	0.51 ± 0.12	0.46 ± 0.09
IVS Systole (mm)	0.80 ± 0.08	0.50 ± 0.10
LVFW Diastole (mm)	0.64 ± 0.12	0.46 ± 0.08
LVFW Systole (mm)	0.90 ± 0.13	0.51 ± 0.13
LVID Diastole (mm)	2.33 ± 0.36	2.55 ± 0.22
LVID Systole (mm)	1.23 ± 0.32	2.27 ± 0.33
Fractional Shortening (%)	47.34 ± 10.64	10.86 ± 9.79

^aAverage M-Mode echocardiographic measurements from the right parasternal short axis view of the heart of 4 WT and 3 bitransgenic mice. IVS (Interventricular Septum), LVFW (left ventricular free wall), LVID (left ventricular internal diameter), mm (millimeters).

Table S6 (related to Figure 6 and Figure S5). **List of differential metabolites in the purine and pyrimidine metabolism^a**

Pathway	Metabolite name	p-value t test	Fold Change
Purine metabolism	AMP	0.016005030	-20.76228369
	GMP	0.004647431	-9.362703288
	AIR	0.005980463	-2.80679423
	Inosine	0.007372458	-2.549259594
	Hypoxanthine	0.049149711	-2.158606562
	Glycine	0.002880878	1.339805793
	Deoxyinosine	6.80491E-08	24.88329957
	Deoxyadenosine	0.000144484	15.20253383
Pyrimidine metabolism	UMP	0.006323849	-7.706238833
	Pseudouridine 5'-phosphate	0.006357483	-7.635914545
	CMP	0.012497728	-5.515799943
	UDP	0.012685871	-2.303684243
	Uridine	0.017885909	-1.651225633
	N-Carbamoyl-L-aspartate	0.018851765	-1.642490867
	Cytidine	0.014050652	-1.617895588
	Thymidine	0.000348291	2.163989536
	Uracil	0.000208663	2.881647745
	Deoxyuridine	8.26473E-08	3.853914213
	Deoxycytidine	6.60698E-07	3.299096232
	Cytosine	1.88958E-06	3.193446704
	3-Ureidoisobutyrate	0.000813166	8.263965385
	dCMP	0.004866022	20.18931581
	Orotidine 5'-phosphate	0.000000001	42.96192763

^a Significant peaks ($p < 0.05$ and FDR < 0.05) were identified using t-statistics and the false discovery rate method by Benjamini & Hochberg (Benjamini and Hochberg, 1995).

Table S7 (related to Figure 6 and Figure S5). **Differential metabolites associated with various heart conditions^a**

Pathway	Metabolite Name	p-value t test	Fold Change
Purine metabolism	Adenosine monophosphate	0.016005	-20.762284
Nitrogen Metabolism	Taurine	0.005979	-1.396908
Amino acid metabolism	L-Glutamic acid	0.001129	-1.752943
	L-Aspartic acid	0.005562	-1.662126
Acyl-Carnitines and fatty acid metabolism	Phosphorylcholine	0.001504	-2.258348
	Glycerophosphocholine	0.007144	-2.122081
	Glycerol 3-phosphate	0.004763	-2.082439
	Propionylcarnitine	0.000051	-2.035061
	Dodecanoic acid	0.011492	-1.834362
	Succinylcarnitine	0.002943	-1.724781
	Butyrylcarnitine	0.000256	-1.660670
	Stearic acid	0.008851	-1.490892
	Dodecanedioic acid	0.007035	-1.373794
	Stearoylcarnitine	0.023869	1.928315
	L-Palmitoylcarnitine	0.006573	2.154932
	3-Hydroxyhexadecanoylcarnitine	0.008714	2.294344
	3-Hydroxy-9-hexadecenoylcarnitine	0.004390	3.026049

	Bilirubin	0.015088	5.216729
<hr/>			
	15(S)-Hydroxyeicosatrienoic acid	0.008840	-2.746080
Prostaglandin metabolism/	Eicosenoic acid	0.000514	-2.176045
Omega Fatty acids	8,11,14-Eicosatrienoic acid	0.000075	-1.666021
	Prostaglandin PGE2 glyceryl ester	0.000018	8.920992

^a Significant peaks ($p < 0.05$ and FDR < 0.05) were identified using t-statistics and the false discovery rate method by Benjamini and Hochberg (Benjamini and Hochberg, 1995).

SUPPLEMENTAL FIGURES

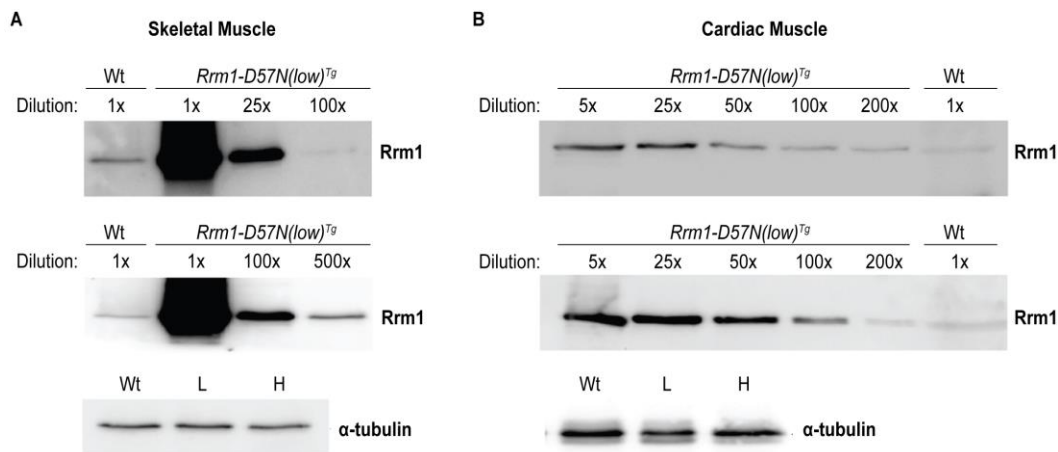


Figure S1 (related to Figure 1). **High-level overexpression of *Rrm1-D57N^{Tg}* in skeletal and cardiac muscle in mice.** (A-B) Dilution series of *Rrm1-D57N(low)^{Tg}* and *Rrm1-D57N(high)^{Tg}* lysates. Serial dilutions were prepared in RIPA lysis buffer before a constant volume was separated on a 10% SDS-PAGE gel. *Rrm1* was detected with mouse monoclonal anti-RRM1 antibody (AD203). Loading control. 25 μ g of each lysate was probed with mouse monoclonal anti- α -tubulin.

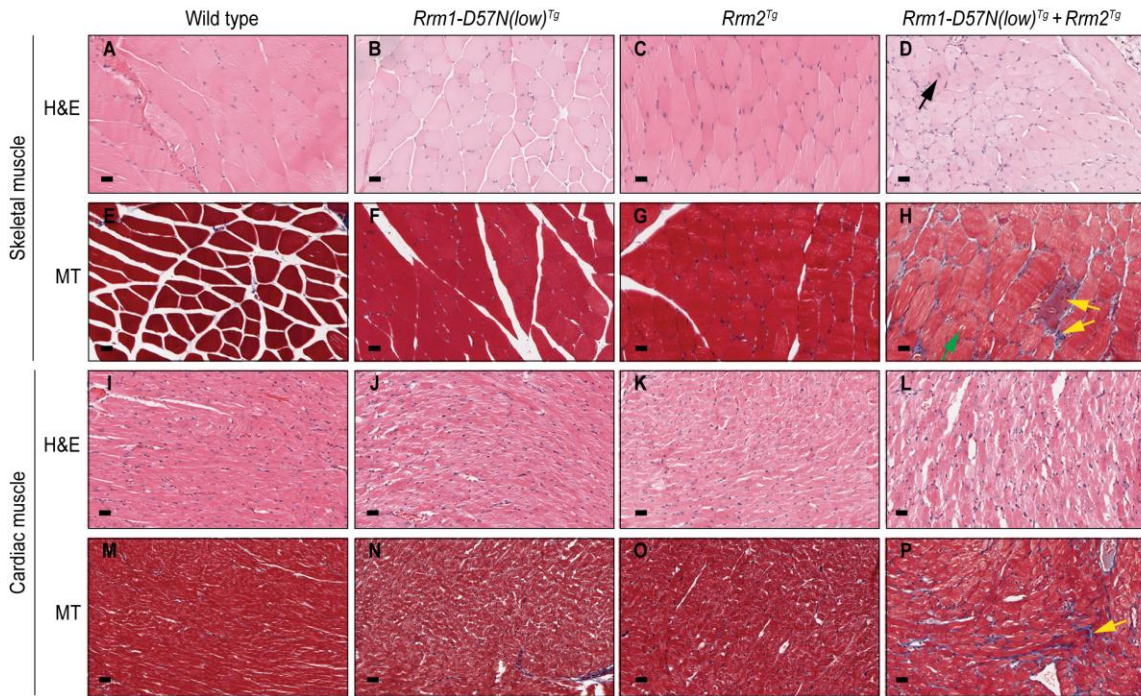


Figure S2 (related to Figure 2 or 3). **Muscle degeneration in *Rrm1-D57N(low)^{Tg} + Rrm2^{Tg}* bitransgenic adult mice.** Tissues from 90-day old mice were fixed overnight in formalin at room temperature prior to embedding and sectioning. Skeletal (**A-H**) and heart (**I-P**) muscles were stained with H&E or Masson's trichrome (MT). Both skeletal and cardiac muscles from bitransgenic mice display irregular fiber size and shape, large internal nuclei (black arrow), interstitial replacement fibrosis (yellow arrows), and vacuoles within muscle fibers (green arrow). Scale bars, 25 μ m.

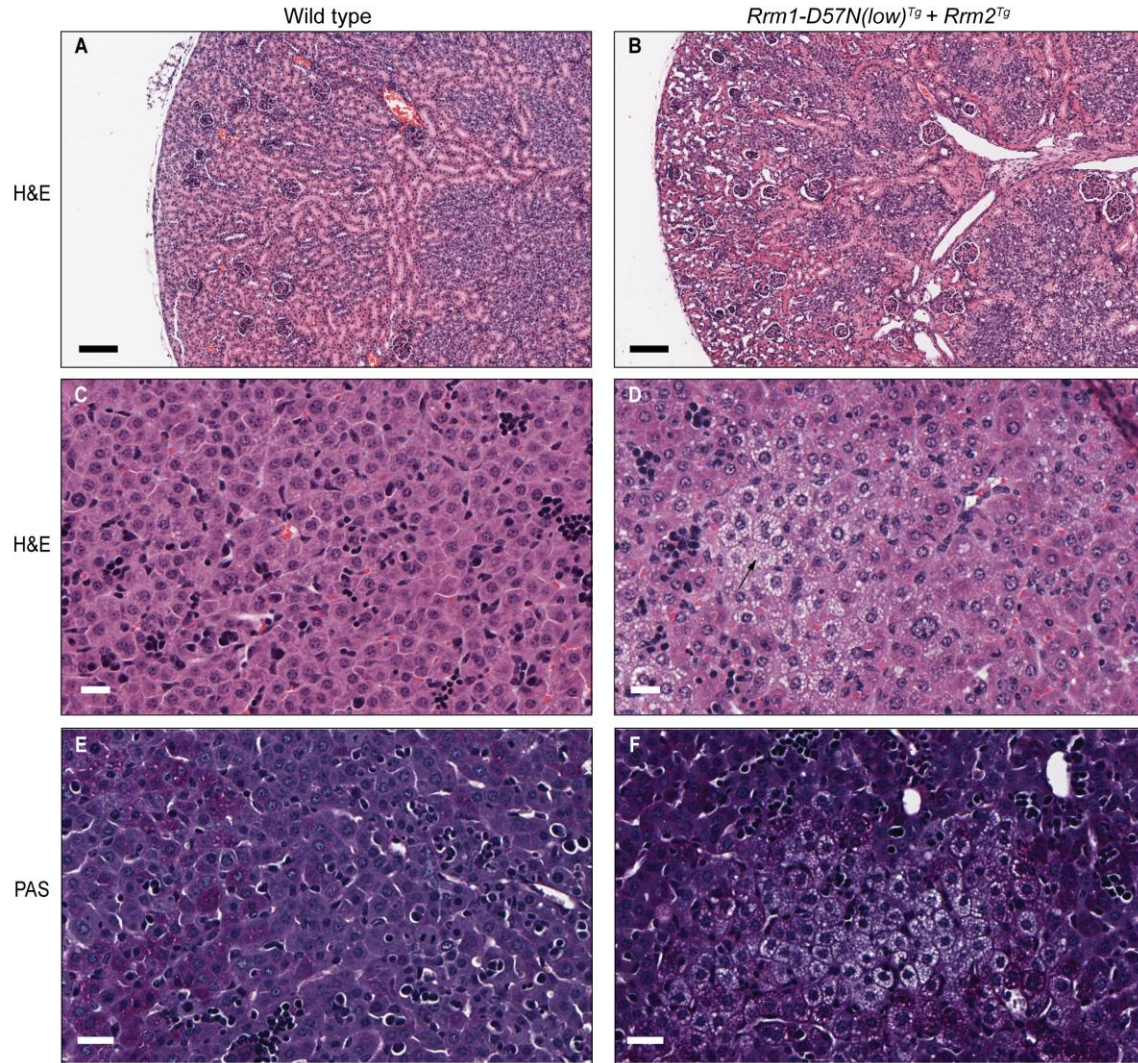


Figure S3 (related to Figure 2 or 3). **Tissue pathology in *Rrm1-D57N^{Tg} + Rrm2^{Tg}* bitransgenic mice.** (A-B) Kidney degeneration in bitransgenic mice. Tissues were harvested from bitransgenic and control littermates at P11 and fixed overnight in 10% formalin. Sections were stained with H&E. The bitransgenic shows degeneration of cortical tubules, dilated tubules in the medulla, and fibrosis. Scale bars, 100 μ m. (C-D) Hepatocellular swelling in bitransgenic liver. Tissues were harvested from bitransgenic and control littermates at P9 and fixed, sectioned, and H&E stained as previously. Black

arrow indicates focus of hepatocytes with abnormal accumulations of lipid or glycogen, leading to swollen appearance. Scale bars, 20 mm. **(E-F)** Periodic acid Schiff's stain of neonate livers from **(C-D)**. Hepatocytes with glycogen accumulation stain fuschia, while hepatocytes with lipid accumulation remain mostly white. Glycogen is abundant in the wild type liver but does not accumulate within hepatocytes. Scale bars, 25 mm.

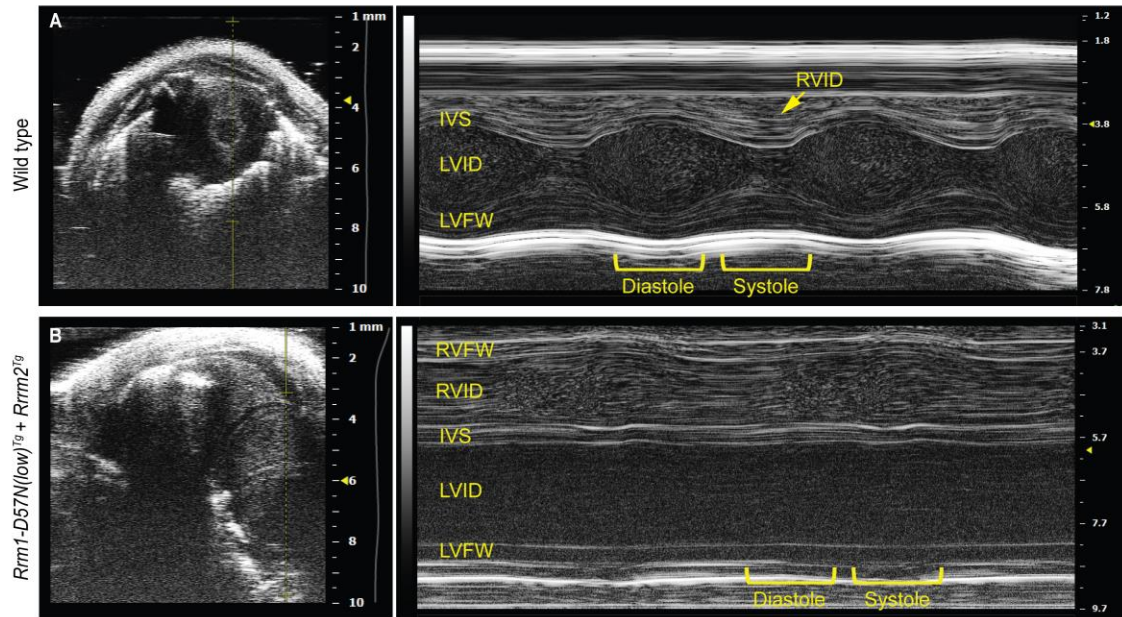


Figure S4 (related to Figure 3). **Representative M-mode echocardiographic images and measurements.** (A-B) Right parasternal short axis view (left panel) and M-mode tracing (right panel) for wild type and bitransgenic hearts. Juvenile mice (6-8 days of age) were anesthetized with isoflurane and echocardiograms were performed using a Visual Sonics Vevo-2100 ultrasound fitted with an MS-700 ultrasound probe. M-mode measurements were obtained from a right parasternal short axis view of the heart at the level of the papillary muscles. IVS (Interventricular Septum), LFW (left ventricular free wall), LVID (left ventricular internal diameter), RVFW (right ventricular free wall), RVID (right ventricular internal diameter).

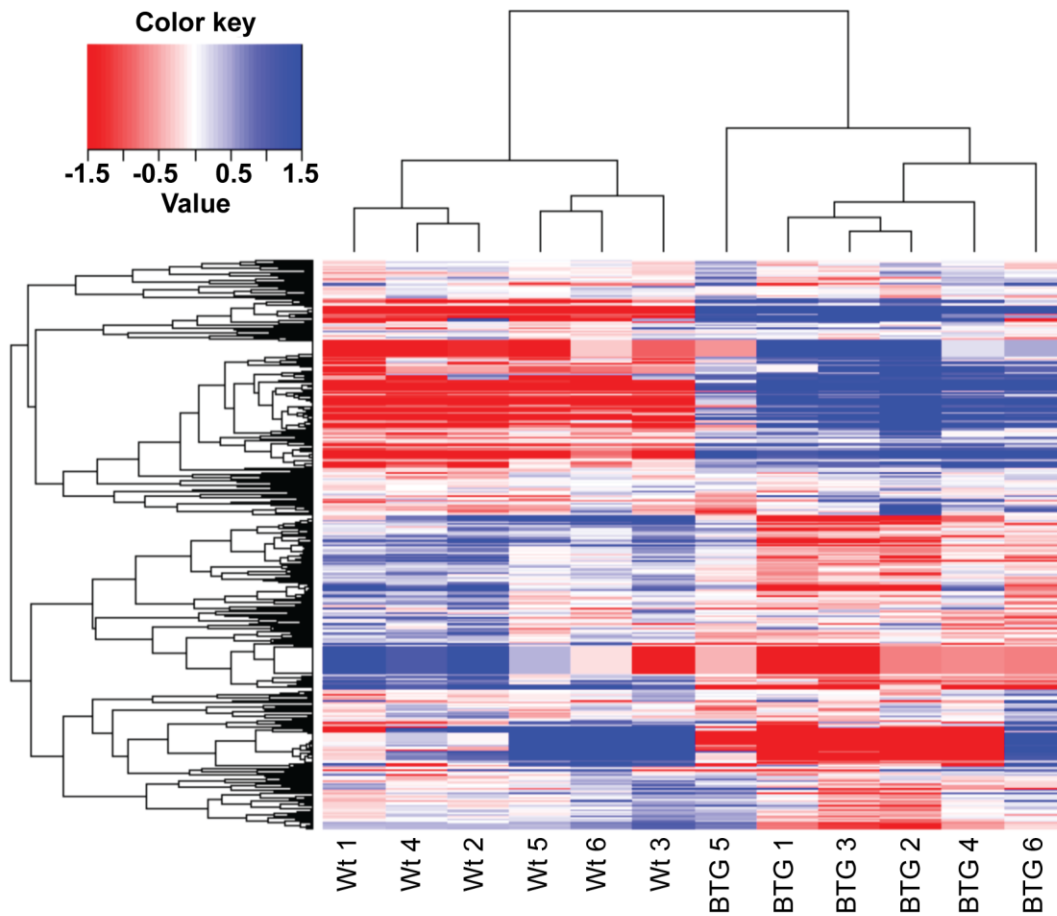


Figure S5 (related to Figure 6). **Hierarchical cluster analysis of metabolites identified using mass spectrometry.** In the clustering heat map, blue indicates upregulation, while red indicates downregulation. The dendrogram and heat map pattern show the separation into two groups (Wild type vs *Rrm1-D57N^{Tg}* + *Rrm2^{Tg}*) without using any prior statistical identification of differential metabolites indicating large overall differences in overall metabolite level.

SUPPLEMENTAL REFERENCES

- Ferraro, P., E. Franzolin, G. Pontarin, P. Reichard, V. Bianchi, 2010 Quantitation of cellular deoxynucleoside triphosphates. *Nucleic Acids Res.* 38(6): 85.
- Kochanowski, N., F. Blanchard, R. Cacan, F. Chirat, E. Guedon, *et al.*, 2006 Intracellular nucleotide and nucleotide sugar contents of cultured CHO cells determined by a fast, sensitive, and high-resolution ion-pair RP-HPLC. *Anal. Biochem.* 348(2): 243-251.
- Tyynismaa, H., K. Peltola Mjosund, S. Wanrooij, I. Lappalainen, E. Ylikallio, *et al.*, 2005 Mutant mitochondrial helicase Twinkle causes multiple mtDNA deletions and a late-onset mitochondrial disease in mice. *Proc. Natl. Acad. Sci. USA* 102(49): 17687-17692.
- Xu, X., J. L. Page, J. A. Surtees, H. Liu, S. Lagedrost, *et al.*, 2008 Broad overexpression of ribonucleotide reductase genes in mice specifically induces lung neoplasms. *Cancer Res.* 68: 2652-2660.
- Ylikallio, E., J. L. Page, X. Xu, M. Lampinen, G. Bepler, *et al.*, 2010 Ribonucleotide reductase is not limiting for mitochondrial DNA copy number in mice. *Nucleic Acids Res.* 38(22): 8208-8218.